UNIVERSIDADE DE SANTIAGO DE COMPOSTELA

Quantum Mechanical Study of the Electronic Structure of Low-Dimensional Systems at the Nanoscale

by

Manuel Pereiro López

A thesis submitted in partial fulfillment for the degree of Doctor of Philosophy

in the

Facultade de Física

Departamento de Física Aplicada

13^{th} July, 2010

Declaration of the Advisor

I, DANIEL BALDOMIR FERNÁNDEZ, professor of the Applied Physics Department at the University of Santiago de Compostela

DECLARE THAT:

- This thesis titled '*Quantum Mechanical Study of the Electronic Structure of Low-Dimensional Systems at the Nanoscale*' and the work presented in it was carried out by MANUEL PEREIRO LÓPEZ under my advising.
- The thesis is submitted in partial fulfillment for the degree of Doctor of Philosophy in the Applied Physics Department at the University of Santiago de Compostela.

Signed: _____

Date: 13^{th} July, 2010

Declaration of Authorship

I, MANUEL PEREIRO LÓPEZ, declare that this thesis titled, '*Quantum Mechanical Study of the Electronic Structure of Low-Dimensional Systems at the Nanoscale*' and the work presented in it are my own. I confirm that:

- This work was done wholly or mainly while in candidature for a research degree at this University.
- Where any part of this thesis has previously been submitted for a degree or any other qualification at this University or any other institution, this has been clearly stated.
- Where I have consulted the published work of others, this is always clearly attributed.
- Where I have quoted from the work of others, the source is always given. With the exception of such quotations, this thesis is entirely my own work.
- I have acknowledged all main sources of help.
- Where the thesis is based on work done by myself jointly with others, I have made clear exactly what was done by others and what I have contributed myself.

Signed:

Date: 13^{th} July, 2010

"In all affairs it's a healthy thing now and then to hang a question mark on the things you have long taken for granted."

Bertrand Russell

UNIVERSIDADE DE SANTIAGO DE COMPOSTELA

Abstract

Facultade de Física
Departamento de Física Aplicada

Doctor of Philosophy

by Manuel Pereiro López

In latter years, a new field has emerged from the understanding, control, and manipulation of objects at nanoscale level (nano-objects). It is commonly known as nanoscience. This field addresses a huge number of important issues starting from basic science and ending in a large variety of technological applications. Among the nano-objects, the small clusters or nanoclusters play a very important role, since they are the bricks of nanoscience. Therefore, the study of small clusters deserves a special attention. On the side of the technological applications in nanoscience, the study of the microscopic details of multilayer transition-metal systems is also very important because in this systems was discovered the giant magnetoresistance (GMR) effect. In this thesis we deal with transition-metal clusters and magnetic multilayers, both from a theoretical point of view, in such a way that the calculated atomic properties have been performed in the framework of the density functional theory. Thus, in the first part, we first studied the electronic structure, geometry, and magnetic properties of cobalt clusters ranging in size from the isolated atom up to a maximum of 13 cobalt atoms. After that, we concentrate our efforts in the study of small silver clusters with a number of atoms less or equal than 23 of which we have calculated the structure, static response to an external electric field, and the magnetic properties. Based on the magnetic properties we have found for these silver clusters, we have suggested a possible application of these clusters in biomedicine as magnetic drug delivery. We have also performed calculations of the electronic structure of the oxidized neutral and charged silver clusters. Eventually, we discussed the magnetic properties of cobalt-manganese alloy clusters, and in particular, the surprising enhancement of the magnetic moment recently observed in dilute CoMn alloy clusters was explained using *ab initio* methods.

On the other hand, in the second part of this thesis, we studied from *ab initio* methods the electronic structure and the magnetic properties of the Fe/Cr trilayer system. After the Fe/Cr system was well characterized from first principles calculations and the layer potentials were calculated, we used the theoretical models that we have developed to calculate the conductivity properties of the Fe/Cr system. We concentrate our efforts in the study of the GMR as a function of the interfacial scattering and the surface roughness. The importance of the *ab initio* monolayer potentials was also stressed in the thesis in order to confirm that the interface monolayers play a dominant role in the intrinsic GMR.

Preface

This thesis presents the work I have done under the supervision of Prof. Daniel Baldomir since joining the SpinTronics' group in the University of Santiago de Compostela. During this period, I have the privilege of working in many different areas, from numerical implementation of some electronic structure codes to the study of the mathematical foundations of density functional theory and the basis of atomic, molecular, and condensed matter physics. Also, in the free time and out of the scope of this thesis, we[1] have written some papers devoted to fundamental questions in electromagnetism and special theory of relativity. As a consequence of our sincere love to the mathematics, which impregnate our soul and I also expect in the future the people surrounding me, we have written some papers in the field of number theory.

The opening statement of the Bible: Genesis 1:1, "In the beginning God created the heavens and the earth," is probably the most famous line ever written. The mapping of the sentence to the situation in the initial stage of our group could be something like "In the beginning there was nothing but instead too much to create". We have not got computers, research projects, national or international colleagues in the cluster research field. We started from the scratch. We concentrate our efforts in the study of the giant magnetoresistance (GMR) effect of Fe/Cr trilayers from the theoretical point of view and in the study of the structural, electronic, and magnetic properties of small transition metal clusters by means of first-principles calculations. The first year and the major part of the second one were days of intense study of

[1] In this thesis "we" will sometimes refer to the author and sometimes to the author and co-authors. This will always be suitable, as per the traditions of written physics.

the main books which opened me the doors for understanding not only the basis of the different approximated methods for solving the Schrödinger equation (Hartree-Fock method, configuration interaction, coupled cluster method, density functional theory, ...) but also the theoretical methods in condensed matter physics. I have always considered that an strong education in mathematics and theoretical physics is the key point for theoretical physicists to deeply understand the consequences of their research. Unfortunately, I have seen that the new generations of PhD students do not share this argument. They prefer to publish the articles as soon as possible to be success but neglecting the theoretical education. I called this the culture of "fast-physics".

Shortly after I came to the Spintronic's group, we managed to access to the vectorial supercomputer machine in the Centro de Supercomputación de Galicia (CESGA) with a very restricted accounts and with a very limited time for the jobs submitted to the queue but however It's important to highlight here that this thesis could not be possible without the help of the CPUs hosted in the CESGA and the people working there. It is also important to remark here our collaboration with Prof. J. E. Arias, the head of the Instituto de Investigacións Tecnolóxicas. In very difficult times for our group, he gave us finantial support for going ahead.

In the field of GMR, we established international contacts with Prof. L. Wojctzak, Dr. K. Warda, Prof. G. Wiatrowski and Dr. P. Mlynarski in the solid state physics department of the Łódź University (Poland) and Dr. Sergey Mankovsky now in the department of chemistry of the Ludwig-Maximilians-Universtat Munchen (Germany). Our collaboration was very fruitful and we published a total number of 27 articles. Recently, I have visited them in Łódź during a stay of 3 months, and the atmosphere was extremely good for the constructive discussion about the theoretical aspects surrounding the GMR effect. In this topic, we had also a collaboration with Prof. H. Kobayashi of the department of chemistry and materials technology in the Kyoto Institute of Technology (Japan). He was visiting us during 1 month and during this period he helped us to use his band-structure code to calculate the electronic structure of Fe/Cr layers.

In the cluster research field, our first international contact was with Prof. M. Castro from the Departamento de Física y Química Teórica of the Universidad Nacional Autónoma de México (México) and also with Dr. P. Mlynarski. Both of them were working with Prof. D. Salahub in the University of Montreal. Prof. D. Salahub is one of the leading authors in the cluster's research field and in his group was developed the deMon's code for calculating the electronic properties of clusters. I was visiting the Castro's group during 6 months in a period of time

where the UNAM was on strike. They were difficult times for me and also for Prof. M. Castro but we managed to continue working in the study of small cobalt clusters. The paper that we obtained there was one of my most cited papers. We have also ties with Prof. E. Roduner from the Institut für Physikalische Chemie in Sttutgart (Germany). He is an experimentalist with an strong experience in the field of clusters. We are trying to understand and explain the giant diamagnetism they have found in Pt_{13} clusters.

Over the latter years, the group was growing with new PhD students which have improved the scientific quality of our group. Thanks to that, the group was able to compete and win new scientific projects to support the majority of the members of the group and also to buy new computers and to extent our knowledge beyond our initial dreams and hopes.

During this period, I have assisted a lot of congress, seminars, and conferences which have reinforced my knowledge about the magnetism and theoretical issues in condensed matter physics. It was a very fruitful period of my life with more than 50 published articles (see Appendix B) and which makes this thesis maybe greater in number of pages than expected. Sometimes it was frustrating because the period of time to obtain the results is large enough but most of the times, I really enjoy my research in physics because the challenges change from day to day.

Contents

List of Figures

List of Tables

Abbreviations

AE	**A**ll-**E**lectron
AF	**A**nti**F**erromagnetic
AP	**A**nti**P**arallel
BFGS	**B**royden-**F**letcher-**G**oldfard-**S**hanno
BSSE	**B**asis **S**et **S**uperposition **E**rrors
CI	**C**onfiguration **I**nteraction
CIP	**C**urrent-**I**n-the-**P**lane
CPP	**C**urrent-**P**erpendicular-to-the-**P**lane
deMon	**de**nsity of **Mon**tréal
DFT	**D**ensity **F**unctional **T**heory
DOS	**D**ensity **o**f **S**tates
ELF	**E**lectron **L**ocalization **F**unction
ERIs	**E**lectron **R**epulsion **I**ntegrals
ESR	**E**lectron **S**pin **R**esonance
FF	**F**inite **F**ield
FLT	**F**erromagnetic **L**ayer **T**hickness
FM	**F**erro**M**agnetic
FP-LAPW	**F**ull **P**otential-**L**inearized **A**ugmented **P**lane **W**ave
GGA	**G**eneralized **G**radient **A**pproximation
GS	**G**round **S**tate
GMR	**G**iant **M**agneto**R**esistance
GTO	**G**aussian-**T**ype **O**rbitals
HF	**H**artree-**F**ock

HLg	**H**OMO-**L**UMO gaps
HOMO	**H**ighest **O**ccupied **M**olecular **O**rbital
IP	**I**onization **P**otential
JT	**J**ahn-**T**eller
KSDFM	**K**ohn-**S**ham-**D**ensity-**F**unctional **M**ethodology
LCGTO	**L**inear **C**ombination of **G**aussian-**T**ype **O**rbitals
LDA	**L**ocal-**D**ensity **A**pproximation
LSDA	**L**ocal-**S**pin **D**ensity **A**pproximation
LUMO	**L**owest **U**noccupied **M**olecular **O**rbital
MBO	**M**ayer **B**ond **O**rder
MCP	**M**odel **C**ore **P**otential
MP	**M**odel **P**otential
MPA	**M**ulliken **P**opulation **A**nalysis
MR	**M**agneto**R**esistance
NS	**N**on**S**pherical
QW	**Q**uantum **W**ell
R2PI	**R**esonant **T**wo-**P**hoton-**I**onization
RB	**R**igid-**b**and
RKKY	**R**uderman-**K**ittel-**K**asuya-**Y**osida
SCF	**S**elf-**C**onsistent **F**ield
SFD	**S**ambe-**F**elton-**D**unlap
SP	**S**later-**P**auling
SPLEED	**S**pin-**P**olarizability **L**ow-**E**nergy **E**lectron **D**iffraction
TDDFT	**T**ime-**D**ependent **D**ensity **F**unctional **T**heory
TM	**T**ransition-**M**etal
VBS	**V**irtual **B**ound **S**tate
VIP	**V**ertical **I**onization **P**otential
VWN	**V**osko-**W**ilk-**N**usair
XC	e**X**change-**C**orrelation

Symbols

Roman symbols

E_a	Adsorption energy
V_a	Atomic volume
E_{bc}	Bulk cohesive energy
E_c	Cohesive energy
$J^{\alpha}_{\mu\sigma}$	Current density
m^*_{σ}	Effective electron mass
$f^0_{\mu\sigma}$	Fermi-Dirac distribution
E_f	Fermi level
k_F	Fermi wave vector
H	Magnetic field
$T_{\mu\sigma}$	Relaxation time
H_s	Saturation field
$\tilde{E}_{SCF}$	SCF energy
$S(\varepsilon)$	Strength function
Z_{TF}	Thomas-Fermi screening
r_{ws}	Wigner-Seitz radius
$v_{xc}(\mathbf{r}, t)$	XC potential

Greek symbols

Γ	Chemical order
σ	Conductivity
$\Delta_2 E$	Disproportionation energy
$\rho(\mathbf{r}, \omega)$	Electronic density
$\Delta\varepsilon$	HOMO-LUMO gap
χ_m	Magnetic susceptibility
$\bar{\alpha}$	Mean static polarizability
δ	Spillout of the electrons
γ^0	Surface energy

Dedicated in loving memory to my father—**Jesús**—*and living family unit*—**Inés, Betty, and Jesús**—*because love is the thread that binds us...*

1 Introduction to the Thesis

> *In exact sciences, every theory has a philosophical, mathematical, and empirical content. All these three aspects are equally important; if we neglect one of them, we sooner or later get into difficulties.*
>
> — Hans Primas

Synopsis

The guiding theme of this thesis is the study of the electronic structure of low-dimensional systems at the nanoscale. Thus, the structure of this thesis is divided in two main blocks. The first one is about the study of the structural, electric, and magnetic properties of small silver, cobalt and cobalt-manganese alloy clusters. The second part of the thesis is devoted to the study of the electronic structure of Fe/Cr trilayers. Moreover, we also study how the giant magnetoresistance (GMR) is affected by the interfacial scattering, surface roughness, ferromagnetic slab thickness and the layer potentials. Both parts of this thesis are studied by means of first-principles methods. In the next Sections, we describe and present a brief introduction to the topic of the transition metal clusters and the GMR.

1.1 Outline of the Thesis

The structure of the thesis is organized as follows: in the first part of the thesis, we begin in Chapter 2 describing the *ab initio* methods employed in the next Chapters to calculate the structural, electronic and magnetic properties of the clusters

studied in this thesis. In CHAPTER 3, we study the electronic structure, geometry, and magnetic properties of cobalt clusters from the atom up to a maximum of 13 atoms. From CHAPTER 4 to CHAPTER 9, we concentrate our efforts in the study of small silver clusters varying the size of the cluster from the atom up to 23 atoms. We have calculated the structure, static response to an external electric field (polarizabilities), and magnetic properties of these clusters in CHAPTERS 4, 5, and 6. In CHAPTER 7, we have suggested a possible application of silver clusters in biomedicine as magnetic drug delivery. We have also performed calculations of the electronic structure of oxidized neutral and charged silver clusters in CHAPTER 8. In CHAPTER 9, we discuss the magnetic properties of cobalt-manganese alloy clusters, in particular, the surprising enhancement of the magnetic moment recently observed in dilute CoMn alloy clusters is explained using *ab initio* methods.

In the second part of the thesis, the CHAPTER 10 is about the theoretical models we have developed to calculate the giant magnetoresistance in Fe/Cr trilayers. The conductivity models are based on the semiclassical Boltzmann equation but they introduce as a new element the "layer potentials" obtained by *ab initio* methods. In CHAPTER 11, we study from *ab initio* methods the electronic structure and the magnetic properties of the Fe/Cr trilayer system. After the Fe/Cr system is well characterized from first principles calculations and the layer potentials were calculated, we employed in CHAPTERS 12 and 13 the models developed in CHAPTER 10 to calculate the conductivity properties of the Fe/Cr system. In CHAPTER 12, we study how the GMR effect is influenced by the interfacial scattering and also the surface roughness while in CHAPTER 13 we stress the importance of the *ab initio* monolayer potentials. The manuscript ends with a summary of the general conclusions in CHAPTER 14.

1.1.1 Transition-metal Clusters

Atomic clusters have been used in literature for a very wide variety of different systems, but perhaps the only common feature is probably their finite size. The term "finite" represents a broad range of sizes from small (a few to a few tens of atoms and molecules) to large (thousands of atoms and molecules). In order to be more precise, in physics the atomic clusters are aggregates of atoms containing from 3 to 10^7 atoms. An example of an eight-atom silver cluster surrounded by 300 helium atoms is plotted in FIGURE 1.1. The emergence and rapid evolution of the field of atomic and molecular clusters are among the most exciting developments in the recent history of natural sciences. The field of clusters covers the traditional disciplines of physics, chemistry, materials science and biology. The variety of sizes would alone be sufficient to make the cluster field a challenging research area. Moreover, the variety of atoms one can use to construct the clusters and the different types of interatomic interactions between the clusters, and the atoms forming the clusters only enhance the diversity and the richness of the field. The study of clusters is important because it represents a state of matter which is in between the isolated

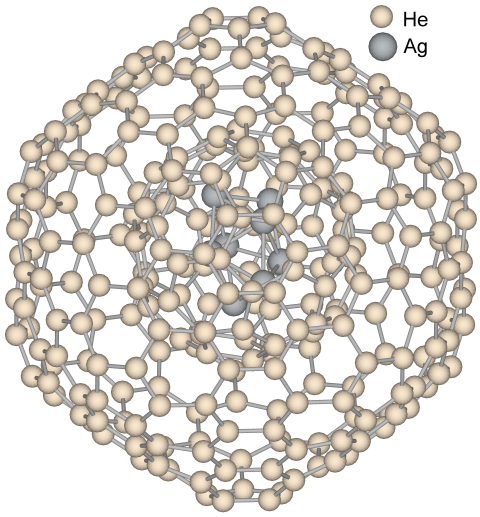

Figure 1.1:
Selected example of an eight-atom silver cluster embedded in a matrix of 300 helium atoms. The helium atoms are forming a buckyball structure.

atoms and the "bulk" materials, and commonly their electronic, magnetic, and even optical properties can differ abruptly with respect to the bulk solid. Thus, for example the clusters, due to their reduced surface/volume ratio, can be used in industrial applications for catalysis, photographic clusters, or industrial alloys. Likewise, the reduced size of the clusters along with the magnetic moment they can retain make them very useful for biomedical applications (therapeutic drug delivery, magnetic separation of labeled cells, and contrast enhancement agents for magnetic resonance imaging applications). From the optical point of view, the clusters are also used for producing paints due to the great variety of colors they can exhibit and the ability for mixing with other substances. Moreover, the study of the evolution of the geometric and electronic structures of clusters and their chemical and physical properties is also of great interest. Thus, one important point to highlight is how large must a cluster be before its properties resemble those of the bulk solid?. The answer to this question depends critically on which properties are being considered and on the nature of the component atoms.

These questions have motivated the development of experimental techniques for producing small clusters as well as a series of experimental and theoretical studies of their structure and properties. Concerning the experimental measurements, cluster experiments can be divided into three main blocks: *production of clusters*; *cluster investigation* where the clusters are probed using spectroscopic techniques; and *cluster detection*. Thus, the first stage of a cluster experiment is the generation of the clusters in a cluster source. The process consists first in a production of atoms or molecules in the gas phase, later the atoms condensate to form the cluster nucleus. In addition, the clusters are growth adding more atoms to the cluster nucleus and in the final step the small clusters merge to form larger clusters. Depending on the nature and conditions of the source (Knudsen cell, supersonic nozzle sources, ion sputtering source, ...), different size distributions of clusters may be

generated. After the clusters are generated, they are investigated by one of the following four media, i.e. molecular beams, inert matrices, surface-supported clusters, and clusters in solids. Finally, the clusters are easily separated and selected, usually according to their masses, by mass spectrometry. Although the experiments in clusters are relevant for the developing of the cluster field, however many cluster properties (e.g. cluster geometries, binding energies and energy barriers) are not easily measured directly from experiment. In this sense, the theoretical models and computational methods have been very useful in helping to interpret spectroscopic and mass spectrometric data. In literature, there are different computational implementations which try to solve the Schrödinger equation. The simplest type of *ab initio* electronic structure calculation is the Hartree-Fock (HF) method which is an extension of the molecular orbital theory but without including the electron correlation. Some extensions of this method, like for example, the configuration interaction (CI) correct the lack of the electron correlation extending the size of the basis set but the problem of this method is that it is extremely computational demanding. For large clusters, there are other approximations like semi-empirical and empirical methods, molecular mechanics or molecular dynamics, however the results obtained with these methods are less precise than, for example, the HF methodology. A method which presents a good balance between computational cost and precision of the obtained results is the density functional theory (DFT) scheme. In DFT, the total energy is expressed in terms of the total one-electron density rather than the wave function like in the HF scheme. This methodology have been adopted in this thesis to obtain the electronic, magnetic, and also optical properties of the studied clusters. Concerning specifically the point about the optical properties, there are some other state-of-the-art techniques like time-dependent DFT, quantum Monte Carlo or Green's-function-based "quasiparticle" methodology that have provided very good results.

The clusters can be classified according to the type of chemical bonding between the atoms forming the aggregate and the type of atoms of which the clusters are composed. Thus, the different kind of clusters are: rare gas or Van der Waals clusters, ionic clusters, semiconductor clusters and metal clusters. In the rare gas clusters, the interactions between inert gas atoms are weak and can be described accurately by central pair forces. The ionic clusters are referred as the clusters which manifest an ionic bonding between the atoms. The semiconductor clusters are made up of those elements which are semiconductors in the bulk solid (carbon, silicon and germanium). The metal clusters are made of metallic atoms. In this thesis, we are dealing only with this kind of clusters, and in particular, the atoms we have selected belong to the transition metals. So hereafter, we refer to the clusters studied in this thesis as "transition metal clusters". The transition metals are characterized by a relatively compact d valence shell containing up to 10 electrons and one has to deal with a lot of electrons whose space and spin distribution is intricate and the

effect of the electron correlation can be important. Although the correlation problem can be relatively easily solved, however the transition metal clusters manifest a lot of problems besides the correlation, namely, open-shell systems involving a large number of electrons, magnetism, close-lying states, metal-metal bonds, core or "semi-core" electrons that occupy the same part of space as the valence shell, fast electrons requiring relativistic corrections, spin-orbit correction, etc.

The first part of this thesis is devoted to the study of the structural, electronic, and magnetic properties of small silver, cobalt, and cobalt-manganese alloy clusters from first-principles methods. The process for calculating this properties consists in: first, give the atomic coordinates of the atoms in the three-dimensional space and perform a geometry optimization. The geometry optimization is the process of determining the stationary points. The stationary points are geometries such that the energy derivative with respect to all displacements of the nuclei is zero. Here is very important to distinguish between stationary points and transition structure. The Hessian matrix contains the second derivatives of the energy and if the eigenvalues are all positive, the frequencies are all real and the stationary point is a local minimum, but however if one eigenvalue is negative, the corresponding frequency is imaginary and the stationary point is called a transition structure. In such a case, the structure should be distorted to find the local minima. Usually, the geometry optimization process requires a lot of CPU time consuming but however it is of tremendous importance because the electronic structure results depend dramatically on the geometry of the cluster. Once the geometry is optimized, the total energy is determined by an approximate solution of the Schrödinger equation from one of the methods mentioned above. Some of the properties that we can obtain are ionization potentials, binding energies, density of states, electron affinities, first and second polarizabilities, magnetic moments, etc. In the next CHAPTERS of part I, we analyze in more detail the physics behind some small transition metal clusters. Particularly, we were able to unravel some of the mysteries surrounding the clusters studied in this thesis from a theoretical point of view.

During the last years, one of the points which has plainly impressed us in the course of our investigations is the remarkable success of density functional theory in describing the electronic, magnetic, and optical properties of the transition metal clusters. The advantages of these theoretical methods are not only the quality of the obtained results in comparison to the experimental ones but also the possibility they offer to understand the physics of the clusters, i.e. how the electrons behave, where they cumulate, how are the main interactions, and in what part of the clusters they are acting. In consequence, these methods allow the theoreticians to "see" the physics like a microscope allowed the biologists to see the bacteria.

1.1.2 Giant Magnetoresistance in Magnetic Multilayers

The giant magnetoresistance effect is likely one of the most fascinating discoveries in thin-film magnetism. It combines both enormous technological potential and

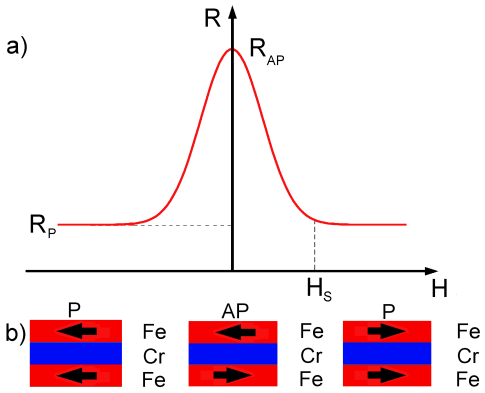

Figure 1.2:
Schematic representation of the GMR effect. a) Change in the resistance of the magnetic trilayer as a function of **H**. b) The magnetization configurations of the trilayer at different magnetic fields. At zero field the magnetizations are aligned antiparallel (AP) while they becomes parallel (P) when the external magnetic field is larger than the saturation field $\mathbf{H}_s$.

deep fundamental physics. It was discovered in 1988 and rapidly it was applied to commercial devices such as hard-disk read-heads, magnetic field sensors, and magnetic memory chips. The discovery of GMR was mainly due to the significant progress in thin-film deposition techniques like molecular beam epitaxy (MBE), sputtering, and electrodeposition. The process of stacking thin films in multilayers gave rise to systems with outstanding magnetic properties, which are totally distinct from those of the constitutive bulk materials. In particular, the metallic magnetic materials, which consist of several ferromagnetic layers separated by non-magnetic layers, are very interesting because they exhibit a wide variety of unique electronic, magnetic, and transport properties. In this thesis, we are only devoted to the trilayers, which consist of two ferromagnetic layers separated by a non-magnetic layer.

The experimental observation of the GMR effect consists in the change of the electrical resistance in response to an applied magnetic field. Thus, it was discovered that the application of a magnetic field, **H**, to a Fe/Cr multilayer [1] or a Fe/Cr/Fe trilayer[1] [2] resulted in a significant reduction of the electrical resistance. The change in the resistance of the trilayer arises when **H** aligns the magnetic moments of the successive ferromagnetic layers, as it is shown schematically in FIGURE 1.2. The antiparallel (AP) alignment of the ferromagnetic layers can be obtained by different methods. One of them is the antiferromagnetic exchange coupling [3], which is a particular case of the interlayer exchange coupling. It is mediated by the itinerant electrons in the metallic spacer layer. The origin of this coupling can be interpreted as a Ruderman-Kittel-Kasuya-Yosida (RKKY) interaction between the localized magnetic moments separated by a non-magnetic spacer. This interaction oscillates between ferromagnetic (FM) and antiferromagnetic (AF) ordering as a function of the spacer thickness, so that it is possible to create an AF coupling for

[1] We have selected in this thesis the study of Fe/Cr/Fe trilayers because it is in this compound and in the Co/Cu case where the GMR values provided by the experiment are the highest ones. Consequently, the Fe/Cr system remains attractive from the point of view of studying the fundamental physics involved.

an appropriate spacer thickness [4]. Other ways to create the AP alignment are introducing different coercitivities of the successive ferromagnetic layers [5], using spin valves [6] or with magnetic granular solids [7].

There are two ways of measuring the electric current in these layered samples. The first one consists in measuring the electric current in the plane of the multilayer, i.e. within the current-in-the-plane (CIP) geometry while the second one consists in measuring the current perpendicular to the multilayer plane, i.e. within the current-perpendicular-to-the-plane (CPP) geometry. This is more difficult to measure experimentally because the CPP resistance is very low. Most experiments reported in bibliography concerning the GMR effect are performed by measuring the current in CIP geometry. For that reason, we have adopted this configuration in our theoretical predictions in the part of this thesis concerned to the GMR effect.

As commented above, the part of this thesis dedicated to the GMR effect is tackled from a theoretical point of view. So, it becomes necessary to summarize briefly the most important theoretical treatments available in literature of this effect. In order to study the GMR effect the theoreticians faced mainly to two questions, i.e. how to calculate the electron conductivity and also how to calculate the complicated electronic structure of the transition metal ferromagnets. Concerning the question about the electronic structure, it can be described either within a simple free-electron approximation or within an accurate *ab initio* band structure method. The free-electron theories are physically more transparent than *ab initio* methods and even they are simple, they can capture some important physics of GMR. This is for example the case of the simple tight-binding models [8]. However, for a quantitative description of GMR becomes necessary the use of more sophisticated approximations like parametrized tight-binding models or Density Functional Theory based-methods [9]. On the other hand, the electronic transport and conductivity properties can be considered either within the semiclassical Boltzmann theory [10] or within quantum-mechanical theory [11]. The applicability of the quantum-mechanical theory relies on the condition for observing quantum size effects, i.e. when the film thickness, d, is less than the mean free path, λ. Thus, for $d > \lambda$ the semiclassical Boltzmann theory provides good results in treating the conduction properties of the GMR effect. We have adopted in this thesis a model based on the Boltzmann theory to describe the electron transport and a DFT method to describe the electronic structure of the Fe/Cr/Fe trilayers.

Finally, concerning the question about the origin of GMR, our experience in this topic led us to the conclusion that there is not just only one reason for explaining the numerical value of the GMR effect, i.e. the microscopic origin is a combination of several sources. As pointed out by Baibich *et al.* [1], spin-dependent scattering is the primary origin of GMR but there are other factors like for example the spin-orbit scattering or the extrinsic (it is a potential due to defects) and intrinsic (it depends on the band structure of the material) scattering potentials. The latter and the interfacial scattering along with the surface roughness are points in which this thesis

is specially interested on, as it will be shown in the next CHAPTERS. Moreover, the GMR has been measured varying different parameters like the composition of the multilayers, the thickness of the magnetic and nonmagnetic layers, roughness, impurity, and temperature. We have decided to calculate the GMR effect varying the thickness of the magnetic layers because it was less studied in the bibliography.

Part I

Structural, Electronic, and Magnetic Properties of Small Transition Metal Clusters

2

First Principles Calculations

> *Make everything as simple as possible, but not simpler.*
>
> — Albert Einstein

Synopsis

In this Chapter, I briefly revise the theoretical foundations of the methods that are employed in this thesis. I only make an exposition of the basic principles of the Density Functional Theory (DFT) but I do not enter in the mathematical subtleties like the Levy constrained-search formulation or also the v- and N-representability of the electron density because the mathematical aspects of the theory is not the objective of this thesis. After that, I expose a practical implementation of DFT in an *ab initio* code like deMon. It is a method that uses a linear combination of Gaussian type orbitals to expand the wavefunction and it is used in this thesis mainly for the calculation of the structural, electronic, and magnetic properties of small transition metal (TM) clusters. In this thesis, we have also calculated the optical properties of the Ag_8 cluster as a method to elucidate its ground-state structure. For this reason, we have used the octopus code which is based on the time-dependent DFT method. This is the topic of the last Subsection of this Chapter.

2.1 Introduction

Since the formulation of the Schrödinger equation great effort have been devoted to solve or approximate it. The analytical solution of this equation is almost impossible when the number of particles is large. In fact, only atoms or diatomic

molecules admit exact or very precise solutions. The difficulties arise mainly due to the wavefunction because the number of parameters needed to approximate the wavefunction and also the grid points necessary to store them grow exponentially with the number of particles. This is also called the many-body problem and was, in the past, one of the most fundamental difficulties in condensed matter theory. So, it was necessary searching for approximations for solving this equation. The Hartree equation was the first attempt to solve this problem, however the main drawback of this method was that the exchange interaction was discarded [12]. Later on, Slater [13] and Fock [14] improved the method including the exchange interaction between the electrons through out the inclusion of an antisymmetric single Slater determinant which is constructed with single-electron states that are varied to minimize the energy. The problem of this approximation is that it neglects the correlations between electrons of different spin. There are other methods which attempt to improve on the description of the many-body wavefunction and hence to cover the full Hilbert space. The canonical example is the configuration interaction (CI) method, [15] where the ground-state wavefunction is expressed as the linear combination of a given number of Slater determinants that minimize the energy. However, this method has the disadvantage that the dimension of a full CI grows exponentially with the number of electrons and basis functions. This inconvenience makes the method inappropriate for the study of larger systems.

Condensed matter physics would be much simpler to study if the two-body electron-electron interaction did not exist. But however, this term is the responsible that the wavefunction cannot be described as a simple product of single-electron orbitals. Observing the difficulties of the aforementioned methods and based on the Hohenberg-Kohn theorem [16], Kohn and Sham [17] in 1965 proposed an alternative approach to the existing methods at that time. The essence of the method was based on mapping the original interacting many-body system onto a one-electron system in an effective (ficticious) potential, but restricted to the condition that the electronic densities of both systems have to be the same. In this idea resides mainly the foundation of the density functional theory. While the method is extremely advantageous to simulate a large number of atoms in a relatively short period of CPU time and with a low memory resources, however DFT has the important drawback that the exchange and correlation potentials have to be approximated. Anyway, the experience gained by the researches during the last 30 years working with DFT method allow us to state that the DFT works rather well in most of the studied systems and can predict with a reasonable degree of accuracy their ground-state properties. For this reason, most of the *ab initio* codes are based on DFT and presumably this theoretical scheme will be popular in the next years. For the aforementioned arguments we have decided to employ the DFT scheme to calculate the structural, electronic, and magnetic properties of the transition metal clusters reported in this manuscript. In the next Sections, we describe briefly in

what consists the DFT and also its practical implementation in *ab initio* codes like deMon and octopus.

2.2 Density Functional Theory: The Kohn-Sham method

In 1964, P. Hohenberg and W. Kohn established the mathematical foundations of the modern Density Functional Theory based on two theorems [16]. In essence the combination of both theorems state that the ground state density, ρ, of an atomic system of interacting electrons determines implicitly all the properties derivable from the Hamiltonian of that system[1]. In consequence, the ground state energy of the aforementioned system with the external potential $v(\mathbf{r})$ can be expressed by the following energy functional:

$$E(\rho) = T(\rho) + \int \rho(\mathbf{r}) v(\mathbf{r})\, d\mathbf{r} + V_{ee}(\rho) \tag{2.1}$$

where $T(\rho)$ is the kinetic energy and V_{ee} represent all electron-electron interaction energies. In DFT, the major problem is the accurate description of $T(\rho)$. This problem is avoided by introducing a non-interacting reference system and treating the part of the Hamiltonian coming from the electron-electron interaction with an approximated functional. For this reason, DFT cannot be considered as an *ab initio* method and maybe it should be referred more properly like a mean field approximation. So, for the non-interacting system (V_{ee}=0) the Kohn-Sham kinetic energy is obtained with the Levy constrained-search [19] as

$$T_{KS}(\rho_0) = \min_{\Psi \mapsto \rho_0} \langle \Psi | \hat{T} | \Psi \rangle = \sum_{i=1}^{N} \langle \psi_i | -\frac{1}{2}\nabla^2 | \psi_i \rangle \tag{2.2}$$

where the minimization is taken over all the antisymmetric N electron wavefunctions Ψ that yields the ground state density ρ_0. $\hat{T}$ is the kinetic energy operator and Ψ is also the Slater determinant composed from the Kohn-Sham orbitals $\psi_i(\mathbf{r})$. The minimization of Equation (2.1) by means of the method of Lagrange multipliers subject to the constrain $\int \rho_0(\mathbf{r})\, d\mathbf{r} = N$ for a system of N electrons with

$$\rho_0(\mathbf{r}) = \sum_{i=1}^{N} |\psi_i(\mathbf{r})|^2 \tag{2.3}$$

[1] In what follows, the derivation of DFT is made for an spinless density. The generalization to spin-dependent DFT is almost straightforward and I refer the reader to Reference [18]. It is an important generalization of DFT when the magnetic properties of the system are relevant.

leads to the Euler equation:

$$\mu = v_{KS}(\mathbf{r}) + \frac{\partial T_{KS}(\rho)}{\partial \rho(\mathbf{r})} \tag{2.4}$$

where μ is the Lagrange multiplier. Therefore, for a given external potential of the Kohn-Sham reference system ($v_{KS}(\mathbf{r})$), one obtains the $\rho_0(\mathbf{r})$ that satisfies the Euler equation simple by solving the Kohn-Sham equations:

$$\left(-\frac{1}{2}\nabla^2 + v_{KS}(\mathbf{r})\right)\psi_i(\mathbf{r}) = \varepsilon_i \psi_i(\mathbf{r}) \tag{2.5}$$

where ε_i are the eigenvalues of the Kohn-Sham equations. In DFT, the Kohn-Sham equation is the Schrödinger equation of a fictitious system (the "Kohn-Sham system") of non-interacting particles that generate the same density as any given system of interacting particles. The Kohn-Sham equation is defined by a local effective (fictitious) external potential, $v_{KS}(\mathbf{r})$, in which the non-interacting particles move. In order to find a more explicit representation of the Kohn-Sham potential, the energy functional is rewritten as:

$$E(\rho) = T_{KS}(\rho) + \int \rho(\mathbf{r}) v(\rho)\, d\mathbf{r} + J(\rho) + E_{xc}(\rho) \tag{2.6}$$

where $J(\rho)$ is the electronic Coulomb energy,

$$J(\rho) = \frac{1}{2}\int\int \frac{\rho(\mathbf{r}_1)\rho(\mathbf{r}_2)}{|\mathbf{r}_1 - \mathbf{r}_2|}\, d\mathbf{r}_1 d\mathbf{r}_2 = \frac{1}{2}\langle \rho(\mathbf{r}_1) || \rho(\mathbf{r}_2)\rangle \tag{2.7}$$

and the symbol $||$ represents the $1/|\mathbf{r}_1 - \mathbf{r}_2|$ operator. Moreover, the new introduced exchange-correlation (XC) energy functional in Equation (2.6) is defined as:

$$E_{xc}(\rho) \equiv T(\rho) - T_{KS}(\rho) + V_{ee}(\rho) - J(\rho) \tag{2.8}$$

This quantity collects all non-classical interactions between the electrons and the difference of the kinetic energies of the interacting and non-interacting N electron system. Thus, as commented above, the accuracy of DFT is mainly determined by the quality of the approximation used for the calculation of $E_{xc}(\rho)$. This is the major problem with DFT because the exact functionals for the exchange and correlation are not known except for the free homogeneous electron gas. However, good approximations have been implemented during the last 30 years. One of the first developed approximations was the local-density approximation (LDA) [20], where the functional depends solely upon the value of the electronic density at each

point in space

$$E_{xc}^{LDA}(\rho) = \int \epsilon_{xc}(\rho)\rho(\mathbf{r})\, d^3\mathbf{r} \tag{2.9}$$

where $\epsilon_{xc}(\rho)$ is the XC energy density, known accurately from quantum Monte Carlo and other many-electron methods [21]. The LDA is so accurate for solids that it is still widely used in condensed matter physics, but however it is less used for atoms and clusters because they bear less equivalence to an uniform electron gas although is not a bad starting point. Many generalizations of the LDA of Equation (2.9) were proposed during the next years after the seminal article in Reference [20], but the first practical one was the generalized gradient approximation (GGA)[22–26],

$$E_{xc}^{GGA}(\rho) = \int \epsilon_{xc}^{GGA}(\rho, \nabla\rho)\rho(\mathbf{r})\, d^3\mathbf{r} \tag{2.10}$$

which introduces the density gradients $\nabla\rho(\mathbf{r})$ as additional local arguments of the XC energy density. Specially in clusters, the GGA functional has improved the results for molecular geometries and ground-state energies. There are other refinements of the GGA functionals, like the meta-GGA ones [27]. These functionals include a further term in the expansion, i.e., the gradient of the density and the Laplacian of the density. The most recent approximations for the XC energy include the hybrid functionals where the exchange part of the energy is substituted by the exact exchange energy calculated with the Hartree-Fock theory [28, 29].

The ground state density is the electronic density that minimizes the energy functional and hence satisfies the Euler equation. Then, performing the functional derivative of the energy functional and comparing with Equation (2.4), the Kohn-Sham potential has the following explicit form:

$$v_{KS}(\mathbf{r}) = v(\mathbf{r}) + \int \frac{\rho(\mathbf{r}')}{|\mathbf{r} - \mathbf{r}'|}\, d\mathbf{r}' + v_{xc}(\rho) \tag{2.11}$$

where the exchange-correlation potential is defined as $v_{xc}(\rho) \equiv \delta E_{xc}(\rho)/\delta\rho(\mathbf{r})$. Inserting the Equation (2.11) in Equation (2.5) yields finally the canonical Kohn-Sham equations:

$$\left(-\frac{1}{2}\nabla^2 + v(\mathbf{r}) + \int \frac{\rho(\mathbf{r}')}{|\mathbf{r} - \mathbf{r}'|}\, d\mathbf{r}' + v_{xc}(\rho)\right)\psi_i(\mathbf{r}) = \varepsilon_i\psi_i(\mathbf{r}) \tag{2.12}$$

This equations have to solved iteratively. In the next two Sections, I describe the solution of these equations using the linear combination of Gaussian-type orbitals (LCGTO) ansatz as it is implemented in deMon code while the octopus code use a grid in real space the solve them.

2.2.1 The deMon Method

deMon (density of Montréal) is a system of programs for DFT calculations of atoms, molecules, and solids [30]. One way to understand deMon code is to look at it in its historical context. During the 1970's, Slater's Xα method had been tried and abandoned by the *ab initio* community [31]. Part of the difficulty was in the scattered wave, muffin-tin implementation of the time. Major numerical improvements came about through the introduction of Gaussian-type orbitals (GTO) and the use of auxiliary fitting functions in the linear combinations of atomic orbital (LCAO)-Xα program [32, 33]. Other major advances were Axel Becke's introduction of efficient, accurate, atom-centered numerical integration, Vosko-Wilk-Nusair's parameterization of the LDA[34] based upon Ceperly and Alder's accurate quantum Monte Carlo calculations of the correlation energy of the homogeneous electron gas, as well as the emergence of good quality GGAs such as those of Becke [35] and Perdew [36]. By the 1980's, it had become clear that it was time to update the old LCAO-Xα strategy and write a modern DFT program with analytic derivatives capable of automatic geometry optimizations by means of new algorithms like for example the most sophisticated Broyden-Fletcher-Goldfarb-Shanno (BFGS) method [37]. This goal was realized in deMon. These and other characteristics make this code one of the most popular among the *ab initio* community. Its main features and the basic theory of its functionalities are explained hereafter.

To avoid unnecessary complications and as commented above, I restrict myself to the closed-shell case. The extension to the open-shell formalism is straightforward and it is explained in more detail in Reference [38]. In deMon code, linear combinations of atomic Gaussian–type orbitals (LCGTO) are used for representing Kohn-Sham orbitals. In this ansatz, the Kohn–Sham orbitals $\psi_i(\mathbf{r})$ are expanded into atomic orbitals as:

$$\psi_i(\mathbf{r}) = \sum_{\mu} c_{\mu i}\, \mu(\mathbf{r}) \tag{2.13}$$

where $\mu(\mathbf{r})$ represents an atomic orbital and $c_{\mu i}$ are the corresponding molecular orbital coefficients. With this expansion, the electronic density can be rewritten in terms of the density matrix:

$$\rho(\mathbf{r}) = \sum_{\mu,\nu} P_{\mu\nu}\, \mu(\mathbf{r})\, \nu(\mathbf{r}) \tag{2.14}$$

where $P_{\mu\nu}$ represents an element of the closed-shell density matrix, defined as:

$$P_{\mu\nu} = 2 \sum_{i}^{occ} c_{\mu i}\, c_{\nu i} \tag{2.15}$$

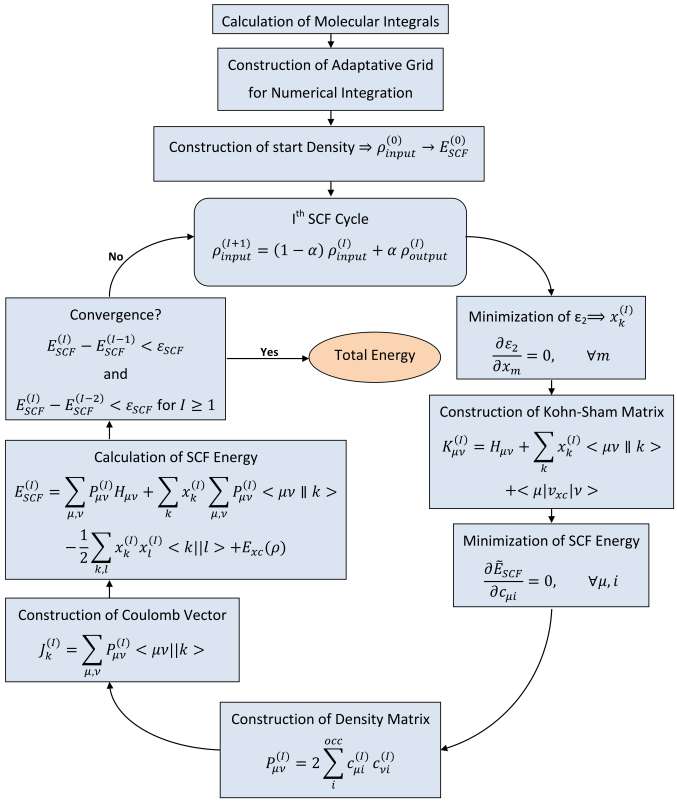

Figure 2.1: Flowchart of the SCF procedure as it is implemented in DEMON code.

Combining EQUATIONS (2.13) and (2.14), the Kohn–Sham self-consistent field (SCF) energy EQUATION (2.6) for a system of $\bar{N}$ atoms can be rewritten in the following form:

$$E_{SCF} = \sum_{\mu,\nu} P_{\mu\nu}\, H_{\mu\nu} + \frac{1}{2} \sum_{\mu,\nu} \sum_{\sigma,\tau} P_{\mu\nu}\, P_{\sigma\tau}\, \langle\, \mu\nu \parallel \sigma\tau \,\rangle + E_{xc}(\rho) \tag{2.16}$$

The Kohn–Sham SCF energy collects all terms depending on the electronic density and the SCF convergence procedure is based on this energy expression, as shown in FIGURE 2.1. It is also important to remark here that the total energy is the sum of E_{SCF} and the nuclear repulsion energy[2], which is calculated from the nuclear charges Z_A and atomic position vectors $\mathbf{A}$ as $\sum_{A>B}(Z_A Z_B)/|\mathbf{A} - \mathbf{B}|$. In

[2]The separation of the electronic and nuclear contributions in the total energy is a consequence of the Born-Oppenheimer assumption, which consists in considering the nuclei of atoms fixed because they are more massive than the electrons. This assumption allows the decoupling of the electronic and nuclear degrees of freedom in the system wavefunction and Hamiltonian.

EQUATION (2.16), $H_{\mu\nu}$ is expressed as:

$$H_{\mu\nu} = \langle\mu| - \frac{1}{2}\nabla^2|\nu\rangle - \sum_{C}^{\bar{\mathrm{N}}}\langle\mu|\frac{Z_C}{|\mathbf{r}-\mathbf{C}|}|\nu\rangle \tag{2.17}$$

and it represents the matrix elements of the core Hamiltonian. They are built from the kinetic and nuclear attraction energy of the electrons and describe the movement of an electron in the nuclear framework. The computation of this matrix scales formally as N^2, where N is the number of the basis functions. The second term in EQUATION (2.16) represents the Coulomb repulsion energy of the electrons and it scales as N^4. However, for the calculation of the exchange–correlation energy, $E_{xc}(\rho)$, a numerical integration has to be performed. This integration scales formally as $N^2 \times G$, where G is the number of grid points used to perform the numerical integration. In DEMON, the calculation of the N^4 scaling Coulomb repulsion energy is avoided by introducing an auxiliary function expansion for the electron density because the calculation of this term represents the most demanding computational task. This improvement reduces the formal scaling of the Coulomb repulsion energy to $N^2 \times M$, where M is the number of auxiliary functions (approximately two to three times N). The variational approximation of the Coulomb potential is based on the minimization of the self-interaction error:

$$\varepsilon_2 = \frac{1}{2}\langle\rho - \tilde{\rho}||\rho - \tilde{\rho}\rangle \tag{2.18}$$

This approximated density, $\tilde{\rho}(\mathbf{r})$, is expanded in primitive Hermite Gaussians $\bar{k}(\mathbf{r})$ which are centered at the atoms:

$$\tilde{\rho}(\mathbf{r}) = \sum_k x_k\,\bar{k}(\mathbf{r}) \tag{2.19}$$

With the LCGTO expansion for $\rho(\mathbf{r})$ and $\tilde{\rho}(\mathbf{r})$ we obtain for ε_2:

$$\begin{aligned}\varepsilon_2 =& \frac{1}{2}\sum_{\mu,\nu}\sum_{\sigma,\tau}P_{\mu\nu}P_{\sigma\tau}\langle\mu\nu||\sigma\tau\rangle - \sum_k x_k\sum_{\mu,\nu}P_{\mu\nu}\langle\mu\nu||k\rangle \\ &+ \frac{1}{2}\sum_{k,l}x_k x_l\langle k||l\rangle\end{aligned} \tag{2.20}$$

Because ε_2 is positive definite, the sum of the first and third term is equal or greater than the second term. With this inequality, an approximated SCF energy, which is

based on EQUATION (2.16) is derived as:

$$\begin{aligned}\tilde{E}_{SCF} = &\sum_{\mu,\nu} P_{\mu\nu}\, H_{\mu\nu} + \sum_{k} x_k \sum_{\mu,\nu} P_{\mu\nu}\, \langle\, \mu\nu \,||\, k \,\rangle \\ &- \frac{1}{2} \sum_{k,l} x_k\, x_l \langle\, k \,||\, l \,\rangle + E_{xc}(\rho)\end{aligned} \tag{2.21}$$

Therefore, only three–center electron repulsion integrals (ERIs) are necessary for the SCF and energy calculation in DEMON. This represents the most accurate energy model available in DEMON.

The SCF procedure, as depicted in FIGURE 2.1, may be divided in two parts. The first one is the determination of the fitting coefficients of the approximated density and the second is the determination of the molecular orbital coefficients. Thus, the expansion coefficients x_k of the approximated density are calculated by the minimization of ε_2 restricted to the constrain of the charge conservation ($\int \tilde{\rho}(\mathbf{r}) d\mathbf{r} = n$), i. e.,

$$\frac{\partial \varepsilon_2}{\partial x_m} = -\sum_{\mu,\nu} \langle \mu\nu || m \rangle + \sum_{k} x_k \langle k || m \rangle = 0, \quad \forall m \tag{2.22}$$

Concerning the second part of the SCF procedure, the variation of $\tilde{E}_{SCF}$ with respect to the molecular orbital coefficients, constraining the Kohn-Sham orbitals to be orthonormal yields:

$$\begin{aligned}\frac{\partial \tilde{E}_{SCF}}{\partial c_{\mu i}} = &\sum_{\nu} \left(H_{\mu\nu} + \sum_{k} x_k \langle \mu\nu || k \rangle + \langle \mu | v_{xc} | \nu \rangle \right) c_{\nu i} \\ &- \sum_{\nu} \sum_{j} S_{\mu\nu} c_{\nu j} \varepsilon_{ji} \;\; \forall\; \mu, i\end{aligned} \tag{2.23}$$

From this equation, we can derive the canonical LCGTO Kohn-Sham equations in matrix form,

$$\mathbf{K}\,\mathbf{c} \;=\; \mathbf{S}\,\mathbf{c}\,\varepsilon \tag{2.24}$$

with the elements of the Kohn-Sham Matrix $\mathbf{K}$ defined as:

$$K_{\mu\nu} = H_{\mu\nu} + \sum_{k} x_k \langle \mu\nu || k \rangle + \langle \mu | v_{xc} | \nu \rangle \tag{2.25}$$

where $\mathbf{c}$ is the molecular orbital coefficient matrix, $\mathbf{S}$ represents the overlap matrix, and ε the Kohn-Sham orbital energies. Thus, as can be seen from FIGURE 2.1, the calculation of the molecular core and electron repulsion integrals, as well as the construction of the grid for the numerical integration of the exchange-correlation contributions are outside the SCF loop. From the start density, which is obtained

from the core Hamiltonian, the first Coulomb vector $J_k^{(0)} = \sum_{\mu,\nu} P_{\mu\nu}^{(0)} \langle \mu\nu || k \rangle$ is constructed. With this vector, the expansion coefficients of the approximated density are calculated and then Kohn-Sham matrix is built. From the diagonalization of the Kohn-Sham matrix a new set of molecular orbital coefficients is obtained. The density matrix is constructed from the new molecular orbital coefficients and then a new Coulomb vector is generated. The SCF cycle is repeated until energy convergence is achieved. Thus, the SCF procedure is terminated once three consecutive values of the total energy differ by less than ε_{SCF} among themselves. In case that the convergence is not reached, the electron density produced by the Ith iteration is mixed with the input density for the Ith iteration to produce the input density of the next iteration:

$$\rho_{input}^{(I+1)} = (1-\alpha)\rho_{input}^{(I)} + \alpha\rho_{output}^{(I)} \tag{2.26}$$

where α is the mixing parameter varying between 0 and 1. The mixing can also be performed with respect to the xc potential, or alternatively, with respect to the whole density matrix.

2.2.2 The OCTOPUS Method

OCTOPUS code is a scientific program aimed at the *ab initio* virtual experimentation on a hopefully ever-increasing range of system types. Electrons are described quantum-mechanically within DFT, and in its time-dependent form (TDDFT) when doing simulations in time. Nuclei are described classically as point particles. Electron-nucleus interaction is described within the pseudopotential approximation. It is specially designed for calculating the excitation spectra of a wide range of systems, like for example transition metal clusters. In the following, we will describe in brief the theory behind OCTOPUS code. I restrict myself to the TDDFT implementation in OCTOPUS code because the DFT part has been described above. The main difference with respect to the DEMON code in the DFT implementation resides in procedure to solve the Kohn-Sham equations. Octopus discretize the Kohn-Sham equations and uses a grid in real space to solve them. This is, the functions are represented by its value over a set of points in real space. Normally the grid is equally spaced and the shape of the simulation region may also be tuned to suit the geometric configuration of the studied system.

In TDDFT formulation the OCTOPUS code performs the time propagation of the electronic orbitals. In essence, the TDDFT extends the basic ideas of ground-state DFT to the treatment of the electronic excitations. The main advantage of the time-dependent Kohn-Sham scheme lies in its computational simplicity compared to other quantum-chemical models such as time-dependent Hartree-Fock or configuration interaction. It is an alternative formulation of the time-dependent quantum mechanics but instead of the wavefunctions, the basic variable is the one-body electron density, $\rho(\mathbf{r}, t)$. The electron density is obtained with the help of a ficticious

system of N non-interacting electrons (the Kohn-Sham system) and with the electrons feeling an effective potential (the time-dependent Kohn-Sham potential) which has to be approximated.

The time-dependent many-body Schrodinger equation is equivalent to the system of N time-dependent one-body Kohn-Sham equations:

$$\mathrm{i}\frac{\partial}{\partial t}\psi_i(\mathbf{r},t) = \left[-\frac{\nabla^2}{2} + v_{KS}(\mathbf{r},t)\right]\psi_i(\mathbf{r},t) \quad (i = 1,\ldots,N) \tag{2.27}$$

The density of the interacting system is calculated in terms of the time-dependent Kohn-Sham orbitals as:

$$\rho(\mathbf{r},t) = \sum_{i=1}^{N} |\psi_i(\mathbf{r},t)|^2 \tag{2.28}$$

The problem in TDDFT as in DFT reduces to know the Kohn-Sham potential because if it is known, then we would obtain the exact Kohn-Sham orbitals, and from these the correct density of the system. The Kohn-Sham potential is similar to the static version and is conventionally separated as:

$$v_{KS}(\mathbf{r},t) = v_{ext}(\mathbf{r},t) + \int \frac{\rho(\mathbf{r},t)}{|\mathbf{r}-\mathbf{r}'|} d^3\mathbf{r}' + v_{xc}(\mathbf{r},t) \tag{2.29}$$

where the first term is the external potential. It is typically the sum of the Coulomb potential generated by each of the nuclei. The second term is the time-dependent Hartree potential and it accounts for the classical electrostatic interaction between the electrons. In OCTOPUS, it comes from the solution of the Poisson's equation which is solved via a conjugate gradients algorithm [39]. Finally, the exchange-correlation potential is an unknown functional of the density, and has to be approximated. It is defined through the equivalence between the interacting and ficticious non-interacting systems. However, in this case, the time-dependence of the exchange and correlation potential introduces the need for an approximation even more extensive than the one made in the time-independent case. So, in OCTOPUS the way to solve this point is implementing the so-called adiabatic approximation. It consists in assuming that the time-dependent xc potential is the time-independent xc potential evaluated at the time-dependent density, i.e.,

$$v_{xc}^{adiabatic}(\mathbf{r},t) = v_{xc}^{gs}|_{\rho=\rho(\mathbf{r},t)} \tag{2.30}$$

where v_{xc}^{gs} is the ground state exchange and correlation potential functional. In consequence, all the approximations implemented in OCTOPUS for the ground state calculations translate immediately for time-dependent calculations.

As commented above, a primary motivation for using a TDDFT methodology is to obtain the optical properties of the studied system. OCTOPUS permits two choices for this, linear response theory *a la* Casida [40] or the explicit time propagation of the system after a perturbation, *a la* Yabana-Bertsch [41]. The latter may not only be used to calculate linear response properties, but also permits to use high-intensity fields after an explicit integration of the time-dependent Kohn-Sham equations in the time domain. However, the TDDFT *a la* Casida consists in a linearized form of EQUATIONS (2.27) and (2.28) that assumes a small external perturbation, and consequently calculate the first-order density-density response in frequency domain. More in detail, the TDDFT in the linear response regime is based on the idea that a small time-dependent perturbation (an electromagnetic field) represented by an externally applied potential $v(\mathbf{r},\omega)$ will result in a time-dependent perturbation of the electronic density $\rho(\mathbf{r},\omega)$. It is linearly related to the size of the perturbation:

$$\delta\rho(\mathbf{r},\omega) = \int \xi(\mathbf{r},\mathbf{r}';\omega)\,\delta v(\mathbf{r},\omega)\,d^3\mathbf{r}' \tag{2.31}$$

where the time-dependence has been transformed into a frequency dependence (ω denotes the frequency) by means of a Fourier transformation. The response of the charge density to a potential that couples to the charge density of the system is represented by the density-density response function $\xi(\mathbf{r},\mathbf{r}';\omega)$. This response function has poles at the excitation energies of the many-body system and consequently, the induced density has also these poles. One can use this analytical property to find a related operator whose eigenvalues are these many-body excitation energies. The TDDFT *a la* Casida is a very successful approximation because the obtained results are, in general, in relatively good agreement with the experiment and overall, it is a very low CPU time consuming compared with the non-linearized TDDFT.

3

Model Potential Density Functional Study of Small Cobalt Clusters, Co_n, $n \leq 6; 13$.

> *In science one tries to tell people, in such a way as to be understood by everyone, something that no one ever knew before. But in poetry, it's the exact opposite.*
>
> — Paul Adrien Maurice Dirac

Synopsis

Small clusters of cobalt atoms, Co_n ($n \leq 6; 13$), were studied with the aid of the program deMon, which is a density functional theory based method. Self-consistent-field Model Core Potential (MCP) calculations, which describe the core electrons of the cobalt atom, were done in concert with the generalized gradient approximation (GGA) and local spin density approximation for the treatment of the exchange-correlation (XC) effects. MCP and all-electron (AE) calculations, at the same level theory, are compared and discussed for Co_2 and Co_3. An emphasis is made on a proper treatment of XC effects. The enhancement of the magnetic moments as well as the bonding properties of these clusters are discussed in terms of the cluster size, symmetry, and a delicate balance between intra- and interatomic exchange and correlation. The obtained GGA-MCP results show a dramatical improvement in the calculated binding energies (BE), which is due to the accurate description of the XC energy, through GGA, and to a substantial reduction of the basis set superposition errors (BSSE). Finally, the present calculations are compared with other theoretical and experimental results obtained for these systems.

3.1 Introduction

The study of transition metal (TM) clusters is nowadays a very active field of research, since this kind of systems exhibits unexpected properties which, aside from its basic importance for the understanding of phenomena such as magnetism, shares a close connection with the design of novel materials, such as magnetic devices. For instance, the rapid development of nanofabrication techniques followed by the discovery of some new and interesting effects, as the Giant Magnetoresistance to be mentioned as primary example, provides another impact for the theoretical study of small TM clusters.

It is recognized that those many-electron systems present themselves a serious challenge for any first principle calculation due to the heavy demand of a proper description of both exchange and correlation (XC) effects. Usually, the size of the cluster as well as the high level of correlation treatment needed causes a rapid failure of traditional *ab-initio* quantum chemistry methods based either on Configuration Interaction (CI) expansion of Slater determinants or Moller–Plesset perturbation techniques. Fortunately, the Density Functional Theory (DFT) [16, 17] based methods, developed recently, offers a computational alternative yet retaining the *ab-initio* level. Among transition atom systems the cobalt clusters have been much less studied than others from the first transition row of elements. Li and Gu [42] have studied small cobalt clusters, using the local spin density approximation (LSDA) of DFT. Other papers devoted to this subject are the works of Jamorski *et al.* [43] and Castro *et al.* [44]. These papers have pointed out that the study of this type of systems requires to go beyond LSDA, namely, the generalized gradient approximation (GGA) should to be used explicitly for an accurate description of their electronic and structural properties. Notwithstanding the sophisticated calculations of the all-electron type, performed on those reports, it was found that the calculated binding energies (BE) and ionization potentials (IP) presents a considerable discrepancy when compared with the available experimental data. For example, the best calculated BE [44] for Fe_2 differs by about 90% and 55% from its experimental counterparts, which among themselves also have serious discrepancies. Such difference between DFT and experiment is not usually observed in conventional systems (those not containing open-shell TM atoms) or molecules where currently are calibrated the proposed XC functionals.

In this Chapter, we have done a systematic study of the structural and electronic properties of small Co_n clusters ($n \leq 6; 13$) using the program deMon. We define the net spin number N as the difference between the number of spin up (α) and down (β) electrons for a given configuration. The core electrons of the cobalt atoms are described through a Model Core Potential (MCP), which, aside from the reduction of the computational time, may produce an improvement in the estimation of those properties that depends on differences of total energies. Our purpose is to show how the structural and electronic properties, of these small

cobalt atoms, evolve with the increase of cluster size. The geometry of all clusters has been optimized, except for Co_{13}. As mentioned [43, 44], the GGA level offers the state-of-the-art treatment of the XC effects and, at the same time, provides a computationally efficient and more precise way of evaluating molecular integrals by means of linear combinations of Gaussian type orbitals. In the present research, the use of a MCP will allow to search for the sources of errors in the calculated ground state (GS) structures as well as in the BE. This DFT alternative approach will indicate the extent of the basis set superposition errors (BSSE) involved in the calculations of the all-electron (AE) type.

In the next SECTION, we will discuss the details of the computations. In SECTION 3.3 our results will be presented and discussed in SECTION 3.4.

3.2 Computational Details

We have used the DFT computational program deMon which is a realization of linear combination of Gaussian type orbitals (LCGTO) solution of the Kohn-Sham DFT system of equations. The theory and numerical details of this realization can be found in REFERENCES [45, 46]. The core electrons of the cobalt atoms are described by the use of a MCP in concert with a 15 electrons orbital basis set. This MCP has been optimized for a specific use in DFT scheme [47] and adapted to deMon. The inner $3p$ shell has been moved into a basis set, thus allowing the explicit treatment of important $3p$–$3d$ correlations in metal systems. Also, the use of MCP minimizes the BSSE which should be taken into account when analyzing close lying states on an all-electron basis set level; and on the other hand, it allows to keep the same computational treatment of cobalt clusters for all nuclearities studied. The grid option FINE of deMon was used in all calculations. This option uses 832 points per atom for fitting the XC terms during self-consistent field (SCF) cycles and, once converged, 2968 points per atom to evaluate the final XC energy. The Vosko-Wilk-Nusair (VWN) parametrization [34] was employed for LSDA calculations, while the GGA treatment of XC was done through Perdew and Wang (PW86) [48] and improved (PW91) [23] nonlocal functional for exchange with Perdew (PW86) [25, 26] and the new (PW91) [23] nonlocal functional for correlation in the Co, Co_2 and Co_3 cases. For the rest of clusters studied in this CHAPTER only the PW86 functional was used for treating the XC effects. An orbital basis set of contraction pattern (63321/5211*/41+) was used in conjunction with the corresponding (5,5;5,5) auxiliary basis set for all-electron calculations, while the orbital valence basis set with contraction pattern (2111/211*/311+) with (5,3,3;5,3,3) auxiliary set was chosen to be appropriate for MCP calculations. Geometry optimizations were performed with the Broyden-Fletcher-Goldfarb-Shanno [49] (BFGS) algorithm with a convergence criterion of 10^{-6} a.u. on the energy and the charge density. In the initial stages, calculations were performed with the SMEAR option, which assigns a fractional

occupation number to orbitals. This option is followed by a parameter which determines the size of the window placed around the Fermi level. At the end of the SCF or geometry optimization procedure, the chosen value for the smear option is small enough that all occupations corresponds to integral occupation numbers.

3.3 The Electronic Structure and Geometry of Cobalt Clusters

3.3.1 Cobalt Atom

The experimental GS of the cobalt atom has the configuration $3d^7 4s^2$ placing its $3d^8 4s^1$ state 0.418 eV higher [50]. In TABLE 3.1, total energies are reported for both spherical and nonspherical (NS) cobalt atoms at AE and MCP levels of treatment. Checking TABLE 3.1, we can conclude that nonspherical calculations at the MCP level improve all theoretical results, of the AE type, so far obtained [43]. Indeed, our present MCP results for the energy separation between the ground, $3d^7 4s^2$, and excited, $3d^8 4s^1$, states of the Co atom (equal to +0.503 eV at the NS-MCP-PW91 or +0.883 eV at the NS-MCP-PW86) is in very good agreement with the experimental value. Note that the more elaborate PW91 functional works much better than the old PW86 one. Surprisingly, the MCP-LSDA level of theory also produces a very good value of +0.376 eV. It should be mentioned that the nonspherical calculations are neither obvious to define (electrons may be assigned to the available spin orbitals in several ways, needed the performance of several calculations to find the minimum energy) nor facile (they require hundreds or thousands of iterations) to converge. When viewed in the context of the inherent ambiguity about treating multiples within Kohn-Sham DFT, which in its present state is essentially a monodeterminantal theory, it seems that high accuracy for the splitting should not be expected for such complex open-shell systems as the cobalt atom. Our relatively good result of MCP calculations can account for a careful choice of i) orbital basis set, ii) optimized potential for the description of the core electrons (MCP Co^{12+}) of the Co atom, which allows the inclusion of relativistic corrections, not taken into account in previous AE calculations [43, 44], and iii) GGA functional. In fact, it has been pointed out by Barden *et al.* [51] that the pure functionals work much better (in our case: LSDA, PW86, and PW91, particularly the last one) than the hybrid ones for systems containing TM atoms.

3.3.2 Cobalt Dimer

We start the cluster calculations with a cobalt dimer. Very few studies have been performed for this system. Since the electronic ground state and equilibrium bond length of Co_2 have not yet been determined experimentally, the understanding of this dimer is quite complicated. A third-law determination, by Kant and Strauss

Table 3.1:
Total energy of the ground and first excited state computed with AE and MCP calculations (LSDA and GGA level). Spherical and nonspherical approximations are used in cobalt atom. We define ΔE=E($4s^1 3d^8$)-E($4s^2 3d^7$). The experimental separation is equal to 0.418 eV (Reference [50]).

			E($4s^2$ $3d^7$) (a.u.)	E($4s^1$ $3d^8$) (a.u.)	ΔE (eV)
MCP					
	Spherical	LSDA	-107.04054	-107.05686	-0.444
		PW91	-107.41956	-107.43929	-0.537
	Nonspherical	LSDA	-107.08156	-107.06772	+0.376
		PW86	-107.56046	-107.52798	+0.883
		PW91	-107.48976	-107.47126	+0.503
AE					
	Spherical	LSDA	-1379.86446	-1379.90151	-1.008
		PW86	-1382.75621	-1382.78809	-0.867
		PW91	-1382.52524	-1382.56450	-1.068
	Nonspherical	LSDA	-1379.89874	-1379.91412	-0.418
		PW86	-1382.80739	-1382.80727	+0.003
		PW91	-1382.57771	-1382.58836	-0.290

[52], yields 1.69 $\pm$0.26 eV for the binding energy. More recent determinations, by Armentrout and co-workers [53, 54], indicate that it should be 1.32 eV [53] or to fall in the 0.7-1.4 eV range [54]. The relatively small value of this property accounts by the scarce number of experimental studies on Co_2. Regarding its vibrational frequency, matrix isolation Raman spectroscopy [55] indicates a value of 296.8 $\pm$0.54 cm^{-1}. As mentioned, there is no experimental value for the equilibrium bond length. Based on Badger's rule, Weisshaar [56] reports an empirical estimate of 2.02 Å. However, the error in this figure is of about 0.35 Å [21]. On the other hand, from the Pauling radius, Kant and Strauss [17] pointed out a value of 2.31 Å for that distance. So, there is a big uncertainty in the empirical estimates for the equilibrium bond length of Co_2. Excellent reviews for Co_2 as well as for other transition metal dimers have been given by Shim [57], Morse [58], and Salahub [59]. More recently, Barden *et al.* [51] reported an exhaustive DFT study of the GS properties of Co_2, as well as of the remaining homonuclear TM dimers of the first series.

Our AE and MCP results for the optimized N=2, 4, and 6 states of the dimer are presented in Figure 3.1, showing excited states at LSDA and GGA levels. AE and MCP calculations give a GS for N=4 being a $^5\Delta_g$ state, in agreement with References [43] and [60]. In Figure 3.2, we can see the electronic structure for different states, only including PW91 functional calculations. Taking into account Figures 3.1 and 3.2, we see that the $^3\Delta_g$ and $^7\Sigma_g$ states are about 1.5 eV above the GS. Moreover, we can probe the differences obtained in bond length following the molecular orbital point of view. The transition from N=4 to N=2 is reached

whether one electron on $\delta_u^{*\alpha}$ antibonding orbital goes to the $\delta_u^{*\beta}$ antibonding function. This type of transition do not change the nature of the bonding, consequently the bond length must be the same. FIGURE 3.1 shows that at AE and MCP levels the difference in bond distance is the same except for the case in which we use the PW86 functional. The problem here is related to π_u molecular orbital because of PW86 functional produces a high splitting in this orbital, and consequently the optimization with BFGS algorithm change a lot. Nevertheless, the PW91 functional does not split π_u molecular orbital giving a outstanding bond length. When we consider the transition from N=4 to N=6, one electron goes from $\delta_u^{*\beta}$ antibonding orbital to $4s(\sigma_u^{*\beta})$ antibonding orbital, which is more antibonding than $\delta_u^{*\beta}$. This new situation introduces an increase in the bond length, as shown in our calculations; see FIGURE 3.1. We note that the tendency in the bond distance behavior when N=4→N=2 and N=4→N=6 is predicted not only at AE calculations like in REFERENCE [43]; it is predicted at MCP calculations as well.

In TABLE 3.2, we present the calculated properties of the Co dimer: equilibrium bond lengths, binding energies, vibrational frequencies, and IPs at LSDA and GGA (PW86 and PW91) level computed taking into account AE and MCP calculations. Analyzing the fifth column of this table, we can see that we obtain 2 Å for the bond length, at MCP level using PW91. Although there is not a good experimental value [52], our results fall inside bar errors given by neighboring dimers [61, 62], i.e., Fe_2 →1.87 Å and Ni_2 →2.02 Å. As mentioned before, we had problems with PW86 (MCP case) because the optimized bond length in concert with BFGS algorithm gave a large value, of 2.40 Å. The reported value of 2.01 Å was computed doing single-point calculations around the optimized bond length 2.00 Å given by PW91 (MCP case). This fact influences our decision to include only PW91 functional when we calculated another nuclearities.

Recently, Barden *et al.* [51] have found that six commonly used DFT functionals (B3LYP, B3P86, BHLYP, BLYP, BP86, and LSDA) are in considerable disagreement with respect to the ground-state occupation of Co_2: they gave the same orbital ordering but fill differently. That is, the electronic GS of Co_2 is very sensitive to the chosen functional. Barden *et al.* [51] concluded that the uncertainty on the GS occupation numbers precludes any strong assertion as to the bond distance of Co_2. Their estimates suggest that Co_2 should have a value between 2.36 and 2.44 Å. This range is outside both of our computed value of 2.00 Å, using PW91-MCP, and of the expected one taken into account the experimental findings for Fe_2 (1.87 Å) and Ni_2 (2.02 Å). Note that our PW86-MCP value of 2.40 Å (obtained by geometry optimization) is inside that range. So, an accurate determination of the equilibrium bond length of Co_2 is still an open problem.

Following with the results quoted in TABLE 3.2, the sixth column shows the binding energy, obtained as a total energy difference between that of the cobalt atom (in the nonspherical approximation) and dimer. PW86 (MCP case) determines that the dimer is nonbonding in bad agreement with REFERENCES [53, 54], as we

Table 3.2:
Electronic properties of Co dimer computed using a MCP and AE calculations. Experimental values are also reported.

			State	R_e (Å)	D_e (eV)	ω_e (cm^{-1})	IP (eV)
MCP							
	LSDA		$^5\Delta_g$	1.96	2.37	444.42	7.13
	GGA	PW86	$^5\Delta_g$	2.01	-0.03	369.30	7.02
		PW91	$^5\Delta_g$	2.00	1.03	415.29	7.37
AE							
	LSDA		$^5\Delta_g$	1.92	4.25	442.18	6.62
	GGA	PW86	$^5\Delta_g$	1.99	2.35	372.81	7.49
		PW91	$^5\Delta_g$	1.92	2.87	454.80	7.33
Exp.							
	Ref. [53]				$\leq$1.32		6.42
	Ref. [54]				0.7 $\leftrightarrow$ 1.4		
	Ref. [64]						6.26 $\pm$ 0.16
	Ref. [63]					280 $\pm$ 20	
	Ref. [55]					296.8 $\pm$ 5.4	

comment above. Nevertheless, the best value is obtained with PW91 (MCP case) compared with the experimental values References [53, 54]. Experiments indicate that Co_2 has a small BE, which complicates its precise determination. Note that the MCP-PW91 result, equal to 1.03 eV, falls in the suggested experimental range: 1.32 or 0.7-1.4 eV. Such a small value may be due to an increase in the number of occupied antibonding molecular orbitals (see Figure 3.2). In this regard, MCP calculations give better results than AE calculations because of the accurate description of the XC energy, through GGA (PW91) and to a substantial reduction of the BSSE, which is the main source of error. On the other hand, the best DFT estimates of Barden *et al.* (those with the use of B3LYP, BLYP, and BP86) indicates that the binding energy of Co_2 should be in the 1.49 to 1.56 eV range, which is near to the third-law determination [52], 1.69 $\pm$0.26 eV, but it is bigger than the most recent determinations by Armentrout *et al.* [53, 54].

In the seventh column of Table 3.2 we can see the vibrational frequency obtained for the more stable structures. The values of the frequency seem to be large when we compare it with experimental values [55, 63], but this can account for a cooperative effect of intrinsic errors of the functional and anharmonicity. A reverse pattern was found by Barden *et al.* [51], their estimates (223-265 cm^{-1}) are smaller than the experimental value. Accurate determinations of vibrational frequencies present nowadays a considerable challenge for the state-of-the-art DFT techniques.

Finally, the eighth column of Table 3.2 shows the ionization potential. In every case, the IP was obtained as the difference of the total energies of neutral dimer and cation. Our calculations overestimate the experimental IP by 0.2$\leftrightarrow$1.07 eV and AE

and MCP calculations present the same tendency, although this trend is improved at LSDA level, strangely. It is worthwhile to mention that although the highest occupied Kohn-Sham orbital is the only one having a direct physical meaning while the remaining ones should be viewed, in principle, as just a pure mathematical construction, which helps solving the effective Kohn-Sham one-particle equations, their numerical similarity to real orbitals is used to make estimations of the degree of (*sp*; *sd*) hybridizations by means of Mulliken population analysis as well as plots of orbitals that, in turn, provide help in the analysis of the bonding mechanisms in molecular structures. The atomic state of a Co atom within the dimer is presented in TABLE 3.3, thus closely resembling the bonding $3d^8 4s^1$ state. Taking into account this fact and the Mayer bond order (see TABLE 3.3), we concluded that the 3*d* orbitals participate in the Co_2 bond, being a double bond. If we increase the precision of the functional, as moving from LSDA to GGA, MCP calculations indicate a bond order below 2 (except the PW86 functional, which gives a value below 3). On the other hand, AE calculations point to the appearance of a bond order slightly above 2. The bond in the Co dimer originates from 3*d* orbitals, which are highly localized, consequently small variations of the metal-metal distance increase or decrease the bond order. Our results show a high sensitivity to the method employed, i.e., we obtain a different set of values depending if the chosen approach is AE (above 2) or MCP (below 2).

3.3.3 Cobalt Trimer

Table 3.3:
The atomic state of a Co atom within the dimer at MCP and AE level. Mayer bond order is also reported.

			s	*p*	*d*	MBO
MCP						
	LSDA		0.98	0.01	7.97	1.66
	GGA	PW86	1.14	0.18	7.68	2.62
		PW91	1.06	0.01	7.87	1.81
AE						
	LSDA		1.05	0.01	7.90	2.14
	GGA	PW86	1.09	0.01	7.85	2.12

For Co_3 the GS corresponds to an obtuse triangle, with N=5 and with bond lengths of 1.994 and 2.537 Å (MCP case). This structure is located 0.39 eV deeper than the equilateral triangle with N=5 and bond lengths of 2.04 Å. Moreover, in our MCP calculations the N=7 higher spin state is located 0.22 eV above the ground state. So, the MCP results indicate that the N=5 C_{2v} state of Co_3 is a likely candidate for the GS of this trimer. The MCP picture differs significantly from the AE one [43], where the structures quoted above are located within a short energy range of 0.08 eV. So, the MCP technique locates more accurately the lowest energy structure, whereas the all-electron calculations tend to collapse the low lying states in a short energy range.

The C_{2v} GS-MCP of Co_3 has two bond lengths of 1.994 Å and one of 2.537 Å. Its all-electron counterpart [43, 44] has two bond lengths of 2.12 Å and one

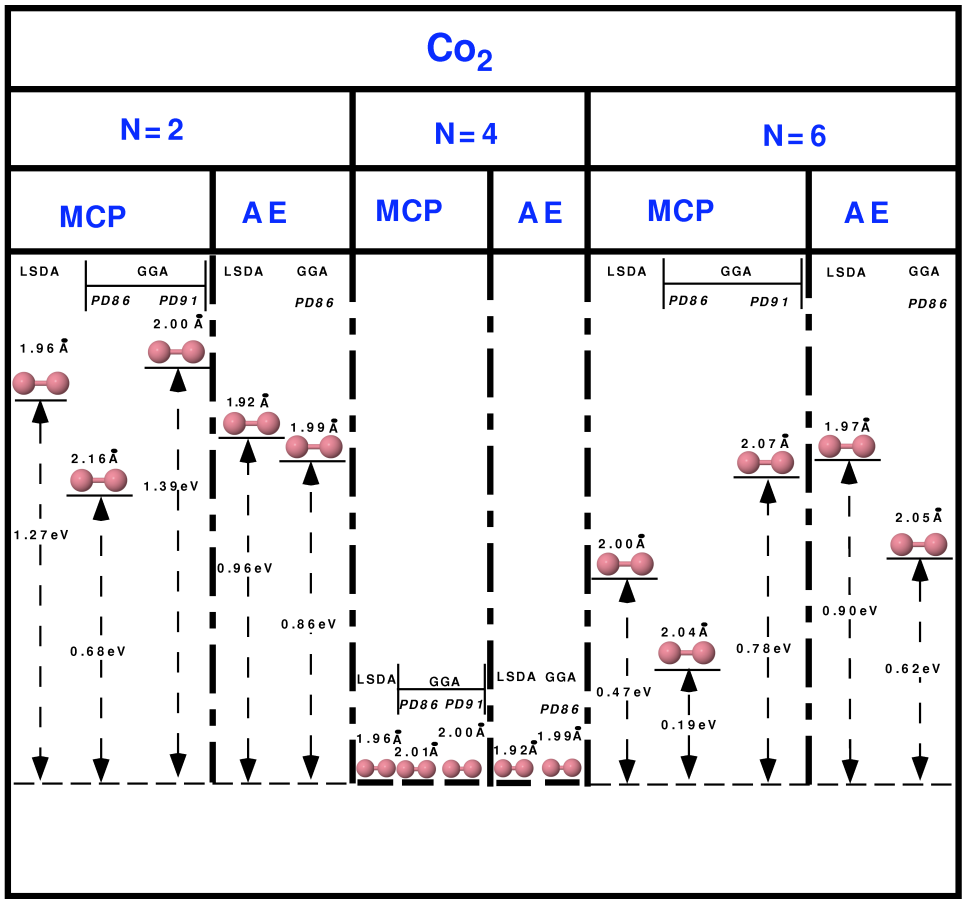

Figure 3.1:
Relative stability of AE and MCP cobalt dimer optimized structures. LSDA and GGA (PW86 and PW91) calculations are reported. We put the ground state at the same level for clarity reasons.

of 2.24 Å. Note that the smaller MCP R_e's are about 0.1 Å shorter than the all-electron ones; while the MCP larger R_e is substantially larger, by about 0.3 Å, than the all-electron one. With respect to the MCP picture, in the former case the AE calculations underestimates slightly the binding, whereas in the later case the AE binding is substantially overestimated. It will be interesting to know the experimental geometry for Co_3; this will give insight about the accuracy of the chosen computational approaches for describing this type of complex clusters.

3.3.4 Cobalt Tetramer

Hereafter, the results are reported only for the MCP case at the GGA level because of the good results they have provided us for the cobalt clusters with $n \leq 3$. The cobalt tetramer has been inspected in a more detailed way than other cobalt clusters

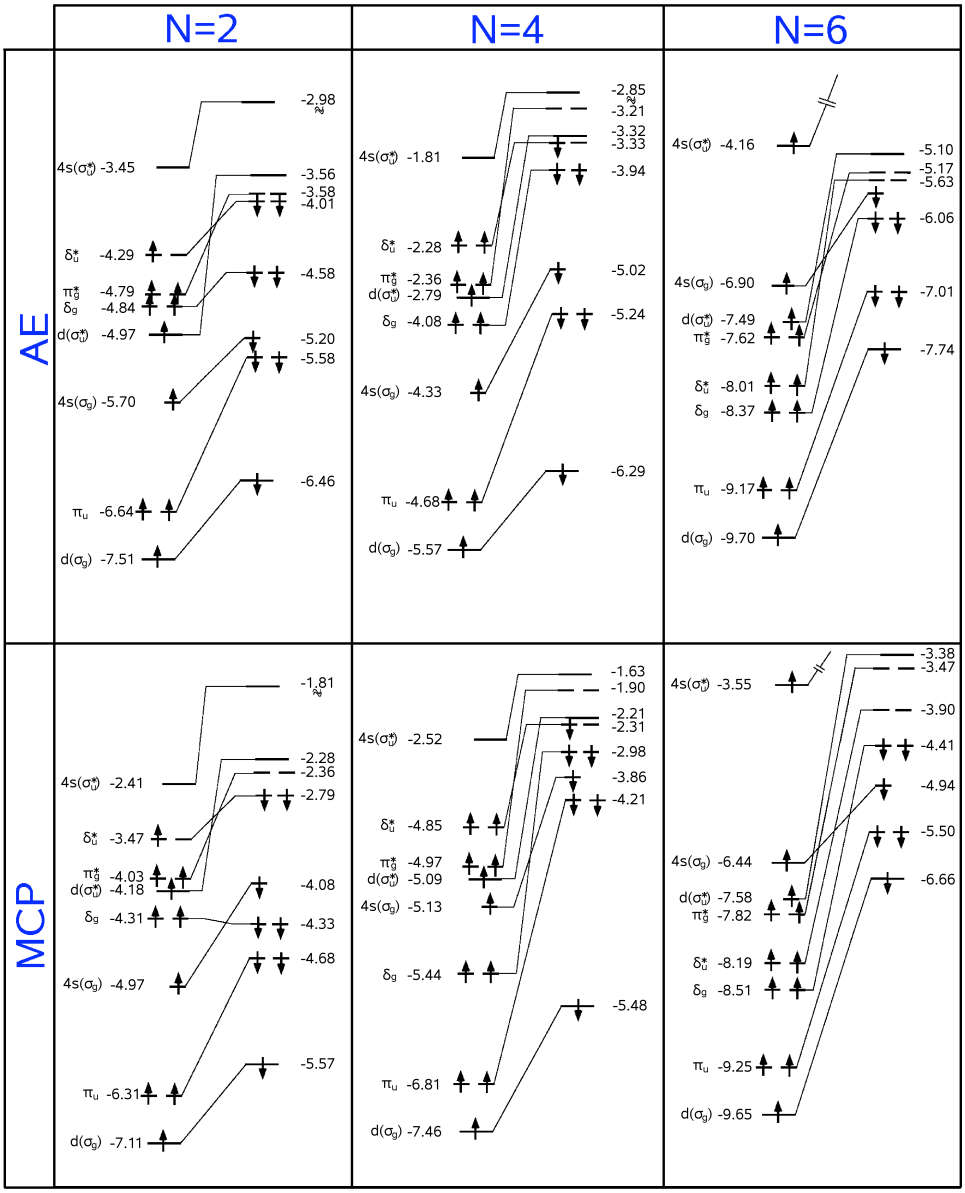

Figure 3.2:
Electronic configuration for different states of the dimer, at AE and MCP level, only including PW91 functional calculations.

where only the most symmetric structures have been extensively examined. At first we investigated the tetrahedral structure. Even with the imposed T_d symmetry constraint there is a huge number of closely lying states and care has to be taken in order to properly assign the ground state. The one we have found corresponds to $N = 10$ with an optimized Co–Co distance of 2.99 Å and binding energy per atom equal to 0.98 eV. The highest occupied Kohn-Sham orbital is of T_2 symmetry, in the majority spin "band" and having two electrons, thus being a candidate for the Jahn-Teller (JT) distortion. The atomic state electron configuration in Co_4 is $s^{1.12}p^{0.29}d^{7.58}$.

Next, we have assumed a square geometry for cobalt tetramer imposing the D_{4h} constraint. The optimized Co–Co distance was also equal to 2.29 Å with $N = 10$. The adjacent spin up/down differences $N = 8$ and $N = 12$ produced less stable states being placed above the ground state by 0.56 eV and 1.85 eV, respectively (vertical values). The optimized T_d structure is more stable than optimized D_{4h} one by 0.96 eV. The analysis of the eigenvalue spectra of Co_4 in the square geometry shows that the highest occupied orbital containing one electron has E symmetry (FIGURE 3.3). Thus, the JT effect is possible here and consequently the symmetry has been lowered from D_{4h} to D_{2h}. The D_{2h} rhombus structure has also been optimized. The ground state has been found for a Co–Co distance equal to 2.19 Å along with a 72 degree angle for $N = 10$. As expected, the optimized D_{2h} structure is more stable than the square geometry by 0.29 eV. Clearly, by choosing the square geometry, other distortions are possible, though, due to the rather small energy differences between different JT structures the quality of both the grid and basis sets must be enhanced–possibly with BSSE corrections. On the other hand, the change of geometry may imply the change in N, therefore changing the magnetic moments. That, in turn, is directly connected with a rather big rearrangement of the XC energies so the JT effects in transition metal clusters *must* be discussed along with the level of XC treatment.

3.3.5 Cobalt Pentamer

The geometry of Co_5 has been assumed as equilateral trigonal bipyramid so the C_{3v} symmetry has been adopted in order to reduce the time of computations during geometry optimizations. The lowest state has been obtained for $N = 13$ and Co–Co distance 2.35 Å although another state with $N = 11$ has also been optimized leading to the same bond distance as in the former case. This state lies only 0.34 eV higher than the ground state and possible JT distortions may lead to new state with, after geometry optimization process, an increased width of a d "band", leading to the partial collapse of magnetic moment, thus yielding the ground state with a smaller local magnetic moment. The Mulliken population analysis gives an average atomic hybridization of cobalt as $s^{1.039}p^{0.462}d^{7.562}$.

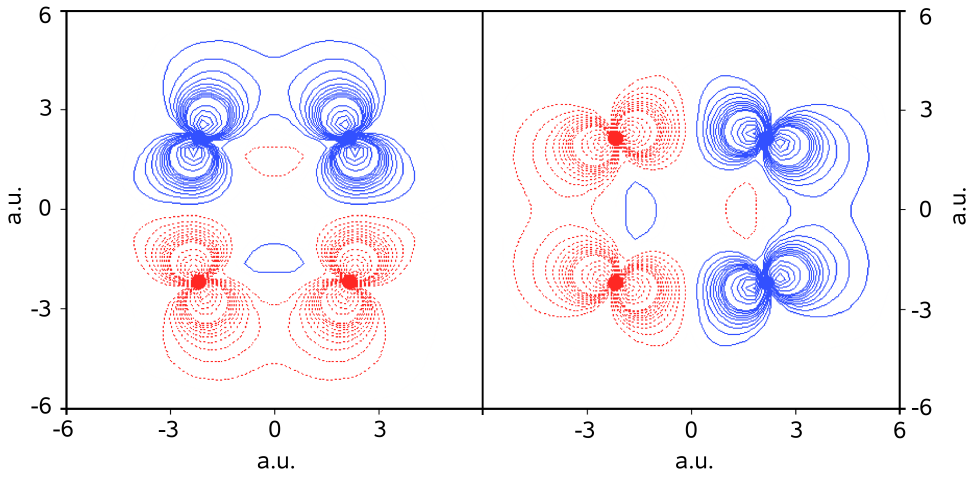

Figure 3.3:
Plots of the $3e_u^{\downarrow}$ orbital of a Co_4 cluster. The symmetry of the cluster is D_{4h}.

3.3.6 Cobalt Hexamer

The Co_6 cluster has been assumed in a form of square bipyramid within of O_h symmetry constraint. The lowest state has been obtained for Co–Co distance 2.28 Å and $N = 14$. This time the highest occupied orbitals are of T_{1u} and T_{2g} symmetry for majority and minority spin, respectively with its full occupancy of 3 electrons. This state is strongly bound, giving the binding energy per atom 1.74 eV. Such bond strength can be explained considering the directional nature of d orbitals. The present structure makes the d orbitals pointing to each other directly thus giving the strongest overlap among all clusters studied. This is also confirmed by auxiliary analysis of Mulliken population giving an average atomic hybridization as $s^{1.068}p^{0.316}d^{7.506}$.

3.3.7 Cobalt 13-atom Cluster

The last cluster studied was Co_{13} within O_h symmetry. Its geometry has not been optimized and the assumed Co–Co distance between central atom and its 12 neighbors corresponds to the Co bulk value of 2.44 Å. However, the spin up/down electron difference N has been optimized in order to get a proper account for the average magnetic moment. The lowest energy was obtained for $N = 27$ while the states with $N = 25$ and $N = 29$ were placed higher by 1.14 eV and 0.13 eV, respectively. One has to notice the small difference between the states with $N = 27$ and $N = 29$. If the geometry had been optimized, the state with $N = 27$ would be more favored and though there would be a tendency of the magnetic moment to collapse due to the increase of the band width, it is very likely that $N = 27$ would be preferred for optimal geometry due to the over 1 eV separation with respect to the $N = 25$ state. The obtained average magnetic moment 2.08 μ_B is in complete

agreement with the extrapolated experimental value [65]. However, there is a big difference between local magnetic moments of central atom and the neighboring ones. The central Co atom is the least bulk-like. It has an excess of charge and a very small magnetic moment, 0.56 μ_B with large negative *sp* contribution almost -1 μ_B while for the 'surface' atoms their magnetic moment is enhanced: 2.204 μ_B where the *d* contribution to this value is essential: 1.92 μ_B. Using the Mulliken population analysis of the eigenvalue spectra the estimated *d* 'band' width is 3.65 eV for spin up and 3.12 eV for spin down. The lowest molecular level is an *s*-like with *p*-type contributions and eigenvalues for different spins yield an *sp* exchange splitting of 0.17 eV. The 'bottom' of *d* type molecular levels is splitted by 0.33 eV.

3.4 Analysis of the Obtained Results and Conclusions

The electronic and structural properties of small cobalt clusters have been studied within the frame of density functional theory. The nonlocal (GGA) treatment of XC, through DFT-based methods, offers the most accurate description of many-body problems in a present-day *ab initio* calculations upon transition metal systems. Also, use of the optimized MCP, with the $3p - 3d$ correlations explicitly treated by shifting the $3p$ shell into a valence basis set, ensures a unified and accurate description of all clusters within a computational method.

The results exhibited in the preceding SECTION confirm our good MCP on cobalt calculations. Some properties, like binding energies, are improved in relation to AE calculations. A critical point that put forward the above idea is the MCP nonspherical calculations on the cobalt atom, placing the configuration $3d^7 4s^2$ as the ground state, in a good agreement with experimental result. In the cobalt dimer, the bond length is close to the reported AE calculations. Nevertheless, properties that are linked directly with energy have a substantial improvement due to a reduction of the BSSE when we consider an MCP. In the case of Co_3, the more stable structure is an obtuse triangle with N=5. MCP locates more clearly this structure as the GS than AE calculations, which tend to collapse the low-lying states in a short energy range.

From now on, the conclusions are referred to the cobalt clusters with $n \geq 4$. All clusters show an abundance of close-lying states. Therefore, for each cluster nuclearity, its ground state has to be assigned with care. The main purpose of this CHAPTER was to show how the basic properties of Co clusters evolve with the cluster size. We imposed some constrains in order to achieve a reasonably short computing time. The key among them was the assumed high symmetry of each cluster studied. The highly symmetric structures exhibit degeneracy of the highest occupied Kohn–Sham orbitals leading therefore to JT distortions. This was investigated partially in the case of a planar tetramer, obtaining results that throw an affirmative answer.

Table 3.4:
Electronic and magnetic properties of cobalt clusters with $n \geq 4$ as a function of cluster size. The spin up/down electron difference N has been optimized. The eigenvalue of highest occupied Kohn–Sham orbital with opposite sign is also shown ($\uparrow$ /$\downarrow$ denote whether it is of majority/minority spin).

Property	Co_4	Co_5	Co_6	Co_{13}
Binding energy per atom (eV)	0.980	0.856	1.743	0.942
Magnetic moment per atom (μ_B)	2.50	2.60	2.33	2.08
"Kohn–Sham" IP (eV)	5.91$\uparrow$	5.99$\uparrow$	6.01$\uparrow$	6.21$\uparrow$
Optimized Co–Co distance (Å)	2.29	2.35	2.28	2.44
Population of d orbital	7.58	7.56	7.51	8.05

Nevertheless, its energetics, as well as the changes of cluster magnetic moments, are small and our general conclusions are still valid. The main results are collected in TABLE 3.4.

As it can be seen, the magnetic moment of Co clusters is enhanced when compared to its bulk value of 1.72 μ_B. That enhancement can be accounted for an increased exchange splitting due to the decrease of the coordination number. On the other hand, the splitting of the majority and minority 'bands' strongly depends on both cluster symmetry and Co–Co distances, thus the 'size effect' with respect to the local magnetic moments has an oscillatory character. The change of bond length affects directly the band widths [59] so, in turn, the local magnetic moments. Therefore, the cluster geometry has to be optimized if the calculated magnetic moment is to be confronted with cluster experimental data. As the cluster size increases so does the 'band' width. This can be clearly seen on FIGURE 3.4 where the Density of States (DOS) curves are sketched.

The DOS has been obtained by a Gaussian broadening (0.2 eV) of each eigenenergy level within s–d–p manifolds. The cluster Fermi level presented in FIGURE 3.4 as a dashed vertical line obtained by the integration of a DOS, lies between partially bonding and mainly antibonding *spd* orbitals specially in the minority spin. This gives a clear indication of the huge number of closely lying excited states for each cluster studied. Also, well below the E_F there is a mainly s-like peak, common to all clusters while the peaks closer to E_F have predominantly d-character, and increasingly, antibonding properties. Another property, which is commonly studied in metal clusters, is the IP, which, as the cluster size increases, should converge to the bulk Fermi level. It has a weak monotonic rather than an oscillatory character with respect to cluster size while the binding energies are oscillatory along with it. The major factor here is the assumed symmetry of the cluster. It is clearly seen in Co_6, where the overlap of d orbitals is the strongest one due to their 'head to head' positioning, thus resulting in the highest binding energy. This is also confirmed by the degree of the d orbitals localization obtained by Mulliken analysis. Our results for Co_{13}, when compared to other theoretical calculations [42],

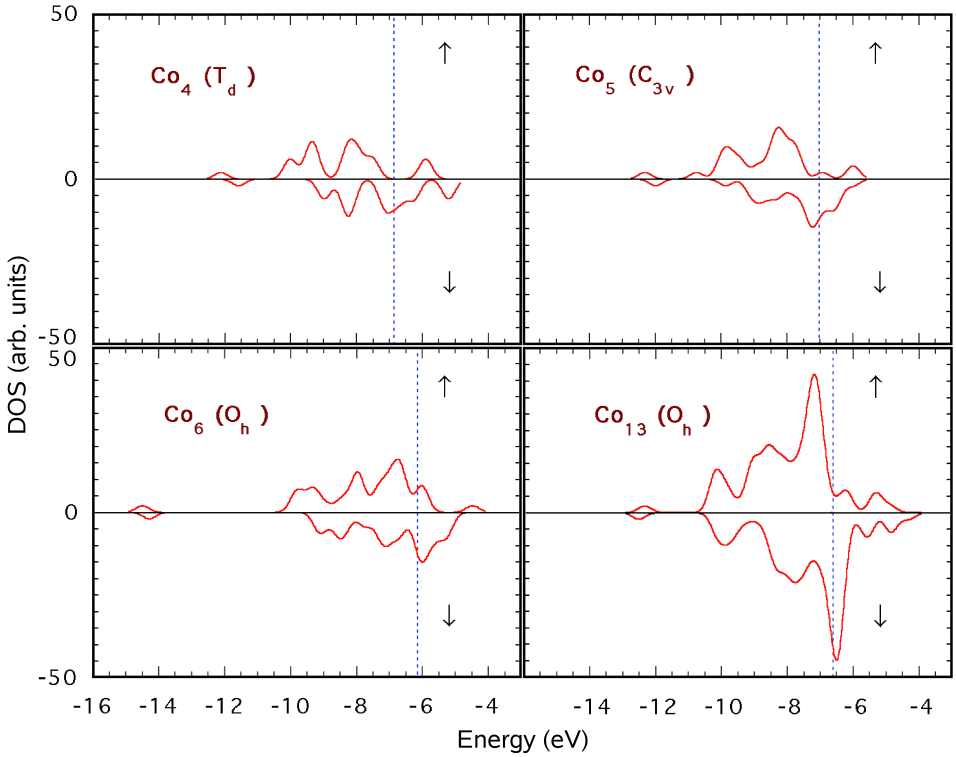

Figure 3.4:
Density of states (DOS) curves for 3-D cobalt clusters. The vertical dashed lines indicate the DOS integrated Fermi level.

are markedly different with respect to the magnetic nature of the Co central atom. In our view, it is the least bulk-like one, with negative *sp* contributions to the net spin moment—a feature which has been recently observed for small Fe_n clusters [66]. Also, the Mulliken population of the molecular levels shows a decreasing contribution of the central atom as their eigenvalues approach the cluster Fermi level. The eigenstates near the Fermi energy are mainly responsible for the creation of the magnetic moment, so its value for the central atom should be small. In the light of these arguments, the *sp* contributions via *sp*–*d* hybridizations indirectly influence local magnetic moments though, undoubtedly, the *rôle* of 3*d* electrons is dominant. As if the *d* orbitals were considered alone they would give the net spin moment of central atom 1.53 μ_B. Clearly, in small transition metal clusters, the *sp* as well as the *s p d* hybridizations are very important and their presence has to be reflected in an appropriate basis sets. Finally, due to the big sensitivity of the local magnetic moments with respect to cluster environment, the subtle balance between mutually opposite XC rearrangements has to be fully taken into account via the high level accuracy of the XC potentials used in self-consistent calculations.

In our opinion, the present results and those given in REFERENCES [43, 44, 67] when viewed together provide both an extensive treatment of cobalt cluster and many first- and second-row dimers with a high level of exchange and correlation descriptions and also valuable experience within density functional methodology.

4

Determination of the Lowest-energy Structure of Ag_8 from First-principles Calculations

> *Too many people miss the silver lining because they're expecting gold.*
>
> — Maurice Setter

Synopsis

The ground-state electronic and structural properties and the electronic excitations of the lowest-energy isomers of the Ag_8 cluster are calculated using density functional theory (DFT) and time-dependent DFT (TDDFT) in real-time and real-space schemes, respectively. The optical spectra provided by TDDFT predict that the D_{2d} dodecahedron isomer is the structural minimum of Ag_8 cluster. Indeed, it is borne out by the experimental findings.

4.1 Introduction

In recent years, a new field has emerged from the understanding, control and manipulation of objects at the nanoscale level (nano-objects). It is commonly known as nanoscience. This field involves physics, chemistry, and even engineering and addresses a huge number of important issues starting from basic science and ending in a large variety of technological applications [68]. Among the nano-objects, the small clusters or nanoclusters play a very important role, since they are the bricks of nanoscience. Therefore, the study of small clusters deserves special attention. In this respect, the steps to follow for a complete description of a cluster can be summarized in the following three questions: What is the lowest-energy structure?,

What is the effect of increasing or decreasing the temperature on the structural properties of a cluster? and the last step deals with the kinetic effects in the formation of the nanocluster. Here, we are only concerned with the first question for the silver octamer, leaving the other two questions open for future investigations.

From the theoretical point of view, first-principles methods give an enormous advantage for understanding, projecting, and inventing new materials that is reflected in the huge number of articles published in the field of materials science. Likewise, density functional theory (DFT) has emerged as a new and promising tool for *ab initio* electronic structure calculations and gives valuable information about the geometry of nanoscale systems [69] but unfortunately it not always predict the correct structure of the cluster under consideration. In this regard, the silver octamer belongs to the group of the controversial systems for which the lowest-energy structure is unresolved by DFT.

Recently, Radcliffe *et al.* [70] have proposed Ag_8 clusters embedded in helium droplets as a suitable system for light amplification based on an optically accessible long-living excited state (E*) and thereby, from the theoretical point of view, the determination of the structure becomes a key point as the first step for identifying and controlling the levels that populate E*. Up to now, it has not been possible to make a reliable theoretical prediction of the most stable structure of Ag_8. A review of the literature reveals that there are two competing geometries in eight-atom clusters of s-electron elements, having T_d and D_{2d} symmetry. In fact, different levels of theories favor different geometries: DFT in its local density approximation (LDA) [71], multireference configuration interaction method [72], a tight-binding approach [73], and many-body perturbation theory-based calculations [74] give the D_{2d} geometrical shape as the lowest-energy structure of Ag_8 whereas the equation-of-motion coupled-cluster method [75], time-dependent DFT only at the LDA level [76], and molecular-dynamics simulations [77] predict a T_d structure as the structural minimum. It was reported in References [72, 75] that the D_{2d} geometry is favored energetically over T_d symmetry when explicit correlation treatments for 5s electrons are included, but since the calculated energy difference between T_d and D_{2d} isomers is very small, the predicted theoretical ordering is uncertain. One way of solving this vexing problem comes from the use of the time-dependent density functional theory (TDDFT) [78] that is a generalization of traditional ground-stationary-state DFT to treat the dynamic response of the charge density to a time-dependent perturbation. TDDFT is a powerful methodology towards the calculation of the optical spectra and thereby gives access to excited-state information.

In this brief Chapter, we calculate the optical response of the T_d and D_{2d} geometries and they are compared with both each other and the experimental findings. The atomic positions were fully optimized with an all-electron DFT implementation at the generalized gradient approximation (GGA) level, representing an improvement over other TDDFT studies in small silver clusters [76]. This work relies on the combination of the traditional DFT and its generalization to excited states, as a

promising tool for elucidating structures that DFT by its own is unable to predict. Here, we demonstrate that the D_{2d} structure is the structural minimum of Ag_8 and the calculated spectra allows us to estimate the interaction of Ag_8 with the surrounding helium or the argon matrix presented in experimental observations.

4.2 Computational Details

With the aim of elucidating the lowest-energy structure of the Ag_8 cluster, we have performed density-functional-theory-based calculations consisting of a linear combination of Gaussian-type-orbitals Kohn-Sham density-functional methodology (LCGTO-KSDFM) to obtain the structural and electronic ground-state properties [79] and a TDDFT implementation to compute the electronic excitations [80]. For the former, all-electron calculations were carried out with DEMON-KS3P5 [79] at the GGA level to take the exchange-correlation (XC) effects into account [81]. An orbital basis set of contraction pattern (633321/53211*/531+) was used in conjunction with the corresponding (5,5;5,5) auxiliary basis set for describing the s, p, and d orbitals [82]. The grid for numerical evaluation of the XC terms had 128 radial shells of points, and each shell had 26 angular points. Spurious one-center contributions to the XC forces, typically found in systems with metal-metal bonds when using a nonlocal functional, are eliminated in a similar way as has been done in Reference [83]. Trial geometries were fully optimized without symmetry and geometry constraints for different multiplicities using the Broyden-Fletcher- Goldfarb-Shanno algorithm [37]. The multiplicities were ranged from 1 to 11, and in all reported structures the singlet state was favored energetically. During the optimization, the convergence criterion for the norm of the energy gradient was fixed to 10^{-4} a.u. while it was 10^{-7} a.u. for the energy and 10^{-6} a.u. for the charge density. For the latter, after inserting the atomic coordinates of the converged structures provided by DEMON-KS3P5 all the dynamical quantities are computed by evolving the electronic wave functions in real time and real space [80]. The electron-ion interaction is described through the Hartwigsen-Goedecker-Hutter relativistic separable dual-space gaussian pseudopotentials [84], and the XC effect was treated in the GGA, implemented via the Perdew-Burke-Ernzerhof functional [22]. The grid in real space to solve the Kohn-Sham equations consists of a sum of spheres around each atom of radius 5.5 Å and a mesh spacing of 0.23 Å. The time step for the propagation of the electronic orbitals was fixed to 0.0013 fs, which ensures the stability of time-dependent propagation. An artificial electronic temperature of 10 K was included according to the Fermi-Dirac function used to distribute the electrons among the accessible states.

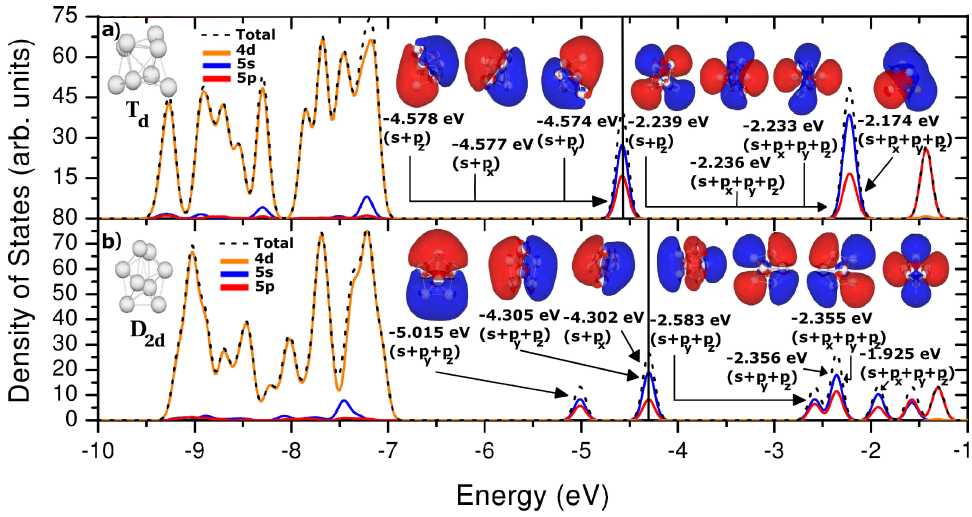

Figure 4.1:
Energy levels, partial, total density of states, and shapes of the delocalized molecular orbitals for the higher-lying occupied and lower-lying unoccupied levels of Ag_8 isomers: a) T_d-TT and b) D_{2d}-DD. The orbitals below the Fermi level are double occupied; for these levels only one molecular orbital is presented. The solid vertical line represents the Fermi level.

4.3 Results and Discussion

After a review of the literature on silver clusters [71–75], we have decided to optimize, as a good candidate to the structural minimum of the octamer, the following isomers of Ag_8: a D_{2d} dodecahedron (D_{2d}-DD), which can also be viewed as a distorted bicapped octahedron, a T_d tetracapped tetrahedron (T_d-TT) and a C_s 1-pentagonal bipyramid (C_s-PBP) in Fournier's notation [71]. The main results [density of states (DOS), optimized structures, polarizabilities, ground state energies, etc.] of the electronic structure calculations are collected in Table 4.1 and FIGURE 4.1. The LCGTO-KSDFM calculations clearly show that the C_s-PBP geometry is energetically far from the lowest-energy structure by an amount of 181.25 meV. Therefore, we will concentrate our attention in D_{2d} and T_d structures.

Despite the fact that the lowest-energy isomer corresponds to a D_{2d} symmetry, it should be noted that the ground-state energy difference between D_{2d}-DD and T_d-TT isomers is very small ($\Delta E_{D_{2d}\rightarrow T_d} = 6.14$ meV) compared to 0.19 eV which is the averaged energy difference between the ground-state structure and the second stable structure of Ag_n ($2 \leq n \leq 12$) [71]. Furthermore, the polarizabilities and the HOMO-LUMO gaps (HLg) do not offer a clear picture for elucidating the structural minimum of the octamer. That is, it is well known that the Ag_8 cluster is a closed-shell system and it was demonstrated experimentally and theoretically that the closure of electronic shell manifests itself in particularly large HLg's (see [73] and references therein); consequently, the HLg's reported in Table 4.1 are on the side

Table 4.1:
Ground-state energies relative to the most stable isomer (D_{2d}-DD) and electronic structure properties of the DFT-optimized Ag_8 cluster isomers. The Fermi level is denoted by E_f and $\Delta\xi$ stands for the HOMO-LUMO gap. The mean static polarizability $\bar{\alpha}$ and the polarizability anisotropy $\Delta\alpha$ were calculated under the influence of an external electric field of strength 0.0005 a.u..

Symmetry	ΔE_{DFT} (meV)	E_f (eV)	$\Delta\xi$ (eV)	$\bar{\alpha}$ (Å^3/atom)	$\Delta\alpha$ (Å^3/atom)
D_{2d}	0.00	-4.302	1.719	6.32	1.22
T_d	6.14	-4.574	2.335	6.46	0.01
C_s	181.25	-4.048	1.327	6.45	1.71

of stabilization of the T_d-TT isomer. As far as the reported polarizabilities are concerned, in molecular electronic distribution studies under the influence of an external electric field, the relevant quantities are the mean static polarizability $\bar{\alpha} = (\sum_{i=1}^{3}\alpha_{ii})/3$ and the polarizability anisotropy $\Delta\alpha$, defined as:

$$\Delta\alpha = \sqrt{\frac{\sum\limits_{\substack{i,j=1,2\\ i<j}}^{2,3}(\alpha_{ii}-\alpha_{jj})^2 + 6\sum\limits_{\substack{i,j=1,2\\ i<j}}^{2,3}\alpha_{ij}^2}{2}}, \tag{4.1}$$

where $\alpha_{ij} = \partial(\mu_e)_i/\partial E_j$ is the ij component of the polarizability tensor under the action of an external electric field E_j. It is not a common procedure to express the polarizability anisotropy such as it was defined in Equation (4.1). The commonly used definition omits the second term $(6\sum_{i,j=1,2;i<j}^{2,3}\alpha_{ij}^2)$ and thus neglects the important influence that the off-diagonal elements of the second-rank polarizability tensor play in the symmetry considerations of the electric charge distribution [85]. The mean static polarizabilities, reported in Table 4.1, are quite similar to each other, showing on average that the electron charge is nearly equally distributed among the three isomers. However, only the polarizability anisotropy of the T_d-TT isomer is clearly reduced. This result tends to stabilize the T_d symmetry over D_{2d} because the less polarizability anisotropy is, the more spherically symmetric the charge distribution is and the latter condition is favored by a closed-shell system like the silver octamer. Indeed, the delocalized molecular orbitals for the higher-lying occupied levels of the D_{2d} and T_d geometries, presented in Figure 4.1, exhibit a hybridization of the atomic 5s levels with the 5p levels leading to a nearly spherical shape, whereas for the lower-lying unoccupied levels, the spherical symmetry becomes less important. The proximity in energy and the corresponding superposition of the spatial distribution of the higher-lying occupied molecular orbitals of the T_d-TT isomer with respect to the ones of the D_{2d}-DD isomer contribute to a spherical symmetrization of the T_d-TT charge distribution.

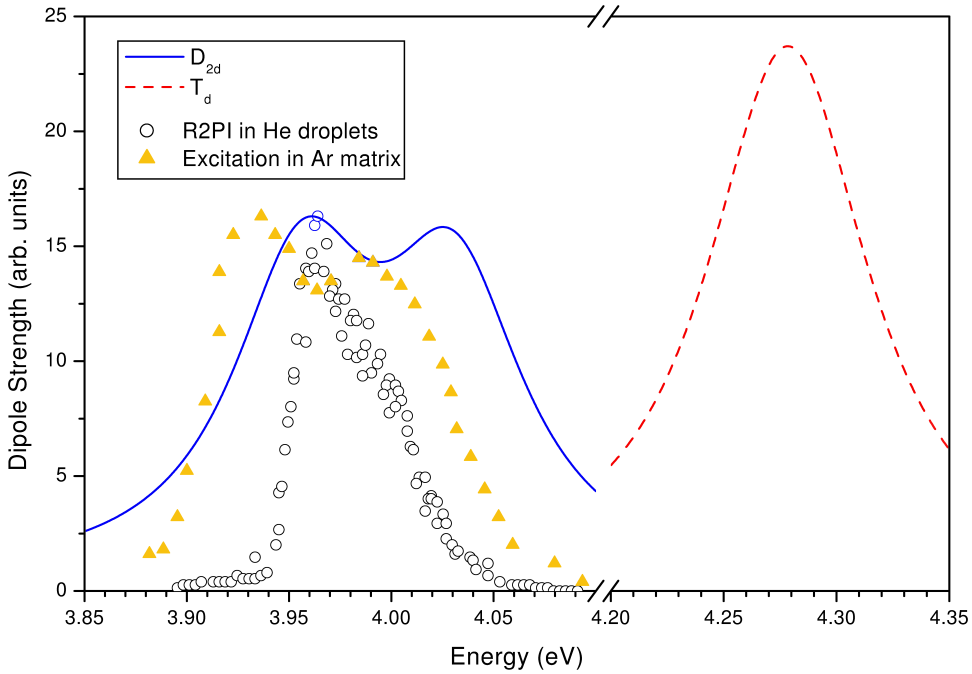

Figure 4.2:
Comparison between two experimental recorded spectra and the calculated spectra for both (solid line) D_{2d}-DD and (dashed line) T_d-TT isomers at a temperature of 10 K. Open circles correspond to the resonant two-photon-ionization (R2PI) spectroscopy on Ag_8 clusters in He droplets [86] while the solid triangles are for the excitation spectrum of Ag_8 excited with monochromatic Xe light in an Ar matrix [87]. The D_{2d}-DD isomer spectrum is in excellent agreement with the experiment whereas the T_d-TT isomer spectrum is around 0.31 eV blueshifted compared to the R2PI spectrum.

The balance of the aforementioned contrary tendencies does not allow a reliable prediction of the structure, such as was discussed in literature [71, 73–75, 77]. The TDDFT calculations using the structural parameters provided by the LCGTO-KSDFM as starting point can shed some light for a better understanding of this vexing controversy on the structure of Ag_8. In this respect, as it is shown in FIGURE 4.2 the calculated spectrum for D_{2d} symmetry is in excellent agreement with the resonant two-photon ionization spectrum reported by F. Federmann *et al.* [86] and the excitation spectrum reported by C. Félix *et al.* [87], whereas the T_d-TT-calculated spectrum only shows one resonant peak and it is about 0.31 eV blueshifted with respect to the experimental measurements. Thus, the LCGTO-KSDFM predicted structure is confirmed by the TDDFT calculations of the optical response when it is compared to the experimental evidences.

Some of the relevant states involved in the transitions that populate the peaks of FIGURE 4.2 are provided through the calculated DOS depicted in FIGURE 4.1. For the D_{2d} isomer, the eigenvalues of the HOMO and HOMO-1 states are both

close together in energy and the HOMO-2 state is 0.7 eV further down, while for the T_d-TT isomer, these three states were grouped together in a window energy of only 3 meV. It is worthwhile to mention here that the T_d-TT isomer has high symmetry, so many states will be degenerate. However, because of small numerical errors, it is quite possible that states that should strictly be degenerate will show as being within very small energy windows. In the energy range displayed in FIGURE 4.2 for D_{2d} symmetry, the TDDFT calculations predict four electronic transitions starting from the twofold degenerate HOMO and HOMO-1 states to two excited states separated 0.07 eV in energy and they give rise to two peaks because of the nearness in energy of the HOMO-1 and HOMO states. In the case of the T_d symmetry, six transitions are predicted, giving rise to only one peak because the two excited states that electronic transitions populate are only 1 meV separated, as commented above.

Some consequences can be extracted going further in the analysis of the calculated spectrum for D_{2d}-DD isomer when it is compared with the experimental references reported in FIGURE 4.2. On one hand, for the case of R2PI experiment we attribute the slight difference in peak position ($\sim$ 3 meV) to the helium environment through the formation of electron bubble states that significantly blue shift the transition [88]. As already mentioned above, our TDDFT calculations also confirm the authors' feeling of REFERENCE [86] that the asymmetry of the peak involves more than one transition. On the other hand, the comparison between the excitation spectrum in Ar matrix [87] and the calculated D_{2d} isomer spectrum allow us to measure the interaction of the Ar matrix with the Ag_8 cluster. Thus, the shift of energy probably due to Ar matrix effects is estimated to be about 25 meV, which is great enough compared to the slight difference in peak position ($\sim$ 3 meV) attributed to the helium surrounding the Ag_8 clusters in the R2PI experiment. Consequently, the use of liquid helium droplets as a spectroscopic matrix has the advantage over argon matrix of providing an environment more suitable for study the electronic excitations of small and free silver clusters.

4.4 Conclusions

In conclusion, we have shown that a combination of a LCGTO-KSDFM and TDDFT approach is able to reproduce the measured optical response of the silver octamer and allow us to elucidate its lowest-energy structure below 10 K. Our calculation thus confirms that the structural minimum of Ag_8 is the D_{2d}-DD isomer, whose geometrical structure is depicted in FIGURE 4.1. The TDDFT calculations have provided a number of electronic transitions involving the resonant peaks shown in FIGURE 4.2 and demonstrate that the R2PI experiment is a good technique to measure experimentally the electronic excitations of bare silver clusters because it is less aggressive than, for example, experiments that consider argon as the spectroscopic matrix.

5

Structure of Small Silver Clusters and Static Response to an External Electric Field

> *Don't gain the world and lose your soul, wisdom is better than silver or gold ...*
>
> — Bob Marley

Synopsis

The static response properties and the structural stability of silver clusters in the size range $1 \leq n \leq 23$ have been studied using a linear combination of atomic Gaussian-type orbitals within the density functional theory in the finite field approach. The Kohn-Sham equations have been solved in conjuction with a generalized gradient approximation (GGA) exchange-correlation functional. A proof that the finite basis set GGA calculation satisfies the Hellmann-Feynman theorem is also included in the Appendix A. The calculated polarizabilities of silver clusters are compared with the experimental measurements and the jellium model in the spillout approximation. Despite the fact that the calculated polarizabilities are in good agreement with both of them, we have found that the polarizability appears to be strongly correlated to the cluster shape and the highest occupied-lowest unoccupied molecular-orbital gap.

5.1 Introduction

Transition-metal clusters play a dominant role in cluster physics [89]. They have attracted the interest of many researchers and consequently the number of publications on that topic have experienced a dramatic increase over the past thirty years

because metal clusters exhibit increasingly interesting structural, electronic, catalytic, as well as optical properties [68, 90]. Likewise, the biomedical applications of nanoclusters have experienced a great impact in the biomedicine community [91].

Among the aforementioned applications and properties of metal clusters, their optical properties that result from the light-matter interaction at the nanoscale level are an area of great current interest [92]. Many of the advances in this area could not have been made possible without the development of the optical spectroscopy techniques that have been indispensable for elucidating the electronic structure of clusters. These experimental techniques can be divided into two groups, that is, nondestructive and destructive methods. In the former methods, also called linear response methods, a weak electromagnetic field interact with the cluster and it absorbs or scatters light without undergoing ionization or dissociation whereas in the destructive methods the ionization is achieved. The nondestructive methods in connection with the linear-response theory have been extensively used to calculate photoabsorption cross sections and specially static dipole polarizabilities.

The static dipole polarizability is a physical observable of metal clusters that has been shown to be closely related to the shape and structural geometry. For example, electronic structure calculations of small Si clusters show that the polarizability is strongly correlated with the shape of the clusters [93]. Likewise, the interplay between theory and experiment is a powerful tool that serves to identify which cluster is observed in the experiments throughout the comparison of the calculated polarizabilities with the experimental ones [94]. Moreover, the static dipole polarizability is also well known to be intimately related to the shell electronic structure. For example, the noble-metal clusters whose optical properties have been extensively studied in literature (mainly from the experimental side) present lower static polarizabilities than alkali metals because they are excellent examples of spherical shell structure. However, in the case of the silver clusters, the influence of d electrons in the static polarizability has been less studied at least from the theoretical point of view and it deserves more investigation. This point, among others, is addressed in this work.

In this Chapter we have employed a density functional theory-based (DFT) calculation within the generalized gradient approximation (GGA) to properly account for the strong correlation effect of the localized d electrons and charge density inhomogeneities. We have studied the structural stability and the static response properties of small silver clusters ranging in size from $n = 1$ up to $n = 23$, where n is the number of atoms forming the cluster. The calculated static polarizabilities are only compared with the available experimental data since, unfortunately, no *ab initio* quantum-molecular calculations have been done so far for the static polarizabilities of silver clusters in the size range covered by our investigation. The available theoretical data are reported in Reference [95] for very small silver clusters with $1 \leq n \leq 8$. The agreement between our values and those of Idrobo *et al.*, who computed the static polarizabilities within the framework of the real

space finite-different *ab initio* pseudopotential method, is excellent in the case of the GGA approximation, which makes the results obtained with the present DFT method more valuable. In addition, we have compared our results with the jellium model in the spillout approximation and the deviation of our results from this model is explained in terms of the electronic structure parameters like highest occupied and lowest unoccupied molecular orbital (HOMO-LUMO) gaps or structural symmetry. We also show and discuss how the d electrons affect the static polarizabilities since when n is sufficiently large, i.e. greater than 18, the polarizability tends to be constant in contrast to the one of the alkali metals. The rest of the CHAPTER is organized as follows. In SECTION 5.2, we present the theoretical background and the computational details along with the computational parameters used in this CHAPTER. Moreover, the structural stability of the silver clusters is studied in detail in SECTION 5.3. The results of our calculations and the influence of the electronic structure observables in the static polarizabilities are given in SECTION 5.4. We conclude with a brief summary of the reported results provided by our *ab initio* calculations in SECTION 5.5. In the Appendix A, we prove that the Hellmann-Feynman theorem is satisfied by the finite basis set density functional framework in the generalized gradient approximation.

5.2 Method and Computational Details

Traditionally there has been two different ways of computing the polarizability of molecular systems. Thus, the polarizability is identified either as the second-order term in the perturbation expansion of the electronic energy with respect to the applied external uniform electric field or as the linear response of the dipole moment to that electric field. Both definitions are equivalent when the Hellmann-Feynman theorem is satisfied. The Hellmann-Feynman theorem holds for an exact solution of the Schrödinger equation and also for some approximate solutions. In particular, it is satisfied by the fully self-consistent finite basis set solutions when the exchange-correlation (XC) energy is approximated by the GGA as shown in the Appendix A.

We have adopted the dipole-moment-based definition as our working definition because in this expression the field occurs only in the first power for the calculation of the polarizability instead of the second as in the energy expansion. The polarizabilities α_{ij} ({i,j}=x,y,z or alternatively {i,j}=1,2,3) are calculated by the finite field (FF) method [96] which consists of computing the electric dipole moment μ_i of a system under the influence of an external electric field F_i according to the following finite-difference relation

$$\alpha_{ij} = \left(\frac{\partial \mu_i(F_j)}{\partial F_j} \right)_{\vec{F}=0} = \lim_{F_j \to 0} \frac{\mu_i(F_j) - \mu_i(-F_j)}{2F_j}. \tag{5.1}$$

In the FF method, one of the most crucial problems to evaluating the derivatives is the choice of an appropriate field strength. Several works have assessed the numerical accuracy of polarizability against different field values and concluded that the best region of linear response is for field strengths ranging from 10^{-4} up to 10^{-2} a.u. [73, 97]. For that reason, we have used a field strength of 5×10^{-4} a.u. that is applied along the molecular axis. At least seven self-consistent field (SCF) runs, with the field strengths 0 and $\pm F_i$, are necessary to calculate the polarizability. Once the polarizability tensor components are computed, the mean static polarizability is calculated as $\bar{\alpha} = (\sum_{i=1}^{3} \alpha_{ii})/3$ and the polarizability anisotropy is defined as

$$\Delta\alpha = \sqrt{\frac{\sum\limits_{\substack{i,j=1,2 \\ i<j}}^{2,3} (\alpha_{ii} - \alpha_{jj})^2 + 6 \sum\limits_{\substack{i,j=1,2 \\ i<j}}^{2,3} \alpha_{ij}^2}{2}} \tag{5.2}$$

in the general axis frame or without the second addended ($6 \sum_{i,j=1,2;i<j}^{2,3} \alpha_{ij}^2$) in the coordinate system which makes the second-rank polarizability tensor α diagonal.

With the aim of studying the static response properties of small silver clusters, Ag_n ($2 \leq n \leq 23$), we have performed density functional theory-based calculations consisting of a linear combination of Gaussian-type-orbitals (LCGTO) Kohn-Sham density-functional methodology as it is implemented in deMon program [79]. All-electron spin-unrestricted calculations were carried out at the GGA level to take the XC effects into account [81]. Local-density approximation (LDA) sometimes yields inaccurate bond lengths and total energies due to the insufficiency in describing the strong correlation effects of the localized d electrons and charge density inhomogeneities. In these regards, the GGA should be a better choice than LDA [98]. For this reason, at the beginning of this work and to satisfy ourselves that the numerical procedure is reliable, we initiate a search of the functional that better fitted the calculated bond length of the silver dimer to the experimental one. The functional developed by Perdew and Wang [81] gave us a bond length of 2.534 Å that is in excellent agreement with the experimental measure (2.53350 Å) reported in Reference [99]. An orbital basis set of contraction pattern (633321/53211*/531+) was used in conjunction with the corresponding (5,5;5,5) auxiliary basis set for describing the s, p, and d orbitals [82]. In deMon, the electron density is expanded in auxiliary basis functions which are introduced to avoid the calculation of the N^4 scaling Coulomb repulsion energy, where N is the number of the basis functions. The grid for numerical evaluation of the XC terms had 128 radial shells of points and each shell had 26 angular points. Spurious one-center contributions to the XC forces, typically found in systems with metal-metal bonds when using a nonlocal functional, are eliminated in a way similar to what has been done in Reference [83]. A wide set of spin multiplicities ranging from 1 to 11 was checked

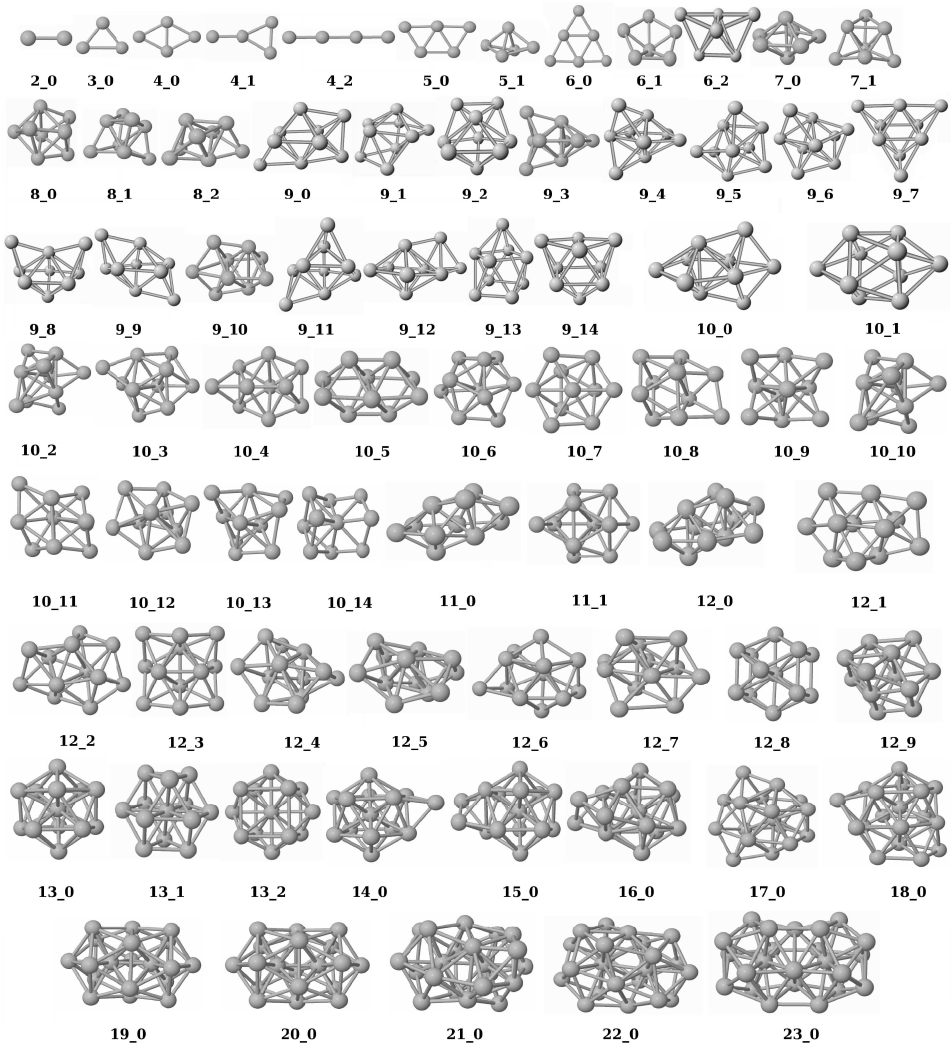

Figure 5.1:
Lowest-energy structures and isomers of Ag_n, $n = 2 - 23$, ordered (from left to right and top to bottom) by increased size and energy. The cluster n_m is the mth energetic isomer with n atoms.

to ensure that the lowest-energy electronic configuration is reached. The geometries were fully optimized without symmetry and geometry constraints using the Broyden-Fletcher-Goldfarb-Shanno algorithm [37]. During the optimization, the convergence criterion for the norm of the energy gradient was fixed to 10^{-4} a.u. while it was 10^{-7} a.u. for the energy and 10^{-6} a.u. for the charge density. The ground state structures and some of the lowest-energy isomers of the silver clusters studied in this Chapter are illustrated in Figure 5.1, since that the polarizability is closely related to the geometrical shape of the cluster.

5.3 Structures of Silver Clusters

FIGURE 5.1 and TABLE 5.1 show the structures, relative energies, first-neighbor distances, and vertical ionization potentials (IP) of the lowest-energy isomers predicted by the simulations for Ag_n clusters with $2 \leq n \leq 23$. The IPs have been calculated as the energy difference between the neutral cluster and the cation. We assign labels to clusters such as n_m, where n indicates the number of atoms and the second number gives the rank in increasing energy order. A huge sampling of trial geometries taken from the literature was evaluated [71]. While for these small clusters, it is nearly impossible to search for all possible geometries, the detailed search that we have carried out gives us some confidence that the ground state structures have been found.

For clusters with size varying from 2 up to 13, we optimized geometries and calculated energies for 78 isomers. We only reported the lowest-energy structures here, but their Cartesian coordinates in Bohr units are available upon request to the authors. We focus on isomers located 50 KJ/mol ($\approx$ 0.5 eV) or less above the lowest-energy structure because this value is considered to represent an error bar for relative energies computed with GGA functionals [100]. Whenever possible we compare the calculated IPs with the experimental ones to rule out the possible candidates to the ground state geometry. We will focus our attention mainly on the lowest energy cluster geometries which are different form the cluster structures reported in previous experimental or theoretical studies. For the rest of clusters, we simply just describe the lowest energy structures. In TABLE 5.1, other low energy isomers are also listed for comparison.

For the clusters with size varying from 14 up to 23, we took the initial guess structures from REFERENCE [101]. Moreover, in the early stage of the geometry optimization process and with the aim of speeding up the calculations, the structure of the silver clusters was first optimized in conjunction with a 17-electron scalar relativistic model core potential designed for the adequate description of the silver dimer bond length [102]. Once the geometry of the cluster was converged for the model core potential, an all-electron structural-relaxation calculation was performed leading to the current lowest-energy structures shown in FIGURE 5.1.

For the silver trimer, we have studied only one structure (isosceles triangle) because the minimum structure is well established in the literature [71, 103]. In the case of Ag_4, the lowest energy structure that we have found is the planar rhombus. The lowest-energy structures for Ag_3 and Ag_4 predicted by our calculations are in good agreement with other *ab initio* results [71, 75, 103].

The ground state structure found for the pentamer is a trapezoid with C_{2v} symmetry. In literature there is a controversy about the assignment of the structural minimum. Some theoretical studies predict as the ground state the planar structure [71, 75, 104] while other ones predict the trigonal bipyramid [103]. On the experimental side, it is worthwhile to mention that different experimental electron spin resonance and Raman spectra of Ag_5 have been interpreted by both trigonal

bipyramid [105] and planar geometries [106], respectively. As shown in TABLE 5.1, the vertical IP calculated for the trapezoid agrees quite well with the experimental result [107] and it is what underpins our predicted lowest-energy structure.

Four structures have been optimized for the Ag_6 cluster[1]. The planar trapezoidal D_{3h} structure resulted to be the most stable but only 0.079 eV lower in energy than the pentagonal pyramid. Both structures exhibit IPs very close to the experimental one and therefore, our *ab initio* calculations do not allow prediction of only one geometry as the structural minimum.

In the case of the silver heptamer, the pentagonal bipyramid (D_{5h} symmetry) is predicted as the lowest energy structure while the tricapped tetrahedron is 0.17 eV higher in energy. Although the relative energy and the ionization potentials do not allow a clear prediction about the minimum geometry, however most of the first principles calculations prior to this work have also obtained the pentagonal bipyramid as the fundamental structure [71, 72, 75, 95, 103].

For the silver octamer, we have decided to optimize as a good candidate to the structural minimum the following isomers: a D_{2d} dodecahedron, which can be viewed as a distorted bicapped octahedron, a T_d tetracapped tetrahedron and a C_s pentagonal bipyramid. Our calculations stabilize first the dodecahedron, secondly but very close in energy the T_d structure, and finally the pentagonal bipyramid with ΔE_{DFT}=0.181 eV. The comparison between the calculated IPs and the experimental measurements reported in REFERENCE [107] favor more the T_d structure than the D_{2d} one, however the assignment of the structural minimum is clearly inverted if we use the experimental IP (6.40 eV) measured in REFERENCE [108]. Our predicted minimum structure is also supported by a very recent REFERENCE where the authors determine the lowest-energy structure of Ag_8 by comparison of the optical spectra provided by time-dependent DFT with the experimental findings [109].

Fifteen structures have been optimized in the case of the Ag_9 cluster. A tricapped-distorted octahedron (C_s) was found for the lowest-energy structure which is in good agreement with the reported structure in REFERENCE [71], while in REFERENCES [75, 103] the ground state geometry is the bicapped pentagonal bipyramid. To satisfy ourself that the bicapped pentagonal bipyramid is not the structural minimum, we studied a wide range of pentagonal bipyramid structures capped with two atoms in different positions. After the geometry optimization, the final geometry is slightly distorted in most of the cases. The structures are plotted in FIGURE 5.1 and denoted as 9_1, 9_2, 9_3, 9_4, 9_5, 9_6, 9_8, 9_9, 9_10, 9_11, and 9_12. It is worthwhile to mention that from 9_0 up to 9_6, the structures are very close in energy and only the IPs of the pentagonal bipyramid structures agrees quite well

[1] During the geometry optimization process, the structure consisting of five atoms forming a pentagon and with the other atom in the center of it converged to the pentagonal pyramid. Therefore, we have decided to strip off any information about this structure because it is the same as the pentagonal pyramid.

with the experimental ones, so in gas-phase experiments it is likely to obtain the bicapped pentagonal bipyramid as the lowest-energy structure.

Contrary to what happened in the case of nanomers, the lowest-energy geometry of Ag_{10} cluster is a pentagonal bipyramid-shaped structure, namely, a tricapped pentagonal bipyramid. With the aim of testing the validity of this structure, we have also optimized a very distorted pentagonal bipyramid but it finally converged to the 10_0 structure. The second structure is a D_{4d} bicapped square antiprism and it is only 0.080 eV higher in energy with respect to the ground state. This structure has been predicted as the fundamental one in REFERENCE [103], nevertheless the comparison of the calculated IPs reported in TABLE 5.1 with the experimental value clearly show that the 10_0 structure is the best candidate to be the minimum structure.

The guess structures for Ag_{11} and Ag_{12} were obtained by adding atoms to the pentagonal bipyramid structure or by removing them from a 13-atom O_h cuboctahedron or from the icosahedral packing. Thus, the lowest-energy structures come from the pentagonal bipyramid shape in both cases while the structures coming from the cuboctahedron or the icosahedral packing are less favored energetically. In the case of the Ag_{11} geometries, we have studied nine isomers but, except for the 11_1 structure, the other ones are energetically far from the lowest-energy structure by an amount greater than 0.5 eV. While the relative energies clearly show that the fundamental structure is the one labeled with 11_0 ($\Delta E_{DFT}^{11\_0 \rightarrow 11\_1} = 0.268$ eV), however the calculated IP (Δ IP^{11_1}=0.02 eV) predicts the 11_1 as the minimum structure, and consequently these two structures would be probably observed in experiments. The same situation occurs for Ag_{12} but in this case more structures can be observed in low-temperature experiments.

Three structures have been selected as possible candidates for the structural minimum of the thirteen-atom silver cluster. They are the icosahedral geometry (I_h symmetry), the cuboctahedron cluster (O_h symmetry), and the D_{2h} structure which is a compact portion of the bcc crystal lattice capped with four atoms as it is illustrated in FIGURE 5.1. After the relaxation of the structures, the ground state geometry predicted by our calculations is the icosahedral structure. Although the calculated IPs are in general in a relatively good agreement with the experimental ones, however they do not add too much information to the determination of the lowest-energy structure. The relative energies of the isomers collected in TABLE 5.1 together with the fact that most of the articles devoted to the study of the structural properties of small silver clusters predict the icosahedral structure as fundamental one, give us some confidence that the icosahedral packing is valid for the Ag_{13} cluster [77, 103, 110].

As we comment above, for the rest of the clusters, that is, from Ag_{14} up to Ag_{23} we took the initial guess structures from REFERENCE [101]. They follow an icosahedral growth sequence capped with a variable number of atoms depending on the cluster size. In general, the calculated IPs are in good agreement with the

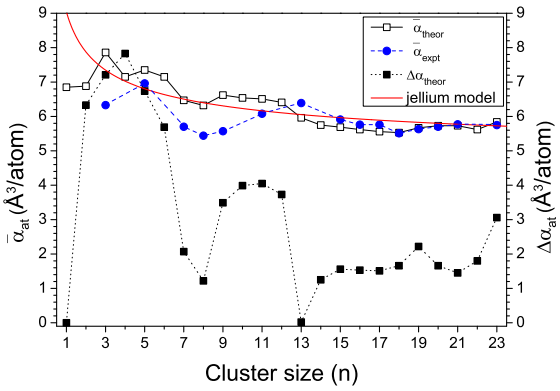

Figure 5.2:
Mean static polarizabilities per atom (open squares) and the polarizability anisotropies per atom (solid squares) of Ag_n clusters calculated with the FF method as a function of the cluster size. The solid circles represent the experimental measurements of the polarizabilities per atom taken from REFERENCE [111]. The solid line represents the prediction from the jellium model. The fitted parameters are given in the text.

experimental measurements which make more valuable the geometries optimized with the DEMON program using as starting point the structures predicted in REFERENCE [101].

5.4 Results and Discussion

The main results of our theoretical calculations concerning the static response properties in conjunction with some selected electronic structure properties of small silver clusters are collected in TABLE 5.2 and FIGURE 5.2. Hereafter, the reported results are only for the ground state structures. We observe that the calculated polarizabilities are in good agreement with the experimental measurements reported in REFERENCE [111]. They approach each other as the cluster size increases because the experimental data are less reliable as the cluster size decreases. The polarizabilities reported by Fedrigo *et al.* [111] were measured at T= 10 K whereas our calculated results are given at T= 0 K. Thus, according to the following relation [112] in the low electric field limit

$$\alpha_{\text{eff}} = \bar{\alpha} + \frac{\mu^2}{3K_{\text{B}}T} \tag{5.3}$$

for clusters having a permanent dipole moment μ, the effective measured polarizability at temperature T is expected to be greater than average polarizability. However we have found that the contribution of the second term in EQUATION (5.3)–calculated at T= 10 K and for the dipole moments collected in TABLE 5.2–is negligible and consequently the influence of the temperature in the confrontation of the calculated polarizabilities and the experimental results can be considered of less importance. It is worth to note that the theoretical polarizabilities oscillate and manifest a decreasing trend such as the experimental values do. It converts the experimental setup designed by Fedrigo *et al.* in a valuable technique to study the electronic properties of small silver clusters. In FIGURE 5.3, we have plotted the

Table 5.1:
Average first-neighbor distance and relative energy of Ag_n cluster isomers with $2 \leq n \leq 23$. The vertical ionization potential (VIP) is compared with the data from REFERENCE [107]. The geometry notation is that of FIGURE 5.1.

$Ag_2 \longmapsto Ag_{10\_4}$						$Ag_{10\_5} \longmapsto Ag_{23\_0}$					
			VIP						VIP		
Cluster	d (Å)	ΔE_{DFT} (eV)	Calc. (eV)	Exp. (eV)	$\lvert\Delta$ IP$\rvert$ (eV)	Cluster	d (Å)	ΔE_{DFT} (eV)	Calc. (eV)	Exp. (eV)	$\lvert\Delta$ IP$\rvert$ (eV)
2_0	2.53	0.000	7.73	7.60	0.13	10_5	2.78	0.397	6.63	6.25	0.38
3_0	2.79	0.000	5.67	6.20	0.53	10_6	2.81	0.495	6.26	6.25	0.01
4_0	2.71	0.000	6.54	6.65	0.11	10_7	2.81	0.506	6.24	6.25	0.01
4_1	2.63	0.242	6.51	6.65	0.14	10_8	2.78	0.553	6.36	6.25	0.11
4_2	2.56	0.563	6.93	6.65	0.28	10_9	2.77	0.617	5.99	6.25	0.26
5_0	2.72	0.000	6.33	6.35	0.02	10_10	2.78	0.626	6.04	6.25	0.21
5_1	2.77	0.430	6.16	6.35	0.19	10_11	2.74	0.703	6.34	6.25	0.09
6_0	2.72	0.000	7.22	7.15	0.07	10_12	2.80	0.720	6.00	6.25	0.25
6_1	2.72	0.079	7.09	7.15	0.06	10_13	2.79	1.151	6.14	6.25	0.11
6_2	2.80	0.534	6.67	7.15	0.48	10_14	2.75	1.133	5.90	6.25	0.35
7_0	2.79	0.000	6.36	6.40	0.04	11_0	2.81	0.000	6.66	6.30	0.36
7_1	2.76	0.170	6.44	6.40	0.04	11_1	2.81	0.268	6.32	6.30	0.02
8_0	2.80	0.000	6.44	7.10	0.66	12_0	2.82	0.000	7.01	6.50	0.51
8_1	2.76	0.006	7.33	7.10	0.23	12_1	2.79	0.117	6.91	6.50	0.41
8_2	2.78	0.181	6.66	7.10	0.44	12_2	2.80	0.161	6.72	6.50	0.22
9_0	2.80	0.000	6.53	6.00	0.53	12_3	2.81	0.411	6.65	6.50	0.15
9_1	2.81	0.039	5.83	6.00	0.17	12_4	2.81	0.417	6.50	6.50	0.00
9_2	2.81	0.039	5.97	6.00	0.03	12_5	2.81	0.422	6.49	6.50	0.01
9_3	2.78	0.052	5.72	6.00	0.28	12_6	2.81	0.652	6.42	6.50	0.08
9_4	2.78	0.056	5.83	6.00	0.17	12_7	2.80	0.802	6.36	6.50	0.14
9_5	2.78	0.070	5.91	6.00	0.09	12_8	2.80	1.039	6.58	6.50	0.08
9_6	2.77	0.089	5.99	6.00	0.01	12_9	2.71	1.039	6.53	6.50	0.03
9_7	2.78	0.145	5.77	6.00	0.23	13_0	2.87	0.000	5.75	6.34	0.59
9_8	2.79	0.154	5.70	6.00	0.30	13_1	2.72	0.305	6.23	6.34	0.11
9_9	2.75	0.182	6.45	6.00	0.45	13_2	2.62	3.568	5.88	6.34	0.46
9_10	2.77	0.204	6.31	6.00	0.31	14_0	2.83	0.000	5.87	6.73	0.86
9_11	2.79	0.211	5.86	6.00	0.14	15_0	2.83	0.000	5.82	6.40	0.58
9_12	2.78	0.214	6.55	6.00	0.55	16_0	2.82	0.000	5.79	6.57	0.78
9_13	2.77	0.218	6.11	6.00	0.11	17_0	2.82	0.000	5.84	6.45	0.61
9_14	2.77	0.221	5.91	6.00	0.09	18_0	2.82	0.000	5.95	6.53	0.58
10_0	2.82	0.000	6.58	6.25	0.33	19_0	2.85	0.000	5.35	6.20	0.85
10_1	2.77	0.080	7.27	6.25	1.02	20_0	2.85	0.000	5.39	6.45	1.06
10_2	2.78	0.158	6.68	6.25	0.43	21_0	2.84	0.000	5.36	5.90	0.54
10_3	2.79	0.205	6.51	6.25	0.26	22_0	2.82	0.000	5.56	6.04	0.48
10_4	2.78	0.221	6.77	6.25	0.52	23_0	2.84	0.000	5.42	6.03	0.61

Table 5.2:
Calculated static response and electronic structure properties of the lowest-energy DFT-optimized Ag_n clusters. The disproportionation energy is denoted by $\Delta_2 E_n$ and $\Delta\xi$ stands for the HOMO-LUMO gap. The mean static polarizability per atom $\bar{\alpha}_{at}$ and the polarizability anisotropy per atom $\Delta\alpha_{at}$ were calculated under the influence of an external electric field of strength 0.0005 a.u.. The absolute value of the dipole moment is denoted by μ.

Cluster	Symmetry	$\Delta_2 E_n$ (eV)	$\Delta\xi$ (eV)	$\bar{\alpha}_{at}$ (Å^3/atom)	$\Delta\alpha_{at}$ (Å^3/atom)	μ (D)
1_0			1.24	6.85	0	0.06
2_0	$D_{\infty h}$	0.74	2.08	6.88	6.33	0.18
3_0	C_{2v}	-0.97	0.70	7.86	7.21	0.58
4_0	D_{2h}	0.28	0.89	7.15	7.83	0.13
5_0	C_{2v}	-0.56	0.55	7.35	6.74	0.17
6_0	D_{3h}	0.43	2.19	7.15	5.69	0.17
7_0	D_{5h}	-0.42	0.43	6.47	2.07	0.30
8_0	D_{2d}	0.79	1.72	6.32	1.22	0.46
9_0	C_s	-0.73	0.37	6.62	3.49	0.54
10_0	D_{2d}	0.43	0.97	6.54	3.99	0.77
11_0	C_1	-0.47	0.28	6.51	4.05	0.41
12_0	C_s	1.21	0.83	6.41	3.73	0.60
13_0	I_h	-0.73	0.62	5.96	0.02	0.66
14_0	C_{3v}	-0.16	0.43	5.75	1.25	0.76
15_0	C_{2v}	-0.02	0.26	5.69	1.56	1.20
16_0	C_s	-0.05	0.21	5.62	1.53	1.18
17_0	C_2	0.17	0.20	5.56	1.51	1.32
18_0	C_s	1.11	0.65	5.53	1.66	0.94
19_0	D_{5h}	-1.10	0.12	5.67	2.22	1.15
20_0	C_{2v}	0.33	0.09	5.73	1.66	1.16
21_0	C_1	0.21	0.15	5.73	1.45	0.94
22_0	C_s	0.12	0.14	5.62	1.80	1.93
23_0	D_{3h}		0.19	5.84	3.06	1.52

average bond length of the lowest-energy structures collected in TABLE 5.1 versus the cluster size. We have observed an abrupt change of the first-neighbor distance from Ag_2 to Ag_3 and from Ag_6 to Ag_7, which is in our opinion a consequence of the structural transition from one dimension 1D to 2D and from (2D) to (3D), respectively. The structural transition clearly affects the static polarizabilities, as we will see below. Moreover, we can see that in general the average bond length approaches to the experimental value of equilibrium interatomic distance of fcc silver solid (2.89 Å) as the cluster size gets bigger [113]. It is a consequence of the very important role of the surface effects in small clusters where most of the atoms belong to the surface.

As far as the static polarizabilities displayed in FIGURE 5.2 is concerned, we observe an odd-even oscillation of the calculated polarizability per atom in function

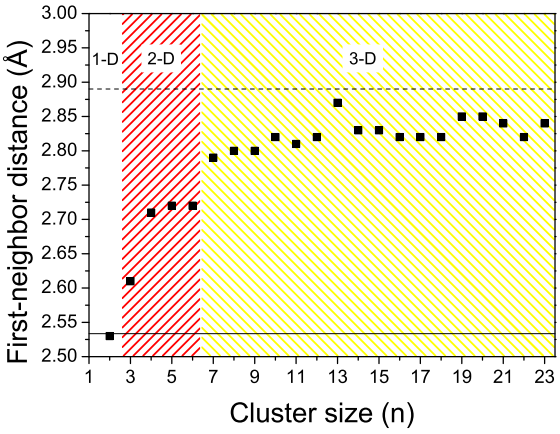

Figure 5.3:
First-neighbor distance plotted against the cluster size. The solid line represents the experimental silver dimer bond length and the dashed line symbolizes the experimental value of the equilibrium interatomic distance of fcc silver bulk. The three different areas stand for the one-dimensional (1D), bidimensional (2D), and three-dimensional (3D) lowest-energy structures of the small silver cluster, respectively.

of the cluster size ranging from the dimer up to the hexamer. This fact is characteristic of clusters of atoms with an odd number of electrons and specially for atoms with a closed d shell and a single valence electron like in the case of noble-metals (Cu, Ag, and Au), or the closely related alkali metals (Li, Na) [114]. The even-odd oscillation of the polarizability up to the hexamer is due to the even-odd oscillation of the HOMO-LUMO gap (see TABLE 5.2 in conjunction with the symmetry of the ground state geometries). Roughly speaking, an increase of the HOMO-LUMO gap is on the side of a chemical stabilization of the cluster but the chemical stability is favored by three-dimensional spherical structures or highly symmetric two-dimensional geometries which lead to a lost of the static polarizability. It is clearly reflected in FIGURE 5.4(a), where clusters with small HOMO-LUMO gaps have larger polarizability than those with large gaps. Thus, the static polarizability oscillates inversely as HOMO-LUMO gap does. The odd-even oscillating trend is broken at $n = 7$ because of the shape transition from the planar to the compact three-dimensional structures and is reflected by a significant decrease in the polarization of Ag_7 despite the fact that the HOMO-LUMO gap decrease in relation to Ag_6 and Ag_8. In this case, the symmetry of the structure dominates over the HOMO-LUMO gap.

From $n = 7$ up to $n = 18$, the static polarizability decreases smoothly in accordance with the expectation that the polarizability per atom of a cluster is a quantity that decreases as the cluster becomes more compact and symmetric. It is borne out by the results displayed in FIGURE 5.4(b) and the inset of FIGURE 5.4(a). With this purpose, we have defined the parameter γ that characterizes the geometry as

$$\gamma = \frac{5\mathrm{tr}\mathbf{I}}{6na^2}, \tag{5.4}$$

where tr$\mathbf{I}$ is the trace of the moment of inertia tensor of the clusters relative to the principal axis frame, n is the number of atoms of the cluster and a stands for the radius of the silver atom ($a \approx 1.45$ Å). In FIGURE 5.4(b) is shown that the

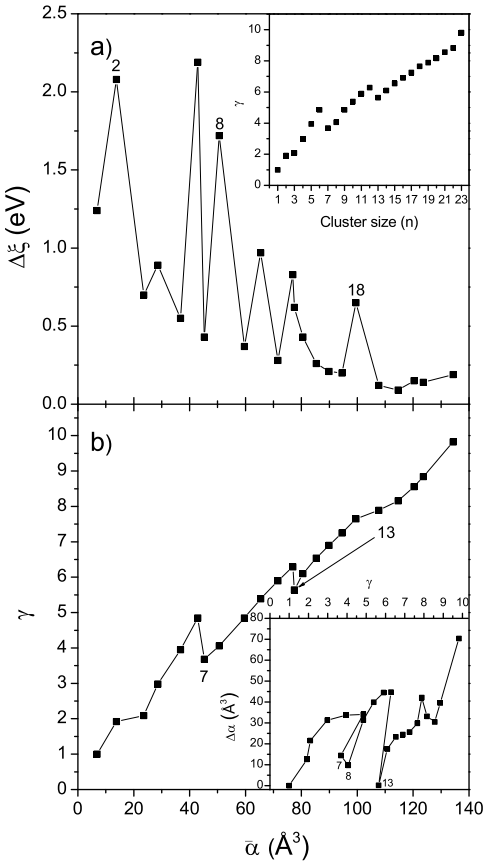

Figure 5.4:
(a) The calculated HOMO-LUMO gap $\Delta\xi$ and (b) the normalized moment of inertia γ plotted against the mean static polarizability. The inset in the upper panel shows the evolution of the normalized moment of inertia versus the cluster size. In the bottom panel, the inset compares the polarizability anisotropy with γ.

larger clusters tend to have higher γ because they are structurally more elongated and consequently it is consistent with the classical picture that the more spherically symmetric the cluster is, the less polarizable it is. An exception is found for Ag_7 and Ag_{13} but the reason will be commented on below in the case of Ag_{13} because for Ag_7 the structure determines the reduction of the polarizability as stated above. Despite the fact that the geometry is a fundamental parameter to describe the polarizability, it is, however, not the only one. It is necessary to take into account the influence of the HOMO-LUMO gap. Generally, the polarizability is a result of the competition between the former and the latter contributions, as is shown in FIGURE 5.4. Two structures (Ag_8 and Ag_{13}) manifest a significant reduction of the polarizability that is clearly reflected in the polarizability anisotropy which measures the symmetry or more specifically the deformation of the charge distribution under the influence of an external electric field in such a way that the less the polarizability anisotropy is, the more spherically symmetric the charge distribution is [see the inset of FIGURE 5.4(b)]. Thus the polarizability anisotropy for Ag_8 and Ag_{13} is clearly reduced since that Ag_8 is a closed-shell cluster with a large HOMO-LUMO gap and Ag_{13} condensates in a highly symmetric structure, i.e., the icosahedral structure

(I_h). The transition from Ag_8 to Ag_9 is accompanied by an enhancement of the polarizability. It is caused by the level structure since that whenever a new level starts to fill, the large spatial extent of the new wave function contributes to the enhancement of the polarizability [115]. That is the reason for the reduced value of the polarizability in the case of the closed-shell structures with n=2, 8, and 18.

From n=19 up to n=23, the mean static polarizability exhibits a trend with a small positive slope. It has been already found in REFERENCE [111]. Fedrigo *et al.* speculates that this tendency is due to the ever increasing role of the *d* electrons as the cluster size grows. They state that a shift to red of the plasmon resonance due to *d* interband transitions corresponds to an enhancement of the polarizability. Our DFT calculations confirm this argument and the very important role of the *d* electrons as the cluster increases in size. In FIGURE 5.5, we show the evolution of the partial density of states with the cluster size. Both *d* and *sp* levels gradually broaden and overlap with each other approximating to an electronic band in the bulk limit. With the aim to clarify the important role of *d* electrons with the size evolution, we have defined the energy separation Δ_{sd} as the difference between highest occupied molecular orbitals belonging to 4*d* states and the lowest occupied molecular orbitals from 5*s* states. The energy separation decreases rapidly from 1.94 eV for Ag_2 to 0.31 eV for Ag_6. The structural transition from planar geometry to a three-dimensional structure gives rise to an increase of the value of Δ_{sd} up to 2.15 eV for Ag_7. After that, it decreases very rapidly up to 0.07 eV for Ag_{14}. For clusters ranging in size from n=15 up to n=23, the influence of 4*d* level is so important that it merges into the 5*s* state. Moreover, the small HOMO-LUMO gap collected in TABLE 5.2 for n=19-23 compared to smaller clusters favors the slightly increase of the mean static polarizability per atom as was commented above.

It is expected that the jellium model can be applied to silver clusters because the electronic configuration of silver is similar to the alkali clusters, where the jellium model has been successfully applied. The solid line in FIGURE 5.2 symbolizes the polarizability predicted by the jellium model. We have fitted our calculated mean static polarizabilities per atom $\bar{\alpha}_{at}$ to an expression given by [116]

$$\bar{\alpha}_{at} = \frac{(n^{1/3} r_{\mathrm{ws}} + \delta)^3}{n}, \tag{5.5}$$

where r_{ws} is the Wigner-Seitz radius and δ represents the spillout of the electrons from the surface of a metallic sphere. The values of the parameters resulting from the fitting to EQUATION (5.5) are $r_{\mathrm{ws}} \approx 1.63$ Å and $\delta \approx 0.45$ Å which are close to the values $r_{\mathrm{ws}} \approx 1.58$ Å and $\delta \approx 0.79$ Å reported in REFERENCE [117] and REFERENCE [89], respectively. The bulk limit of EQUATION (5.5) predicts a value for the bulk atomic polarizability of 4.33 $Å^3$/atom that is lesser than those of the alkali metals like for example Na which is around 9 $Å^3$/atom [118]. As commented above, it is due to the ever increasing role of the *d* electrons since that the screening of *d* electrons (core polarization) tends to reduce the polarizability. Despite the fact

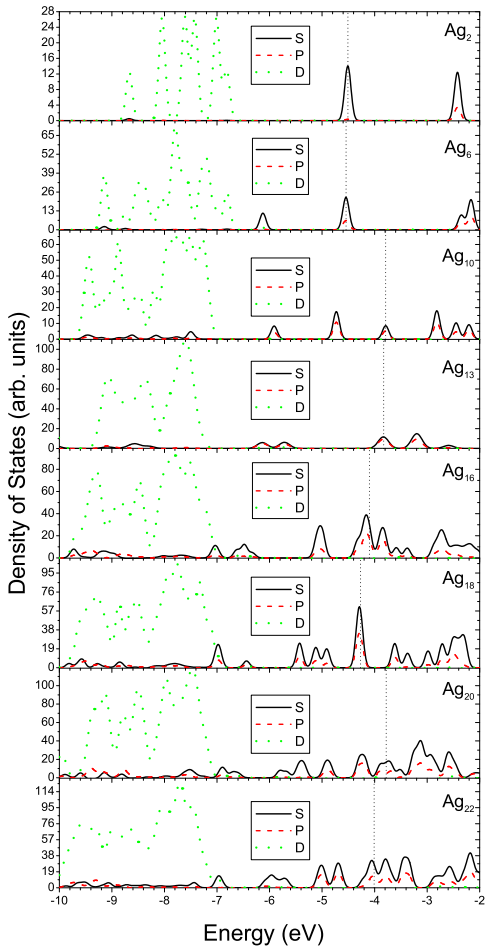

Figure 5.5:
Evolution of the partial density of states of the higher-lying occupied and lower-lying unoccupied levels with the cluster size. The solid, dashed, and dotted lines represent the contribution of the $5s$, $5p$, and $4d$ orbitals to the total density of states, respectively. The dotted vertical line represents the Fermi level.

that the jellium model in the spillout approximation predicts on average the trend of the polarizability per atom in function of the cluster size, it cannot account for the more interesting quantum mechanical effects. Thus deviations of the calculated polarizabilities from the predictions of Equation (5.5) are "true" quantum effects. As commented above, it is in part due to the shell effects.

In Table 5.2, we have collected the numerical values of the disproportionation energy, that is defined as

$$\Delta_2 E_n = E_{n+1} + E_{n-1} - 2E_n, \tag{5.6}$$

where E_n is the total energy provided by our DFT calculations of the cluster with n atoms. It represents the relative stability of a cluster with n atoms in comparison to clusters with $n+1$ and $n-1$ atoms and consequently a peak in $\Delta_2 E_n$ indicates that the cluster with size n is very stable because a shell has been filled. The disproportionation energy shows that clusters with n=2, 8, and 18 have particularly

stable configurations and consequently the polarizability is considerably reduced, as is shown in FIGURE 5.2. Whenever a shell starts to fill, the polarizability increases and deviates from the jellium model. As the size of the silver clusters increases, the HOMO-LUMO gap becomes smaller (see TABLE 5.2) so that the shell effects are less important and the deviation of the jellium model is negligible.

5.5 Conclusions

In this CHAPTER, the structural stability along with the static response properties of silver clusters in the size range $1 \leq n \leq 23$ have been studied by means of the finite field method implemented in the Kohn-Sham density-functional methodology [79]. The IPs reported in this CHAPTER for the lowest-energy structures are in general in a relatively good agreement with the experimental measurements and most of the structures predicted in this CHAPTER as the fundamental ones were already reported in former publications. Likewise, the calculated polarizabilities are in good agreement with the experimental measurements reported in REFERENCE [111]. The competition between the HOMO-LUMO gap and the structural symmetry on one side or the shell structure and the disproportionation energy on the other side are the quantum-mechanical effects that deviates the calculated polarizabilities from the jellium model. For bigger cluster sizes the quantum-mechanical effects can be considered of less importance, and therefore both theoretical approaches, i.e., the *ab initio* DFT calculations and the jellium model, approach each other.

6

Unexpected Magnetism of Small Silver Clusters

> *It seems that if one is working from the point of view of getting beauty in one's equations, and if one has really a sound insight, one is on a sure line of progress.*
>
> — Paul Adrien Maurice Dirac

Synopsis

The ground-state electronic and magnetic properties of small silver clusters Ag_n ($2 \leq n \leq 22$) have been studied using a linear combination of atomic Gaussian-type orbitals within the density functional theory. The results show that the silver atoms, which are diamagnetic in a bulk environment, can be magnetic when they are grouped together in clusters. The Ag_{13} cluster with icosahedral symmetry has the highest magnetic moment per atom among the silver clusters studied. The cluster symmetry and the reduced coordination number specific to small clusters are revealed as a fundamental factor for the onset of magnetism.

6.1 Introduction

In the last two decades, the research field of clusters has shown rapid development in both experimental and theoretical investigations [119], since the clusters are well suited for several applications. For example, there has been a traditional interest in applications to catalysis [120], due to the considerable surface to volume ratio of clusters. More recently, clusters or nanoparticles that possess magnetic properties have offered exciting new opportunities for biomedical applications including (i)

magnetic separation of labeled cells; (ii) therapeutic drug delivery; (iii) hyperthermic treatment for malignant cells; (iv) contrast enhancement agents for magnetic resonance imaging applications; and (v) also very recently for manipulating cell membranes [91, 121, 122].

Clusters are on the borderline between atoms and bulk, and thereby they play an important role in understanding the transition from the microscopic structure to the macroscopic structure of matter. Although $4d$ and $5d$ transition metal atoms have unfilled localized d states, none of them are magnetic. Only a few of the $3d$ transition metals form magnetic solids. Thus, from the magnetic point of view, one of the long-standing problems in condensed matter physics is to understand why some nonmagnetic metals become magnetic when they condense into clusters. There are two factors characteristic of clusters that mainly contribute to the onset and enhancement of the magnetism, namely, the reduced coordination number and the high symmetry, since symmetry enables degeneracy and degeneracy spawns magnetism [123–125]. According to this, an icosahedral structure is a good candidate for the appearance of the magnetism because the maximal degeneracy of an irreducible representation of the icosahedra (I_h) group is 5 whereas all other cluster symmetries allow at most three fold degeneracy, as was reported by Reddy *et al.* for Pd, Rh, and Ru [126].

In this Chapter, we present first-principles calculations on small silver clusters exhibiting an important magnetism, which has not been predicted until now. In the present work we study the evolution of the magnetism of silver clusters as a function of the cluster size and special emphasis is placed on the effects of cluster symmetry. We show that some of the studied clusters exhibit magnetic behavior which is not present in bulk silver. To the best of our knowledge, nobody has predicted or even observed magnetism in small bare silver clusters; however, our computational simulations anticipate the onset and enhancement of magnetism for the silver clusters that include special conditions like high symmetry and reduced coordination number. In this respect, the Ag_{13} cluster exhibits the highest magnetic moment among the studied clusters and converges into a stable structure.

6.2 Method

With the aim of studying the magnetic properties of small silver clusters Ag_n ($2 \leq n \leq 22$), we have performed density-functional-theory-based calculations consisting of a linear combination of Gaussian-type-orbitals Kohn-Sham density-functional methodology as implemented in the deMon program package [79]. All-electron spin-unrestricted calculations were carried out at the generalized gradient approximation (GGA) level to take the exchange-correlation (XC) effects into account [81]. Local-density approximation sometimes yields inaccurate bond lengths and total energies due to the insufficiency in describing the strong correlation effect of the localized d electrons and charge density inhomogeneities. In these regards, the GGA

should be a better choice [98]. For this reason, at the beginning of this work and to satisfy ourselves that the numerical procedure is reliable, we initiate a search for a functional that better fitted the calculated bond length of the silver dimer to the experimental one. We found that the functional that better fitted the bond length was the one developed by Perdew and Wang [81], given a bond length of 2.535 Å, which is in excellent agreement with the experimental measure (2.53350 Å) reported in Reference [99]. An orbital basis set of contraction pattern (633321/53211*/531+) was used in conjunction with the corresponding (5,5;5,5) auxiliary basis set for describing the s, p, and d orbitals [82]. The grid for numerical evaluation of the XC terms had 128 radial shells of points and each shell had 26 angular points. Spurious one-center contributions to the XC forces, typically found in systems with metal-metal bonds when using a nonlocal functional, are eliminated in a similar way as has been done in Reference [83]. The geometries were fully optimized without symmetry and geometry constraints using the Broyden-Fletcher-Goldfarb-Shanno algorithm [37]. During the optimization, the convergence criterion for the norm of the energy gradient was fixed to 10^{-4} a.u., while it was 10^{-7} a.u. for the energy and 10^{-6} a.u. for the charge density. A wide set of spin multiplicities ranging from 1 up to a maximum of 10, depending on the cluster size, was checked to ensure that the lowest-energy electronic and magnetic configuration is reached. In Table 6.1, we collect the energy difference for several spin states. We observe that the majority of the clusters are very stable from the magnetic point of view, since the energy difference of the excited spin states relative to the most stable spin configuration is greater than 24 meV/atom $\approx$ 273 K/atom. The only exception to this behavior occurs for clusters with size varying from n=19 up to n=22 (Ag_{19}-Ag_{22}), which can be better described as "magnetically fluxional".

A huge sampling of trial geometries taken from the literature was evaluated. While for these small clusters it is nearly impossible to search for all possible geometries, the detailed search that we have carried out give us some confidence that the structural minimum has been found. A detailed study about the structural stability and the static response properties of these small silver clusters has been published in Chapter 5 (see also Reference [127]). Consequently, the ground-state structures of Ag_n (n=2-22) employed in this study and plotted in Figure 6.1 are those of the Chapter 5 (Reference [127]). It is worthwhile to mention the fact that other authors did not find the icosahedron as the global minimum of Ag_{13} and, in consequence, the magnetic properties of Ag_{13} and even Ag_{14} predicted by us could differ from those in other work [128].

6.3 Results and Discussion

One of the criteria for a cluster to be used as a potential building block for a nanomaterial is its chemical stability relative to other clusters of the same material. With the aim of studying the stability of Ag_2-Ag_{22} clusters, we have plotted the gaps

Table 6.1:
Energy differences between various spin states relative to the most stable spin configuration. The energy is given in units of eV/atom and M is the spin multiplicity. The parameter n represents the number of atoms forming the silver cluster.

Even-numbered Clusters							Odd-numbered clusters						
		M							M				
n		1	3	5	7	9	n		2	4	6	8	10
2	$D_{\infty h}$	0.000	0.721	4.282			3	C_{2v}	0.000	0.670	2.833		
4	D_{2h}	0.000	0.155	1.190			5	C_{2v}	0.000	0.348	1.274		
6	D_{3h}	0.000	0.367	0.755			7	D_{5h}	0.000	0.304	0.656		
8	D_{2d}	0.000	0.283	0.525			9	C_s	0.000	0.269	0.454		
10	D_{2d}	0.000	0.178	0.398			11	C_1	0.000	0.203	0.337		
12	C_s	0.000	0.159	0.265			13	I_h	0.238	0.228	0.000	0.437	0.803
14	C_{3v}	0.515	0.499	0.000	0.087	0.821	15	C_{2v}	0.494	0.00	0.061		
16	C_s	0.493	0.000	0.039	0.164		17	C_2	0.000	0.032	0.621	0.242	
18	C_s	0.000	0.034	0.079	0.179		19	D_{5h}	0.000	0.023	0.068	0.668	
20	C_{2v}	0.005	0.000	0.048	0.131		21	C_1	0.000	0.016	0.075	0.155	
22	C_s	0.495	0.000	0.016	0.067								

between the highest occupied (HOMO) and lowest unoccupied (LUMO) molecular orbitals and the cohesive energies in FIGURE 6.2(a),(b). The cohesive energies for Ag clusters are fitted to a linear regression and compared in FIGURE 6.2(b) with the spherical droplet model of Miedema [129],

$$E_c(n) = E_{bc} - \left(\frac{36\pi}{n}\right)^{1/3} {\gamma^0}{V_a}^{2/3}, \tag{6.1}$$

where E_{bc} is the bulk cohesive energy, $\gamma^0 = 7.8\times10^{18}$ eV/m^2 is the surface energy of the bulk silver, V_a is the atomic volume, and n is the number of atoms in the cluster. Despite the fact that some clusters ($2\leq n \leq 6$) are far from spherical, our calculated cohesive energies are in good agreement with the Miedema's model. Indeed, the bulk cohesive energy predicted by our calculations (2.63 eV/atom) differs by only 10% from the experimental findings (2.95 eV/atom) [130], giving us confidence that the lowest-energy structures plotted in FIGURE 6.1 are reliable. In FIGURE 6.2(a) we can see that the most stable even-numbered clusters are Ag_2, Ag_6, Ag_8, and Ag_{18}. Except for Ag_6, this is a consequence of the closure of the electronic shell [131]. For the odd-numbered clusters, the HOMO-LUMO gaps decrease monotonically as the cluster size increase, except for the Ag_{13} cluster. The large HOMO-LUMO gap of Ag_{13} relative to the odd-numbered clusters enhances its chemical stability and inertness, as well as its ability to assemble into magnetic nanoparticles, because it is a magnetic cluster with a considerable magnetic moment per atom, as is discussed below.

Our results on the magnetic properties of the Ag_n ($2\leq n \leq 22$) clusters are most

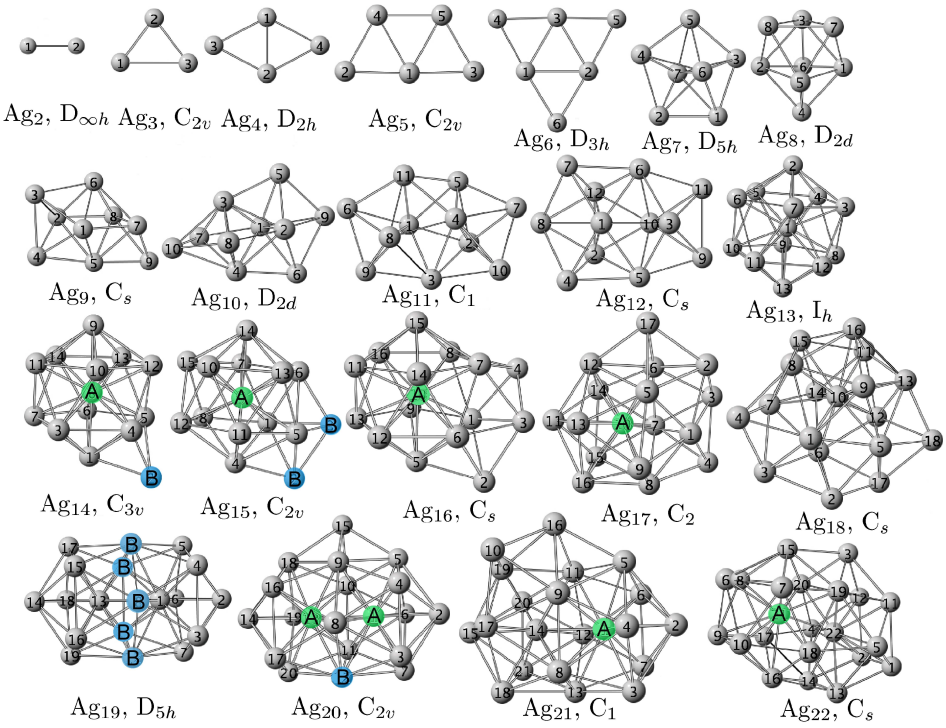

Figure 6.1:
Lowest-energy structures and symmetry point groups assigned to the Ag_n ($2 \leq n \leq 22$) clusters. The magnetic moments, namely, m, of the atoms labeled with the capital letters A (-1.5 $\mu_B \leq m \leq$-0.4 μ_B) and B (-0.1 $\mu_B \leq m \leq 0$ μ_B) are aligned antiferromagnetically to the other ones.

fascinating, if not unexpected, compared with the silver bulk magnetic properties. Indeed, the silver bulk magnetic ordering is well known to be diamagnetic, as can be inferred from its negative magnetic susceptibility (χ_m=-19.5×10^{-6} cm^3/mol), whereas silver atoms when they coagulate to a cluster become either magnetic or non magnetic depending on the cluster size, as is shown in TABLE 6.1 and FIGURE 6.3 .

For Ag_2, Ag_8, and Ag_{18} clusters, our calculations clearly show that they are highly stable with large HOMO-LUMO gaps [see FIGURE 6.2(a)] and diamagnetic [see FIGURE 6.3]. The phenomenon can be understood simple from the two-, eight-, and 18-electron rule, as described by the cluster shell models [132]. This rule predicts transition metal clusters to be stable and diamagnetic when the valence shell of the metal atom contains two, eight, or 18 electrons that completely fill electron shells, forming closed electronic structures with paired spins.

From Ag_3 up to Ag_{12} excluding Ag_2 and Ag_8, the cluster topologies converge into a geometry where all atoms belong to the surface [FIGURE 6.1], and consequently have a reduced coordination number [FIGURE 6.3(b)]. This condition favors

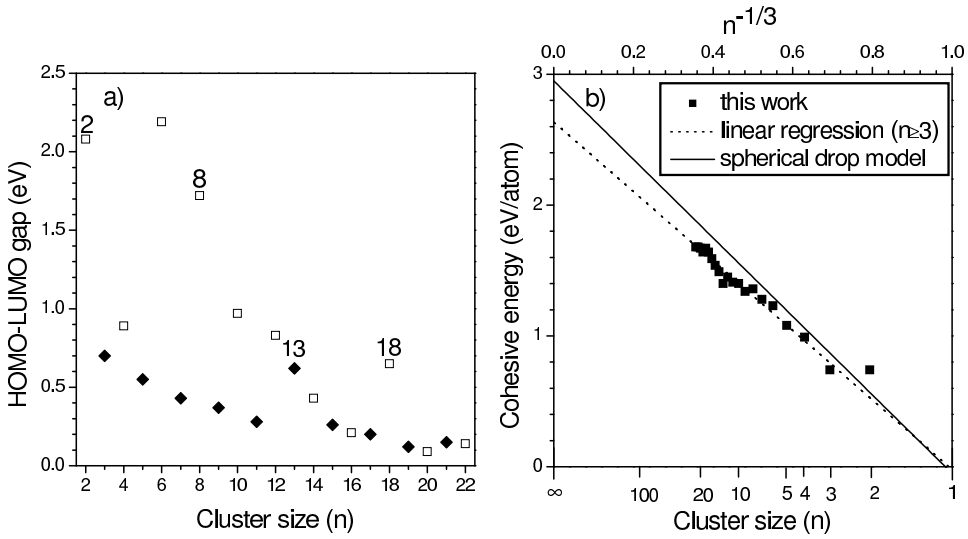

Figure 6.2:
(a) The HOMO-LUMO gap and (b) cohesive energy per atom of small silver clusters as a function of the cluster size n ($2 \leq n \leq 22$). The empty and filled points represent the even- and odd-numbered clusters, respectively.

a reduced charge accumulation in nearest neighbor atoms which according to the calculated Mulliken population analysis (MPA) is less than 0.1 electron per atom in average. Likewise, a Mayer bond order analysis reveals that silver atoms are sharing the unpaired $5s$ electrons, forming a covalent bond, and thereby low-spin configurations are expected. For example, the even-numbered clusters become diamagnetic because they have an even number of $5s$ electrons that create a cloud of paired $5s$ electrons [FIGURE 6.3(a)], whereas for the odd-numbered clusters the electronic configuration with one unpaired spin electron is favored energetically over all the feasible spin configurations studied in this work. The resulting odd-numbered clusters retain an average magnetic moment per atom that decreases monotonically with the increase of the coordination number [FIGURE 6.3(a),(b)] since the orbital overlap expands as the coordination number does, as was reported for Fe, Co, and Ni in REFERENCE [133] and for 13-atom clusters of Pd, Rh, and Ru in REFERENCE [126].

In FIGURE 6.3(a), we can see that Ag_{13} exhibits the highest average magnetic moment per atom among the studied clusters. To understand the origin of this considerable magnetic moment (0.39 μ_B/atom), we show in FIGURE 6.4(a)-(d3) the electron localization function (ELF) [35] and the densities of states (DOSs) for the inner- and the outer-shell atoms. The MPA reveals that the electron charge transfers from the outer-shell Ag atoms to the central Ag atom, which gains an excess of charge of about 0.8 electrons. The charge transfer, which is favored by the icosahedral symmetry, can be described graphically from our corresponding

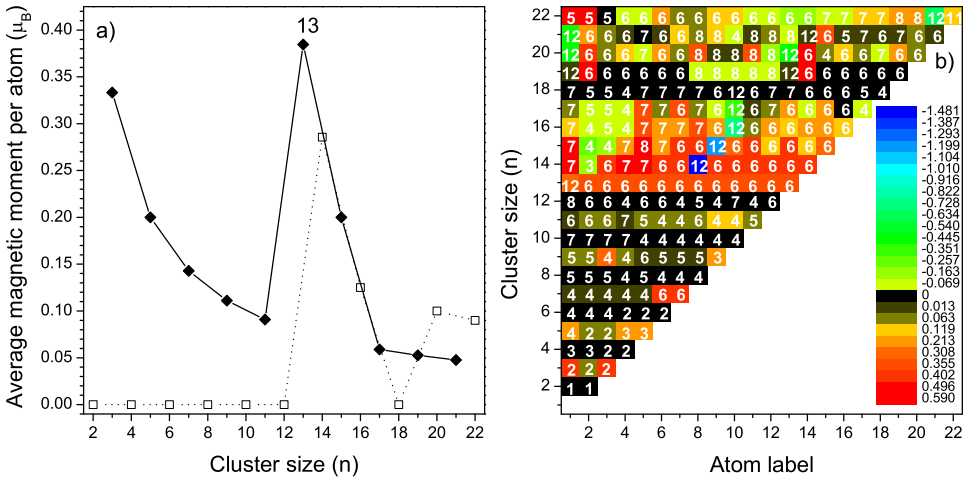

Figure 6.3:
Evolution of magnetic moment per atom of the most stable cluster isomers of each size. (a) Average magnetic moment per atom versus cluster size. The empty and filled points denote the same as in FIGURE 6.2. (b) Color representation of the magnetic moment per atom of each silver cluster. The numbers inside the small charts denote the coordination number. On the right side, the color palette gives information about the numerical values of the atomic magnetic moments. The numbers labeling every atom of each cluster in FIGURE 6.1 are closely related to the ones displayed on the x-axis.

ELF plot. In FIGURE 6.4(a)-(c), the contour plot of the ELF indicates a slight concentration of the light blue color (0.15-0.30 in bar color) surrounding the central atom, and gives rise to an enhancement of the electron localization around the inner atom. The large coordination number of the central Ag atom results in an enhancement of the overlap of its 4*d* orbitals with those of other outer-shell Ag atoms. Therefore, for the inner atom the charge transfer populates mainly the lower-energy 4*d* states ($\sim$ -10.2 eV) with reduced exchange splitting, whereas for the outer-shell atoms these states become less occupied, as is shown in FIGURE 6.4(d1)[1], (d2), and FIGURE 6.4(d3), respectively. Thereby, the charge transfer lead to a small loss of the spin-up DOS at the Fermi level for the inner atom compared with the outer-shell atoms and, consequently, the inner atom has weaker magnetism (0.35 μ_B/atom) and the outer-shell atoms enhance their magnetic moments (0.39 μ_B/atom) giving rise to an increase of the average magnetic moment of the Ag_{13} cluster.

From Ag_{14} to Ag_{22}, except for Ag_{18} which has already been studied above, the clusters converge into a distorted icosahedral symmetry in which, depending on the cluster size, the number of inner atoms is either one or two (see FIGURE 6.1). In this case, the MPA confirms a charge transfer mainly from the peripheral atoms to the

[1]In FIGURE 6.4(d1), we show the DOS for the atom labeled with the number 2 in FIGURE 6.1 as a representative example of the DOS for the outer-shell atoms, since from symmetry considerations the external atoms have all similar DOS plot.

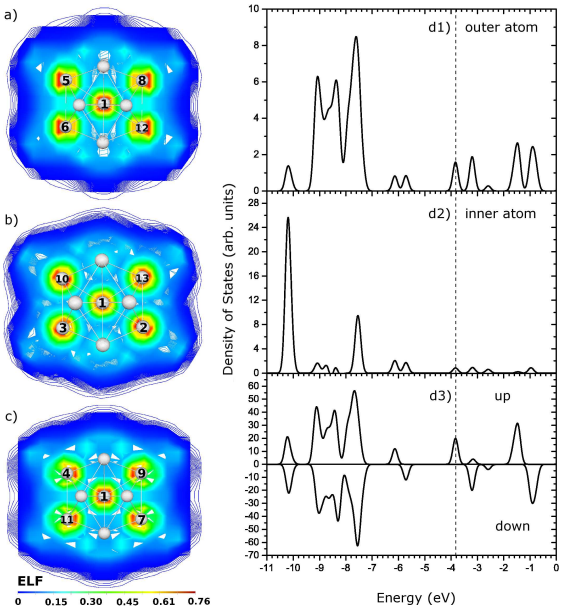

Figure 6.4:
Contour plot of the electron localization function for the three mutually orthogonal golden planes [(a), (b), (c)] of the icosahedral symmetry and densities of states for the outer-shell atoms (d1) and inner atom (d2) in an Ag_{13} cluster. The spin-polarized DOS is shown in (d3). The dashed vertical line represents the Fermi level.

inner ones even greater than in the Ag_{13} case. This effect decompensates the spin pairing state and gives rise to an antiferromagnetic alignment of the inner atoms to the outer ones, and thus the clusters decrease the total magnetic moment compared with the Ag_{13} cluster, as is shown in FIGURE 6.1 and FIGURE 6.3(b). It is also observed in FIGURE 6.3(a) that the average magnetic moment per atom decreases as the cluster size gets bigger up to $n = 19$, and then oscillates, tending to decrease. The phenomenon can be understood simply from the loss of symmetry that reduces orbital degeneracy and weakens magnetism [134]. According to this tendency, we expect for clusters greater in size an enhancement of the magnetic moment, as long as the cluster stabilizes in a geometry of high symmetry (e.g., Ag_{55} and Ag_{75}).

6.4 Conclusions

In conclusion, we have shown that the silver atoms can be magnetic when they are grouped together in small clusters. In particular, the Ag_{13} cluster exhibits the highest magnetic moment per atom among the studied silver clusters, due to its high symmetry and degeneracy.

7

Biomedical Applications of Small Silver Clusters

> *No lower can a man descend than to interpret his dreams into gold and silver.*
>
> — Kahlil Gibran

Synopsis

The ground-state properties of small silver clusters Ag_n $(2 \leq n \leq 24)$ have been studied using a linear combination of atomic Gaussian-type orbitals within the density functional theory. The results show that the Ag_{13} clusters, due to their noticeable magnetic moment and their considerable highest occupied-lowest unoccupied molecular orbital gap, are a promising candidate for the magnetic applications of nanoparticles. In particular, our study suggests that the silver nanoclusters made out of Ag_{13} clusters, as building blocks, are suitable for possible future applications in biomedicine, since they could improve some present-day difficulties of magnetic nanoparticles such as toxicity and opsonization.

7.1 Introduction

Every year, nearly 1.4 million Americans are diagnosed with the cancer and another 600,000 die from it [135]. Unfortunately, the traditional methods of treating malignant tumors such as radiation, chemotherapy, or surgery are very invasive, and consequently, they have adverse side effects. A desired objective for oncologists for many years has been to destroy the malignant cells maintaining the normal cells unperturbed. In this sense, magnetic nanoparticles have revealed as a promising candidate for pushing the cancer treatment closer than ever before.

Present-day technology allows us to build, control, and manipulate magnetic nanoparticles with high precision and, consequently, the biomedical applications of these particles have been increasing during the last years. For example, they have been used for (i) magnetic separation of labeled cells, (ii) therapeutic drug delivery, (iii) hyperthermic treatment for malignant cells, (iv) contrast enhancement agents for magnetic resonance imaging applications, (v) and also very recently, for manipulating cell membranes [91, 121, 122]. The experience in this field tells us that an ideal nanoparticle for the aforesaid applications should be biocompatible, resistant to corrosion and aggregation, as well as a strong magnet. Unfortunately, most of the conventional magnetic nanoparticles do not fit the conditions to be ideal since, if they are strong magnets, then they can easily be oxidized [136]. Although the oxidation problem can be solved coating the nanoparticles with biocompatible polymers, however, it likely enhances the possibility that the particles after injected into the bloodstream are more coated by the components of blood and thereby, it increases the activity of the undesirable opsonization process.

In this CHAPTER, we start briefly describing the inertness, stability, and magnetic properties of small silver clusters Ag_n ($2 \leq n \leq 24$) that have been previously studied in detail in REFERENCE [137]. Based on these properties, we have found that Ag_{13}, due to the considerable magnetic moment and inertness, is a promising candidate to be an ideal magnetic cluster for biomedical applications. To extend our considerations to a more realistic case, we suggest a method to assemble Ag_{13} clusters into nanoparticles in a similar way as it was done in REFERENCE [138] for silver and gold nanoparticles.

7.2 Computational Details

In order to study the electronic structure of small silver clusters Ag_n ($2 \leq n \leq 24$), we have performed density functional theory-based calculations consisting of a linear combination of Gaussian-type-orbitals Kohn-Sham density-functional methodology as implemented in the DEMON program package [79]. All-electron spin-unrestricted calculations were carried out at the generalized gradient approximation level to take the exchange-correlation (XC) effects into account [81]. An orbital basis set of contraction pattern (633321/53211*/531+) was used in conjunction with the corresponding (5,5;5,5) auxiliary basis set for describing the s, p, and d orbitals. The grid for numerical evaluation of the XC terms had 128 radial shells of points and each shell had 26 angular points. Spurious one-center contributions to the XC forces, typically found in systems with metal-metal bonds when using a nonlocal functional, are eliminated in a similar way as has been done in REFERENCE [83]. A wide set of spin multiplicities ranging from 1 to 11 were checked to ensure that the lowest-energy electronic configuration is reached. During the optimization, the convergence criterion for the norm of the energy gradient was fixed to 10^{-4} a.u. while it was 10^{-7}

a.u. for the energy and 10^{-6} a.u. for the charge density. For clusters with size varying from 2 up to 12, we have taken the initial geometries from the REFERENCE [71] whereas all other cluster structures were taken from REFERENCE [101]. After that, the geometries were fully optimized, without taking explicitly the symmetry and geometry constraints, using the Broyden-Fletcher-Goldfarb-Shanno (BFGS) algorithm [37] to obtain the structural minima.

7.3 Results and Biomedical Applications

One of the criteria for a cluster to be used as a potential building block for a nanomaterial is its chemical stability relative to other clusters of the same material. With this aim, we have collected in TABLE 7.1 the highest occupied-lowest unoccupied molecular orbital (HOMO-LUMO) gaps of the most stable isomers of silver cluster in the size range from $n = 2$ up to $n = 24$. In the case of even-numbered clusters, we can see that the larger HOMO-LUMO gap is for Ag_2, Ag_6, Ag_8, and Ag_{18}, whereas for the odd-numbered clusters the HOMO-LUMO gap decreases monotonically as the cluster size increases, except for Ag_{13}. In the former case, the larger stability of the cited clusters is due to closure of the electronic shell whereas in the latter case, it does not. However, we have found that Ag_{13} cluster does not follow the HOMO-LUMO gap trend of the odd-numbered clusters, so that the large HOMO-LUMO gap of Ag_{13} relative to the odd-numbered clusters enhances its chemical stability and inertness. With the aim of clarifying this point more in detail, we have studied the reactivity of the Ag_{13} cluster with O_2 molecule. The optimized structure is plotted in FIGURE 7.1. The structural properties of the cluster show that the Ag-O average bond length is 2.47 Å. This result is in accordance with tendency of previous reported results on the oxidation of silver clusters ranging in size from 1 up to 7 atoms [139]. In REFERENCE [139], the Ag-O distance increases with the number of silver atoms forming the cluster and it goes from 2.284 Å for the silver atom up to 2.316 Å for the heptamer. Moreover, our results provide for the O-O bonding length a value of 1.31 Å, which is greater than the bond length of the O_2 molecule (1.243 Å) and agrees quite well with the tendency predicted in REFERENCE [139], where the addiction of silver atoms to the cluster results in a increase of the O-O bond length. Indeed, we have also analyzed

Table 7.1:
Calculated HOMO-LUMO gap ($\Delta\varepsilon$) for silver clusters with size ranging from n=2 up to n=24. Among the odd-numbered clusters, the 13-atom cluster shows one of the largest $\Delta\varepsilon$.

n	$\Delta\varepsilon$	n	$\Delta\varepsilon$	n	$\Delta\varepsilon$	n	$\Delta\varepsilon$
2	2.08	8	1.72	14	0.43	20	0.09
3	0.70	9	0.37	15	0.26	21	0.15
4	0.89	10	0.97	16	0.21	22	0.14
5	0.55	11	0.28	17	0.20	23	0.19
6	2.19	12	0.83	18	0.65	24	0.12
7	0.43	13	0.62	19	0.12		

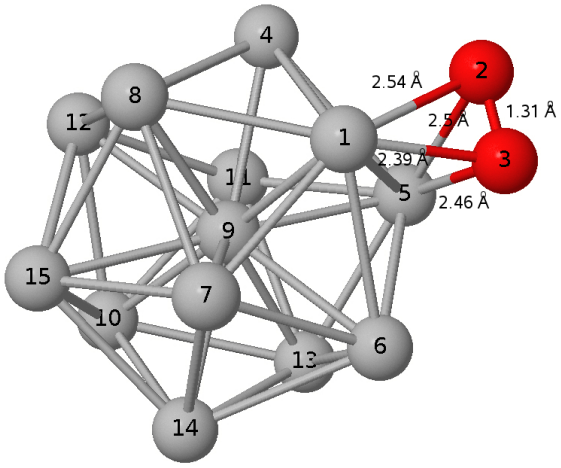

Figure 7.1:
Optimized structure of the ground state $Ag_{13}O_2$ cluster with spin multiplicity equal to 6. The oxygen atoms are labeled with the numbers 2 and 3. The rest of silver atoms form an icosahedron.

the chemical bonding of the $Ag_{13}O_2$ cluster with the Mayer bond order. The results for the silver atoms bounded by the O_2 molecule are collected in TABLE 7.2. The bonding between the oxygen and silver atoms is very weak, however, the bonding between silver atoms (atoms labeled 1 and 5 in FIGURE 7.1) is stronger. Moreover, the Mulliken population analysis reveals that the oxygen atoms (atoms labeled 2 and 3 in FIGURE 7.1) do not transfer charge with the silver atoms and, thus, they tend to avoid bonding with O_2 molecule. Consequently, the Ag_{13} cluster elongates the Ag-O and O-O bond lengths and weakens the bonding with oxygen molecule and in consequence, makes more difficult the reaction with O_2.

Table 7.2:
Mayer bond order for the silver atoms involved in the chemical bonding with the oxygen molecule. The numbers labeling the atoms are closely related with the ones in FIGURE 7.1.

	Ag-1	Ag-5
O-2	0.05974	0.05602
O-3	0.08258	0.06431
Ag-5	1.42027	

Our results on the magnetic properties of the Ag_n ($2 \leq n \leq 24$) clusters are most fascinating, if not astonishing, compared with the silver bulk magnetic properties. The silver bulk magnetic ordering is well-known to be diamagnetic, whereas silver atoms when they coagulate to a cluster become either magnetic or nonmagnetic depending on the cluster size, as is shown in FIGURE 7.2. We can see that the most interesting cluster from the magnetic point of view is Ag_{13} with spin multiplicity (M) equal to 6. In FIGURE 7.3, we have schematically represented the inner- and outer-shell atoms of Ag_{13} when they are grouped forming an icosahedral structure. The large magnetism is a consequence of the high symmetry (icosahedral symmetry) and orbital degeneracy, i. e., the MPA extracted from our calculations reveals that the electron charge transfers from the outer-shell Ag atoms to the inner Ag atom which gains an excess of charge of about 0.8 electrons. Thereby, the charge transfer leads to a small loss of the spin-up density of states at the Fermi level for the inner atom compared with the

outer-shell atoms and, consequently, the inner atom weakens its magnetism (0.35 μ_B) and the outer-shell atoms enhance their magnetic moments (0.39 μ_B) giving rise to an increase of the average magnetic moment of the Ag_{13} cluster. The rest of the studied silver clusters do not appear so interesting magnetic behavior as in the Ag_{13} clusters case. Only the Ag_{14} cluster presents a considerable magnetic moment since its geometric structure is still very close to the icosahedral structure. Although the oxidation of the 13-atom silver cluster is unlikely, however we have also studied the influence of the O_2 molecule in the magnetic properties of the Ag_{13} and the results show that the magnetism could be slightly affected by the presence of the O_2 molecule, tending to decrease the multiplicity to 4. The values of the total energy relative to the energy of the ground state cluster (M=4) are $\Delta E \approx 0.12$ eV for M=6 and $\Delta E \approx 1.49$ eV for M=8. From Ag_2 up to Ag_{12}, the even clusters are nonmagnetic while the odd clusters are doublet states. It is a consequence of the electronic configuration, i. e., the even-numbered clusters have an even number of $5s$ electrons that create a cloud of paired $5s$ electrons, whereas for the odd-numbered clusters, the electronic configuration with one unpaired spin electron is favored energetically over the whole feasible spin configurations studied in this work. From the Ag_{14} to the Ag_{18} cluster, the magnetic moment monotonically decreases as the cluster gets bigger, whereas from Ag_{19} to Ag_{24}, it oscillates tending to increase slightly. In this size range (Ag_{14}-Ag_{24}), the clusters coagulate into distorted icosahedral structures, which are more distorted as the cluster size increase. The phenomenon can be understood simply from the loss of symmetry that reduces orbital degeneracy and weakens magnetism.

A novel point to note for possible future applications of magnetic silver clusters is in biomedicine. Although the biomedical applications of the magnetic nanoparticles have been successfully applied to many aspects of biomedical and biological investigations, however, some problems arise when the nanoparticles are injected inside the body since magnetic nanoparticles are less easily destroyed or inactivated by cells than many nonmagnetic ones. Amongst these problems, we underline the toxicity and the opsonization of the injected magnetic nanoparticles [91, 121, 122]. Nanofabricated magnetic nanoparticles of small silver clusters could shed some light on these problems, that is, the 13-atom cluster could be a good candidate for overcoming the aforementioned difficulties. Besides its high symmetry, the large HOMO-LUMO gap of Ag_{13} (see Table 7.1) contributes to be inert and enhance its ability to assemble into magnetic nanoparticles since it retains a considerable magnetism, as is shown in Figure 7.2. Thus, the advantage of nanofabricated silver clusters using Ag_{13} as a building block is two fold. Firstly, the toxicity is avoided and, consequently, the biocompatible polymers used to shield the magnetic particles from the surrounding environment can be suppressed, such as was proposed for iron nanoparticles coated by a thin layer of gold in Reference [140]. Secondly, the suppression of the polymers coating the magnetic nanoparticles likely enhances the possibility that the silver particles, after injected into the bloodstream are less coated by components

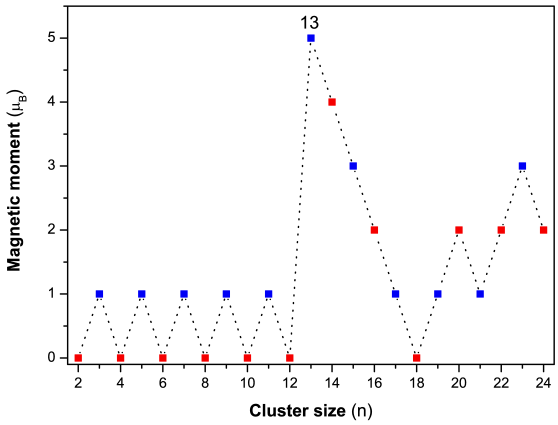

Figure 7.2:
Evolution of the magnetic moments vs cluster size. The highest magnetic moment occurs for Ag_{13} cluster. Except for the Ag_{14}, the rest of the studied clusters do not manifest so interesting magnetic behavior.

of the circulation and, thereby, it decreases the activity of the opsonization process, since the silver particles are smaller in size and inertness.

Finally, we propose a mechanism to assemble the 13-atom clusters into nanoparticles that is very similar to the diamondlike structure synthesized in Reference [138] for a binary nanoparticle crystal composed by silver and gold clusters. A schematic representation of the mechanism is plotted in Figure 7.3. To study the stability of this envisioned nanoparticle, we made use of the "basin-hopping" algorithm as it is implemented in the GMIN code [141]. In this code, the basin-hopping algorithm combined with a Monte Carlo method which decides the search strategy of the minimum, attempts to find out the global potential energy minimum for a collection of atoms provided as input. We performed a simulation with 100 steps in the basin-hopping run at a temperature of T= 0 K. The silver atoms were described by a Gupta potential [142] and the geometry was optimized with the BFGS algorithm. The simulation found 28 structures as possible candidates to the lowest energy geometry. The energetic results show that the lowest energy structure is the diamondlike structure. The other obtained structures are distortions of the diamondlike structure with energies ranging from 0.32 up to 4.70 eV relative to the ground state structure.

As it has been shown above, when the silver clusters coagulate in structures of high symmetry (for example, as in the Ag_{13} case), the orbital overlapping and degeneracy are favored resulting in a transfer charge which gives rise to an ionic bonding mediated by a Coulomb interaction. Thus, our proposal consists in arranging the 13-atom clusters on a diamond lattice with each Ag_{13} cluster surrounded by four oppositely charged neighbors at the vertices of a tetrahedron (see Figure 7.2). The strength of the interaction between these metallic 13-atom silver clusters should be mediated by short-range electrostatic potentials in a similar way as the 12 outer-shell atoms interact with the inner atom in the icosahedral structure of Ag_{13} cluster. We have found in the case of the Ag_{13} silver cluster that the spin magnetic moment of the 13 atoms couple ferromagnetically each other because of the low electron

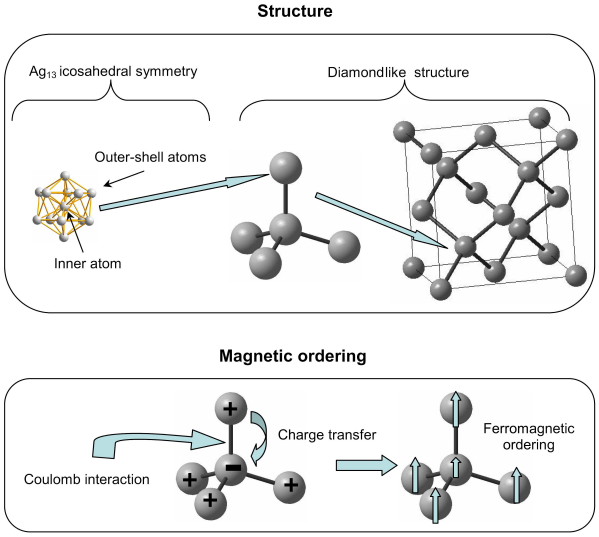

Figure 7.3:
Schematic representation of the proposal to assemble the 13-atom clusters into nanoparticles. The short-range electrostatic interaction between the Ag_{13} clusters should produce a ferromagnetic ordering in the nanoparticle with diamondlike structure.

transfer from the outer-shell atoms to the inner atom, which makes the inner atom not align antiferromagnetically to the outer-shell atoms. Likewise, it is expected that the nanoparticle crystallized in diamondlike lattice and made of Ag_{13} clusters as a building block follows the same trend as Ag_{13} atoms do. The situation is very interesting from the magnetic and biomedical points of view because on one side, the ferromagnetic ordering enlarges quite enough the total magnetic moment of the nanoparticle and on the other side, the applied external magnetic field needed to guide the nanoparticles inside the body to the cancerous region is lower in strength.

7.4 Conclusions

In conclusion, we have shown that the appreciable magnetism and the considerable stability along with the inertness of Ag_{13} cluster to be assembly into magnetic nanoparticles become it as a good candidate for biomedical applications since it could improve some present-day difficulties of magnetic nanoparticles like toxicity and opsonization.

8

Density Functional Study of the Oxidation of Small Neutral and Charged Silver Clusters

> *Let the rain kiss you. Let the rain beat upon your head with silver liquid drops. Let the rain sing you a lullaby.*
>
> — Langston Hughes

Synopsis

We have studied the energetic and structural stability of the interaction of molecular oxygen with small neutral, anionic, and cationic silver clusters, Ag_n ($3 \leq n \leq 8$). The calculations have been carried out using a linear combination of atomic Gaussian-type orbitals within the density functional theory as it is implemented in the deMon code. The O_2 molecule has been placed in different positions surrounding the cluster, in order to increase the configurational space of the structural minima. We have found that the oxidized cation and neutral clusters undergo a 2D-3D structural transition even before than the nonoxidized counterparts. Moreover, our results show that the adsorption energies on the cationic and neutral silver oxide clusters manifest an odd-even alternation pattern. Likewise, the average magnetic moment of the O_2 radical in the charged and neutral silver environment tends to be greater than the charged and neutral bare diatomic oxygen molecule.

8.1 Introduction

Clusters are part of everyday life and their presence is very important for industry. We are usually unaware of the fact that clusters form aerosols, automobile exhaust,

clays, or colours. In recent years, the transition-metal clusters have played an important role in cluster physics [89], since these clusters are well suited for several applications. Some examples are found in catalysis [120], biomedicine [121], or in photographic process [143].

More recently, the adsorption of small molecules by metal clusters has attracted significant attention, both from the experimental and from the theoretical side [144–146]. With the recent increasing use of nanomaterials, understanding the oxidation at nanometer scale is of great interest. In particular, the silver metal has attracted an especial attention because of its astonishing charge transfer behaviour which manifest, for example, in its fascinating bactericidal properties [147] or its large fluorescence enhancement [148]. In this regards, the silver atom with the electronic configuration [Kr] $4d^{10}$ $5s^1$ has one electron in the outer shell and thus, in the oxidation process it could act as a single-electron donor whereas the O_2 could act as a single-electron acceptor. Although this reasoning can be considered in general as true, we will show in this CHAPTER that some other ingredients are needed to explain how the charge transfer evolves with the cluster size.

Up to now, in literature less or null attention has been paid to the evolution of the magnetic moment of the O_2 radical with the cluster oxide size. Recently, it has been predicted the Ag_{13} cluster could be magnetic [137] and it was suggested that the silver nanoclusters made of Ag_{13} clusters, as building blocks, are promising candidates for the magnetic applications of nanoparticles in biomedicine [149]. In consequence, if the O_2 radical manifest an important magnetic contribution to the silver cluster, it could modify the magnetic properties of the silver clusters in such a way that they could be enhanced or diminished, affecting consequently their biomedical applications. The study of the magnetic moment of the O_2 radical in silver environment along with the electronic and stability properties of the anionic, cationic, and neutral oxide silver clusters will be the scope and matter of analysis in this CHAPTER.

8.2 Computational Details

With the aim of studying the structural, electronic, and magnetic properties of small anionic ($Ag_nO_2^-$), cationic ($Ag_nO_2^+$), and neutral (Ag_nO_2) silver oxide clusters with $3 \leq n \leq 8$, we have performed density functional theory-based calculations consisting of a linear combination of Gaussian-type-orbitals (LCGTO) Kohn-Sham density-functional methodology as it is implemented in DEMON program [79]. Pseudopotential spin-unrestricted calculations were carried out at the generalized gradient approximation (GGA) to take the exchange-correlation (XC) effects into account [81]. Local-density approximation (LDA) sometimes yields inaccurate bond lengths and total energies due to the insufficiency in describing the strong correlation effects of the localized *d* electrons and charge density inhomogeneities. In these regards, the

GGA should be a choice better than LDA as was described in more detail in REFERENCES [98] and [127]. An orbital basis set of contraction pattern (2211/2111/121) for silver atoms and (3111/311/1) for oxygen atoms was used in conjunction with the corresponding (3,7;3,7) and (5,3;5,3) auxiliary basis set for describing the s, p, and d orbitals of silver atoms and s and p orbitals of oxygen atoms, respectively [82]. In DEMON, the electron density is expanded in auxiliary basis functions which are introduced to avoid the calculation of the N^4 scaling Coulomb repulsion energy, where N is the number of the basis functions. Likewise, we have used a model core potential for describing the 30 core electrons of silver atom and 2 electrons in the case of oxygen. The contraction pattern was (6;9,6,4) for silver and (5:6) for oxygen. The grid for numerical evaluation of the XC terms had 128 radial shells of points and each shell had 26 angular points. Spurious one-center contributions to the XC forces, typically found in systems with metal-metal bonds when using a nonlocal functional, are eliminated in a similar way as has been done in REFERENCE [83]. A wide set of spin multiplicities ranging from 1 to 6 were checked to ensure that the lowest-energy electronic configuration is reached. The geometries were optimized without symmetry constraints using the Broyden-Fletcher-Goldfarb-Shanno algorithm [37]. During the optimization, the convergence criterion for the norm of the energy gradient was fixed to 10^{-3}-10^{-4} a.u. while it was 10^{-5} a.u. for the energy and 10^{-4} a.u. for the charge density. The ground state structures of the anionic, cationic, and neutral silver oxide clusters studied in this CHAPTER are illustrated in FIGURE 8.1.

8.3 Results and Discussion

To study the level of oxidation of anionic, cationic, and neutral silver clusters, we have optimized a great number of structures. Hereafter n stands for the number of silver atoms forming the cluster. We initiate the calculations using as guess structures essentially two geometry configurations: in one of them, the diatomic oxygen molecule was positioned perpendicular to the silver cluster surface and in the other one it was located parallel to the surface. The lowest-energy structures obtained after the geometry optimization are show in FIGURE 8.1. One feature we have observed is that the oxidized cation and neutral clusters undergo a 2D-3D structural transition for the clusters with $n = 4$. The rest of clusters coagulate in structures slighted distorted from the lowest-energy structures of the nonoxidized silver clusters, except for the case of Ag_8O_2. The onset of this structural transition does not appears for their counterparts, in fact, the neutral silver clusters [127] become to be 3D structures for $n = 7$ whereas the charged silver clusters [128] anticipate the aforementioned onset for $n = 6$. Thus, the oxygen atoms force the rhombohedral structure of the silver atoms to adopt a bent structure, with a torsion measured from the planar rhombus which in the case of the cation with an angle of 133.3° is greater than the neutral (158.8°). The reason for the strong distortion

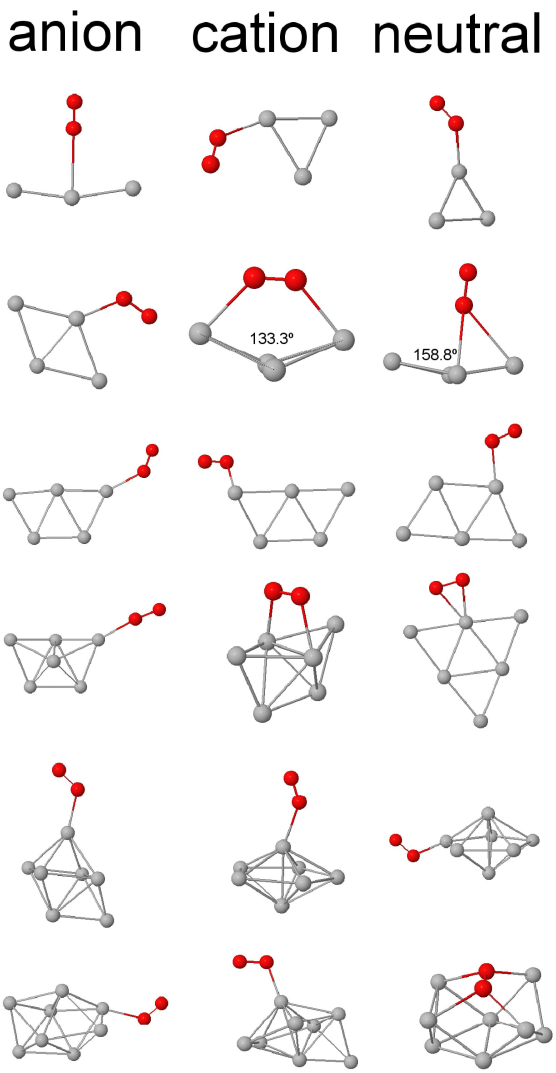

Figure 8.1:
Lowest energy structures of the anionic, cationic, and neutral silver oxide clusters. The spheres in red and grey represent oxygen and silver atoms, respectively. The silver atoms of the cationic and neutral tetramer oxide coagulate in a bent rhombus forming an angle of 133.3° and 158.8°, respectively.

of the aforementioned silver clusters relies on the octet rule. The $Ag_4O_2^-$ cluster has one electron excess with respect to the neutral cluster (extra electron), what makes that the oxygen closer to the silver atom fulfills the octet rule, i.e., the outer electron shell of oxygen atom needs two electrons to complete the total of eight. One comes from the $5s$ shell of the silver atom and the other one is the extra electron. Consequently, in this case only one Ag-O bonding is required to stabilize the molecule. However, the cationic cluster presents a defect of one electron. To fulfill the octet rule the O-O bonding length should increase to form a single bond instead of a double bond like in the case of O_2 molecule (every oxygen atom only have to share one electron). In TABLE 8.1, we can see how the O-O bond length has increased from 1.12 Å (value for the bare diatomic oxygen molecule) to 1.26 Å, which is in good agreement with the predictions of the octet rule. To fulfill the

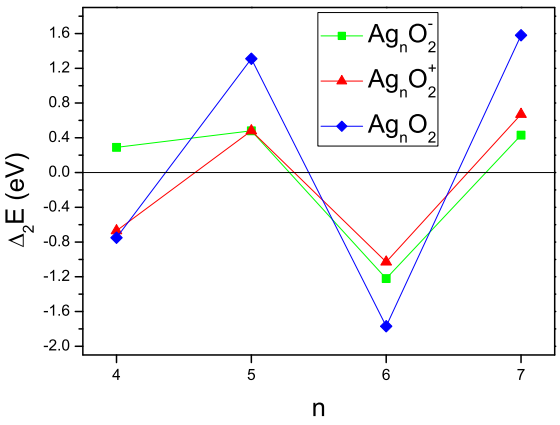

Figure 8.2:
Disproportionation energy ($\Delta_2 E$) versus the anionic, cationic, and neutral silver oxide cluster size.

octet rule, every oxygen atom has to be bounded by silver atoms and consequently, it gives rise to a distortion of the structure. The same reasoning follows for Ag_4O_2 and Ag_8O_2.

Table 8.1:
Bonding length between the oxygen-oxygen and silver-oxygen atoms for $Ag_nO_2^-$, $Ag_nO_2^+$, and Ag_nO_2. We have taken the average value of the bonding length for the clusters where the number of bonds between silver and oxygen atoms is greater than one. The case $n = 0$ represents the value for the bare oxygen diatomic molecule. The values of the Ag-O bond for $n = 0$ were taken from REFERENCE [139]. The interatomic distances are given in Å.

	anion		cation		neutral	
n	d_{O-O}	d_{Ag-O}	d_{O-O}	d_{Ag-O}	d_{O-O}	d_{Ag-O}
0	1.36	2.56	1.12	2.42	1.21	2.28
3	1.24	3.00	1.22	2.24	1.27	2.11
4	1.30	2.16	1.26	2.38	1.24	2.88
5	1.28	2.17	1.22	2.49	1.28	2.17
6	1.27	2.20	1.30	2.25	1.34	2.11
7	1.27	2.14	1.23	2.14	1.25	2.23
8	1.31	2.16	1.25	2.10	1.32	2.46

For every cluster we have studied, we have found that the oxygen atom closer to the silver cluster core always becomes as an acceptor of electrons. The results of the charge transfer are collected in TABLE 8.2 for the Ag-O bond. The diagonal elements of the Mayer bond order matrix give information about the order of the bond and the rest of elements provide us with information about the charge transfer. A positive value means that the charge is transferring from the silver atoms to the oxygen. The positive sign of the charge transfer is the other ingredient what underpins the octet rule because in contrary case, it is impossible to fill the outer oxygen shell with 8 electrons.

In FIGURE 8.2, we have plotted the evolution of the disproportionation energy with the neutral and charged silver oxide clusters size. The disproportionation energy is defined as

$$\Delta_2 E_n = E_{n+1} + E_{n-1} - 2E_n, \tag{8.1}$$

where E_n is the total energy provided by our *ab initio* calculations of the cluster with n atoms. It represents the relative stability of a cluster with n atoms in comparison to its neighbors, i.e., the clusters with $n+1$ and $n-1$ atoms. A positive peak in Δ_2E indicates that the cluster with size n is very stable. According to this definition, we can see in FIGURE 8.2 that the clusters with an odd number of atoms are more stable than the clusters with an even number of atoms. This oscillating behaviour has also been reported in REFERENCES [127] and [128] for the nonoxidized silver clusters and it is closely related to the highest occupied molecular orbital-lowest unoccupied molecular orbital (HOMO-LUMO) gap because an increase of the HOMO-LUMO gap is on the side of a chemical stability of the cluster. In FIGURES 8.3a), b), and c) we show the oscillating behaviour of the HOMO-LUMO gap for Ag_n^-, Ag_n^+, and Ag_n, respectively. The same explanation can be adopted for $Ag_nO_2^+$ and Ag_nO_2 clusters, as shown in FIGURE 8.3d) for $4 \leq n \leq 7$. However, in the case of the anionic silver oxide clusters only the cluster with $n = 4$ breaks the HOMO-LUMO gap oscillation. The calculations give us a greater value of the HOMO-LUMO gap than expected according to this explanation. This is the reason for which the anionic cluster with $n = 4$ is so stable compared with $Ag_4O_2^+$ and Ag_4O_2, as shown in FIGURE 8.2.

With the aim of studying the adsorption of O_2 molecule on the silver clusters, we have plotted in FIGURE 8.4 the adsorption energy (E_a) as a function of the neutral and charged silver oxide cluster size. The adsorption energy is defined for the neutral cluster as:

$$E_a = (E_{Ag_n} + E_{O_2}) - E_{Ag_nO_2} \tag{8.2}$$

where E_{Ag_n}, and $E_{Ag_nO_2}$ are the total energies of the nonoxidized, and oxidized silver clusters. The E_{O_2} represents the total energy of the geometry optimized oxygen dimer. Similarly, the adsorption energy is defined for the charged silver oxide cluster. An enhancement of the adsorption energy is on the side of the stabilization of the Ag-O bond, i.e., the more positive the E_a is, stronger the Ag-O bond is. We have observed in FIGURE 8.4 that the adsorption energies on the cationic and neutral silver oxide clusters manifest an odd-even alternation pattern. The same oscillation has been found in REFERENCE [139] but this time for the anionic silver oxide clusters instead of cationic ones. The oscillating pattern relies, as commented above, on the HOMO-LUMO gap oscillation. Thus, an increase or decrease of the HOMO-LUMO gap tends to chemically stabilize or destabilize the cluster and thus lowering or raising the total energy, respectively. Consequently, the adsorption energy oscillates because it is a parameter that directly depends on the total energy. Moreover, we have also found that the greater values of E_a are for the anionic silver oxide clusters, specially the cases with $n = 4$ and $n = 8$. In this two cases, the O-O bonding length is 1.30 Å and 1.31 Å, respectively. These values are very close to the bonding length of the anionic oxygen dimer (1.36 Å) compared with the other anionic silver oxide clusters and the O-Ag bonding length is in general lesser than the other anionic clusters (see TABLE 8.1), and thus favoring their stabilization. In

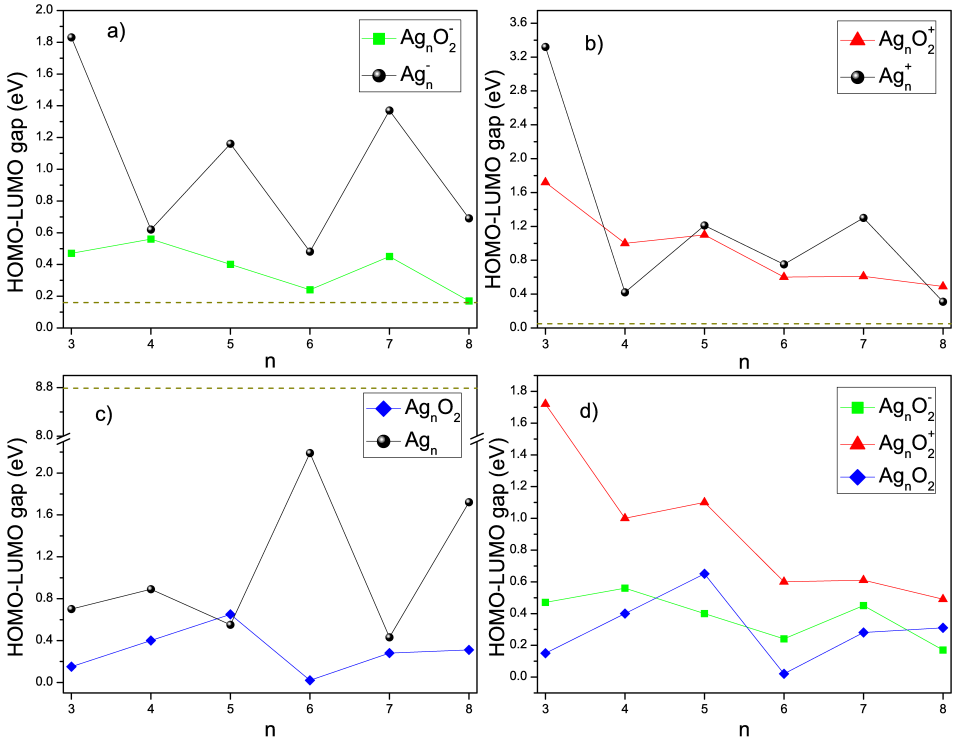

Figure 8.3:
HOMO-LUMO gap for the oxidized and bare silver clusters. The dashed horizontal lines represent the value of the HOMO-LUMO gap for the anionic (a), cationic (b), and neutral (c) bare diatomic oxygen molecule. The values of the HOMO-LUMO gap in (c) for bare neutral silver clusters were taken from Reference [127].

Table 8.1, we have collected the bonding length between the oxygen-oxygen and silver-oxygen atoms for the neutral and charged silver oxide clusters. We observe that the anionic clusters shorten the O-O distance and the Ag-O bonding length except for the case $n = 3$, however the cationic and neutral silver oxide clusters elongates the O-O distance whereas the Ag-O bonding length is shortened, except for $n = 5$ in cationic clusters and for the tetramer ($n = 4$) and octamer ($n = 8$) in the neutral clusters. Consequently, a shortening of the O-O and Ag-O bonding length is on the side of an increment in the adsorption energy and an elongation of the O-O and Ag-O ($n = 5$ for cationic cluster and $n = 4, 8$ for neutral) penalizes the E_a. Most of the cationic and neutral silver oxide clusters show a relatively high E_a because the Ag-O bonding length is shortened.

In Figures 8.3a), b), and c) we have compared the HOMO-LUMO gap between the neutral and charged silver oxide clusters and the nonoxidized ones. Special attention deserves the cases $n = 3$, 5, and 7 for anionic complexes, $n = 3$ and 7 for the cationic clusters and $n = 6$ and 8 for the neutral clusters. In these special cases, the HOMO-LUMO gap for the nonoxidized clusters is very high, which means

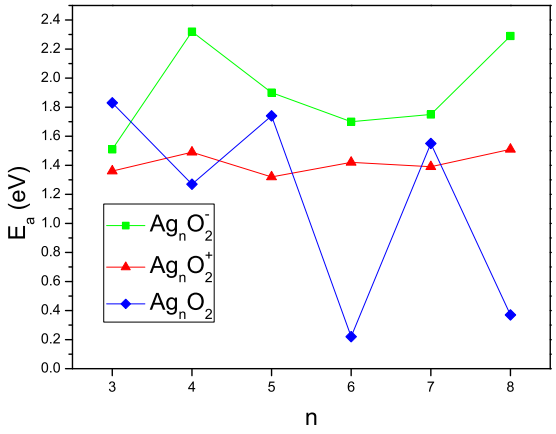

Figure 8.4:
Adsorption energy (E_a) for the anionic, cationic, and neutral silver oxide clusters with $3 \leq n \leq 8$.

that they are very stable structures. However, the interaction with the oxygen diatomic molecule makes them to be less stable. Interestingly, the HOMO-LUMO gap of the nonoxidized clusters is in average greater than the oxidized clusters and consequently, the oxidation of silver clusters is expected to be of less importance in the range of silver oxide clusters studied in this CHAPTER.

Table 8.2:
Mayer bond order for the anionic, cationic, and neutral silver oxide clusters. The Mayer bond order is only given for the bonding between the oxygen and silver atoms with the least bonding length.

n	anion	cation	neutral
3	0.010	0.030	0.006
4	0.210	0.230	0.100
5	0.020	0.090	0.180
6	0.290	0.360	0.120
7	0.440	0.080	0.040
8	0.120	0.320	0.170

Concerning the question about the evolution of the magnetic moment of the O_2 radical with the cluster size, we have shown in FIGURE 8.5 the average magnetic moment of O_2 radical versus n. We see that it oscillates around the average value of 0.7 μ_B, 0.8 μ_B, and 0.6 μ_B for the anionic, cationic, and neutral silver oxide clusters, respectively. In the whole three cases, the average magnetic moment of the O_2 radical is greater than the corresponding neutral and charged bare diatomic oxygen molecule (0.5 μ_B for the charged clusters and 0 μ_B for the neutral clusters). It is a consequence of the charge transferring from the silver atoms to the oxygen and thus it enlarges the spin decompensation. The only exception is the case $n = 6$ for the neutral clusters. This is because the Ag_6O_2 cluster has very low adsorption energy (see FIGURE 8.4) which provokes that silver cluster core is less bounded by the oxygen diatomic molecule. Consequently, the cluster should be less stable as is shown in FIGURE 8.2.

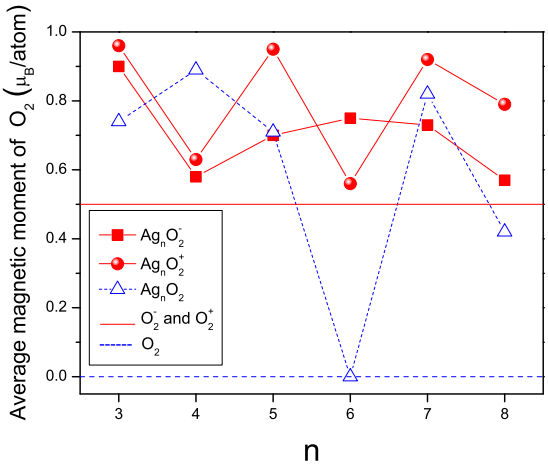

Figure 8.5:
Average magnetic moment per atom of the oxygen dimer versus the number of silver atoms forming the anionic (square), cationic (circle), and neutral (triangle) clusters. The dashed and solid horizontal lines are for neutral and anionic-cationic bare O_2 clusters, respectively.

8.4 Conclusions

In conclusion, we have firstly shown is this Chapter that the oxidized cation and neutral clusters undergo a 2D-3D structural transition for the clusters with $n = 4$ and the explanation for this transition relies on the octet rule. Secondly, we have observed by means of the disproportionation energy that the clusters with an odd number of atoms are more stable than the clusters with an even number of atoms. The HOMO-LUMO gap has revealed as a good parameter for explaining the oscillating behaviour of the disproportionation energy plotted against the cluster size. Thirdly, we have also observed that the adsorption energies on the cationic and neutral silver oxide clusters manifest an odd-even alternation pattern, which have already been predicted in Reference [139] but in this case for the anionic clusters instead of the cationic ones. The HOMO-LUMO gap and the structural properties of these clusters helped us to understand the oscillating behaviour. Moreover, we found that the HOMO-LUMO gap of the nonoxidized clusters is in average greater than the oxidized cluster which allows us to conclude that the reactivity of the silver clusters with the oxygen diatomic molecule is of less importance. This ability is a critical point to take into account, especially if one pretends to use the magnetic silver nanoclusters in biomedical applications because if the oxidation is negligible, then the opsonization process can be minimized. Finally, we have studied the evolution of the average magnetic moment of the O_2 radical in function of the cluster size. In most of the clusters, the charge transferring from the silver atoms to the O_2 radical justify the elevated magnetic moment found for the O_2 radical in comparison with the bare O_2 molecule.

9

Origin of the Anomalous Slater-Pauling Curve in cobalt-manganese Alloy Clusters

> *Anomalies bug me.*
>
> — Dr. Greg House

Synopsis

Surprising enhancement of the magnetic moments recently observed in dilute Co-Mn alloy clusters is explained using *ab initio* electronic structure calculations. The calculated magnetic moments generally agree with the reported experimental data. An equation for calculating the magnetic moments of the Co-Mn alloy clusters has been derived to correct the deviations predicted by the rigid-band model and the virtual bound states approximation. A new strategy is proposed to obtain the ground-state structures of the Co-Mn clusters and it was also put to the test of the experiment.

9.1 Introduction

The exploration of bimetallic transition metal (TM) clusters is emerging as a promise field of research because of the new opportunities they offer for developing magnetic recording devices and cluster-assembled materials with functions for medical applications [150, 151]. Although the electronic and magnetic properties of bare TM clusters have been actively studied for several years, however less attention has been paid to their alloys because they represent both an experimental and theoretical challenge. Thus, for experimentalists is very difficult to control the stoichiometry of the alloy clusters using chemical methods, and for theoreticians, the determination of the ground-state geometries becomes a very difficult task, as commented later

in the main text of this CHAPTER. The recent observation of the average magnetic moment enhancement in dilute Co-Mn alloy clusters [152] that contradicts the bulk behavior has presented an entirely unexpected dimension on the subfield of magnetic alloy clusters and it could pave the way for future possible applications such as, for example, in biomedicine as magnetic sensors. Although the search for the origin of the aforementioned observation has actively stimulated the research on Co-Mn alloy clusters [152–155], however the answer still remains elusive. A possible explanation is based on the assumption that a virtual bound state (VBS) is formed below the highest occupied molecular orbital (HOMO) level and near the Mn site [152]. A VBS can be defined in the potential scattering model as a resonant scattering near impurity atoms in the host which induces a narrow peak in the conduction band density of states (DOS). Originally, the VBS model was developed by Friedel [156] to explain many of the physical properties of bulk magnetic alloys containing dilute magnetic species. It represents an improvement over the rigid-band (RB) model which is based on the assumption that the s and d bands are rigid in shape as atomic number of the alloy changes [157]. In this CHAPTER, our calculations demonstrate that the origin of the anomalous behavior of the Slater-Pauling (SP) curve of Co-Mn alloy clusters does not require the formation of a VBS as suggested in REFERENCE [[152]], but is explained directly in terms of the magnetic moment provided by the Mn atoms and the "spin-flipping" of the electrons belonging to the Co-Mn bonding. Thus, with the aim of studying the magnetic properties of Co-Mn alloy clusters and elucidating the anomalous behavior of their SP curve, we have performed spin-unrestricted density-functional theory(DFT)-based calculations as implemented in the DEMON program package [79].

9.2 Method and Structural Properties

The electronic system consisting in Ω nuclei and η electrons is assumed to be described by the next Hamiltonian, which expressed in second quantization and in the Born-Oppenheimer nonrelativistic approximation reads as

$$\begin{aligned}\hat{H} = &\sum_{ij}^{\eta}\sum_{\nu\mu} c^{*}_{\nu i}c_{\mu j}\left(\langle\nu|-\frac{1}{2}\triangle|\mu\rangle-\sum_{k}^{\Omega}Z_k\langle\nu|\,|\mu\rangle\right)\hat{a}^{\dagger}_i\hat{a}_j \\ &+\frac{1}{2}\sum_{ijkl}^{\eta}\sum_{\nu\mu\alpha\beta} c^{*}_{\nu i}c^{*}_{\mu j}c_{\alpha k}c_{\beta l}\langle\nu\mu|\,|\alpha\beta\rangle\,\hat{a}^{\dagger}_i\hat{a}^{\dagger}_k\hat{a}_l\hat{a}_j+\hat{V}^{\mathrm{GGA}}_{xc}\left(\rho^{\sigma},\nabla\rho^{\sigma}\right)\end{aligned} \tag{9.1}$$

where the Kohn-Sham orbitals $|i\rangle$ were expanded into atomic orbitals $|i\rangle=\sum_{\mu}c_{\mu i}\,|\mu\rangle$ in the linear combination of Gaussian type-orbitals ansatz. The orbital basis sets of contraction pattern (2111/211*/311+) and (2211/311/411) were used in conjunction with the corresponding (5,3,3;5,3,3) and (3,4;3,4) auxiliary basis sets for Co

and Mn, respectively [82]. Likewise, *ad hoc* model core potentials with contraction pattern (4:7,4) and (5:7,4) have been used for describing the inner electrons of Co and Mn atoms, respectively [98]. The kinetic and nuclear attraction energy of the electrons in an environment of Z_k nuclear charges are described by the one-electron term. The $||$ symbol represents the $1/|\mathbf{r}-\mathbf{k}|$ operator, where $\mathbf{r}$ and $\mathbf{k}$ are the electron and nuclear position vectors, respectively. The two-electron operator represents the Coulomb repulsion energy of the electrons. In this case, the symbol $||$ represents the $1/|\mathbf{r}_1-\mathbf{r}_2|$ operator for the electrons with coordinates $\mathbf{r}_1$ and $\mathbf{r}_2$. The last term in EQUATION (9.1) is the exchange-correlation energy and we have used here the form proposed in REFERENCES [[23, 24]] which is a function of the spin-dependent electron density ($\rho^\sigma, \sigma = \uparrow, \downarrow$) and its gradient in the generalized gradient approximation (GGA). We have adopted the former GGA functional in our DFT calculations because it was reported in REFERENCE [[98]] that it represents a dramatical improvement in the calculated binding energies of Co clusters. The total energy of the system is calculated adding the nuclear repulsion energy ($\sum_{a>b}^{\Omega}(Z_a Z_b)/|\mathbf{r}_a-\mathbf{r}_b|$) to the electronic contribution. A wide set of spin multiplicities ranging from 1 up to a maximum of 61, depending on the selected cluster, was checked to ensure that the lowest-energy electronic and magnetic configuration is reached. More information about the computational details can be found elsewhere [137]. Hereafter, all calculated results refer only to the Co-Mn alloy 20 atom clusters. We have also performed electronic structure calculations of some guessed geometries of the Co-Mn alloy clusters with $\Omega = 25$ and 30 in a range of Mn concentration less than 0.3, but the obtained results slightly differ from that of the $\Omega = 20$ case, i.e., we observed that the calculated magnetic moments of clusters with $\Omega = 25$ and 30 increase with the impurity concentration as $\Omega = 20$ clusters do. Accordingly, the conclusions drawn from the Co-Mn clusters with $\Omega = 20$ can be extended to clusters with greater size.

The search for the global minima of the Co-Mn alloys 20 atom clusters was planned as a multistage strategy combining an unbiased search method, i.e., a basin-hopping [141] algorithm, in conjuction with a molecular mechanics method [158]. In the reoptimization procedure of the clusters, we have made use of the Polak-Ribière algorithm [159] without any symmetry constraint and the root-mean-square gradient was set to 10^{-4} Kcal/(mol Å). In a first stage of the calculation method, the initial guessed structures of the Co_{20} cluster were taken from three different sources, namely, the structures were provided by the *GMIN* code [141] which uses the basin-hoping algorithm, the existing databases [101], and proposed by us. After that, they were reoptimized with the *HyperChem* code [158] with the intention to obtain the ideal candidate to the lowest-energy structure of the Co_{20} cluster. The converged guessed structures are illustrated in FIGURE. 9.1 and the structural and energetic parameters are reported in TABLE 9.1. The ground-state structure (Co_{20_0}) is a capped double icosahedron. The cohesive energy and the number of nearest-neighbor Co-Co bonds reveal that the most stable structure is also the

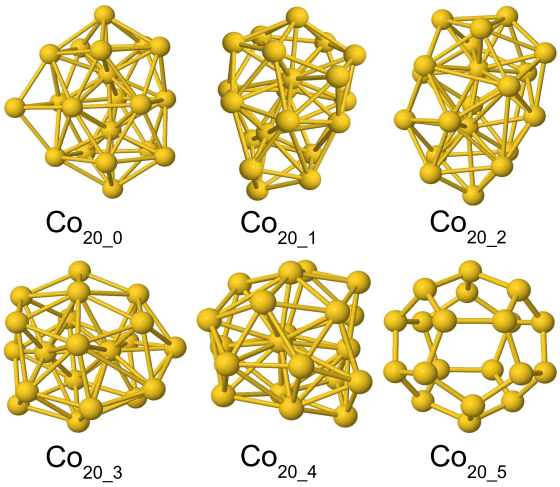

Figure 9.1:
Illustration of the guessed structures of the Co_{20} cluster. The structures are ordered from left to right and top to bottom by increased relative energy. The notation Co_{20_m} stands for the mth energetic isomer.

most compact one although the average first-neighbor distance is a little bit higher than the rest of structures plotted in FIGURE 9.1. In a second stage, the rest of guessed structures of the Co_mMn_n alloy clusters were built from the geometry of the Co_{20} cluster but this time $m-n$ Co atoms swap positions with n Mn atoms. The assumption is underpinned by three arguments: first, the ionic radii (r_a) of Co and Mn atoms are pretty close, i. e. 1.25 Å and 1.26 Å, respectively [160]. Second, we have calculated the size of the Thomas-Fermi screening [156] outside the atomic sphere of the Mn atoms (Z_{Mn})

$$Z_{TF} = Z_{Mn}\left(1 + r_a\sqrt{4\pi\eta(\epsilon_{HOMO})}\right)e^{-r_a\sqrt{4\pi\eta(\epsilon_{HOMO})}} \tag{9.2}$$

and it is vanishingly small because the DOS at the HOMO level [$\eta(\epsilon_{HOMO})$] provided by our DFT calculations are large [see FIGURE 9.2(c)], so that the exponent in EQUATION (9.2) is $r_a\sqrt{4\pi\left\langle\eta(\epsilon_{HOMO})\right\rangle} \simeq 247.58$, where $\langle\eta(\epsilon_{HOMO})\rangle$ represents the average over the lowest-energy Co-Mn alloy series clusters with $\Omega = 20$. Thus, the size effects are negligible and the addition of Mn atoms to the cluster should slightly distort their environment. Third, we have performed a geometry optimization of Co_3, Co_2Mn_1, Co_4, and Co_3Mn_1 clusters by means of spin-unrestricted DFT calculations [79] and the results show that the elongation of the Co-Mn average bond length with respect to the Co-Co one is less than 0.15 Å. In consequence, the substitution of cobalt atoms by Mn atoms should slightly distort the geometric structure of the clusters. This fact has also been observed in REFERENCE [152].

Another specific difficulty of alloy clusters is the great number of possibilities they offer to distribute the solute atoms over the sites at a given geometrical arrangement of the atoms. Thus, for example, in the case of $Co_{10}Mn_{10}$ the number of possible homotops for a geometry with inequivalent positions is $C_{10}^{20} = \frac{20!}{10!^2} \simeq 1.8\times10^5$.

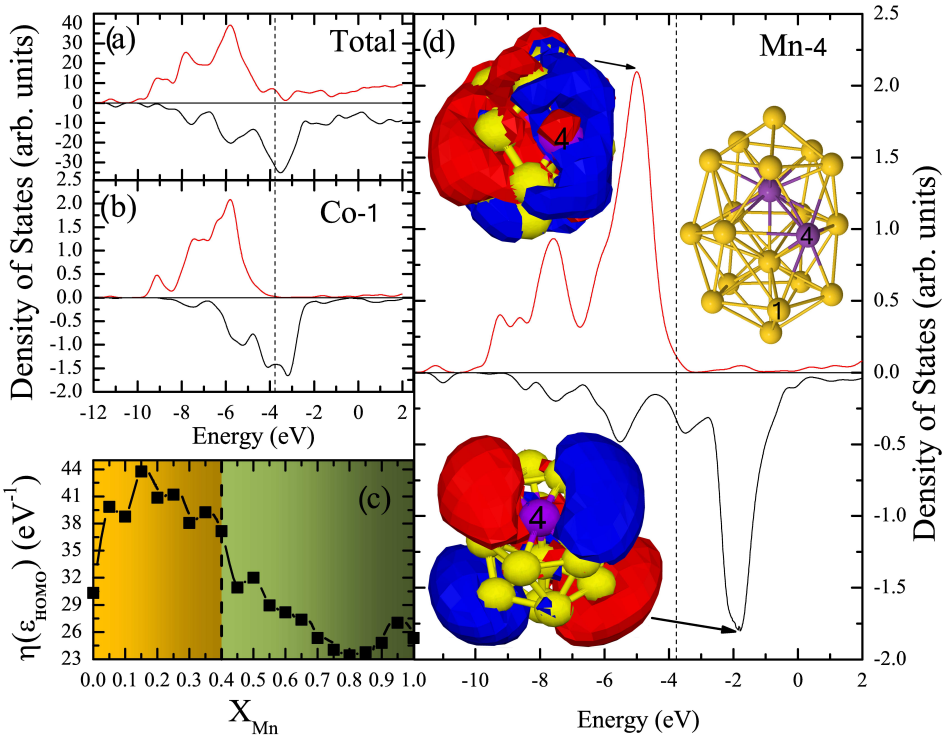

Figure 9.2:
Plot of the spin-polarized DOS for (a) $Co_{18}Mn_2$, (b) Co-1 and (d) Mn-4, where the labels 1 and 4 represent the site number of Co and Mn atoms, respectively. In (b) and (d), we have only plotted the contribution of the *d* orbitals because *s* and *p* orbitals are of less importance. The upper-half part of the figures is for spin-up electrons while the lower-half is for the spin-down electrons. The atoms of (b) and (d) are labeled in the geometric structure. We have also plotted the shape of the delocalized molecular orbitals for the higher-lying occupied and lower-lying unoccupied levels of $Co_{18}Mn_2$ cluster with the aim of showing the bonding and antibonding character of the orbitals, respectively. The dotted vertical lines represent the HOMO level. In (c), DOS at the HOMO level is plotted against the Mn concentration.

With the aim of overcoming the aforementioned point, we have planned out a strategy consisting in optimize the geometries of the 20 homotops belonging to the $Co_{19}Mn_1$ cluster. As starting point, every structure was built from the optimized geometry of Co_{20} cluster but substituting a Co by a Mn atom at the 20 accessible positions of the cluster. After that, we performed a geometry optimization of the 20 homotops to obtain the stability of them as a function of the position occupied by the Mn atom. The rest of Co-Mn alloy clusters were created by replacing the cobalt atoms by Mn atoms at the positions with the lowest energy and once again they were reoptimized in geometry. We examined the method for the case of $Co_{18}Mn_2$ homotops where one of the two Mn atoms was attached to the position with the lowest energy and the other Mn was positioned in the rest of available sites. After

Table 9.1:
Average first-neighbor distance (d_{Co-Co}), number of nearest-neighbor Co-Co bonds (N_{Co-Co}) per atom, relative (ΔE), and cohesive (E_c) energies of Co_{20} cluster isomers. The geometry notation is that of FIGURE 9.1. The point groups are determined from REFERENCE [161].

Cluster	Point group	d_{Co-Co} (Å)	N_{Co-Co}/atom	ΔE (eV)	E_c(eV)
Co_{20_0}	C_{2v}	2.46	3.55	0.00	1.78
Co_{20_1}	C_1	2.39	3.00	0.26	1.76
Co_{20_2}	C_1	2.38	3.05	0.35	1.76
Co_{20_3}	C_1	2.39	2.85	0.95	1.73
Co_{20_4}	C_1	2.39	2.85	0.98	1.73
Co_{20_5}	I_h	2.44	1.50	7.85	1.38

the optimization procedure, we have observed that the lowest-energy structure was the one with Mn atoms in the lowest-energy positions and the energy of the other geometries was estimated to be 3.22 eV greater than the ground-state cluster. We have also put the geometry optimization method to the test of the experiment [162] as shown in TABLE 9.2. The ionization potentials provided by our DFT calculations are in good agreement with the available experimental results and consequently, our reported structures should be very close to the ground-state structures of the Co-Mn alloy series clusters with $\Omega = 20$. The lowest-energy structures are illustrated in FIGURE 9.3 and the geometrical properties are collected in TABLE 9.3. The Co-Mn alloy geometries converged in slightly distorted structures of that of the Co_{20}. In particular, the distance of the atom labeled as 12 in FIGURE 9.3 to the rest of atoms belonging to the cluster is gradually reduced with the enhancement of the Mn concentration up to the $Co_{15}Mn_5$ cluster which elongates the distance. For the rest of clusters, the distance persists approximately unaltered. This point is reflected in the average nearest-neighbor distance for Co-Co bonding reported in TABLE 9.3. It is also important to comment that the average nearest-neighbor distances for the Co-Co, Mn-Mn, and Co-Mn bondings are in general very close each other (see TABLE 9.3). This results favor the assumption commented above that the addition of Mn atoms just only alters a little bit the geometry of the ground-state structure of Co_{20} cluster. To conclude the structural discussion, and with the aim to show how the Mn atoms diffuse into the Co ones, it is convenient to define an order parameter that is positive and close to 1 when the phase separation or segregation takes place and close to 0 when the mixing or disorder is the main contribution to the arrangement of the Mn atoms in the cluster. The parameter which meets the aforementioned conditions is the chemical order and it is thus defined as

$$\Gamma = \frac{N_{i-i} + N_{j-j} - N_{i-j}}{N_{i-i} + N_{j-j} + N_{i-j}} \tag{9.3}$$

where N_{i-j} represents the number of nearest-neighbor i-j bonds (with i=Co and

Table 9.2:
Ionization potentials (in eV) for Co_mMn_n clusters with $\Omega = 20$. The experimental data were taken from REFERENCE [162].

n	0	1	2	3	4	5
Theory	5.45	5.54	5.60	5.38	5.51	5.40
Experiment	5.45	5.44	5.37	5.34	5.31	5.23

j=Mn). The values of Γ reported in TABLE 9.3 are plotted in FIGURE 9.4. It is easily observed in FIGURE 9.4 the asymmetry of the chemical order parameter with respect the dash vertical line. Thus, at low concentrations of Mn atoms Γ decreases more rapidly than for higher concentrations of them so that the mixing is favored in an interval of X_{Mn} ranging approximately from 0.15 to 0.65. The reason for that behavior is attributed to the positions occupied by the Mn atoms in the range of low concentration. As can be seen from FIGURE 9.3, the impurity atoms swap positions with the inner Co atoms. The number of bondings between the inner positions and the rest of atoms is higher than the outer-shell positions. Thus, the number of Co-Mn bondings is favored for lower concentrations of the impurity and in consequence Γ decrease rapidly. But however, for higher concentrations of the Mn atoms, the process is not inverted and the cobalt atoms occupy mainly the outer-shell positions instead of the inner ones.

9.3 Results and Discussion

The anomalous behavior of the SP curve in Co-Mn alloy clusters compared to the CoMn bulk [163, 164] is shown in FIGURE 9.5. The magnetic moments per atom (empty star symbol) increase with a slope of 1.83 μ_B up to a Mn concentration of 40%, after which the average magnetic moments tend to decrease with increasing Mn concentration. The above results are in very good agreement with the available experimental measurements (filled star symbol) reported in REFERENCE [152] (1.7 μ_B and 40%, respectively). The discrepancy with the numerical data (about 0.6 μ_B in average) may be related to the omission of the orbital moment contribution since the total magnetic moment is $\langle\vec{M}\rangle = 2\langle\vec{S}\rangle + \langle\vec{L}\rangle$. However, according to the results of the calculations performed for binary TM clusters reported in REFERENCE [153], the orbital moments represent a very small correction to the total magnetic moment and consequently underpins our approximation. Likewise, the source of error could also be ascribed to a wrong assignment of the ground-state structures of Co-Mn alloy cluster, but however it is unlikely because the measured value of the magnetic moment [144] in the case of the Co_{20} cluster is about 2.04 μ_B which is very close to our predicted value of 2.00 μ_B.

The negative slope ($\sim$ 6.0 μ_B per Mn substitution) of the SP curve for the bulk CoMn alloy, which is in contrast to the cluster behavior, is explained on the basis of the VBS concept [156], i. e., a resonant scattering of the conduction electrons at the

Table 9.3:
Structural properties of the lowest-energy Co-Mn alloy clusters with $\Omega = 20$. We report the average nearest-neighbor distance for the Co-Co, Mn-Mn, and Co-Mn bondings. The chemical order defined in EQUATION (9.3) is also provided in the last column. The interatomic distances are given in Å.

Cluster	d_{Co-Co}	d_{Mn-Mn}	d_{Co-Mn}	Γ
Co_{20}	2.46			1.00
$Co_{19}Mn_1$	2.39		2.42	0.63
$Co_{18}Mn_2$	2.38	2.51	2.40	0.45
$Co_{17}Mn_3$	2.38	2.31	2.40	0.22
$Co_{16}Mn_4$	2.40	2.39	2.37	0.13
$Co_{15}Mn_5$	2.49	2.43	2.42	0.17
$Co_{14}Mn_6$	2.49	2.43	2.45	0.08
$Co_{13}Mn_7$	2.50	2.46	2.43	0.06
$Co_{12}Mn_8$	2.50	2.46	2.44	0.06
$Co_{11}Mn_9$	2.50	2.45	2.44	0.04
$Co_{10}Mn_{10}$	2.50	2.45	2.44	0.11
Co_9Mn_{11}	2.50	2.45	2.44	0.08
Co_8Mn_{12}	2.49	2.45	2.44	0.08
Co_7Mn_{13}	2.48	2.46	2.45	0.17
Co_6Mn_{14}	2.49	2.46	2.45	0.28
Co_5Mn_{15}	2.48	2.46	2.46	0.28
Co_4Mn_{16}		2.46	2.46	0.39
Co_3Mn_{17}		2.46	2.46	0.55
Co_2Mn_{18}		2.46	2.46	0.72
Co_1Mn_{19}		2.46	2.47	0.84
Mn_{20}		2.46		1.00

Mn sites which induces a narrow peak above the Fermi level for both spin channels. This point was confirmed by *ab initio* band structure calculations [165]. In the case of the Co-Mn alloy clusters, the first attempt to explain the positive slope was also based on the assumption of the existence of a VBS but this time only the majority-spin VBS was conjectured to remain below the HOMO level [152]. However, we can rule out the existence of the VBS and come to the same conclusion if we admit two hypothesis: first, the assumptions of the naive RB model are valid and second, the spin-up d band of the alloy is fully occupied [166]. See, as an example, FIGURE 9.2(a) above. Thus, under these conditions the alloy moment per average atom is given by

$$\langle \mu_{alloy} \rangle = \langle \mu_{host} \rangle - c\Delta Z \mu_B \tag{9.4}$$

where c is the impurity concentration per atom and ΔZ is the atomic number difference of the impurity relative to the host. For Co host doped with Mn impurities, $\Delta Z = -2$ and the slope of the average alloy magnetic moment relative to the host is positive and proportional to 2 μ_B, which is relatively close to the experimental value (1.7 μ_B) and our reported result (1.83 μ_B). The VBS approximation can

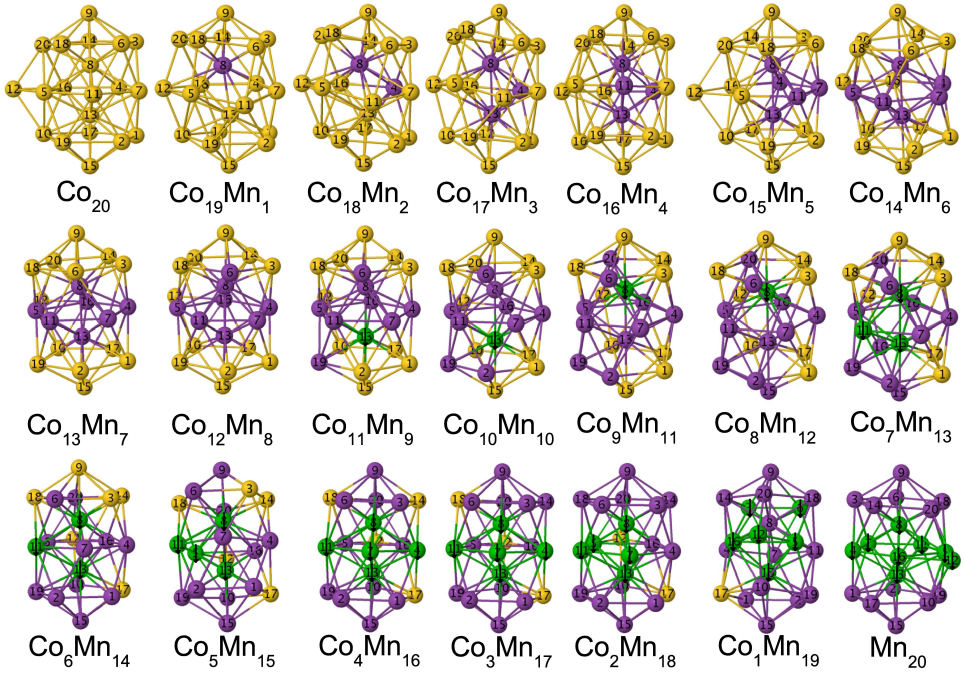

Figure 9.3:
Illustration of the ground-state structures for Co-Mn binary clusters with $\Omega = 20$. Co atoms are shown with yellow spheres whereas Mn atoms are represented with spheres in magenta. The green color represents the Mn atoms that couple antiferromagnetically with the rest of atoms of each cluster.

predict successfully the SP curve behavior in most of the TM solid alloys whereas its application to alloy clusters is less reliable because of the lack of a periodic crystalline lattice [167]. Moreover, the VBS and RB model fail to predict the behavior of the SP curve for Mn concentrations greater than 40 % because they are only valid for small concentrations of impurities.

We have derived a formula for the average magnetic moment of Co-Mn alloys that corrects EQUATION (9.4) and takes into account the antiferromagnetic (AF) coupling between the impurities:

$$\langle \mu_{\text{alloy}} \rangle = m \langle \mu_{\text{Co}} \rangle + (n - g(n)) \left\langle \mu^{\uparrow}_{\text{Mn}} \right\rangle - g(n) \left\langle \mu^{\downarrow}_{\text{Mn}} \right\rangle \tag{9.5}$$

where m and n are the number of Co and Mn atoms in the cluster, respectively, and $g(n)$ is the number of Mn atoms that couple antiferromagnetically with the rest

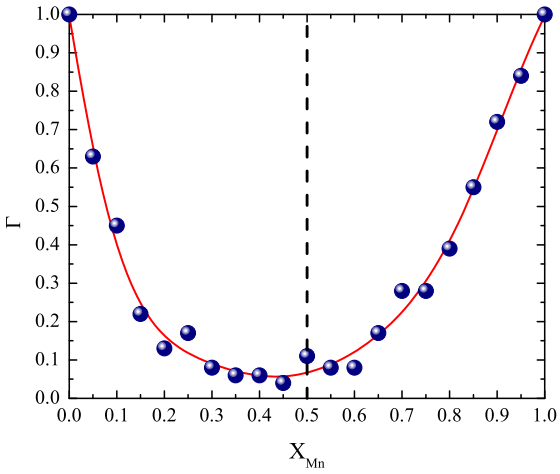

Figure 9.4:
Chemical order parameter as a function of the Mn concentration. The solid line is a polynomial fitting to the numerical values of Γ and serves as a guide to the eye to appreciate the asymmetry of the chemical order parameter with respect to the dash vertical line (midpoint of the Mn concentration).

of atoms[1] (see TABLE 9.4). In FIGURE 9.3, we have also plotted in green the Mn atoms that couple antiferromagnetically to their neighbors. The averaged magnetic moments per atom and per clusters with different Mn compositions obtained from our DFT calculations for Co and Mn atoms are $\langle \mu_{\mathrm{Co}} \rangle = 1.93$, $\left\langle \mu^{\uparrow}_{\mathrm{Mn}} \right\rangle = 3.30$, and $\left\langle \mu^{\downarrow}_{\mathrm{Mn}} \right\rangle = 2.15\ \mu_B/atom$. The values (diamond points) provided by EQUATION (9.5) are plotted in FIGURE 9.5. To gain more insight into the physics behind EQUATION (9.5) and based on the results provided by the electronic structure calculations, we have identified a double mechanism that explains the magnetic enhancement trend for Co-Mn clusters below 40% of Mn concentration and the successive fast dropping of the magnetic moment.

The first mechanism resides in the role played by the Mn atoms, as reflected in EQUATION (9.5). First, the clusters increase their magnetic moments due to the addition of the Mn moments up to a maximum of 2.7 $\mu_B/atom$ and then they decrease their moments because of the AF alignment of some Mn atoms with the rest of atoms belonging to the cluster. We have plotted in FIGURE 9.6 the magnetization density of $Co_{12}Mn_8$ and $Co_{11}Mn_9$ to see how the clusters evolve from a ferromagnetic (FM) configuration to an AF at a critical concentration of the impurity. The red surface surrounding the Mn atom indicates an AF coupling with the rest of atoms while the blue surface indicates a FM alignment. The onset of Mn atoms with negative magnetic moment resides mainly in a Mn-Mn charge transferring. The values of $\mathrm{N}^{\uparrow}_{\mathrm{Mn-Mn}}$ and $\mathrm{N}^{\downarrow}_{\mathrm{Mn-Mn}}$ reported in TABLE 9.4 indicate that

[1]The numerical values of $g(n)$ provided by our DFT calculations are

$$g(n) = \begin{cases} \theta(n-8.5) & 1 \le n \le 12 \\ \theta(n-14.5)+3 & 13 \le n \le 15 \\ 5 - \frac{(n-23)}{24}\Pi_{i=16}^{18}(n-i) & 16 \le n \le 20 \end{cases},$$

where $\theta(n)$ is the Heaviside theta function.

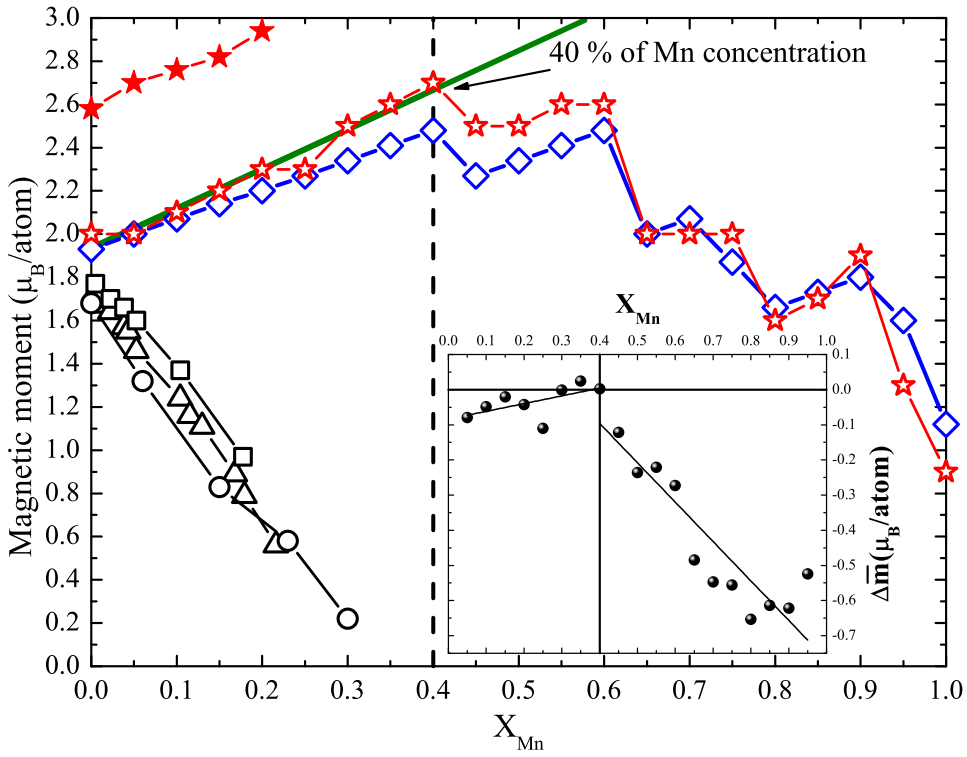

Figure 9.5:
Magnetic moments per atom of Co_mMn_n clusters with $\Omega = 20$ calculated in this work (empty star symbol) and measured in REFERENCE [152] (filled star symbol). The data for the Co-Mn bulk are taken from REFERENCE [163] (△ and □ symbols) and REFERENCE [164] (◯ symbol). The solid line represents the linear fitting of the magnetic moments for the clusters with $n \leq 8$ and it retains a slope of 1.83 μ_B. The diamond points are the expecting magnetic moments according to EQUATION (9.5). The inset represents the difference between the magnetic moments per atom of the Co first neighbors of Mn atoms ($\bar{m}_{alloy}$) in the Co_mMn_n and their Co counterparts ($\bar{m}_{Co_{20}}$) in Co_{20} cluster ($\Delta\bar{m} = \bar{m}_{alloy} - \bar{m}_{Co_{20}}$) as a function of Mn concentration. The linear fitting is a guide to the eye.

the AF Mn atoms are the ones which establish more bondings with the rest of Mn atoms in relation to the FM Mn atoms. To exemplify the explanation, we have plotted in FIGURE 9.7 the spin-polarized DOS for the Mn-13 and Mn-16 atoms of the $Co_{11}Mn_9$ cluster. The Mn-13 atom is coupled antiferromagnetically to the rest of Mn and Co atoms (see FIGURE 9.3). The elevated number of bondings make that the Mn-13 atom share more electrons with its Mn environment. This produces a charge transferring from the spin-up channel of the Mn-13 atom to the spin-up channel of the Mn atoms surrounding it, that is for example the case of Mn-16. Thus, at a critical number of the Mn-Mn bondings (close to 7) the Mn-13 atom becomes antiferromagnetic.

The second mechanism involves also the Co atoms and the "spin-flipping" of the electrons belonging to the Co-Mn bonding. Although the explanation have been

Table 9.4:
Average magnetic moments (in $\mu_B/atom$) and number of Mn atoms [g(n)] that couple antiferromagnetically with the rest of atoms belonging to each cluster of the Co_mMn_n series, and with n ranging from 9 up to 20. The notation $N^{\uparrow}_{Mn-Mn}$ ($N^{\downarrow}_{Mn-Mn}$) represents the average number of nearest neighbor bonds between a FM (AF) Mn atom and the rest of Mn atoms.

n	9	10	11	12	13	14	15	16	17	18	19	20
$\mu^{\downarrow}_{Mn}$	-0.98	-1.11	-1.45	-1.50	-2.39	-2.49	-2.31	-2.73	-2.67	-2.27	-2.97	-2.95
g(n)	1	1	1	1	3	3	4	5	5	5	6	8
$N^{\uparrow}_{Mn-Mn}$	4.6	4.9	4.4	5.1	4.9	5.3	5.1	5.3	5.7	5.9	6.8	6.2
$N^{\downarrow}_{Mn-Mn}$	7.0	8.0	8.0	8.0	8.3	8.7	8.5	8.4	8.8	9.4	7.3	8.8

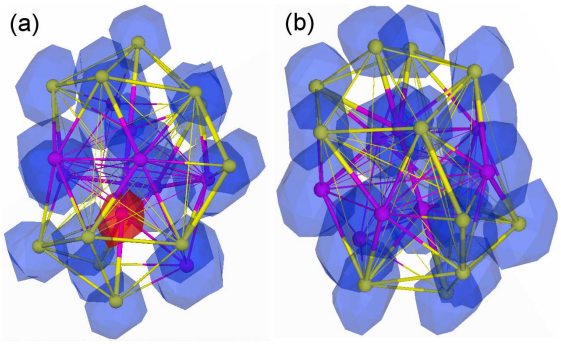

Figure 9.6:
Isosurface plot of the magnetization density ($m(\mathbf{r}) = [\rho^{\uparrow}(\mathbf{r}) - \rho^{\downarrow}(\mathbf{r})]\mu_B$) for (a) $Co_{11}Mn_9$ and (b) $Co_{12}Mn_8$. The Co and Mn atoms are illustrated by the yellow and magenta spheres, respectively. The blue surfaces represent a positive value for the magnetization density whereas the red surface indicates a negative value.

exemplified to the $Co_{18}Mn_2$ cluster, it is applicable to the rest of calculated clusters with $1 \leq n \leq 8$. For these clusters, the DOS of Mn atoms shows a higher-lying occupied bonding orbital for spin-up electrons and a lower-lying (a few eV above HOMO level) empty antibonding orbital for spin-down electrons [see FIGURE 9.2(d)], while for Co first neighbor atoms the DOS manifests an increase of the spin-up population [see FIGURE 9.2(b)]. In consequence, and based on the Mulliken population analysis, the electrons involved in the Co-Mn bonding move from the spin-down channel of Mn atoms to the spin-up channel of the Co first-neighbor atoms. This mechanism contributes to raise the magnetic moment of both Mn and Co neighbor atoms [see inset and text of the caption in FIGURE 9.5]. However, the process stops at a critical concentration of the Mn atoms because the spin-up channel of the available Co atoms does not admit more electrons. Thus, in the range with n varying from 9 to 19, the process reverse and there is a charge transferring from the Mn spin-up channel to the Co neighbors spin-down one. In this case, the Mn and also the Co neighbor atoms [see inset in FIGURE 9.5] decrease their moments.

It is also interesting finally to comment that the nonmonotonic decrease in the magnetic moments at the area above 40 % of Mn concentration (see FIGURE 9.5) is attributed to the discontinuity of g(n) with the concentration of the Mn impurity. Thus, for example, g(n) is equal to 1 in the range $9 \leq n \leq 12$. The average magnetic moments of the AF Mn atoms reported in TABLE 9.4 are approximately constant

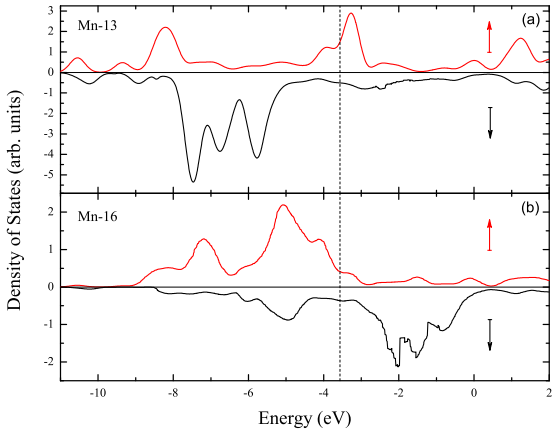

Figure 9.7:
Plot of the spin-polarized DOS for (a) Mn-13 and (b) Mn-16 atom of $Co_{11}Mn_9$ cluster. The upper-half area of figure (a) and (b) is for spin-up electrons while the lower-half area is for spin-down electrons. The dotted vertical line represents the HOMO level.

in this range and consequently the total magnetic moment per atom of the clusters with $9 \leq n \leq 12$ is not reduced. The behavior changes drastically for n=13, where g(13)=3 and $\mu^{\downarrow}_{\mathrm{Mn}-13}$=-2.39 $\mu_B/atom$. The onset of the discontinuity in g(13) and the consequently enhancement of $\mu^{\downarrow}_{\mathrm{Mn}-13}$ causes a reduction in the total magnetic moment of Co_7Mn_{13} cluster. The same kind of explanation still persists for the rest of clusters with higher Mn concentration.

9.4 Conclusions

In summary, the magnetic moment enhancement of Co-Mn clusters below 40% of Mn concentration and its successive fast dropping has been explained using first-principles electronic structure calculations. The explanation resides mainly on the magnetic role played by the Mn atoms and the "spin-flipping" of the electrons belonging to the Co-Mn bonding. Moreover, a new formula [EQUATION (9.5)] has also been proposed for calculating the magnetic moments of the Co-Mn alloy clusters. This equation represents an improvement over the results provided by both the RB model and the VBS approximation.

Part II

Conductivity and Magnetism in Fe/Cr Trilayers

10

Theoretical Model for the Giant Magnetoresistance

> *The methods of theoretical physics should be applicable to all those branches of thought in which the essential features are expressible with numbers.*
>
> — Paul Adrien Maurice Dirac

Synopsis

We present an analytical model for introducing the roughness of the interfaces into giant magnetoresistance along with the electron scattering at the interfaces. In the next Chapters, this model in accordance with the layer potentials provided by our *ab initio* calculations will be used for calculating the conductivity properties of the Fe/Cr trilayer system.

10.1 Introduction

Giant Magnetoresistance (GMR) is a phenomenon consisting in the change of the electrical resistivity which occurs in systems containing magnetic layers separated by a nonmagnetic spacer layer when the magnetic order in magnetic neighboring samples jumps from their antiparallel to their parallel configuration. This effect was originally discovered in Fe/Cr sandwiches[2] and multilayers[1, 168]. In this Chapter, we focus on extending the Hood and Falicov model [169] by introducing the roughness and the electron scattering at the interfaces. Thus, in Section 10.2 we introduce the Boltzmann's transport equation along with the boundary conditions and the roughness characteristics of the latter equation in Section 10.3. Finally, we calculate the conductivity of the considered system in Section 10.4.

10.2 Boltzmann's Transport Equation

In order to calculate the conductivity distribution, we write the Boltzmann's equation as

$$v^z \frac{\partial g^\alpha_{\mu\sigma}(v,z)}{\partial z} + \frac{\partial f^0_{v\sigma}(v)}{\partial v^\alpha} = -\frac{g^\alpha_{\mu\sigma}(v,z)}{\tau_{\mu\sigma}} - \frac{g^\alpha_{\mu\sigma}(v,z) - g^\alpha_{v\,-\sigma}(v,z)}{\tau_{\mu\uparrow\downarrow}} \tag{10.1}$$

where $g^\alpha_{\mu\sigma}$ is the function to be determined, $f^0_{\mu\sigma}$ the equilibrium Fermi-Dirac distribution, which is homogeneous across the layers μ (in our case a trilayer, so $\mu = 1, 2, 3$), and $\alpha = x, z$[1]. The collision term consists of two parts: the first is the ordinary term where $\tau_{\mu\sigma}$ stands for the relaxation time associated with the electrons of spin σ in layer μ and the additional term is proportional to the difference between the electron density for two opposite orientations of spins divided by the reorientation relaxation time denoted by $\tau_{\mu\uparrow\downarrow}$. For low-temperature processes, it is reasonable to assume that this last term is mainly linked to the roughness of the interfaces.

After some analysis, we obtain the solution

$$g^{\alpha\pm}_{\mu\sigma}(v,z) = B^{\alpha\pm}_{\mu\sigma}\left[1 - F^\pm_{\mu\sigma}(v) e^{\frac{-q^\pm_\mu z}{v_z}}\right], \tag{10.2}$$

where + (-) stands for $v^z \geq 0$ ($v^z < 0$),

$$q^\pm_\mu = \frac{1}{2}\left[\left(\frac{1}{\tau_{\mu\uparrow}} + \frac{1}{\tau_{\mu\downarrow}} + \frac{2}{\tau_{\mu\uparrow\downarrow}}\right) \pm \sqrt{\left(\frac{1}{\tau_{\mu\uparrow}} - \frac{1}{\tau_{\mu\downarrow}}\right)^2 + \left(\frac{2}{\tau_{\mu\uparrow\downarrow}}\right)^2}\right], \tag{10.3}$$

$$B^{\alpha\pm}_{\mu\sigma} = \frac{\frac{\partial f^0_{\mu\sigma}}{\partial v_\alpha} + a_{\mu\sigma}\frac{\partial f^0_{\mu-\sigma}}{\partial v^\alpha}}{\tau^*_{\mu-\sigma} q^+_\mu q^-_\mu}, \tag{10.4}$$

$$F^\pm_{\mu\sigma} = 1 - \frac{C}{B^{\alpha\pm}_{\mu\sigma}}, \tag{10.5}$$

and where $\tau^*_{\mu\uparrow\downarrow} = \tau_{\mu\uparrow\downarrow}\frac{g^0_{\mu\sigma}}{g^0_{\mu-\sigma}}$, while C is a integration constant, and using the Matthiessen's rule, i.e., assuming a mixing independent mechanism for the spin currents, we have

$$\frac{1}{\tau^*_{\mu\sigma}} = \frac{1}{\tau_{\mu\sigma}} + \frac{1}{\tau_{\mu\uparrow\downarrow}}, \tag{10.6}$$

[1] We assume that the conductivity properties along the x and y directions are the same due to the symmetry of the multilayers

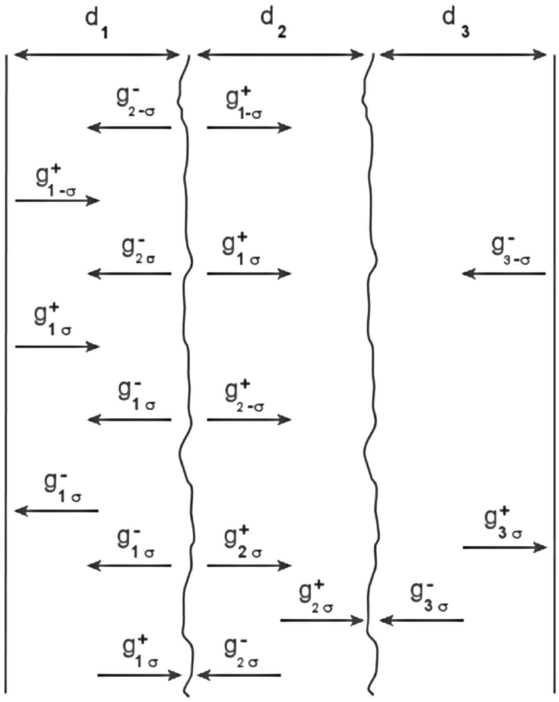

Figure 10.1:
Diagram of the boundary conditions.

so that the parameter

$$a_{\mu\sigma} = \frac{\tau^*_{\mu-\sigma}}{\tau_{\mu\uparrow\downarrow}} \frac{m_{\mu\sigma}}{m_{\mu-\sigma}} \tag{10.7}$$

is a function of the effective masses $m_{\mu\sigma}$ and $m_{\mu\,-\sigma}$.

10.3 Boundary Conditions and Roughness Characteristics

Let us now introduce the boundary conditions for solving explicitly the above equations, including the roughness at the interfaces (see FIGURE 10.1).

At the outer surfaces, we have

$$g^{\alpha+}_{1\sigma} = P_{\alpha\sigma} g^{-}_{1\sigma} + \bar{P}_{\alpha-\sigma} g^{-}_{1-\sigma} \quad at \;\; z = 0, \tag{10.8}$$

and

$$g^{\alpha-}_{3\sigma} = P_{\beta\sigma} g^{+}_{3\sigma} + \bar{P}_{\beta-\sigma} g^{+}_{3\sigma} \quad at \;\; z = d. \tag{10.9}$$

The specular factors $P_{\alpha\sigma}$ and $P_{\beta\sigma}$ take values between 0 and 1, which give completely diffusive or specular scattering at these surfaces, respectively. Moreover, $P_{\alpha\sigma} + \bar{P}_{\alpha-\sigma} = P_\alpha$ and $P_{\beta\sigma} + \bar{P}_{\beta-\sigma} = P_\beta$. At the interfaces A and B, the boundary

conditions introduced [169] for the Boltzmann's distribution $g^{\alpha}_{\mu\sigma}(v,z)$ describe the reflection R and transmission T coefficients given by

$$R^{\sigma}_{\nu\mu}(v,v^z) = \left|\frac{1-h^{\sigma}_{\nu\mu}(v,v^z)}{1+h^{\sigma}_{\nu\mu}(v,v^z)}\right|^2 \tag{10.10}$$

and

$$T^{\sigma}_{\nu\mu}(v,v^z) = \frac{4\,\mathrm{Re}\,h^{\sigma}_{\nu\mu}(v,v^z)}{|1+h^{\sigma}_{\nu\mu}(v,v^z)|} = 1 - R^{\sigma}_{\nu\mu}, \tag{10.11}$$

where Re means the real part of the function

$$h^{\sigma}_{\nu\mu} = \frac{\left[\frac{E-V_{\nu\sigma}}{E-V_{\mu\sigma}} - \sin^2\theta\right]^{1/2}}{\cos\theta}, \tag{10.12}$$

with ν and μ being the two layers and θ the angle of incidence, measured with respect to the z axis of an electron of energy $E = \frac{1}{2}m_{\nu\sigma}v^2 + V_{\nu\sigma}$ in layer ν with spin σ and velocity v, moving in a constant potential $V_{\nu\sigma}$. This potential will be calculated from *ab initio* methods in the next Chapters. Assuming reversibility of the trajectories, we have the condition

$$\frac{\sin\theta_{\nu}}{\sin\theta_{\mu}} = \left[\frac{E-V_{\mu\sigma}}{E-V_{\nu\sigma}}\right]^{1/2}. \tag{10.13}$$

The boundary conditions at the interfaces are shown in Figure 10.1, where we have represented the interdiffusion region with the roughness characterized by the functions $\zeta_{1,2}(x,y)$, which are, in general, unknown and may be written in their Fourier representation as

$$\zeta(x,y) = \sum_{k,l} a_{k,l}(\cos(\omega x))^k(\cos(\omega y))^l, \tag{10.14}$$

where a_{kl} and ω are parameters characterizing the roughness [170]. These parameters can be determined independently by experimental techniques, such as the scanning tunneling microscopy. The average value $\langle\zeta(x,y)=0\rangle$, with respect to x and y, extends over the whole surface. The average value $\langle\zeta^2(x,y)\rangle = \zeta_0^2$ is then a very convenient statistical parameter of the theory. The local distances are given by $z_1 = d_1 + \zeta_1(x+y)$ and $z_2 = d_1 + d_2 + \zeta_2(x+y)$, and the boundary conditions at such surfaces are:

$$
\begin{aligned}
g^-_{1\sigma} =& S_{A\sigma}R_{12\sigma}g^+_{1\sigma} + S_{A\sigma}T_{21\sigma}g^-_{2\sigma} + \bar{S}_{A-\sigma}R_{12-\sigma}g^+_{1-\sigma} + \bar{S}_{A-\sigma}T_{21-\sigma}g^-_{2-\sigma},\\
g^+_{2\sigma} =& S_{A\sigma}R_{21\sigma}g^-_{2\sigma} + S_{A\sigma}T_{12\sigma}g^+_{1\sigma} + \bar{S}_{A-\sigma}R_{21-\sigma}g^-_{2-\sigma} + \bar{S}_{A-\sigma}T_{12-\sigma}g^+_{1-\sigma}\\
& at\ \ z = d_1 + \zeta_1(x,y);\\
g^-_{2\sigma} =& S_{B\sigma}R_{23\sigma}g^+_{2\sigma} + S_{B\sigma}T_{32\sigma}g^-_{3\sigma} + \bar{S}_{B-\sigma}R_{23-\sigma}g^+_{2-\sigma} + \bar{S}_{B-\sigma}T_{32-\sigma}g^-_{3-\sigma},\\
g^+_{3\sigma} =& S_{B\sigma}R_{32\sigma}g^-_{3\sigma} + S_{B\sigma}T_{23\sigma}g^+_{2\sigma} + \bar{S}_{B\sigma}R_{32-\sigma}g^-_{3-\sigma} + \bar{S}_{B-\sigma}T_{23-\sigma}g^+_{2-\sigma}\\
& at\ \ z = d_1 + d_2 + \zeta_2(x,y).
\end{aligned}
$$

The parameters $S_{A\sigma}$ and $\bar{S}_{A\ -\sigma}$ are connected via the polarizability of the surface, i.e., $\bar{S}_{A\ -\sigma} = p_A S_{A\sigma}$ (the same is for $S_{B\sigma}$ and $\bar{S}_{B-\sigma}$) and they are factors that indicate the degree of electron scattering at interfaces A and B for spin σ and $-\sigma$. The polarizability factor can be measured experimentally by techniques, such as the *spin-polarizability low-energy electron diffraction* (SPLEED).

From Equation (10.2), we see that the averaging procedure involves the factors

$$
R^A_{\nu\sigma}(\zeta_1) = \langle e^{\frac{\mp q^{\pm}\zeta_1}{v^z}} \rangle;\ R^B_{\nu\sigma}(\zeta_2) = \langle e^{\frac{\mp q^{\pm}\zeta_2}{v^z}} \rangle \tag{10.15}
$$

with respect to the (x,y) plane. Using a series expansion, we have

$$
R^{AB}_{\nu\sigma}(\zeta_1,\zeta_2) = \sum_{k=0}^{\infty} \frac{1}{k!} \left(\frac{\mp q^{\pm}_{\nu}}{v^z} \right)^k \langle \zeta_1, \zeta_2 \rangle, \tag{10.16}
$$

where $\langle \zeta_1^{2k+1}, \zeta_2^{2k+1} \rangle = 0$ is expected, while $\langle \zeta_1^{2k}, \zeta_2^{2k} \rangle$ determine the roughness character. Notice that the particular case $\langle \zeta_1^{2k}, \zeta_2^{2k} \rangle = (\langle \zeta_1^2, \zeta_2^2 \rangle)^k$ determines a Gaussian stochastic distribution, which is the usual case used, and has the polarization parameter $\langle \zeta_1^2, \zeta_2^2 \rangle = \zeta_0^2$.

10.4 Calculation of the Conductivity

The current density along the electric field E^{α} in each layer μ for electrons with spin σ is given by [169]

$$
J^{\alpha}_{\mu\sigma}(z) = -|e| \left(\frac{m_{\mu\sigma}}{h} \right)^3 \int_v v^{\alpha} f_{\nu\sigma}(v, z; E^{\alpha}) d^3v, \tag{10.17}
$$

where h is Planck's constant, $|e|$ the electric charge, $m_{\mu\sigma}$ the effective mass and $f_{\mu\sigma}(v, z; E^{\alpha})$ the Boltzmann's distribution function, which can be written as

$$
f_{\mu\sigma}(v, z; E^{\alpha}) = f^0_{\mu\sigma}(v) - \frac{|e|E^{\alpha}}{m_{\mu\sigma}} g^{\alpha}_{\mu\sigma}(v, z), \tag{10.18}
$$

when $E^{\alpha} \to 0$. From the ohmic law, we obtain the conductivity

$$\sigma^{\alpha}_{\mu\sigma}(z) = \frac{e^2}{m_{\mu\sigma}} \left(\frac{m_{\mu\sigma}}{h}\right)^3 \int v^{\alpha} g^{\alpha}_{\mu\sigma}(v,z). \tag{10.19}$$

In cylindrical coordinates, we have $d^3v = \bar{v}d\bar{v}d\phi dv^z$, where $\bar{v}^2 + (v^z)^2 = v^2$ and $d\varepsilon = m_{\mu\sigma}\bar{v}d\bar{v}$, assuming $\varepsilon = \frac{1}{2}m_{\mu\sigma}v^2 + V_{\mu\sigma}$. Thus,

$$d^3v = \frac{d\varepsilon}{m_{\mu\sigma}} d\phi v du \tag{10.20}$$

and

$$\begin{aligned}\sigma^{\alpha}_{\mu\sigma}(z) =& \frac{e^2}{m^2_{\mu\sigma}} \left(\frac{m_{\mu\sigma}}{h}\right)^3 \times \\ & \int v^{\alpha} v \frac{\left(m_{\mu\sigma}\frac{\partial f^0_{\mu\sigma}}{\partial\varepsilon} + m_{\mu-\sigma}a_{\mu\sigma}\frac{\partial f^0_{\mu-\sigma}}{\partial\varepsilon}\right)v^{\alpha}}{\tau^*_{\mu-\sigma}(q^+_{\mu}q^-_{\mu})} \times \\ & \left[1 - F^{\pm}_{\mu\sigma}(v,u)e^{\frac{q^{\pm}_{\mu}z}{vu}}\right] du d\phi d\varepsilon,\end{aligned} \tag{10.21}$$

where $u = \frac{v^z}{v}$. Giving that the derivative, with respect to the energy, of the equilibrium Fermi-Dirac distribution is

$$\frac{\partial f^0_{\mu\sigma}}{\partial\varepsilon} = \delta(\varepsilon - \varepsilon_{F_{\mu\sigma}}), \tag{10.22}$$

we obtain

$$\begin{aligned}\sigma^{x}_{\mu\sigma} =& \frac{e^2}{m^2_{\mu\sigma}} \left(\frac{m_{\mu\sigma}}{h}\right)^3 \times \\ & \int_{-1}^{1} \pi v^3_{F_{\mu\sigma}}(1-u^2)B^{\alpha\pm}_{\nu\sigma}\left[1 - F^{\pm}_{\mu\sigma}(v_{F_{\mu\sigma}},u)e^{\frac{q^{\pm}_{\mu}z}{v_{F_{\mu\sigma}}u}}\right] du,\end{aligned} \tag{10.23}$$

and

$$\sigma^{z}_{\mu\sigma} = \frac{e^2}{m^2_{\mu\sigma}} \left(\frac{m_{\mu\sigma}}{h}\right)^3 \int_{-1}^{1} 2\pi v^3_{F_{\mu\sigma}} u^2 B^{\alpha\pm}_{\nu\sigma}\left[1 - F^{\pm}_{\mu\sigma}(v_{F_{\mu\sigma}},u)e^{\frac{q^{\pm}_{\mu}z}{v_{F_{\mu\sigma}}u}}\right] du, \tag{10.24}$$

where $v_{F_{\mu\sigma}}$ is the Fermi velocity.

11

Ab-initio Calculations of Magnetic Properties of Fe-Cr Trilayer as a Function of Ferromagnetic Slab Thickness

> *There are two possible outcomes: if the result confirms the hypothesis, then you've made a measurement. If the result is contrary to the hypothesis, then you've made a discovery.*
>
> — Enrico Fermi

Synopsis

Most of the articles devoted to the giant magnetoresistance phenomenon take into account only the thickness variation of the spacer. Within this work, we study the magnetic behavior on the trilayer system Fe/Cr/Fe (0 0 1) after changing the thickness of the magnetic layers (Fe layers) and keeping the spacer constant (Cr layers). The calculations were done at the *ab initio* level by means of density functional theory, solving the Kohn-Sham equations with the full-potential linearized augmented plane-wave method. These results show an oscillatory behavior of magnetic moment per atom as a function of the iron monolayers number.

11.1 Introduction

Progress in thin-film fabrication techniques has made possible, only quite recently, the construction of thin magnetic transition metal layers, separated by very thin nonmagnetic layers (known as spacers), to form sandwiches, or superlattices. The multilayer system Fe/Cr/Fe has played a fundamental role because of the giant

magnetoresistance (GMR) phenomenon that was discovered in it [1]. The fundamental theoretical explanation for this effect can be understood within the Mott two-current model for electrical conductivity in metals [171]. This model considers the total conductivity as the sum of separate contributions from spin-up and spin-down electrons, giving us two magnetic channels for conduction. The model assumes an interaction of the spin-dependent scattering [172] of the conduction electrons with the parallel or antiparallel alignment of magnetic moments in adjacent magnetic layers. As a consequence of this fact, the resistivity is strongly dependent with the magnetic configurations at the interfaces.

The control of the spacer thickness with great accuracy, keeping constant the width of the magnetic layers, was the main preoccupation of the experimental physicists for a long time, because they thought that this factor was the important one. The variation of the thickness of the magnetic layers remained without experimental values until quite recently [173].

In this Chapter, we present an explicit demonstration of how the magnetic layer thickness changes the magnetism at the interfaces in an important way. What is very appealing to note is that we obtain an oscillating magnetic behavior directly from the atomic interaction calculated with *ab initio* techniques and without invoking the Ruderman-Kittel-Kasuya-Yosida (RKKY) model, which is the usual accepted physical picture for explaining the magnetic coupling in itinerant magnetism relevant to the GMR effect.

11.2 Computational Details

Ab initio electronic structure calculations were performed within the framework of density functional theory in the local spin density approximation. The exchange-correlation potential was used in the form of Vosko, Wilk and Nusair [34]. This method is extremely advantageous for computing the electronic structure of magnetic multilayers, because it was designed to take into account the slab geometry and the interaction between the outer layer of the multilayer system and vacuum. The Kohn-Sham equations were solved using the full-potential linearized augmented plane-wave (LAPW) method in slab geometry [174, 175]. The valence states were calculated in a scalar-relativistic approximation. A grid of 15 **k**-points in an irreducible wedge of the 2D Brillouin zone (BZ) was used during the iterations, and 45 **k**-points for the last iteration. Inside the muffin-tin (MT) spheres, basis functions with angular momentum components up to l=8 were included. The charge density and potential within the MT spheres were expanded into the lattice harmonics with an angular momentum up to l=6. More than 60 augmented plane waves per atom were used for variational basis set. Calculations were carried out for the slab consisting of three monolayers of Cr (0 0 1) and a variable number of monolayers ($1 \leq N \leq 7$) for Fe. The lattice constant for Fe and Cr was assumed to be Cr bulk-like,

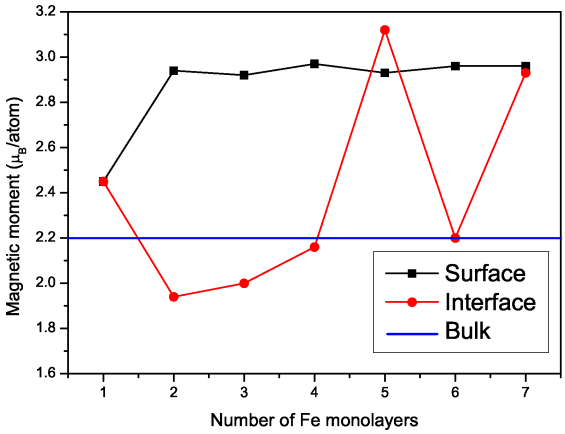

Figure 11.1:
Evolution of the surface (squares) and interface (circles) Fe magnetic moment with the increase of the Fe film thickness.

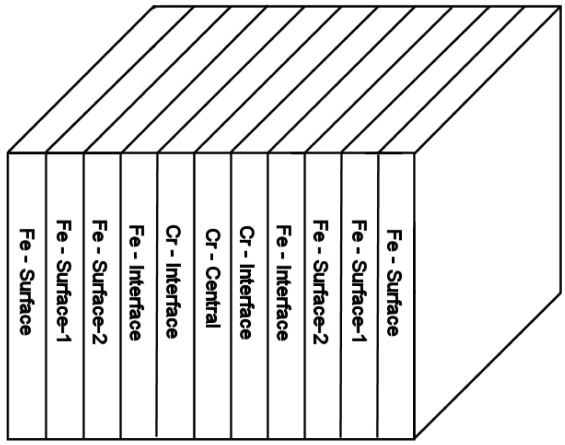

Figure 11.2:
NFe/3Cr/NFe general configuration picture.

i.e., a_0=5.44 a.u.. The reason for making such a choice was that we have seen very small difference in the results when different values were used.

11.3 Results and Discussion

Density functional calculations using the LAPW method were done for the NFe/3Cr/-NFe system with $1 \leq N \leq 7$ (N denotes the number of monolayers). The main results of the current CHAPTER are contained in TABLES 11.1, 11.2, and FIGURE 11.1. For the sake of notation, a brief comment on TABLES 11.1 and 11.2 is required to be understood: **Fe-Interface** stands for the monolayer of Fe which is closest to a Cr monolayer; **Cr-Interface** denotes the monolayer of Cr that is closest to a Fe monolayer; **Cr-Central** is the central monolayer of the Cr slab, that is, the second of the three Cr monolayers; **Fe-Surface** stands for the external monolayer of the Fe film; and **Fe–Surface-1**, **Fe–Surface-2**, **Fe–Surface3**, ..., are the corresponding monolayers inside the Fe slab. To clarify more precisely this nomenclature, see FIGURE 11.2.

Table 11.1:
DOS at Fermi energy level and magnetic moment for N = 5, 7. ML stands for monolayer.

Layer	Magnetic moment (μ_B)	DOS (E_F) majority spin	DOS (E_F) minority spin
Fe(5 ML)–Surface	2.93	0.17	2.50
Fe(5 ML)–Surface-1	2.35	0.27	0.92
Fe(5 ML)–Surface-2	2.41	0.39	0.29
Fe(5 ML)–Surface-3	1.79	0.48	0.79
Fe(5 ML)–Interface	3.12	0.32	0.21
Cr(5 ML)–Interface	-0.94	0.52	0.45
Cr(5 ML)–Central	0.64	0.20	0.14
Fe(7 ML)–Surface	2.96	0.17	2.70
Fe(7 ML)–Surface-1	2.24	0.46	0.44
Fe(7 ML)–Surface-2	2.29	0.47	0.22
Fe(7 ML)–Surface-3	2.21	0.52	0.37
Fe(7 ML)–Surface-4	2.27	0.62	0.13
Fe(7 ML)–Surface-5	1.77	0.55	0.32
Fe(7 ML)–Interface	2.93	0.50	0.14
Cr(7 ML)–Interface	-0.75	0.51	0.25
Cr(7 ML)–Central	0.50	0.49	0.46

First, we describe briefly the computational results obtained following the LAPW method. Having a look at FIGURE 11.1, we can appreciate that the magnetic moment on the interface depends on the thickness of the Fe layers and exhibits oscillatory behavior with the increase of the Fe layer number (circles in FIGURE 11.1). However, the magnetic moment on the surface of bulk has a quasilinear behavior as a function of N, if we do not take into account the special case N=1. In fact, the bulk magnetic moment value is 2.25 μ_B (solid line in FIGURE 11.1), and the surface magnetic moment data give us a mean value of $2.95 \pm 0.02\mu_B$. The small size of the standard deviation (0.02 μ_B) confirms the quasi-linear behavior of the surface magnetic moment just noted. The first point that is remarkable to discuss is the comparison between the surface and bulk magnetic moment. The fact that the surface magnetic moment (2.95 μ_B) is greater than the bulk value (2.25 μ_B) is not surprising. The increase is due to the surface atoms having a lower coordination number than those of the bulk and reduced symmetry as well. There is a surface-induced d-band narrowing, so that one would expect a higher density of states (DOS) at the Fermi level, as shown in TABLES 11.1 and 11.2, for example, for N=7 the total DOS(E_F) is 2.87 on Fe(7ML)–Surface, nevertheless from Fe(7ML)–Surface-1 to Fe(7ML)–Surface-5, the total DOS(E_F) is 0.90, 0.69, 0.89, 0.75, and 0.87, respectively. The second outstanding feature in FIGURE 11.1 is the magnetic moment interface oscillation involving the large values for N=5 and 7. A complete discussion of this behavior can be found in REFERENCE [176]. That reference states that the large magnetic moment is mainly due to resonances with a high degree

Table 11.2:
DOS at Fermi energy level and magnetic moment for N = 1, 2, 3, 4, and 6. ML denotes monolayer.

Layer	Magn. Moment (μ_B)	DOS (E_F) majority spin	DOS (E_F) minority spin
Fe(1 ML)–Interface	2.45	0.54	3.76
Cr(1 ML)–Interface	-0.62	0.95	0.50
Cr(1 ML)–Central	0.62	0.63	0.94
Fe(2 ML)–Surface	2.94	0.13	2.88
Fe(2 ML)–Interface	1.94	0.39	0.64
Cr(2 ML)–Interface	-0.47	0.81	0.83
Cr(2 ML)–Central	0.35	0.33	0.50
Fe(3 ML)–Surface	2.92	0.14	2.12
Fe(3 ML)–Surface-1	2.43	0.15	0.62
Fe(3 ML)–Interface	2.00	0.32	0.44
Cr(3 ML)–Interface	-0.75	0.53	0.40
Cr(3 ML)–Central	0.71	0.21	0.23
Fe(4 ML)–Surface	2.97	0.17	2.32
Fe(4 ML)–Surface-1	2.27	0.28	0.34
Fe(4 ML)–Surface-2	2.49	0.26	0.57
Fe(4 ML)–Interface	2.16	0.34	0.53
Cr(4 ML)–Interface	-0.5	0.89	0.63
Cr(4 ML)–Central	0.50	0.25	0.4
Fe(6 ML)–Surface	2.96	0.08	1.72
Fe(6 ML)–Surface-1	2.25	0.23	0.36
Fe(6 ML)–Surface-2	2.41	0.38	0.28
Fe(6 ML)–Surface-3	2.25	0.41	0.34
Fe(6 ML)–Surface-4	2.34	0.28	0.21
Fe(6 ML)–Interface	2.20	0.26	0.47
Cr(6 ML)–Interface	-0.65	0.49	0.25
Cr(6 ML)–Central	0.58	0.52	0.48

of localization in the interface layer introduced by quantum-well states. Moreover, the oscillating behavior on the Fe layer interface is conditioned by the creation of quantum-well states.

Next, we connect our computational results with the GMR effect, treating in particular how the calculated parameters (DOS, magnetic moment, ...) enable deductions about the GMR effect, only at least qualitatively. Our density of states calculations show that there is an oscillatory magnetic behavior on the Fe/Cr interfaces, as we commented before. This oscillation is due partly to the thickness of the Fe layers, as we demonstrate below, because it is necessary to consider the superposition of the magnetism of the Fe and Cr under thickness changes, which could be examined with a physical model as RKKY. For N=5, 7 we have a special behavior on the Fe/Cr interface (see Figure 11.3 and Table 11.1), which deserves more detailed comment. The first characteristic that we obtain, different from what

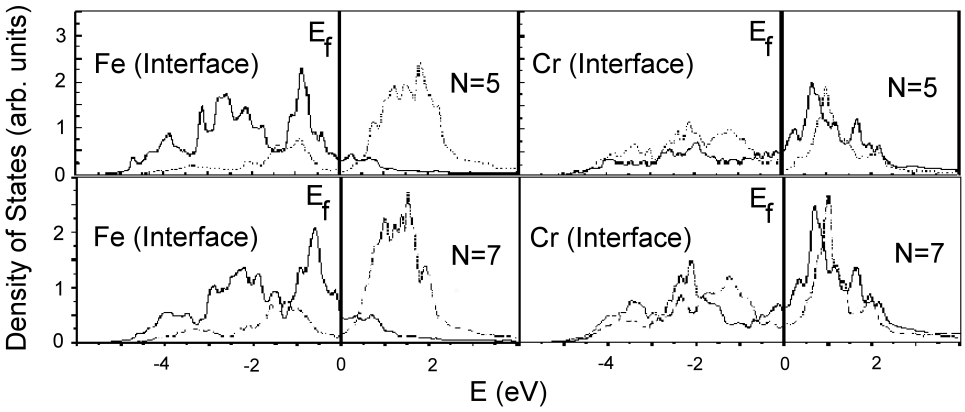

Figure 11.3:
Density of States for Fe-Interface with N=5 and 7. Solid and dashed lines mean majority and minority spin, respectively.

happens for N=1, 2, 3, 4, and 6 is that we see how the majority spins are the main contribution at the Fermi level. Notice that the DOS(E_F) minority spin for N=1, 2, 3, 4, and 6 has the corresponding values 3.76, 0.64, 0.44, 0.53, and 0.47, respectively. For N=5, 7 the corresponding values are 0.21 and 0.14, respectively. As can be inferred, these values are much lower than the previous ones (see FIGURE 11.4). We observe that the minority spin channels are very small for these special cases in comparison with the ones seen above. In fact, the lowest value for N=1, 2, 3, 4, and 6 is 0.44, which is 50 % lower than the highest value for N=5, 7 which is 0.21. In FIGURE 11.4, we can see clearly the criteria employed to consider the magnetic channels to be insignificant for N=5, 7. The second feature to examine is the fact that the magnetic moment per atom on the interface increases very strongly for these two cases N=5, 7. The underlying reason that explains this, is related not only to iron layer thickness but also to the contribution of the induced magnetism in the chromium layer. We must remark that chromium is a quite special transition metal which exhibits an itinerant antiferromagnetic order in body-centered cubic (bcc) crystalline symmetry structure (see REFERENCE [177]). The negative Cr magnetic moment is due to the antiferromagnetic behavior of chromium, with oscillations in the direction (001). Moreover, we have found that the state with an alignment opposite that of Cr and Fe magnetic moments has a smaller energy. On the interface we can see in TABLES 11.1 and 11.2 that the chromium induces an oscillating magnetic moment per atom whose values are -0.62, -0.47, -0.75, -0.50, -0.94, -0.65, and -0.75 μ_B for $1 \leq N \leq 7$ layers, respectively. For the iron magnetic moment, we can see that the values are 2.45, 1.94, 2.00, 2.16, 3.12, 2.20, and 2.93 μ_B, which also oscillate but with a very different shape (see FIGURE 11.5). The addition of both oscillations gives the total magnetic moment on the interface, which also oscillates, as we can see in FIGURE 11.5. This fact confirms the outstanding role of

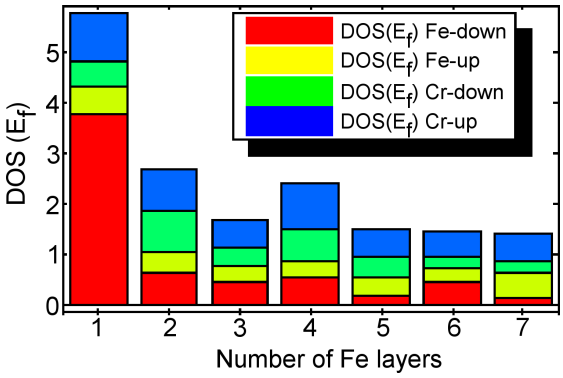

Figure 11.4:
Density of States at the Fermi level for Fe-Interface and Cr-Interface.

Cr in the magnetism of Fe, helping us to understand (if we observe how the DOS behaves for both kind of atoms on the interface) that the interlayer coupling constant J for Fe/Cr is much higher than the other multilayers made with nonmagnetic transition metals, such as Fe/Ag, Fe/Au, Fe/Cu or Fe/Al (see Reference [178]). Taking into account the last comments, our DOS calculations show that there is essentially only one magnetic channel on the iron-chromium interface for N=5, 7 (see Figure 11.2 and Table 11.1) and a very high increase of the magnetism on its interfaces, being the other channel quasiequal to zero, the one of the minority spin density. Nevertheless, for N=1, 2, 3, 4, and 6 we obtain both kind of magnetic polarizations: up and down (see Figure 11.6 and Table 11.2). This situation is very interesting for the GMR effect if we accept that this phenomenon is mainly due to the scattering of the electrons on these interfaces, i.e., the spin-polarized electrons, on the one hand, enhance their velocity when they find the magnetic polarizability of the impurity parallel to the magnetic layer. On the other hand, the spin-polarized electrons diminish their velocity when they find the polarizability in opposite direction. Therefore, we have a spin valve effect in which there is a selection of one of the two possible magnetic channels, and this drives a decrease or an increase of the conductivity [172], depending on whether the electrons are parallel or antiparallel to the magnetic polarization of the interface.

Following the spirit of Zahn *et al.* [179] or the monographic in Reference [180], it would be possible to calculate the GMR from the *ab initio* techniques, using the data discussed above. Within the Boltzmann mechanism, once the density of states is determined, the conductivity may be calculated when the relaxation time for the scattered electrons is known. This task is studied more in detail in Chapter 13.

11.4 Conclusions

In summary, we have shown at *ab initio* level that the variation of the number N of Fe atomic layers (thickness of Fe layers) induces an oscillating magnetic moment on the interface of the multilayer system Fe/Cr/Fe. For N=5 and 7, we obtain a

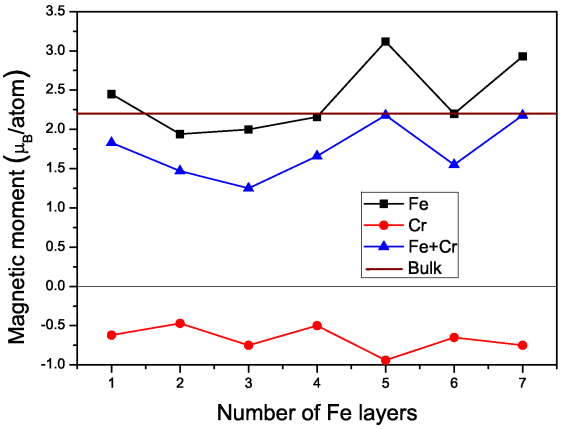

Figure 11.5:
Magnetic moment as a function of the Fe layer number on Fe-Interface and Cr-Interface.

great enhancement of the magnetic moment at the interface. This oscillation creates parallel or antiparallel orientations of the magnetic moments with respect to the conduction electrons when a difference of potential is introduced, and this gives a very different resistivity depending on the magnetic structure of the system. This has an immediate application to the GMR of this multilayer material.

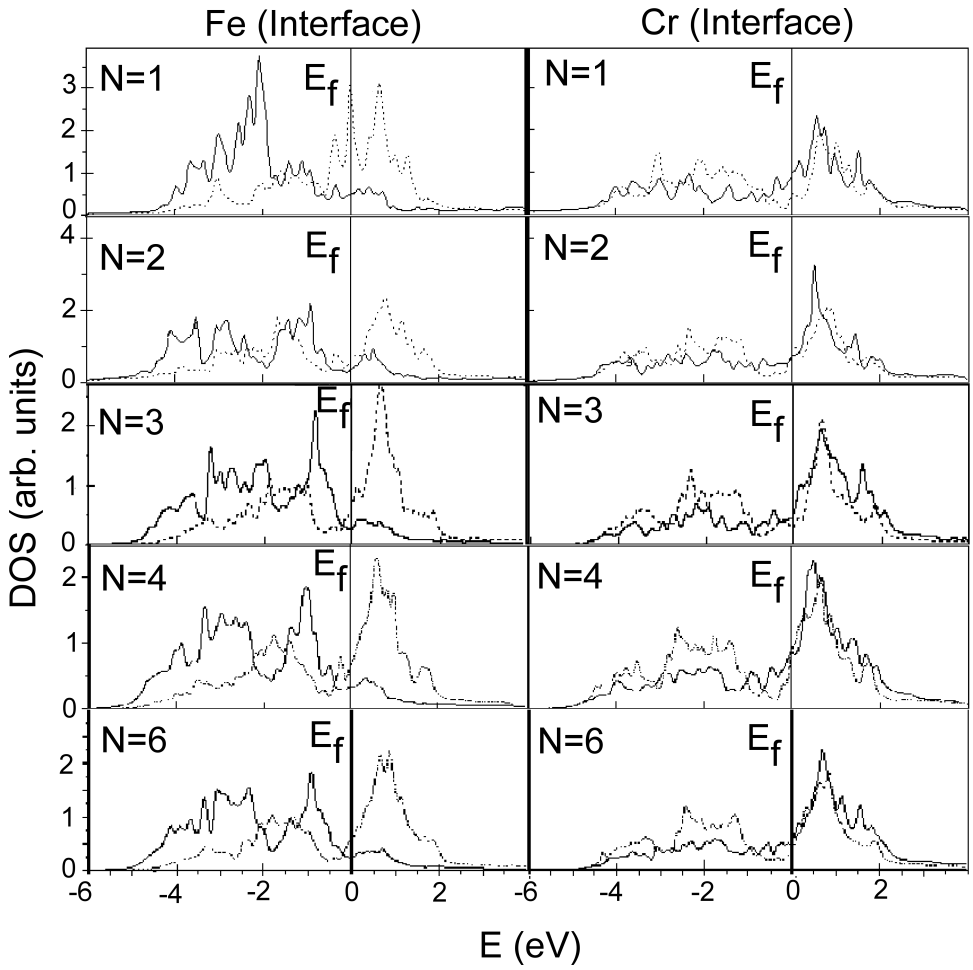

Figure 11.6:
Density of States for Fe-Interface and Cr-Interface with N=1,2,3,4, and 6. Solid and dashed lines mean majority and minority spin, respectively.

12

Influence of Interfacial Scattering and Surface Roughness on Giant Magnetoresistance in Fe/Cr Trilayers using *ab initio* Layer Potentials

> *Nobody will deny that there is at least some roughness everywhere.*
>
> — Benoit Mandelbrot

Synopsis

Ab initio full-potential linearized augmented plane-wave (FP-LAPW) method combined with the semiclassical Boltzmann formalism was employed to calculate the giant magnetoresistance ratio in the trilayers nFe/3Cr/nFe ($1 \leq n \leq 8$). The present results emphasize the very important role of the ferromagnetic layer as well as the interfacial scattering and surface roughness on the giant magnetoresistance effect.

12.1 Introduction

The discovery of giant magnetoresistance (GMR) effects in Fe/Cr multilayers has triggered a large number of studies on the transport properties of magnetic multilayers. In spite of many experimental and theoretical investigations, the description of the phenomenon is not completed and makes a challenge for many researches. The GMR in multilayers occurs inside a layered structure made of ferromagnetic layers sandwiched between nonmagnetic layers (spacers) and stacked along the direction orthogonal to the layer planes. Control of the spacer thickness with great accuracy, keeping constant the width of the magnetic layers, was the main preoccupation of experimentalists for a long time ago, but the variation of the ferromagnetic layer

thickness (FLT) and its interest on giant magnetoresistance had remained without experimental values until quite recently [181]. This fact is understandable because most of these experiments were suggested by the existing models of the interaction between magnetic layers [182], where the FLT is in most cases assumed as constant. Thus, only a few number of theoretical publications have explored the influence of the variation of the FLT in GMR: first-principles [183] or tight-binding models [184] and Heisenberg type Hamiltonians [185]. Unfortunately, the role of the interfacial scattering or even the surface roughness has been omitted in the publications mentioned above for the Fe/Cr system. In this CHAPTER, however we present an explicit demonstration of how the FLT influences the GMR ratio via the layer potentials calculated by means of DFT, interfacial scattering, and surface roughness.

12.2 Model and Computational Details

Ab initio electronic structure calculations were performed within the framework of the density functional theory (DFT) in the local spin density approximation. The Kohn-Sham equations were solved using the full-potential linearized augmented plane-wave (FP-LAPW) method in slab geometry [174]. Calculations were carried out for the slab consisting of 3 monolayers of Cr(001) and a variable number of monolayers ($1 \leq n \leq 8$) for Fe. The lattice constant for Fe and Cr was assumed to be Cr bulk-like, that is, a_0=5.44 a.u.. The reason for making such a choice was that we have seen very small differences in the results when different values were used.

We have chosen for our present GMR calculations the Boltzmann equation formalism based on the model single-band representation of the energies ($E = \frac{1}{2}mv^2 + V_{\nu\sigma}$) of electrons with a spin σ moving with velocity v in a constant layer potential $V_{\nu\sigma}$. This choice is very appropriate for the scope of this CHAPTER because it links the microscopic parameters given by DFT like density of states, Fermi energy or layer potentials with the macroscopic ones defined in Boltzmann equation-type models like effective masses or relaxation times [180]. Since the layer potentials are the electron energies corresponding to the bottom of the conduction band, they have been taken to be equal to the energies of s, p electrons in the Γ point of 2D Brillouin zone (BZ), since we assume that these electrons have the main contribution to the conductivity. To describe the spin-dependent conductivity within our model, these energies have been split by the value ΔE^{d-band} which is equal to the energy splitting of majority- and minority-spin d-bands in Fe layers while in Cr layers the potential values have been taken as equal for both spin directions:

$$V_{\nu\sigma} = E_{\nu}^{s,p-band}(\mathbf{k}=0) - \nu\sigma\Delta E^{d-band}, \tag{12.1}$$

where the layer is denoted by $\nu = 1$ for Fe slab and $\nu = 0$ for Cr slab. Moreover, the electron spin in Bohr magneton units is $\sigma = +\frac{1}{2}$ for spin-up electrons and $\sigma = -\frac{1}{2}$ for spin-down electrons. Note that the confinement of electrons within

a two-dimensional slab results in quantization of electron states in the direction perpendicular to the plane of this slab (z direction). This quantum-size effect is essential, especially when the slab thickness is restricted to several atomic layers [186] and this was taken it into account in our present calculations.

An extended Boltzmann equation formalism [172] was developed in describing the electronic transport in the Fe/Cr/Fe trilayer system. It consists of solving the Boltzmann equation in the relaxation time approximation

$$v^z \frac{\partial g^\alpha_{\mu\sigma}}{\partial z} + \frac{\partial f^0_\mu}{\partial v^\alpha} \frac{dv_\alpha}{dt} = -\frac{g^\alpha_{\mu\sigma}}{\tau_\sigma}, \tag{12.2}$$

where $g^\alpha_{\mu\sigma}(v,z)$ is the unknown function to be determined, τ_σ is the relaxation time for spin σ and $f^0_\mu(v)$ the equilibrium Fermi-Dirac distribution which is homogeneous across the layer μ (in our case a trilayer, so $\mu = 1,2,3$) and $\alpha = x,y$ accounts for the in-plane coordinates. The physical picture of the electrons involved in transport crossing through the potential barrier lead us to define the coefficients for coherent transmission and specular reflection. We assume that the carriers are embedded within the potential $V_{\nu\sigma}$ of each layer (different potentials for majority V_M and for minority V_m spins as well as V_s for the spacer electrons). These potentials were determined using the density functional theory described above. Thus, the reflection and transmission coefficients are calculated in terms of the layer potential values through the relations given in Reference [172]. Finally, the latter parameters are included in the boundary conditions at the interfaces and at the two outer surfaces in the trilayer system in order to solve Equation (12.2). It is usually assumed that at the outer surfaces of the considered trilayer the specular factors $P_{\alpha\sigma}$, $P_{\beta\sigma}$ provide a measure of the surface roughness, varying their values from 0 (completely diffusive scattering) to 1 (completely specular scattering). The sum over the spin contribution allow us to define the P_α and P_β parameters: $P_{\alpha\sigma} + P_{\alpha-\sigma} = P_\alpha$ and $P_{\beta\sigma} + P_{\beta-\sigma} = P_\beta$. In semiclassical approach, the interfaces A and B of trilayer are represented by the parameters $S_{A\sigma}, S_{A-\sigma}, S_{B\sigma}$, and $S_{B-\sigma}$ which can vary from 0 to 1 and they are the factors that indicate the degree of electron scattering at interfaces A and B for spin σ and $-\sigma$. It was reported in Reference [187] that a large magnetic moment appears in the interface layer, mainly due to highly localized interface states. It means that for a certain configuration of the Fe/Cr interface, the peak of the potential appears and it constitutes the physical source of scattering for an electron with a given spin. The scattering of electrons on this potential, having the interfacial origin, can be represented via the values of $S_{A\sigma}$ and $S_{B\sigma}$ in the semiclassical approach. In the same way we can interpret the coefficient P_α and P_β, but they are represented by the scattering of the electrons on a potential coming from the surface contribution. The value of GMR depends crucially on the values of these parameters [188].

After solving the EQUATION (12.2) restricted to the boundary conditions reported in REFERENCE [172] accounting the specular and interfacial factors, the total current in plane (CIP) is obtained after averaging the current density over the whole thickness of the film along the electric field E^{α} in each layer μ and for the electron with spin σ. It results in

$$J^{\alpha} = e\left[\frac{m_{\mu\sigma}}{h}\right]^{3} \sum_{\mu=1}^{3} \sum_{\sigma=\uparrow\downarrow} \int_{0}^{d} \int v^{\alpha} g_{\mu\sigma}(v, z, E^{\alpha}) d\mathbf{v} dz, \tag{12.3}$$

where $m_{\mu\sigma}$ is the electron effective mass, e the electric charge, and h the Planck's constant. The total conductivity of the sample is $\sigma^{\alpha} = \left(\frac{dJ^{\alpha}}{dE}\right)_{E=0}$ and whence the magnetoresistance (MR) is defined as $\frac{\Delta\rho^{\alpha}}{\rho^{\alpha}} = \frac{\sigma^{\alpha}_{\uparrow\uparrow} - \sigma^{\alpha}_{\uparrow\downarrow}}{\sigma^{\alpha}_{\uparrow\uparrow}}$, where ρ^{α} is the resistivity. The MR is found by calculating independently the conductivity $\sigma^{\alpha}_{\uparrow\uparrow}$, $\sigma^{\alpha}_{\uparrow\downarrow}$ in each layer. It is usually supposed that at outer surfaces $P_{\alpha\sigma} + P_{\alpha-\sigma} = P_{\beta\sigma} + P_{\beta-\sigma} = P_{\alpha} = P_{\beta} = P$ and at the interface $S_{A\sigma} = S_{B\sigma} = S_M$ or S_m (S_M, S_m for majority and minority spins, respectively). This assumption comes from the translational symmetry of our considered structure and fortunately, it reduces the numbers of parameters.

12.3 Results, Discussion, and Conclusions

The dependence of the MR on the value of the parameter P, responsible for the boundary condition at outer surfaces of the sample, is shown in FIGURE 12.1-a), where the potentials were taken from REFERENCE [188]. The three curves represent the value of the MR for different values of S_M and S_m at the interfaces. The value of the MR increases with P, except in the region where S_M=S_m =1 where we observe monotonic decrease. The same tendency in the behavior of GMR curves is observed in FIGURE 12.1-b), where the potentials were extracted from our *ab initio* calculations, although the values of the MR are higher than the ones of FIGURE 12.1-a). The values of the MR in FIGURE 12.1-b) for the parameters S_M=S_m =1 (parameters responsible for spin-dependent scattering of electrons at interfaces) are larger than the ones of the curves with S_M=0.2, S_m=0.9 for P data less than 0.7. However, the opposite situation is observed in FIGURE 12.1-a). It is evident from FIGURES 12.1-a) and 12.1-b) that not only the values of parameters P, S_M, and S_m but also the values of the potential influence the MR calculations.

Within the Boltzmann approach, the value of the layer potential is usually taken as a constant, however, for very thin films the value of this potential depends on the thickness of the sample as it was reported in REFERENCE [189]. In the case of ultrathin films, the conduction electron transport behavior is influenced by the thickness of the sample (not only the thickness of the spacer but also the thickness of the ferromagnetic layer). In REFERENCE [189], we discuss the influence of the

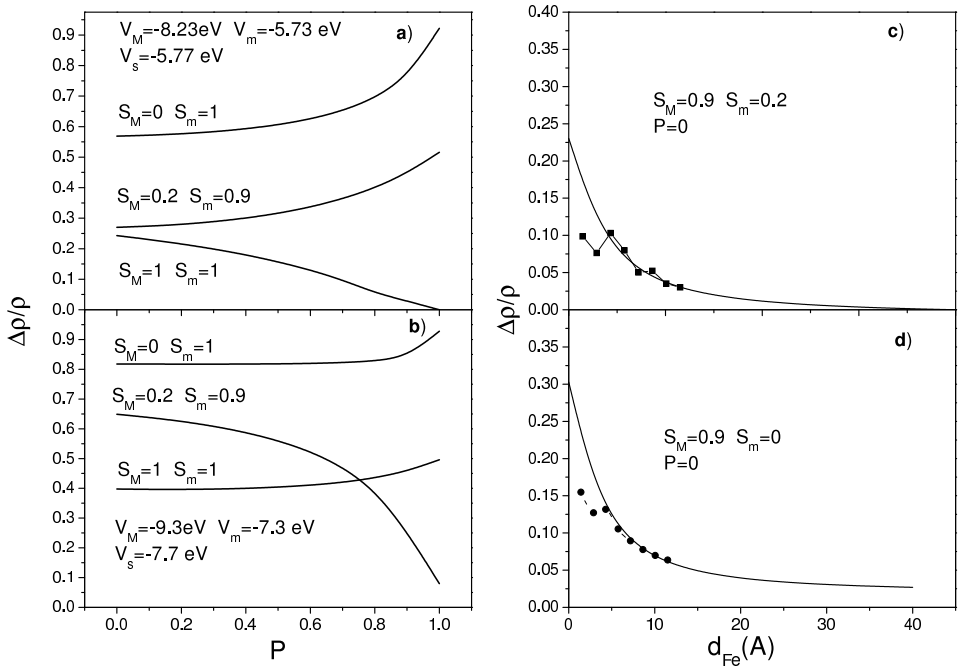

Figure 12.1:
a) and b) show the variation of MR as a function of the parameter P. c) and d) show the MR versus the FLT for the potentials taken from REFERENCE [188] and our *ab initio* calculations, respectively. In a) and b) cases, we have fixed d_s=4.33 Å and d_{Fe}=10 Å for the Fe/Cr/Fe trilayer. In c) and d) cases, the dashed curve is a guide to the eye.

sample thickness on some electronic properties like the Fermi energy, distribution of electrons and their spin polarization. We justify some parameters introduced to the model potential whose values for spacer and ferromagnetic metals depend on the layer thickness. The values of this potential as function of FLT were determined using the DFT methods described earlier. The dependence of the MR on the thickness of the ferromagnetic layer d_{Fe} is shown in FIGURE 12.1-c). The values of the MR obtained for the thickness-dependent potential are indicated by full rectangles. The MR shows the oscillations with the first, second, and third local maximum around 1.4, 4.3, and 8.6 Å, respectively. The connecting dashed line is just a guide to the eye and the full curve is calculated using the potential values taken from REFERENCE [188]. In FIGURE 12.1-d), we present also the MR as a function of the FLT, d_{Fe}, for the following parameters: S_M=0.9, S_m=0, and P=0. The values of the MR for the potentials determined from DFT are indicated by full dots. We observe that the MR oscillates weakly with the second peak around 4.3 Å, being the thickness of the oscillation not larger than 5.6 Å. These oscillations vanish very fast and the MR behavior is in agreement with the value of the MR calculated for the constant potential V_M =-8.23 eV, V_m=-5.73 eV, and V_s=-5.77 eV (full curve) reported in REFERENCE [188]. It is worthwhile to emphasize here that

if we use the semiclassical model in which each layer is represented by the quantum well with constant potential, the oscillatory behavior in the MR is hidden. Only the proper treatment and choice of the potential allows us to obtain the oscillatory behavior even in the semiclassical approach. Thus, the DFT results [190] confirm the important role of the interface, specially the significant increase of magnetic moment at the interface for different spin orientations. This fact finds its reflection in a significant change of potential at the interface for different spins. Therefore, the different contribution of the interface potential to the spin-dependent scattering allow us to conclude that it is one of the main mechanisms responsible for GMR in multilayers.

13

Calculations of Giant Magnetoresistance in Fe/Cr Trilayers using Layer Potentials Determined from *ab-initio* Methods

> *The theory of metallic resistance abounds in mysteries.*
>
> — Meaden

Synopsis

The *ab initio* full-potential linearized augmented plane-wave method explicitly designed for the slab geometry was employed to elucidate the physical origin of the layer potentials for the trilayers nFe/3Cr/nFe (001), where n is the number of Fe monolayers. The thickness of the transition-metal ferromagnet has been ranged from $n = 1$ up to $n = 8$ while the spacer thickness was fixed to three monolayers. The calculated potentials were inserted in the Fuchs-Sondheimer formalism in order to calculate the giant magnetoresistance (GMR) ratio. The predicted GMR ratio was compared with the experiment and the oscillatory behavior of the GMR as a function of the ferromagnetic layer thickness was discussed in the context of the layer potentials. The reported results confirm that the interface monolayers play a dominant role in the intrinsic GMR.

13.1 Introduction

Advances in ultrathin-film fabrication techniques have made possible, only quite recently, the construction of thin magnetic transition-metal layers, separated by very thin non-magnetic layers (spacers), forming superlattices or sandwiches. The

Fe/Cr/Fe multilayer system has played a fundamental role because the giant magnetoresistance (GMR) was first discovered on it [1]. Control of the spacer thickness with great accuracy, keeping constant the width of the magnetic layers, has been the main preoccupation of the experimentalists for a long time, because this factor is one of the basic conditions for obtaining great values of GMR as well as the coupling constant between the magnetic layers, but the variation of the magnetic layer thickness and its influence on GMR had remained without experimental measurements until quite recently [173, 181]. This fact is understandable because most of these experiments have been guided by the so far existing models in either the quantum-well (QW) [191] or the Ruderman-Kittel-Kasuya-Yosida (RKKY) picture [192]. These models study the oscillatory exchange coupling of the magnetic layers, mediated by the electrons in the spacer, as a function of the spacer thickness with ferromagnetic layer thickness remaining constant in most of the studied layered structures. However, in this CHAPTER, we focus our attention on the GMR effect produced by the variation of the magnetic layer thickness and surprisingly we have found an oscillating magnetic behavior of the magnetic layers. The explanation resides more in the presence of QW states than invoking the RKKY-like models, as we will see below.

Nowadays, it is well known that the interface between layers plays a dominant role in the GMR and obviously it depends strongly on the materials of the sample [193]. However, the controversy about whether GMR originates from bulk or interface scattering is still open [179]. This CHAPTER will threw some light on this controversy because we calculate the contribution to GMR coming from the bulk and the interface layers. Moreover, we will show that the magnetic properties change as a function of the ferromagnetic layer thickness (FLT) and the contribution to the GMR effect of this system is not negligible as we will prove using the Boltzmann model where the potentials are calculated from the *ab initio* data. Thus, we obtain the density of states (DOS) and energy bands for different FLTs and through them we can calculate the potentials. A remarkable fact is that the former potentials are numerically close to those reported by Hood and Falicov [188, 194] which were chosen without an explicit justification. Thanks to considering the full electronic structure of these materials, we are able to obtain directly the magnetoresistance of these Fe/Cr/Fe samples in a good agreement with the experiment, at least for a certain interval of the ferromagnetic layer thickness [181]. It should be stressed that our *ab initio* calculations and the interpretation through Boltzmann formalism can give us information about some confusion areas where the mesoscopic concepts play a fundamental role such as in the case of the interface. For systems of reduced dimensions (which in this CHAPTER corresponds to a number of iron monolayers (MLs) less than four) the physical magnitudes such as the magnetic moments, conductivity, or even the spin change drastically their behavior, having striking consequences for the magnetoresistance effect, as for example a considerable enhancement of the GMR ratio.

In the present Chapter, we investigate the GMR for the layer potentials of Fe/Cr/Fe trilayers determined by means of density functional theory (DFT) calculations as a function of the thickness of the Fe layer. Our study is also restricted to the case of current in plane geometry (CIP). Although the study of GMR versus the spacer thickness is well described in literature, only a few articles are devoted to the case of a variable ferromagnetic layer. Nevertheless, we have found that the study of this case is more suitable for investigating the intrinsic origen of GMR. In order to show and explain our results we have organized the Chapter as follows: in Section 13.2 we present the method of calculation. The Fe/Cr/Fe trilayer system is described and the physical origin of the layer potentials is determined according to the DFT calculations. Likewise, a brief description of the effective electron masses is presented in the next subsection. After this, the transport model is introduced in such a way that it allows us to use the data based on DFT calculations, in particular, for the relaxation time and the effective mass. The method is developed in order to describe the electronic transport of the Fe/Cr/Fe trilayers in analogy to the evolution of the Co/Cu multilayer conductivity [195]. In Section 13.3 the results of our calculations are discussed and the predictions for GMR properties are reported. Section 13.4 includes some remarks and a brief summary.

Thus, the aim of the present Chapter is to describe GMR properties by means of the data obtained within DFT method and applied to the Fuchs-Sondheimer formalism extended for trilayers.

13.2 Method of Calculation and Computational Details

13.2.1 Self-consistent Calculations

Ab initio electronic structure calculations were performed within the framework of density functional theory in the local spin density approximation (LSDA). The exchange-correlation potential was used in the form of Vosko-Wilk-Nusair [34]. As was reported in Reference [196], the use of LSDA instead of the generalized gradient approximation (GGA) in Fe/Cr trilayers is adequate because GGA improves only the geometry optimization, while the energy calculations (in particular, Fermi energy) are more or less the same. Since we use a fixed geometry and the transport properties depend only on the Fermi energy, it is not necessary at all to use the GGA. The Kohn-Sham equations [20] were solved using the full-potential linearized augmented plane-wave (FP-LAPW) method in slab geometry [174, 175]. This method is extremely advantageous for computing the electronic structure of magnetic multilayers, because it was designed to take into account the slab geometry and the interaction between the outermost monolayers of the trilayer system and vacuum. Thus, our method guarantees that all trilayer systems investigated in this Chapter are two-dimensional translational invariants. To our best knowledge,

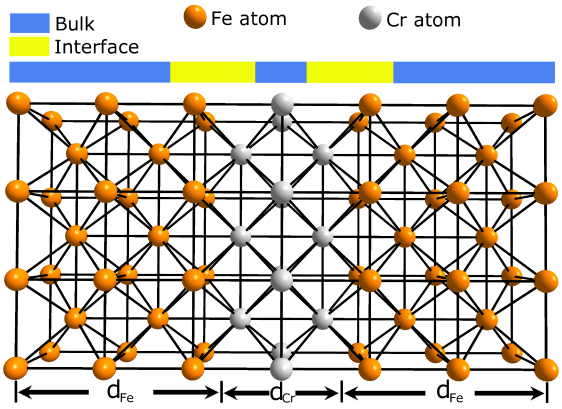

Figure 13.1:
Schematic picture of the generic $Fe_n/Cr_3(001)$ system. The bulk and interface monolayers are indicated in the figure.

this is the first attempt to account specifically for the slab geometry of layers in contrast with other methodologies where the two-dimensional invariance is achieved by inserting vacuum layers to separate the interaction between the slabs [197]. The valence states were calculated in a scalar-relativistic approximation. A grid of 15 **k**-points in an irreducible wedge of the 2D Brillouin zone (BZ) was used during self-consistent field (SCF) cycles and, once converged, a mesh of 45 **k**-points was considered to evaluate the final energy. Inside the muffin-tin spheres, basis functions with angular momentum components from 1 up to 8 were included. The charge density and potential within the muffin-tin spheres were expanded into the lattice harmonics with angular momentum from 1 up to 6. More than 60 augmented plane waves per atom were used for the variational basis set.

13.2.2 Fe/Cr/Fe Trilayers

Calculations were carried out for the slab consisting of 3 monolayers of Cr(001) and a variable number of Fe monolayers ($1 \leq n \leq 8$), where n is the number of Fe monolayers. The Fe layers are intrinsically ferromagnetic and the Cr layers are intrinsically antiferromagnetic (see column 4 of Tables 13.1 and 13.2). Figure 13.1 shows the schematic picture of 3 ML Cr in between 5 ML Fe for the bcc crystal orientation (001). We consider the monolayers to be in the x-y plane and stacked along the z direction. It is well known that the magnetic properties, DOS, and energy bands depend strongly upon the atomic structures of the thin films. Therefore, it is necessary to begin with an optimized structure for Fe_n/Cr_3 system. Nevertheless, no further attempt was made to relax the lattice parameter, i.e. the lattice constant for Fe and Cr was assumed to be Cr bcc bulk-like, that is, a_0=2.88 Å, because we observed small differences in the obtained results when these constants were taken differently.

Table 13.1:
Computational results for Fe_n/Cr_3 trilayers (n=1-4,6,8) along with the layer potentials calculated according to EQUATION (13.2) and the relaxation times provided by EQUATION (13.6) with c=8.34×10^{-5}. The symbol m denotes magnetic moment per atom, $\rho_\nu(\varepsilon_F)$ is the density of states at the Fermi level, and $V_{\nu\sigma}$ represents the potential of the majority and minority spins per monolayer.

Trilayer	E_F (eV)	ML	m $\left(\frac{\mu_B}{\text{at.}}\right)$	$\rho_\nu(\varepsilon_F)$ (eV^{-1})		$V_{\nu\sigma}$ (eV)		$\tau^*_{\nu\sigma}$ $(10^{-13}\ \text{s})$	
				↑	↓	↑	↓	↑	↓
		Fe(1)	2.45	0.54	3.76	-6.90	-4.90	3.07	0.87
Fe_1/Cr_3	-4.32	Cr(1)	-0.62	0.95	0.50	-7.30	-7.30	2.35	1.58
		Cr(2)	0.62	0.63	0.94	-7.30	-7.30	1.56	2.96
		Fe(1)	2.94	0.13	2.88	-8.19	-5.83	9.05	0.81
		Fe(2)	1.94	0.39	0.64	-7.86	-6.14	3.28	3.27
Fe_2/Cr_3	-3.97	Cr(1)	-0.47	0.81	0.83	-7.69	-7.69	1.65	1.61
		Cr(2)	0.35	0.33	0.50	-7.69	-7.69	4.04	2.67
		Fe(1)	2.92	0.14	2.12	-8.7	-6.3	7.45	0.94
		Fe(2)	2.43	0.15	0.62	-8.5	-6.4	7.28	3.11
Fe_3/Cr_3	-4.32	Fe(3)	2.00	0.32	0.44	-8.3	-6.7	3.58	4.00
		Cr(1)	-0.75	0.53	0.40	-6.3	-6.3	3.75	4.97
		Cr(2)	0.71	0.21	0.23	-6.3	-6.3	4.47	8.65
		Fe(1)	2.97	0.17	2.32	-9.3	-7.3	5.37	0.45
		Fe(2)	2.27	0.28	0.34	-9.3	-7.3	3.26	4.36
		Fe(3)	2.49	0.26	0.57	-9.3	-7.3	3.51	2.60
Fe_4/Cr_3	-4.32	Fe(4)	2.16	0.34	0.53	-9.3	-7.3	2.68	2.79
		Cr(1)	-0.50	0.89	0.63	-7.2	-7.2	1.71	2.42
		Cr(2)	0.50	0.25	0.40	-7.2	-7.2	6.09	3.81
		Fe(1)	2.96	0.08	1.72	-9.4	-7.3	11.16	0.86
		Fe(2)	2.25	0.23	0.36	-9.4	-7.3	3.88	4.11
		Fe(3)	2.41	0.38	0.28	-9.4	-7.3	2.35	5.29
		Fe(4)	2.25	0.41	0.34	-9.4	-7.3	2.18	4.36
Fe_6/Cr_3	-3.95	Fe(5)	2.34	0.28	0.21	-9.4	-7.3	3.19	7.05
		Fe(6)	2.20	0.26	0.47	-9.4	-7.3	3.44	3.15
		Cr(1)	-0.65	0.49	0.25	-7.6	-7.6	2.79	5.47
		Cr(2)	0.58	0.52	0.48	-7.6	-7.6	2.63	2.85
		Fe(1)	2.98	0.04	1.91	-9.3	-7.3	22.81	0.78
		Fe(2)	2.19	0.14	0.36	-9.3	-7.3	6.52	4.11
		Fe(3)	2.35	0.10	0.44	-9.3	-7.3	9.13	3.37
		Fe(4)	2.19	0.14	0.34	-9.3	-7.3	6.52	4.36
		Fe(5)	2.26	0.13	0.30	-9.3	-7.3	7.02	4.94
Fe_8/Cr_3	-3.97	Fe(6)	2.25	0.17	0.39	-9.3	-7.3	5.37	3.80
		Fe(7)	2.35	0.17	0.32	-9.3	-7.3	5.37	4.63
		Fe(8)	2.13	0.36	0.71	-9.3	-7.3	2.54	2.09
		Cr(1)	-0.64	1.01	0.43	-7.7	-7.7	1.32	3.10
		Cr(2)	0.49	0.29	0.46	-7.7	-7.7	4.59	2.89

Table 13.2:
Computational results for Fe_n/Cr_3 trilayers (n=5, 7) along with the layer potentials calculated according to EQUATION (13.2) and the relaxation times provided by EQUATION (13.6) with c=8.34×10^{-5}. The symbols are the same as in TABLE 13.1.

Trilayer	E_F (eV)	ML	m $\left(\frac{\mu_B}{\text{at.}}\right)$	$\rho_\nu(\varepsilon_F)$ (eV^{-1})		$V_{\nu\sigma}$ (eV)		$\tau^*_{\nu\sigma}$ $(10^{-13}\ \text{s})$	
				↑	↓	↑	↓	↑	↓
		Fe(1)	2.93	0.17	2.50	-9.4	-7.3	5.04	0.61
		Fe(2)	2.35	0.27	0.92	-9.4	-7.3	3.31	1.61
		Fe(3)	2.41	0.39	0.29	-9.4	-7.3	2.29	5.11
Fe_5/Cr_3	-4.56	Fe(4)	1.79	0.48	0.79	-9.4	-7.3	1.86	1.88
		Fe(5)	3.12	0.32	0.21	-9.4	-7.3	2.79	7.05
		Cr(1)	-0.94	0.52	0.45	-7.4	-7.4	2.77	3.20
		Cr(2)	0.64	0.20	0.14	-7.4	-7.4	7.21	10.30
		Fe(1)	2.96	0.17	2.70	-9.3	-7.3	5.37	0.55
		Fe(2)	2.24	0.46	0.44	-9.3	-7.3	1.98	3.37
		Fe(3)	2.29	0.47	0.22	-9.3	-7.3	1.94	6.73
		Fe(4)	2.21	0.52	0.37	-9.3	-7.3	1.76	4.00
Fe_7/Cr_3	-4.02	Fe(5)	2.27	0.62	0.13	-9.3	-7.3	1.47	11.39
		Fe(6)	1.77	0.55	0.32	-9.3	-7.3	1.66	4.63
		Fe(7)	2.93	0.50	0.14	-9.3	-7.3	1.83	10.58
		Cr(1)	-0.75	0.51	0.25	-7.7	-7.7	2.61	5.32
		Cr(2)	0.50	0.49	0.46	-7.7	-7.7	2.72	2.89

13.2.3 Layer Potentials

The single band model representation leads to the energies

$$E_{\nu\sigma}(k) = \frac{1}{2} m^*_\sigma (v_\sigma(k))^2 + V_{\nu\sigma} \tag{13.1}$$

of electrons moving in the intrinsic potential $V_{\nu\sigma}$ with the spin σ in monolayer ν and velocity $v_\sigma(k)$. The intrinsic potentials require for these calculations to be determined on the basis of *ab initio* DFT calculations described in SECTION 13.2.1. Since these values are the electron energies corresponding to the bottom of conductivity band, they were taken to be equal to the energies of s, p electrons at the Γ-point of the 2D BZ, since we assume that these electrons make the main contribution to the conductivity. To describe the spin-dependent conductivity within our model, these energies were split by the value ΔE^{d-band} which is equal to the energy splitting of majority and minority-spin d-bands in Fe layers while in Cr layers the potential values were taken the same for both spin directions. Thus,

$$V_{\nu\sigma} = E_\nu^{s,p-band}(\mathbf{k}=0) - \zeta\sigma\Delta E^{d-band} \tag{13.2}$$

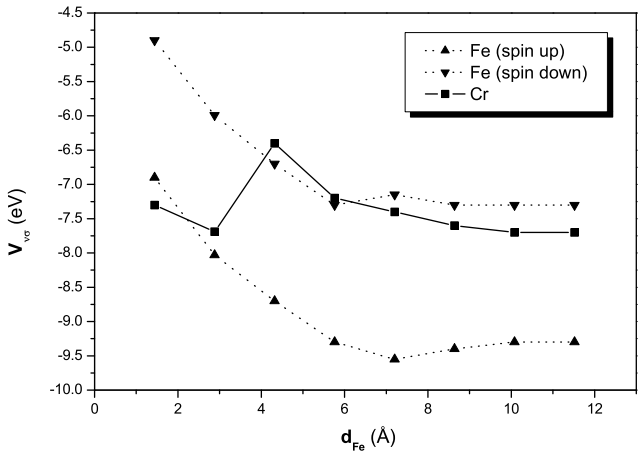

Figure 13.2: Dependence of the Fe majority (triangles), Fe minority (inverted triangles), and Cr (squares) layer potentials versus the FLT, d_{Fe}, for a fixed Cr thickness, d_{Cr} = 4.32 Å. For $n \leq 3$, the values of the layer potentials are given on average.

where $\zeta = 1$ for the Fe slab and $\zeta = 0$ for the Cr slab. Note that the spin electron in Bohr magneton units is $\sigma = +\frac{1}{2}$ for majority electrons and $\sigma = -\frac{1}{2}$ for minority electrons and the confinement of electrons within two-dimensional slab results in quantization of electron states in the direction perpendicular to the plane of this slab (z-direction). This quantum-size effect is essential, especially when the slab thickness is restricted to several atomic layers [186, 198, 199]. Therefore, we took it into account in our present calculations when the thickness of Fe film was equal to one, two, or three atomic layers.

Since the quantum-well electronic states, in the case of ultrathin Fe films, are well localized in single atomic layer, we assume that the physical properties on this layer are determined mainly by the states which have a degree of localization in the layer more than 60%. The energy of the electron state at the Γ-point corresponding to the energy band with high localization in the ith atomic layer were taken as the ith potential value. In the case of a thicker Fe film ($n \geq 4$) the electron states are more delocalized and they cannot be related to only one atomic layer, therefore we took in these cases the values of potentials $V_{\nu\sigma}$ common for a whole Fe film. The potential values in the Cr film always had the same value for all Cr atomic layers. The variations of the layer potentials for $n \geq 4$ are expected to be quite small because of the delocalization of the electron states, as is shown in FIGURE 13.2.

13.2.4 Description of the Effective Mass

The effective mass parameter m^*_σ can be calculated by means of the standard procedure of DFT applied to the band structure calculations. An example of the complicated spin-dependent band structure provided by our DFT calculations is showed in FIGURE 13.3 for the Fe_5/Cr_3 system. The effective masses have been calculated as the second derivative of the s, p electronic band energy $E_\sigma(k)$ close to the Fermi level with respect to the Fermi wavevector k_F and evaluated at the

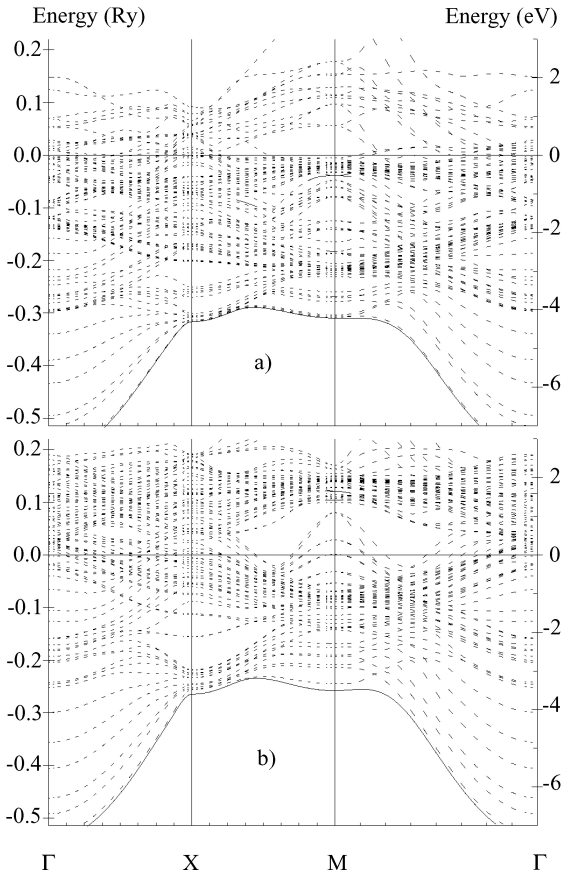

Figure 13.3:
Energy bands of the majority-spin states (a) and the minority-spin states (b) for the Fe_5/Cr_3 system. Solid lines represent the states with more than 50% of localization in the interface Fe layer. The Fermi level is at 0 eV.

Γ-point, according to the following relation

$$\frac{1}{m_\sigma^*} = \frac{1}{\hbar^2}\left(\frac{d^2E_\sigma(k)}{dk^2}\right)_{k=k_F}. \tag{13.3}$$

The energy band close to the Fermi level could always be approximated by a second-order polynomial in all considered systems. This argument is what underpins the parabolic approximation adopted in Section 13.2.3. The numerical evaluation of the effective masses is collected in Table 13.3. We can observe that our calculated effective masses are close to 4 m_e, that is the value assumed for the effective mass in Fe and Cr [188, 200]. To the best of our knowledge, no effective masses have been reported for Fe/Cr multilayers. In layered materials, we have only found the effective masses for Cu thin films deposited on the fcc Co film and they are in good agreement with the ones reported in Table 13.3 [201].

13.2.5 The Transport Model

In order to consider the transport properties using the DFT data, the electronic transport for the Fe/Cr/Fe trilayers can be described by the Boltzmann formalism [5, 188, 194, 202–204] applied to the current in plane geometry. In every monolayer, the electric current is then determined by appropriate distribution functions in terms of the velocity v_z in the direction z perpendicular to the interface for the electron with spin up and spin down due to the translational symmetry in the plane of the film. The electrons involved in transport are embedded within the potentials $V_{\nu\sigma}$ of each monolayer ν. These potentials were determined using the DFT data in conjunction with EQUATION (13.2).

Table 13.3: The spin-dependent effective mass parameters in units of the free electron mass (m_e).

Trilayer	$m^*_\uparrow$ (m_e)	$m^*_\downarrow$ (m_e)
Fe_1/Cr_3	3.15	3.98
Fe_2/Cr_3	3.55	4.59
Fe_3/Cr_3	3.56	4.62
Fe_4/Cr_3	3.85	5.08
Fe_5/Cr_3	3.92	5.13
Fe_6/Cr_3	3.95	5.17
Fe_7/Cr_3	3.93	5.20
Fe_8/Cr_3	3.93	5.20

With the aim of calculating the conductivity we write the Boltzmann equation in the relaxation time $\tau^*_{\nu\sigma}$ approximation for the distribution functions $g^\beta_{\nu\sigma}$ ($\beta = +, -$) which are determined with respect to the electric field applied in the direction of the electric current. The solutions are found taking into account the boundary conditions at the outer surfaces, namely $g^+_{1\sigma} = P_{1\sigma} g^-_{1\sigma}$ (at z=0) and $g^-_{n\sigma} = P_{n\sigma} g^+_{n\sigma}$ (at z=2($n+1$)a_0) with $g^+_{\nu\sigma}$ and $g^-_{\nu\sigma}$ standing for the solutions with $v^z \geq 0$ and $v^z < 0$, respectively. In order to extend our considerations to a more realistic case from the physical point of view, we define the specularity factor $P_{\nu\sigma}$ on the basis of the physical picture of the electrons involved in transport crossing through the potential barrier. In this case the value of $P_{\nu\sigma}$ corresponds to the specularity factor in the Fuchs-Sondheimer [205, 206] conductivity theory of thin films and leads to the effective result

$$P_{\nu\sigma}(\theta) = \frac{1 - \frac{(\chi_{\nu\sigma})^2 \cos^4\theta + 2}{1 + (\chi_{\nu\sigma})^2 \cos^4\theta}}{1 - \frac{(\chi_{\nu\sigma})^2 \cos^4\theta + 2}{(\chi_{\nu\sigma})^2 \cos^4\theta} \exp\left(-\frac{a_0}{\tau^*_{\nu\sigma} v^2 \cos\theta}\right)} \tag{13.4}$$

for ν ranging from 1 up to $2n + 3$, that is an alternative version to other models which assume the coefficients for coherent transmission and specular reflections determined quantum mechanically by matching free electron wavefunctions and their derivatives at each interface (see FIGURE 13.1). In EQUATION (13.4), θ is the angle of incidence of electrons measured with respect to the z-axis. The parameter $\chi_{\nu\sigma}$ is defined in terms of the Fermi velocity v_F as

$$\chi_{\nu\sigma} = \frac{2 m^*_\sigma \tau^*_{\nu\sigma} v_F^2}{\hbar} \tag{13.5}$$

where m^*_σ is the effective mass of σ electrons. From the physical point of view $\chi_{\nu\sigma}$ represents the ratio of the electron free path with respect to the de Broglie wavelength.

The distribution functions $g^\alpha_{\nu\sigma}$ depend on the relaxation times $\tau^*_{\nu\sigma}$ which can be evaluated in terms of the DFT calculations by means of the Fermi golden rule. The relaxation time can be expressed as follows [180]:

$$(\tau^*_{\nu\sigma})^{-1} = \frac{c}{\hbar}\rho_\nu(\varepsilon_F)(V_{\nu\sigma})^2 \tag{13.6}$$

where $\rho_\nu(\varepsilon_F)$ is the local density of states per monolayer ν at the Fermi energy; c is the number of the scattering centers relative to the total number of atoms and it plays the role of a calibration factor in order to compare it with the average values in the case of samples discussed in the literature. The Equation (13.6) is important for thin films due to the presentation of the relaxation time distribution across a sample.

The total current in CIP geometry along the direction α defined by the electric field $\mathbf{E}^\alpha$ is obtained after averaging the current density over the whole thickness of the film and it is given by the relation [188, 194]

$$J^\alpha = \frac{-|e|}{d}\sum_{\nu=1,\sigma=\uparrow\downarrow}^{2n+3}\left[\frac{m^*_\sigma}{2\pi\hbar}\right]^3\int_0^d\int v^\alpha g^\beta_{\nu\sigma}(\mathbf{v},z,E^\alpha)d\mathbf{v}dz \tag{13.7}$$

where e is the electric charge and d is the length of the sample in the z direction. Assuming that the total conductivity of a sample can be defined as $\Sigma = 1/\rho = (dJ^\alpha/dE)_{E=0}$, and the magnetoresistance (MR) ratio as $\Delta\rho/\rho_s = (\rho_{\uparrow\downarrow} - \rho_{\uparrow\uparrow})/\rho_{\uparrow\downarrow}$, then the theoretical predictions of the GMR can be obtained straightforwardly. It is worth to emphasize that the MR ratio is found by calculating independently the resistivities for the parallel ($\rho_{\uparrow\uparrow}$) and the antiparallel ($\rho_{\uparrow\downarrow}$) alignment of the magnetic moments in adjacent magnetic layers. The present approach remains in analogy to the calculations of Zahn *et al.* [195], who use the semiclassical Boltzmann theory with a spin independent relaxation time approximation. However, in our case, the relaxation time is not only spin dependent but also shows a local character.

Concerning the problem of whether GMR originates from bulk or interface scattering, we consider the contribution to MR from bulk and interface layers separately. An example to allocate the bulk and interface layers where bulk and interface scattering occurs is plotted in Figure 13.1. We have discretized the conductivity layer by layer with appropriate boundary conditions. Thus, the summation of the conductivity of the bulk layers and the conductivity of the interface layers was done independently to obtain the bulk and interface contributions to MR.

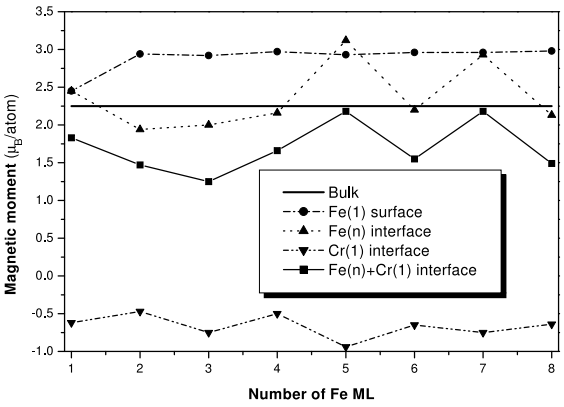

Figure 13.4:
Behavior of the surface (circles) and interface (triangles) Fe magnetic moment versus Fe film thickness. Inverted triangles represent the value of the Cr interface magnetic moment and the squares correspond to the numerical sum of the Fe and Cr interface magnetic moments. The solid line is the magnetic moment of the Fe bulk which is equal to 2.25 μ_B.

13.3 Results and Discussion

13.3.1 Layer Magnetic Moments and Potentials

First, we describe briefly the computational results obtained using the LAPW method. The numerical results of our calculations along with the layer potentials calculated according to EQUATION (13.2) and the relaxation times provided by EQUATION (13.6) are presented in TABLES 13.1 and 13.2.[1]

According to FIGURE 13.4, the behavior of the magnetic moment versus the Fe film thickness for the interface Fe layer is nonmonotonic in contrast with the surface Fe magnetic moment which ranges monotonically from 2.45 μ_B for $n = 1$ up to 2.98 μ_B for $n = 8$ (see fourth column of TABLES 13.1 and 13.2 for Fe(1) ML). We have also found the existence of highly localized states at the Fe/Cr interface when the Fe film thickness is not too small ($n \geq 4$). These states can result in the onset of a big magnetic moment in the interface Fe layer as also occurs at the surface. However, the localization of these states near the interface means that they should not be affected by the thickness of Fe film and the magnetic moments near the Fe/Cr interface should be independent of the Fe film thickness. This is a feature that, in our opinion, is due to the QW states, which are delocalized throughout the slab and their energy changes together with increase of the Fe film thickness [187]. The QW states have a resonance with the interface states for $n = 4$, 6, and 8. Consequently, the interface states become less localized, which results in a decrease of their exchange splitting as well as in a decrease of the interface Fe magnetic moment. The opposite behavior is found for the case $n = 5, 7$ leading to an increase of the interface Fe magnetic moment, such as is shown in FIGURE 13.4.

In this paragraph, our computational results are put in relation with the GMR effect, with the aim of enabling deductions about the effects that enhance the GMR,

[1]For the sake of notation, a brief comment on TABLES 13.1 and 13.2 is required: Cr(1) stands for the monolayer of Cr that is closest to a Fe monolayer; Cr(2) is the central monolayer of the Cr slab, that is, the second of the three Cr monolayers; Fe(1) stands for the external monolayer of the Fe Film; and Fe(2), Fe(3), ..., are the corresponding monolayers inside the Fe slab.

at least from a qualitative point of view. The quantitative predictions will be showed in SECTION 13.3.2. For $n = 5$, 7 we have a special behavior on the Fe/Cr interface (see TABLE 13.2), which deserves a more detailed comment. The first characteristic that we obtain, different from what happens for $n = 1, 2, 3, 4, 6$, and 8, is that we observe that the majority spins are the main contribution at the Fermi level (see FIGURE 13.5(a)). Notice that the DOS(ε_F) minority spin for $n = 1, 2, 3, 4, 6, 8$ has the corresponding values 3.76, 0.64, 0.44, 0.53, 0.47, and 0.71, while for $n = 5, 7$ they are 0.21 and 0.14, respectively. As can be inferred, these values are much lower than the previous ones (in FIGURE 13.5(b), we can see clearly the criterion employed to consider the magnetic channels to be insignificant for $n = 5, 7$, where the dash-dot line is the border line between negligible and appreciable channels). In fact, the lowest value for n=1,2,3,4,6 and 8 is 0.44, which is above the dash-dot line. Thus, we observe that the minority spin channels are very small for these two special cases in comparison with the ones seen above. The above comments lead us to conclude that our electronic structure calculations within DOS column graphs presented in FIGURE 13.5 show that there is essentially only one magnetic channel (semimetallic) on the iron-chromium interface for $n = 5, 7$ (see FIGURE 13.5(a)-(b) and TABLE 13.2) and a very high increase of the magnetism on its interfaces, since the other channel is the one of the minority spin density, quasiequal to zero. Nevertheless, for $n = 1, 2, 3, 4, 6$, and 8 we obtain both kinds of magnetic polarizations: up and down (see TABLE 13.1). This situation is very interesting for the GMR effect if we accept that this phenomenon is mainly due to the scattering of the electrons on these interfaces (a feature which will be discussed in SECTION 13.3.2), that is, the spin-polarized electrons on the one hand, enhance their velocity when they find the magnetic polarizability of the impurity parallel to the magnetic layer, but, on the other hand, the spin-polarized electrons diminish their velocity when they find the polarizability in opposite direction. Therefore, we have a spin valve effect in which there is a selection of one of the two possible magnetic channels, and this drives a decrease or an increase of the conductivity, depending on whether the electrons are parallel or antiparallel to the magnetic polarization of the interface.

13.3.2 GMR Predictions

So far, the models based on the Boltzmann equation specially developed for describing the multilayer transport properties introduce the potentials as a parameter or consider them in a semiempirical way [188, 194]. The value of this potential is usually taken as a constant; however, for ultrathin films the potential depends on the thickness of the sample as it was reported in REFERENCE [189] and, consequently, the electronic transport is influenced by the thickness of the sample (not only the thickness of the spacer but also the thickness of the ferromagnetic layer). Contrary to the usual procedure described in the literature, in this CHAPTER, the values of the potentials as a function of the FLT were determined using the DFT methods

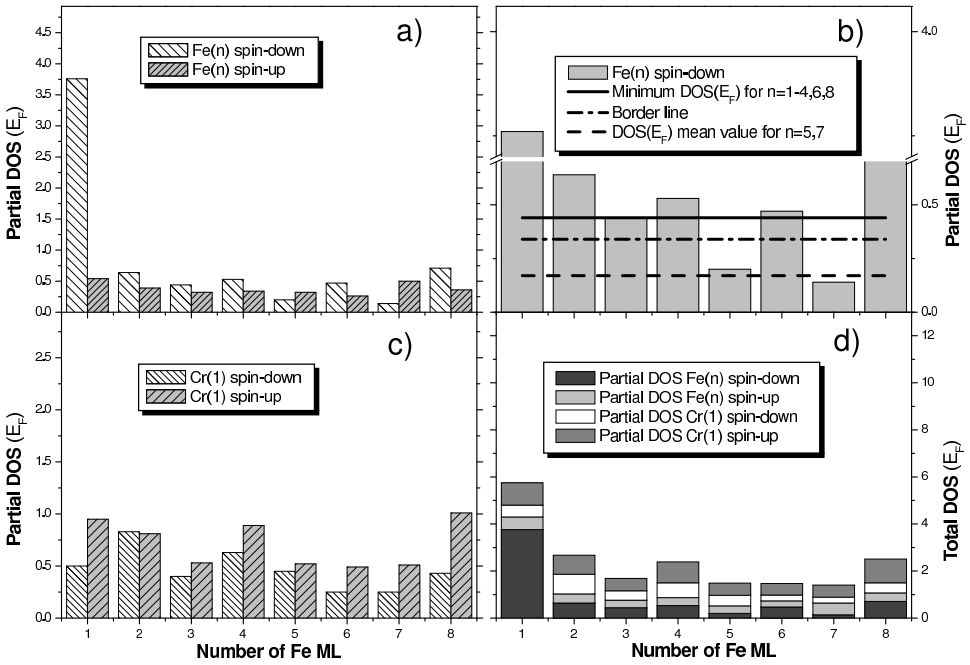

Figure 13.5:
Column graph exhibiting the partial DOS(ε_F) versus the Fe layer thickness for (a) the Fe interface ML spin-up and down, (b) Fe interface ML spin-down and (c) Cr interface ML spin-up and down polarization. (d) shows the total DOS(ε_F) as function of the FLT. The dash-dot line in (b) establishes a reasonable criterion for considering the minority spin channels insignificant for the case $n = 5, 7$.

described earlier (see FIGURE 13.2, TABLES 13.1 and 13.2). The dependence of the MR ratio on the thickness of the ferromagnetic layer d_{Fe} is shown in FIGURE 13.6. The values of the MR ratio obtained for the thickness dependent potential are indicated by full rectangles and they were calculated for a dilute concentration of scattering centres, that is, for c=8.34×10^{-5} [180]. The calculated MR exhibits an oscillatory behavior for a thickness in the range of the x axis displayed by FIGURE 13.6, although the oscillations appear at wrong periodicity compared with the experiments reported in REFERENCE [181]. In the light of the present calculations, we can conclude that the oscillatory character of the GMR comes mainly from a variable potential distribution through out the thin film, since the oscillatory behavior of the GMR is hidden as long as the potential is allowed to be constant, as it happens for example in the case of the semiclassical model in which every layer is represented by a quantum well with a constant potential [188]. The MR ratio shown in FIGURE 13.6 exhibits two maxima: the first one at around 4 Å and the second one close to the 8 Å. Thus, although the period of oscillations is wrong compared to the experiment [181], the second maximum agrees quite well with the measurements and we can observe in FIGURE 13.6 that the theoretical and experimental values

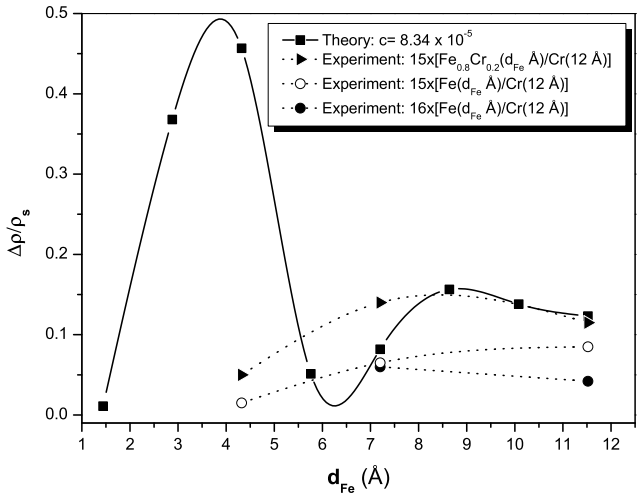

Figure 13.6:
Plot of the calculated (solid line) and experimental [181] (dashed lines) MR ratio as a function of the ferromagnetic layer thickness.

remain in good agreement in the interval of $d_{Fe} \geq 8$ Å. Only the proper treatment and choice of the potential allows us to obtain the oscillatory behavior even in the semiclassical approach [109]. The important problem, which has up till now omitted in the literature, is the determination of the potential at the interface or even proper treatment of the interface. It is a well known fact that at the interface there exists a significant change of the potential but this change is not of abrupt character. At the interface there is a transition region where the interdiffusion and the spin mixing take place while the change of the potential should be continuous according to the background.

We note that even though on one hand the GMR effect depends strongly on the temperature [207] and on another hand we are comparing our data (0 K) with the ones reported by Okuno *et al.* (77 K) at different temperatures, the influence of the temperature in the interval [0,77] can be considered negligible [207]. The discrepancy of our results with the experimental ones is less than about 10-15 % for $n \geq 4$, which represents an improvement with respect to other *ab-initio* calculations [208]. The aforementioned small discrepancy can be due to the high number of layers (multilayers) considered in the experiment in comparison with the reduced number of layers (trilayer) of our Fe/Cr sample. For the sake of comparison with the results reported by Okuno *et al.*, it is noteworthy that a remarkable message from our results is the low-dependence behavior of GMR with the number of Fe/Cr layers because the average value of the GMR ratio as a function of the Fe layer thickness is around 0.1 for $n \geq 4$ in our calculations and in the experimental results. In order to explain this low-dependence behavior, our proposal consists in considering a quasi-linear dependence of resistance of different number of Fe/Cr layers. Thus, after calculating the GMR ratio, the proportional constant is divided by itself, having no appreciable effect in GMR. This tendency disappears for the case of two or three iron monolayers leading to a considerable GMR ratio as shown in FIGURE 13.6,

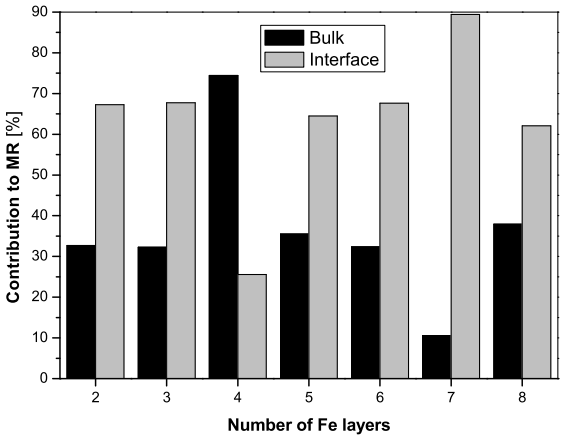

Figure 13.7:
Bulk and interface contribution to the total MR ratio versus the thickness of the ferromagnetic layer for c=8.34×10^{-5}.

since the electron states are more localized and, thus, they favor an increase of the layer potentials.

We should remind the reader that studies of transport in metallic superlattices (and particularly for trilayers) are affected by many inherent complexities of the material. Many possible complications arise in these types of artificial material, among them, interfacial interdiffusion at various lateral length scales [209–211], bulk defects, structural changes as a function of an individual layer and overall thicknesses, different length scales affecting the structure, the boundary conditions on the outermost layers and differences in the magnetotransport along the different directions in the superlattices. But the key point in the mechanism of GMR is the relative importance of bulk and interfacial scattering. Measurements as a function of layer thickness have claimed that the GMR originates from the bulk and that the interfacial roughness does not play a crucial role [212, 213] even in the current perpendicular to plane configuration. Other measurements, in which the interface was modified by the addition of small amounts of interfacial impurities, claim that the interfacial scattering plays a dominant role [214]. The bulk and interface contribution to the total MR ratio as a function of the Fe monolayers is shown in FIGURE 13.7. The results, except for the case n=4, clearly show that the monolayers that belong to the interface dominate the GMR because the potential abruptly changes in this region and it becomes in an important source of scattering. However, in the case n=4, since the potential barrier is less important than the other cases (see in FIGURE 13.2 the square and the inverted-triangle for n=4), the influence of the bulk monolayers becomes more important. Likewise, in this anomalous case, the reduced contribution of the interface scattering favors a diminishment of the total MR, that is reflected in FIGURE 13.6.

The last measurements reported in REFERENCE [215] and extensive comparative studies of the growth, structure, magnetization, and magnetotransport in Fe/Cr superlattices show that the intrinsic GMR originates from interfacial scattering and is determined by the interface width [109]. This experimental fact confirms the results

shown in FIGURE 13.7 and our earlier conclusion that the interface should be treated physically not as an ideal plane but as a transition zone between different materials where we can observe a mixture of two compounds (interdiffusion) and where not only a significant change of the potential but also a different kind of magnetism take place [193]. The DFT results [98] discussed in SECTION 13.3.1 confirm the important role of the interface, specially the significant increase of magnetic moment at the interface for $n = 5, 7$ (see FIGURE 13.4). This fact finds its reflection in a significant change of the potential at the interface for different spin polarizations (see FIGURES 13.2 and 13.5). The difference in interface potential constitutes the main physical reason for different scattering of electrons with different spin orientation and it is the main mechanism responsible for GMR in multilayers.

13.4 Conclusions

We have shown that using the two combined methods: the *ab initio* methodology for the accurate calculation of the potentials and the semiclassical approach based on the Fuchs-Sondheimer formalism, we obtain the GMR values for the trilayer Fe/Cr/Fe system which oscillates versus the thickness of the ferromagnetic layers. In literature, the GMR oscillations versus the nonmagnetic spacer are emphasized while the role of ferromagnetic layer is considered sporadically. In the ordinary semiclassical approach the oscillations of this kind do not exist; however, our calculations can predict this oscillatory behavior for ultrathin layers. Our results based on DFT calculations for the Fe/Cr system emphasize the very important role of the FLT via thickness dependent potential as well as the contribution of the interface to the GMR ratio. It is worthwhile to notice that the present approach does not contain any semiempirical parameter apart from the calibration constant c.

14

General Conclusions

> *Be yourself and think for yourself; and while your conclusions may not be infallible, they will be nearer right than the conclusions forced upon you.*
>
> — Elbert Hubbard

First-principles calculations are a fundamental tool to understand many experiments and make new predictions. Density functional theory is one of the most used methodologies to simulate systems with a large number of atoms at a relatively high degree of accuracy. Thus, this thesis is dedicated to the study of low-dimensional systems at the nanoscale level in the framework of DFT. In particular, we have selected clusters (nanoscale level) and trilayers (low-dimensional system) because of the important nanotechnological applications they retain. In consequence, in the first part of this thesis we have studied the electronic structure, geometry, and magnetic properties of transition metal clusters while in the second part the study was focused in the magnetic properties of the Fe/Cr trilayer system.

Concerning the cluster's topic, we first studied the electronic, structural and magnetic properties of small cobalt clusters. The nonlocal (GGA) treatment of exchange and correlation effects within DFT scheme offers the most accurate description of 'many-body' problem in a present day *ab-initio* calculations upon transition metal systems. Also, the use of the optimized model potential with the $3p$–$3d$ correlations explicitly treated by shifting the $3p$ shell into a valence basis set ensures a unified and accurate description of all clusters within a computational method. All clusters have shown an abundance of close-lying states. The magnetic moment of Co clusters is enhanced when compared to its bulk value of 1.72 μ_B. That enhancement can be accounted for an increased exchange splitting due to the decrease of the coordination number. In our opinion, the present results and those taken from References [43, 67] when viewed together provide both an extensive treatment of

cobalt cluster and many first- and second-row dimers with high level of exchange and correlation descriptions and also valuable experience within density functional methodology.

In silver clusters, we have shown that a combination of a LCGTO-KSDFM and TDDFT approach is able to reproduce the measured optical response of the silver octamer and allow us to elucidate its lowest energy structure. Moreover, the response of these clusters to an external electric field have shown us that the polarizability is strongly correlated to the cluster shape and the HOMO-LUMO gap. Concerning the point about the magnetic properties of these clusters we have also shown that the silver atoms can be magnetic when they are grouped together in small clusters. Particularly, the Ag_{13} cluster exhibits the highest magnetic moment per atom among the studied silver clusters due to its high symmetry and degeneration. Based on the magnetic properties of these silver clusters, our study suggests that the silver nanoclusters made out of Ag_{13} clusters, as building blocks, are suitable for possible future applications in biomedicine, since they could improve some present-day difficulties of magnetic nanoparticles like toxicity and opsonization. One of the problems of injecting the clusters into the blood is the oxidation but we have seen that the reactivity of the silver clusters with the oxygen diatomic molecule is of less importance. This ability is a critical point to take into account, especially if one pretends to use the magnetic silver nanoclusters in biomedical applications because if the oxidation is negligible, then the opsonization process can be minimized.

Our study on CoMn alloy clusters is the typical example where a DFT technique helps to reveal a not well-understood experiment and also to predict some properties of these clusters. Thus, the explanation of the surprising enhancement of the magnetic moments recently observed in dilute CoMn alloy clusters resides mainly on the magnetic role played by the Mn atoms and the "spin-flipping" of the electrons belonging to the Co-Mn bonding. Moreover, the calculations predict a fast dropping of the CoMn magnetic moment above 40 % of the Mn concentration.

In the second part of this thesis, we first characterized the Fe/Cr trilayer system from *ab initio* methods. Thus, we have shown that the variation of the number N of Fe atomic layers (thickness of Fe layers) induces an oscillating magnetic moment on the interface of the multilayer system Fe/Cr/Fe. For N=5 and 7 we obtain a great enhancement of its magnetism. This oscillation creates parallel or antiparallel magnetism with respect to the conduction electrons, when a difference of potential is introduced, and this gives a very different resistivity depending on the magnetic structure of the system.

Eventually, we have shown that using the two combined methods: the *ab initio* methodology for the accurate calculation of the potentials and the semiclassical approach based on the Fuchs-Sondheimer formalism, we obtain the GMR values for the trilayer Fe/Cr/Fe system which oscillates versus the thickness of the ferromagnetic layers. In literature, the GMR oscillations versus the nonmagnetic spacer are emphasized while the role of ferromagnetic layer is considered sporadically. In

ordinary semiclassical approach the oscillations of this kind do not exist, however our calculations can predict this oscillatory behavior for ultrathin layers. Our results based on DFT calculations for Fe/Cr system emphasize the very important role of the FLT via thickness dependent potential as well as the contribution of the interface (interfacial scattering) and surface roughness to the GMR ratio. Thus, our DFT results in CHAPTER 13 confirm the importance of the interface, specially the significant increase of magnetic moment at the interface for different spin orientations. This fact finds its reflection in a significant change of the potential at the interface for different spins. Therefore, the different contribution of the interface potential to the spin-dependent scattering allow us to conclude that it is one of the main mechanisms responsible for GMR in multilayers.

A

Hellman-Feynman Theorem

The purpose of this appendix is to show that the finite basis set GGA calculation holds the Hellmann-Feynman theorem when fully converged in the framework of density functional theory [216]. We have restricted ourselves for brevity of the formulas to wave functions without spin polarization; however, this is not a substantial restriction and the extension to spin-unrestricted orbitals is straightforward.

We have selected the ansatz in which the Kohn-Sham orbitals $\psi_i(\mathrm{r})$ are represented by linear combinations of atomic Gaussian-type orbitals $\chi_j(\mathrm{r})$. Thus, the orthonormal Kohn-Sham orbitals are given by

$$\psi_i(\mathrm{r}) = \sum_j c_{ij}\chi_j(\mathrm{r}), \tag{A.1}$$

where c_{ij} are the corresponding molecular orbital coefficients. With this expansion we find the following relation for the electronic density:

$$\rho(\mathrm{r}) = \sum_{i,j} P_{ij}\chi_i(\mathrm{r})\chi_j(\mathrm{r}), \tag{A.2}$$

where P_{ij} represents an element of the density matrix, defined as $P_{ij} = 2\sum_k^{occ} c_{ik}c_{jk}$. Using Equation (A.1) for the LCGTO expansions of the Kohn-Sham orbitals subject to the orthonormalization condition and the electronic density described in Equation (A.2), the variationally minimized Kohn-Sham SCF energy expression may be written after some manipulation as

$$\begin{aligned} E_{SCF}(\lambda) = &\sum_{ij} P_{ij}H_{ij}(\lambda) + \frac{1}{2}\sum_{ijkl} P_{ij}P_{kl}(ij|kl)(\lambda) \\ &- 2\sum_{ijk}\epsilon_k\left[c_{ki}c_{jk}S_{ij}(\lambda) - 1\right] + E_{XC}(\rho(\lambda), \nabla\rho(\lambda)), \end{aligned} \tag{A.3}$$

where H_{ij} represents the matrix elements of the core Hamiltonian and they are built from the kinetic and electron-nuclear interaction energies. The second term represents the Coulomb repulsion energy of the electrons and the term E_{XC} is the XC energy in the GGA. We use the notation $(ij|kl) = \int\int \psi_i(1)\psi_j(1)(1/r_{12})\psi_k(2)\psi_l(2)dr_1 dr_2$, and λ is any parameter at all which affects the Hamiltonian of the system. The quantities ϵ_k are one-electron eigenvalues for the occupied orbitals and S is the overlap matrix defined as $S_{ij} = \langle\chi_i|\chi_j\rangle$.

Assuming a gradient-corrected form for the XC energy $E_{XC} = \int g(\rho, |\nabla\rho|^2)dr$ and upon differentiation of the energy with respect to λ we find

$$\begin{aligned}\nabla_\lambda E = &\sum_{ij} P_{ij}\nabla_\lambda H_{ij} + \frac{1}{2}\sum_{ijkl} P_{ij}P_{kl}\nabla_\lambda(ij|kl) - 2\sum_{ijk}\epsilon_k c_{ki}c_{jk}\nabla_\lambda S_{ij} \\ &+ \sum_{ij} P_{ij}\left(\langle\nabla_\lambda i|E_{XC}|j\rangle + \langle i|E_{XC}|\nabla_\lambda j\rangle + \langle i|\frac{\partial g}{\partial\rho}\nabla_\lambda\rho|j\rangle\right. \\ &\left. +2\langle i|\frac{\partial g}{\partial|\nabla\rho|^2}\nabla_\lambda(|\nabla\rho|)|j\rangle\right). \end{aligned} \tag{A.4}$$

The XC contribution to the derivative of the energy involves derivatives of the wave function either explicitly or implicitly throughout the electronic density. Denoting a_i as a parameter of the wave functions that can be an exponent or positions of the basis functions, the functional derivative of the wave function can be written as $|\nabla_\lambda i\rangle = |\partial i/\partial a_i\rangle(da_i/\lambda)$. Thus we can optimize all parameters a_i so that the derivative of the XC energy can be neglected as well as the two-electron contribution of the Hamiltonian operator of Equation (A.3). Considering that the overlap matrix is independent of the perturbation λ as, for example, in the case of an uniform external electric field, the third term depending on the derivative of the overlap matrix vanishes. Consequently,

$$\nabla_\lambda E = \langle\nabla_\lambda H\rangle, \tag{A.5}$$

which means that the fully self-consistent finite basis set solutions satisfy the Hellmann-Feynman theorem in the framework of DFT when the XC energy is approximated by the GGA implementation.

List of Publications

1.- D. Baldomir, **M. Pereiro**, M. Iglesias, L. Wojtczak, and P. Mlynarski, *PROGRESS IN SURFACE SCIENCE* 59, 187-196 (1998).

2.- P. Mlynarski, D. Baldomir, M. Valladares, M. Iglesias, D. Suarez-De-Lis, and **M. Pereiro**, *Non-Crystalline and Nanoscale Materials* I, 208-211 (1998).

3.- P. Mlynarski, D. Baldomir, M. Valladares, M. Iglesias, D. Suarez-De-Lis, and **M. Pereiro**, *Non-Crystalline and Nanoscale Materials* I, 445-450 (1998).

4.- P. Mlynarski, M. Iglesias, **M. Pereiro**, D. Baldomir, and L. Wojtczak, *VACUUM* 54, 151-154 (1999).

5.- P. Mlynarski, M. Iglesias, **M. Pereiro**, D. Baldomir, and L. Wojtczak, *VACUUM* 54, 143-149 (1999).

6.- K. Warda, L. Wojtczak, D. Baldomir, **M. Pereiro**, and J. E. Arias, *VACUUM* 63, 163-169 (2001).

7.- **M. Pereiro**, D. Baldomir, M. Iglesias, C. Rosales, and M. Castro, *INTERNATIONAL JOURNAL OF QUANTUM CHEMISTRY* 81, 422-430 (2001).

8.- **M. Pereiro**, S. Man' kovsky, D. Baldomir, M. Iglesias, P. Mlynarski, M. Valladares, D. Suarez, M. Castro, and J. E. Arias, *COMPUTATIONAL MATERIALS SCIENCE* 22, 118-122 (2001).

9.- K. Warda, L. Wojtczak, D. Baldomir, and **M. Pereiro**, *SURFACE REVIEW AND LETTERS* 8, 271-279 (2001)

10.- S. V. Man'kovsky, V. T. Cherepin, D. Baldomir, and **M. Pereiro**, *METALLOFIZIKA I NOVEISHIE TEKHNOLOGII* 23, 435-443 (2001).

11.- K. Warda, L. Wojtczak, G. Wiatrowski, D. Baldomir, **M. Pereiro**, and J. E. Arias, *CZECHOSLOVAK JOURNAL OF PHYSICS* 52, 157-160 (2002).

12.- G. Wiatrowski, K. Warda, L. Wojtczak, D. Baldomir, **M. Pereiro**, and J. E. Arias, *SURFACE SCIENCE* 507-510, 517-521 (2002).

13.- S. V. Man' kovsky, D. Baldomir, and **M. Pereiro**, *INTERNATIONAL JOURNAL OF QUANTUM CHEMISTRY* 91, 234-238 (2003).

14.- **M. Pereiro**, D. Baldomir, S. Man' kovsky, and J. Arias, *INTERNATIONAL JOURNAL OF QUANTUM CHEMISTRY* 91, 245-251 (2003).

15.- **M. Pereiro** and D. Baldomir, *AMERICAN MATHEMATICAL MONTHLY* 110, 744-745 (2003).

16.- K. Warda, L. Wojtczak, G. Wiatrowski, D. Baldomir, **M. Pereiro**, and J. E. Arias, *PHYSICA STATUS SOLIDI A-APPLIED RESEARCH* 196, 117-120 (2003).

17.- K. Warda, L. Wojctzak, G. Wiatrowski, D. Baldomir, **M. Pereiro**, and J. E. Arias, *ACTA PHYSICAE SUPERFICIERUM* 7, 171-176 (2004).

18.- D. Baldomir, **M. Pereiro**, M. Iglesias, V. Pardo, J. Botana, J. E. Arias, K. Warda, G. Wiatrowski, and L. Wojtczak, *ACTA PHYSICAE SUPERFICIERUM* 7, 95-103 (2004).

19.- K. Warda, L. Wojtczak, G. Wiatrowski, D. Baldomir, **M. Pereiro**, and J. E. Arias, *CZECHOSLOVAK JOURNAL OF PHYSICS* 54, 217-220 (2004).

20.- K. Warda, L. Wojtczak, G. Wiatrowski, D. Baldomir, **M. Pereiro**, and J. Arias, *JOURNAL OF MAGNETISM AND MAGNETIC MATERIALS* 272-276, e1433-e1434 (2004).

21.- G. Wiatrowski, D. Baldomir, K. Warda, **M. Pereiro**, L. Wojtczak, and J. E. Arias, *JOURNAL OF MAGNETISM AND MAGNETIC MATERIALS* 277, 285-292 (2004).

22.- V. Pardo, P. Blaha, M. Iglesias, D. Baldomir, K. Schwarz, **M. Pereiro**, J. Botana, and J. E. Arias, *JOURNAL OF MAGNETISM AND MAGNETIC MATERIALS* 290-291, 349-352 (2005).

23.- **M. Pereiro** and D. Baldomir, *PHYSICAL REVIEW A* 72, 045201-1–045201-4 (2005).

24.- **M. Pereiro**, J. Botana, D. Baldomir, K. Warda, L. Wojtczak, S. V. Man' kovsky, M. Iglesias, V. Pardo, and J. E. Arias, *JOURNAL OF MAGNETISM AND MAGNETIC MATERIALS* 290-291, 392-395 (2005).

25.- M. Iglesias, A. Rodriguez, P. Blaha, V. Pardo, D. Baldomir, **M. Pereiro**, J. Botana, J. E. Arias, and K. Schwarz, *JOURNAL OF MAGNETISM AND MAGNETIC MATERIALS* 290-291, 396-399 (2005).

26.-M. Pereiro and D. Baldomir, *DXITOS* Xaneiro, 6-7 (2006).

27.- K. Warda, L. Wojtczak, D. Baldomir, **M. Pereiro**, and J. Arias, *MATERIALS SCIENCE-POLAND* 24, 731-735 (2006).

28.- K. Warda, L. Wojctzak, D. Baldomir, **M. Pereiro**, and J. Arias, *PHYSICA STATUS SOLIDI (C)* 3, 73-76 (2006).

29.- J. Botana, **M. Pereiro**, D. Baldomir, J. E. Arias, K. Warda, and L. Wojtczak, *JOURNAL OF MAGNETISM AND MAGNETIC MATERIALS* 316, e360-e364 (2007).

30.- **M. Pereiro**, D. Baldomir, S. V. Man' kovsky, K. Warda, J. E. Arias, L. Wojtczak, and J. Botana, *JOURNAL OF PHYSICS-CONDENSED MATTER* 19, 106210-1–106210-14 (2007).

31.- D. Baldomir, J. Rivas, D. Serantes, **M. Pereiro**, J. E. Arias, M. C. Buján-Núñez, and C. Vázquez-Vázquez, *JOURNAL OF NON-CRYSTALLINE SOLIDS* 353, 790-792 (2007).

32.- **M. Pereiro** and D. Baldomir, *PHYSICAL REVIEW A* 75, 033202-1–033202-10 (2007).

33.- **M. Pereiro**, D. Baldomir, and J. E. Arias, *PHYSICAL REVIEW A* 75, 063204-1–063204-6 (2007).

34.- K. Warda, L. Wojtczak, **M. Pereiro**, D. Baldomir, and J. Arias, *JOURNAL OF MAGNETISM AND MAGNETIC MATERIALS* 316, e320-e322 (2007).

35.- D. Baldomir, J. Rivas, D. Serantes, **M. Pereiro**, J. E. Arias, M. C. Buján-Núñez, and C. Vázquez-Vázquez, *JOURNAL OF NON-CRYSTALLINE SOLIDS* 353, 793-795 (2007).

36.- D. Serantes, D. Baldomir, **M. Pereiro**, J. E. Arias, C. Mateo-Mateo, M. C. Buján-Núñez, C. Vázquez-Vázquez, and J. Rivas, *JOURNAL OF NON-CRYSTALLINE SOLIDS* 354, 5224-5226 (2008).

37.- J. Botana, **M. Pereiro**, D. Baldomir, H. Kobayashi, and J. E. Arias, *THIN SOLID FILMS* 516, 5144-5149 (2008).

38.- J. Botana, **M. Pereiro**, D. Baldomir, J. E. Arias, K. Warda, and L.Wojtczak, *JOURNAL OF APPLIED PHYSICS* 103, 07B716-1–07B716-3 (2008).

39.- **M. Pereiro**, D. Baldomir, J. Botana, J. E. Arias, K. Warda, and L. Wojtczak, *JOURNAL OF APPLIED PHYSICS* 103, 07A315-1–07A315-3 (2008).

40.- D. Serantes, D. Baldomir, **M. Pereiro**, J. Rivas, C. Vázquez-Vázquez, M. C. Buján-Núñez, and J. E. Arias, *PHYSICA STATUS SOLIDI (A)-APPLICATIONS AND MATERIALS SCIENCE* 205, 1349-1353 (2008).

41.- K. Warda, **M. Pereiro**, L. Wojctzak, D. Baldomir, J. Castro, and J. Arias, *MATERIALS SCIENCE-POLAND* 26, 1077-1082 (2008).

42.- D. Baldomir, D. Serantes, **M. Pereiro**, J. Rivas, C. Vázquez-Vázquez, M. C. Buján-Núñez, and J. E. Arias, *PHYSICA STATUS SOLIDI (A)-APPLICATIONS AND MATERIALS SCIENCE* 205, 1343-1348 (2008).

43.- **M. Pereiro**, D. Baldomir, and J. E. Arias, *PHYSICAL REVIEW B* 80, 075412-1–075412-8 (2009).

44.- D. Serantes, D. Baldomir, **M. Pereiro**, B. Hernando, V. M. Prida, J. L. Sánchez LLamazares, A. Zhukov, M. Ilyn, and J. González, *JOURNAL OF PHYSICS D: APPLIED PHYSICS* 42, 215003-1–215003-9 (2009).

45.- D. Serantes, D. Baldomir, **M. Pereiro**, B. Hernando, V. M. Prida, J. L. Sánchez Llamazares, A. Zhukov, M. Ilyn, and J. González, *PHYSICAL REVIEW B* 80, 134421-1–134421-6 (2009).

46.- J. Botana, **M. Pereiro**, D. Baldomir, and J. E. Arias, *THEORETICAL CHEMISTRY ACCOUNTS* 122, 297-304 (2009).

47.- J. Botana, **M. Pereiro**, D. Baldomir, D. Serantes, J. E. Arias, *JOURNAL OF NANOSCIENCE AND NANOTECHNOLOGY* 10, 2787-2790 (2010).

48.- **M. Pereiro**, D. Baldomir, and J. E. Arias, *Scientific American (Int. Edition Investigación y Ciencia)* 403, 12-13 (2010).

49.- D. Baldomir, D. Serantes, **M. Pereiro**, J. Botana, J. E. Arias, S. H. Masunaga, and J. Rivas, *JOURNAL OF NANOSCIENCE AND NANOTECHNOLOGY* 10, 2717-2721 (2010).

50.- D. Serantes, D. Baldomir, **M. Pereiro**, J. Botana, V. M. Prida, B. Hernando, J. E. Arias, e J. Rivas, *JOURNAL OF NANOSCIENCE AND NANOTECHNOLOGY* 10, 2512-2517 (2010).

51.- **M. Pereiro**, J. Botana, D. Baldomir, D. Serantes, and J. E. Arias, *JOURNAL OF NANOSCIENCE AND NANOTECHNOLOGY* 10, 2594-2599 (2010).

52.- S. Goy-López, J. Juárez, A. Cambón, J. Botana, **M. Pereiro**, D. Baldomir, P. Taboada, and V. Mosquera, *JOURNAL OF MATERIALS CHEMISTRY* 20, 6808-6814 (2010).

53.- J. Botana, **M. Pereiro**, D. Baldomir, and J.E. Arias, accepted in *JOURNAL OF CHEMICAL PHYSICS*.

54.- D. Baldomir, **M. Pereiro**, and J. E. Arias, accepted in COMPEL.

55.- **M. Pereiro**, D. Baldomir, and J. E. Arias, submitted to *JOURNAL OF CHEMICAL PHYSICS*.

Bibliography

[1] M. N. Baibich, J. M. Broto, A. Fert, F. V. Dau, F. Petroff, P. Eitenne, G. Creuzet, A. Friederich, and J. Chazelas, Phys. Rev. Lett. **61**, 2472 (1988).

[2] G. Binash, P. Grünberg, F. Saurenbach, and W. Zinn, Phys. Rev. B **39**, 4828 (1989).

[3] P. Grünberg, R. schreiber, Y. Pang, M. B. Brodsky, and H. Sowers, Phys. Rev. Lett. **57**, 2442 (1986).

[4] S. S. P. Parkin, N. More, and K. P. Roche, Phys. Rev. Lett. **64**, 2304 (1990).

[5] J. Barnas, A. Fuss, R. E. Camley, P. Grunberg, and W. Zinn, Phys. Rev. B **42**, 8110 (1990).

[6] B. Dieny, V. S. Speriosu, S. S. P. Parkin, B. A. Gurney, D. R. Wilhoit, and D. Mauri, Phys. Rev. B **43**, 1297 (1991).

[7] A. Berkowitz, J. R. Mitchell, M. J. Carey, A. P. Young, S. Zhang, F. E. Spada, F. T. Parker, A. Hutten, and G. Thomas, Phys. Rev. Lett. **68**, 3745 (1992).

[8] W. A. Harrison, *Electronic Structure and the Properties of Solids* (Dover, New York, 1989).

[9] H. Ehrenreich and D. Turnbull, eds., *Solid State Physics* (Acad. Press, Orlando, 1984), vol. 38, p. 136.

[10] N. W. Ashcroft and N. D. Mermin, *Solid State Physics* (Saunders College, Philadelphia, 1976).

[11] S. Datta, *Electronic Transport in Mesoscopic Systems* (Univ. Press, Cambridge, 1995).

[12] D. R. Hartree, Proc. Cambridge Philos. Soc. **24**, 89 (1928).

[13] J. C. Slater, Phys. Rev. **35**, 210 (1930).

[14] V. Fock, Z. Phys. **61**, 126 (1930).

[15] C. D. Sherrill and H. F. Schaefer, Adv. Quantum Chem. **34**, 143 (1999).

[16] P. Hohenberg and W. Kohn, Phys. Rev. **136**, B864 (1964).

[17] W. Kohn and L. J. Sham, Phys. Rev. **140**, A1133 (1965).

[18] U. von Barth and L. Hedin, J. Phys. C: Solid State Phys. **5**, 1629 (1972).

[19] R. G. Parr and W. Yang, *Density-Functional Theory of Atoms and Molecules* (Oxford University Press, New York, 1989).

[20] W. Kohn and L. J. Sham, Phys. Rev. **140**, A1133 (1965).

[21] J. P. Perdew, J. Tao, and S. Kümmel, *Recent Advances in Electron Correlation Methodology* (ACS Books, Washington, DC, 2004).

[22] J. P. Perdew, K. Burke, and M. Ernzerhof, Phys. Rev. Lett. **77**, 3865 (1996).

[23] J. P. Perdew, J. A. Chevary, S. H. Vosko, K. A. Jackson, M. R. Pederson, D. J. Singh, and C. Fiolhais, Phys. Rev. B **46**, 6671 (1992).

[24] J. P. Perdew, J. A. Chevary, S. H. Vosko, K. A. Jackson, M. R. Pederson, D. J. Singh, and C. Fiolhais, Phys. Rev. B **48**, 4978 (1993).

[25] J. P. Perdew, Phys. Rev. B **33**, 8822 (1986).

[26] J. P. Perdew, Phys. Rev. B **34**, 7406E (1986).

[27] J. Tao, J. P. Perdew, V. N. Staroverov, and G. E. Scuseria, Phys. Rev. Lett. **91**, 146401 (2003).

[28] A. D. Becke, J. Chem. Phys. **98**, 1372 (1993).

[29] J. P. Perdew, M. Ernzerhof, and K. Burke, J. Chem. Phys. **105**, 9982 (1996).

[30] DeMon2k, Andreas M. Köster, Patrizia Calaminici, Mark E. Casida, Roberto Flores-Moreno, Gerald Geudtner, Annick Goursot, Thomas Heine, Andrei Ipatov, Florian Janetzko, Jorge M. del Campo, Serguei Patchkovskii, J. Ulises Reveles, Dennis R. Salahub, Alberto Vela, deMon developers, 2006.

[31] J. C. Slater, Adv. Quantum Chem. **6**, 1 (1972).

[32] H. Sambe and R. H. Felton, J. Chem. Phys. **62**, 1122 (1975).

[33] B. I. Dunlap, J. W. D. Connolly, and J. Sabin, J. Chem. Phys. **71**, 3396 (1979).

[34] S. H. Vosko, L. Wilk, and M. Nusair, Can. J. Phys. **58**, 1200 (1980).

[35] A. D. Becke and K. E. Edgecombe, J. Chem. Phys. **92**, 5397 (1990).

[36] J. P. Perdew, Phys. Rev. B **33**, 8822 (1986).

[37] H. B. Schlegel, *Modern Electronic Structure Theory* (World Scientific, Singapore, 1995), chap. 8, p. 459.

[38] C. C. J. Roothaan, Rev. Mod. Phys. **32**, 179 (1960).

[39] A. Castro, A. Rubio, and M. J. Stott, Can. J. Phys. **81**, 1151 (2003).

[40] C. Jamorski, M. E. Casida, and D. R. Salahub, J. Chem. Phys. **104**, 5134 (1996).

[41] K. Yabana and G. F. Bertsch, Phys. Rev. B **54**, 4484 (1996).

[42] Z. Li and B. Gu, Phys. Rev. B **47**, 13611 (1993).

[43] C. Jamorski, A. Martínez, M. Castro, and D. Salahub, Phys. Rev. B **55**, 10905 (1997).

[44] M. Castro, C. Jamorski, and D. R. Salahub, Chem. Phys. Lett. **271**, 133 (1997).

[45] D. R. Salahub, M. E. Castro, R. Fournier, and E. I. Proynov, *Relativistic and Electron Correlation Effects in Molecules and Solids* (Plenum Press, New York, 1994), vol. 318, p. 411.

[46] H. Sellers and J. T. Golab, eds., *Theoretical and Computational Approches to Interface Phenomena* (Plenum Press, New York, 1994), p. 187.

[47] J. Andzelm, E. Radzio, and D. R. Salahub, J. Chem. Phys. **83**, 4573 (1985).

[48] J. P. Perdew and Y. Wang, Phys. Rev. B **33**, 8800 (1986).

[49] H. B. Schlegel, *Ab initio Methods in Quantum Chemistry-I* (Wiley, New York, 1987).

[50] C. E. Moore, *Atomic energy levels*, natl. bur. stand. (U.S.), Circ. No. 467; U.S. GPO: Washington (1971).

[51] C. J. Barden, J. C. Rienstra-Kiracofe, and H. F. S. III, J. Chem. Phys. **113**, 690 (2000).

[52] A. Kant and B. Strauss, J. Chem. Phys. **41**, 3806 (1964).

[53] D. A. Hales, C. X. Su, L. Lian, and P. B. Armentrout, J. Chem. Phys. **100**, 1049 (1994).

[54] L. M. Russon, S. Heidecke, M. K. Birke, J. Conceicao, M. D. Morse, and P. B. Armentrout, J. Chem. Phys. **100**, 4747 (1994).

[55] J. G. Dong, Z. Hu, R. Craig, J. R. Lombardi, and D. M. Lindsay, J. Chem. Phys. **100**, 1049 (1994).

[56] J. C. Weisshaar, J. Chem. Phys. **90**, 1429 (1988).

[57] I. Shim, Mat. Fys. Medd. K. Dan. Vidensk. Selsk. **41**, 147 (1985).

[58] M. D. Morse, Chem. Rev. **86**, 1049 (1986).

[59] D. R. Salahub, *Ab-initio Methods in Quantum Chemistry – II* (John Wiley & Sons Ltd., New York, 1987).

[60] D. A. Hales, C. X. S. ans L. Lian, and P. B. Armentrout, J. Chem. Phys. **100**, 1049 (1994).

[61] P. A. Montano and G. K. Shenoy, Solid State Commun. **35**, 53 (1980).

[62] H. Purdum, P. A. Montano, G. K. Shenoy, and T. Morisson, Phys. Rev. B **25**, 4412 (1982).

[63] D. G. Leopold and W. C. Lineberger, J. Chem. Phys. **85**, 51 (1986).

[64] E. K. Parks, T. D. Klots, and J. P. Riley, J. Chem. Phys. **92**, 3813 (1990).

[65] J. Bucher, D. Douglas, and L. Bloomfield, Phys. Rev. Lett. **66**, 3052 (1991).

[66] A. Vega, J. Dorantes-Dávila, and L. Balbás, Phys. Rev. B **47**, 4742 (1993).

[67] D. C. Patton, D. V. Porezag, and M. R. Pederson, Phys. Rev. B **55**, 7454 (1997).

[68] F. Baletto and R. Ferrando, Rev. Mod. Phys. **77**, 371 (2005).

[69] P. Jena, S. N. Khanna, and D. K. Rao, *Density Functional Theory of Molecules, Clusters, and Solids* (Kluwer Academic, Dordrecht, 1995), chap. 5.

[70] P. Radcliffe, A. Przystawik, T. Diederich, T. Döppner, J. Tiggesbäumker, and K.-H. Meiwes-Broer, Phys. Rev. Lett. **92**, 173403 (2004).

[71] R. Fournier, J. Chem. Phys. **115**, 2165 (2001).

[72] V. Bonačić-Koutecký, V. Veyret, and R. Mitric, J. Chem. Phys. **115**, 10450 (2001).

[73] J. Zhao, J. Yang, and J. G. Hou, Phys. Rev. B **67**, 085404 (2003).

[74] M. N. Huda and A. K. Ray, Phys. Rev. A **67**, 013201 (2003).

[75] V. Bonačić-Koutecký, L. Cespiva, P. Fantucci, and J. Koutecky, J. Chem. Phys. **98**, 7981 (1993).

[76] K. Yabana and G. F. Bertsch, Phys. Rev. A **60**, 3809 (1999).

[77] S. Erkoç and T. Yilmaz, Physica E **5**, 1 (1999).

[78] M. Casida, *Recent Advances in Density Functional Methods* (World Scientific, Singapore, 1995), pt. 1.

[79] A. St-Amant and D. R. Salahub, Chem. Phys. Lett. **169**, 387 (1990), URL http://www.demon-software.com/public_html.

[80] M. A. L. Marques, A. Castro, G. F. Bertsh, and A. Rubio, Comput. Phys. Commun. **151**, 60 (2003).

[81] J. P. Perdew and Y. Yang, Phys. Rev. B **46**, 12947 (1992).

[82] S. Huzinaga, J. Andzelm, M. Klobukovski, E. Radzio-andzelm, Y. Sakai, and H. Tatewaki, *Gaussian Basis Sets for Molecular Calculations* (Elsevier, Amsterdam, 1984).

[83] L. Versluis and T. Ziegler, J. Chem. Phys. **88**, 322 (1988).

[84] C. Hartwigsen, S. Goedecker, and J. Hutter, Phys. Rev. B **58**, 3641 (1988).

[85] Y. J. Alvarado, N. Cubillan, P. H. Labarca, A. Karam, F. Arrieta, O. Castellano, and H. Soscn, J. Phys. Org. Chem. **15**, 154 (2002).

[86] F. Federmann, K. Hoffmann, N. Quaas, and J. P. Toennies, Eur. Phys. J. D **9**, 11 (1999).

[87] C. Felix, C. Sieber, W. Harbich, J. Buttet, I. Rabin, W. Schulze, and G. Ertl, Phys. Rev. Lett. **86**, 2992 (2001).

[88] A. Bartelt, J. D. Close, F. Federmann, N. Quaas, and J. P. Toennies, Phys. Rev. Lett. **77**, 3525 (1996).

[89] W. A. de Heer, Rev. Mod. Phys. **65**, 611 (1993).

[90] M. Brack, Rev. Mod. Phys. **65**, 677 (1993).

[91] Q. A. Pankhurst, J. Connolly, S. K. Jones, and J. Dobson, J. Phys. D:Appl. Phys. **36**, R167 (2003).

[92] U. Kreibig and M. Vollmer, *Optical Properties of Metal Clusters* (Springer, Berlin, 1995).

[93] K. Deng, J. Yang, and C. T. Chan, Phys. Rev. A **61**, 025201 (2000).

[94] I. Moullet, J. L. Martins, F. Reuse, and J. Buttet, Phys. Rev. Lett. **65**, 476 (1990).

[95] J. C. Idrobo, S. Ogut, and J. Jellinek, Phys. Rev. B **72**, 085445 (2005).

[96] H. A. Kurtz, J. J. P. Stewart, and K. M. Dieter, J. Comput. Chem. **11**, 82 (1990).

[97] I. Vasiliev, S. Ogut, and J. R. Chelikowsky, Phys. Rev. Lett. **78**, 4805 (1997).

[98] M. Pereiro, D. Baldomir, M. Iglesias, C. Rosales, and M. Castro, Int. J. Quantum Chem. **81**, 422 (2001).

[99] B. Simard, P. A. Hackett, A. M. James, and P. R. R. Langridge-Smith, Chem. Phys. Lett. **186**, 415 (1991).

[100] S. Chretien and D. R. Salahub, Phys. Rev. B **66**, 155425 (2002).

[101] D. J. Wales, J. P. K. Doye, A. Dullweber, M. P. Hodges, F. Y. Naumkin, F. Calvo, J. Hernández-Rojas, and T. F. Middleton, *The cambridge cluster database*, URL http://www-wales.ch.cam.ac.uk/CCD.html.

[102] E. R. J. Andzelm and D. R. Salahub, J. Chem. Phys. **83**, 4573 (1985).

[103] J. Zhao, Y. Luo, and G. Wang, Eur. Phys. J. D **14**, 309 (2001).

[104] Z. F. Liu, W. L. Yim, J. S. Tse, and J. Hafner, Eur. Phys. J. D **10**, 105 (2000).

[105] J. A. Howard, R. Sutcliffe, and B. Mile, Surf. Sci. **156**, 214 (1985).

[106] T. L. Hasiett, K. A. Bosnick, and M. Moskovits, J. Chem. Phys. **108**, 3453 (1998).

[107] C. Jackschath, I. Rabin, and W. Schulze, Z. Phys. D: At., Mol. Clusters **22**, 517 (1992).

[108] K. LaiHing, P. Y. Cheng, and M. A. Duncan, Z. Phys. D:At., Mol. Clusters **13**, 161 (1989).

[109] M. Pereiro and D. Baldomir, Phys. Rev. A **72**, 045201 (2005).

[110] K. Michaelian, N. Rendón, and I. L. Garzón, Phys. Rev. B **60**, 2000 (1999).

[111] S. Fedrigo, W. Harbich, J. Belyaev, and J. Buttet, Chem. Phys. Lett. **211**, 166 (1993).

[112] C. J. F. Bottcher, ed., *Theory of Electric Polarization* (Elsevier, Amsterdan, 1973), chap. 5, p. 165.

[113] C. Kittel, ed., *Introduction to Solid State Physics* (Wiley, New York, 2005), chap. 1, p. 20.

[114] P. Calaminici, A. M. Koster, A. Vela, and K. Jug, J. Chem. Phys. **113**, 2199 (2000).

[115] M. J. Puska, R. M. Nieminen, and M. Manninen, Phys. Rev. B **31**, 3486 (1985).

[116] D. R. Snider and R. S. Sorbello, Phys. Rev. B **28**, 5702 (1983).

[117] L. H. Bennett, R. W. Mebs, and R. E. Watson, Phys. Rev. **171**, 611 (1968).

[118] G. Tikhonov, V. Kasperovich, K. Wong, and V. V. Kresin, Phys. Rev. A **64**, 063202 (2001).

[119] H. Haberland, ed., *Clusters of Atoms and Molecules: Theory, Experiment, and Clusters of Atoms.* (Springer, Berlin, 1994).

[120] C. R. Henry, Surf. Sci. Rep. **31**, 235 (1998).

[121] C. C. Berry and A. S. G. Curtis, J. Phys. D:Appl. Phys. **36**, R198 (2003).

[122] P. Tartaj, M. del Puerto Morales, S. Veintemillas-Verdager, T. González-Carreno, and C. J. Serna, J. Phys. D:Appl. Phys. **36**, R182 (2003).

[123] J. A. Alonso, Chem. Rev. (Washington, D. C.) **100**, 637 (2000).

[124] I. M. L. Billas, A. Chatelain, and W. A. de Heer, Science **265**, 1682 (1994).

[125] S. N. Khanna and S. Linderoth, Phys. Rev. Lett. **67**, 742 (1991).

[126] B. V. Reddy, S. N. Khanna, and B. I. Dunlap, Phys. Rev. Lett. **70**, 3323 (1993).

[127] M. Pereiro and D. Baldomir, Phys. Rev. A **75**, 033202 (2007).

[128] E. M. Fernández, J. M. Soler, I. L. . Garzón, and L. C. Balbás, Phys. Rev. B **70**, 165403 (2004).

[129] A. R. Miedema, Z. Metallkd. **69**, 287 (1978).

[130] C. Kittel, *Introduction to Solid State Physics* (Wiley, New York, 2005), chap. 3, p. 50, 8th ed.

[131] M. Pereiro and D. Baldomir, Phys. Rev. A **72**, 045201 (2005).

[132] R. H. Crabtree, *The Organometallic Chemistry of the Transition Metals* (Wiley, New York, 1988).

[133] F. Liu, M. R. Press, S. N. Khanna, and P. Jena, Phys. Rev. B **39**, 6914 (1989).

[134] B. I. Dunlap, Phys. Rev. A **41**, 5691 (1990).

[135] J. X. A. Jemal, R. Siegel and E. Ward, CA Cancer J. Clin. **60**, 277 (2010).

[136] Q. Sun, A. K. Kandalam, Q. Wang, P. Jena, Y. Kawazoe, and M. Marquez, Phys. Rev. B **73**, 134409 (2006).

[137] M. Pereiro, D. Baldomir, and J. E. Arias, Phys. Rev. A **75**, 063204 (2007).

[138] A. M. Kalsin, M. F. Paszewski, S. K. Smoukov, K. J. M. Bishop, and B. A. Grzybowski, Science **312**, 420 (2006).

[139] J. Zhou, Z.-H. Li, W.-N. Wang, and K.-N. Fan, Chem. Phys. Lett. **421**, 448 (2006).

[140] E. E. Carpenter, J. Magn. Magn. Mater. **225**, 17 (2001).

[141] D. J. Wales and J. P. K. Doye, J. Phys. Chem. A **101**, 5111 (1997).

[142] F. Cleri and V. Rosato, Phys. Rev. B **48**, 22 (1993).

[143] P. Fayet, F. Granzer, G. Hegenbart, E. Moisar, E. Moisar, B. Pischel, and L. Wöste, Phys. Rev. Lett. **55**, 3002 (1985).

[144] M. B. Knickelbein, J. Chem. Phys. **125**, 044308 (2006).

[145] M. Schmidt, A. Masson, and C. Bréchignac, Phys. Rev. Lett. **91**, 243401 (2003).

[146] M. Schmidt, P. Cahuzac, and C. Bréchignac, J. Chem. Phys. **118**, 10956 (2003).

[147] A. D. Russell and W. B. Hugo, Prog. Med. Chem. **31**, 351 (1994).

[148] L. A. Peyser, A. E. Vinson, A. P. Bartko, and R. M. Dickson, Science **291**, 103 (2001).

[149] M. Pereiro, D. Baldomir, J. Botana, J. E. Arias, K. Warda, and L. Wojtczak, J. Appl. Phys. **103**, 07A315 (2008).

[150] J. Bansmann, S. H. Baker, C. Binns, J. A. Blackman, J.-P. Bucher, J. Dorantes-Dávila, V. Dupuis, L. Favre, D. Kechrakos, A. Kleibert, et al., Surf. Sci. Rep. **56**, 189 (2005).

[151] C. Binns, K. N. Trohidou, J. Bansmann, S. H. Baker, J. A. Blackman, J.-P. Bucher, D. Kechrakos, A. Kleibert, S. Louch, K.-H. Meiwes-Broer, et al., J. Phys. D: Appl. Phys. **38**, R357 (2005).

[152] S. Yin, R. Moro, X. Xu, and W. A. de Heer, Phys. Rev. Lett. **98**, 113401 (2007).

[153] G. Rollmann, S. Sahoo, A. Hucht, and P. Entel, Phys. Rev. B **78**, 134404 (2008).

[154] S. Ganguly, M. Kabir, S. Datta, B. Sanyal, and A. Mookerjee, Phys. Rev. B **78**, 014402 (2008).

[155] N. Shen, J. Wang, and L. Zhu, Chem. Phys. Lett. **467**, 114 (2008).

[156] J. Friedel, Nuovo Cim. (Suppl.) **7**, 287 (1958).

[157] J. C. Slater, J. Appl. Phys. **8**, 385 (1937).

[158] HyperChem(TM) Professional 7.51, Hypercube, Inc., 1115 NW 4th Street, Gainesville, Florida 32601, USA.

[159] R. Fletcher, *Practical Methods of Optimization* (John Wiley & Sons, Chichester, 1996), chap. 4, p. 83.

[160] C. Kittel, *Introduction to Solid Physics* (John Wiley & Sons, Hoboken, 2005), p. 71.

[161] HTTP://www.colby.edu/chemistry/PChem/scripts/ABC.html.

[162] G. M. Koretsky, K. P. Kerns, G. C. Nieman, M. B. Knickelbein, and S. J. Riley, J. Phys. Chem. A **103**, 1997 (1999).

[163] J. Crangle, Philos. Mag. **2**, 659 (1957).

[164] R. Poerschke, *Magnetic Properties of Metals: d-Elements, Alloys and Compounds* (Springer-Verlag, Berlin, 1991), chap. 2, p. 52.

[165] V. S. Stepanyuk, R. Zeller, P. H. Dederichs, and I. Mertig, Phys. Rev. B **49**, 5157 (1994).

[166] R. C. O'Handley, *Modern Magnetic Materials: Principles and Applications* (John Wiley & Sons, New York, 2000), chap. 5, p. 153.

[167] J. Friedel, Adv. Phys. **3**, 446 (1954).

[168] J. Krebs, P. Lubitz, A. Chaiken, and G. A. Prinz, Phys. Rev. Lett. **63**, 1645 (1989).

[169] R. Hood, L. Falicov, and D. Penn, Phys. Rev. B **49**, 368 (1994).

[170] H. Zahouani, Bull. Soc. Sci. Lettres (Lodz), Rech. Deform. **XX**, 131 (1995).

[171] N. Mott, Proc. Roy. Soc. **156**, 386 (1936).

[172] D. Baldomir, M. Pereiro, M. Iglesias, L. Wojtczak, and P. Mlynarski, Prog. Surf. Sci. **42**, 187 (1998).

[173] P. J. H. Bloemen, M. T. Johnson, M. T. H. van de Vorst, R. Coehoorn, J. J. de Vries, R. Jungblut, J. aan de Stegge A. Reinders, and W. J. M. de Jonge, Phys. Rev. Lett. **72**, 764 (1994).

[174] V. T. Cherepin, A. A. Ostroukhov, and V. N. Tomilenko, Poverkhnost' (Surface) **6**, 43 (1986).

[175] M. Weinert, J. Math. Phys. **22**, 2433 (1981).

[176] S. Man'kovsky, D. Baldomir, and M. Pereiro, Int. J. Quant. Chem. **91**, 234 (2003).

[177] R. J. C. D. T. Pierce, J. Ungaris and M. D. Stiles, J. Magn. Magn. Mater. **200**, 290 (1999).

[178] U. Hartmann, *Magnetic Multilayers and Giant Magnetoresistance* (Springer-Verlag, Berlin, 2000).

[179] P. Zahn, J. Binder, I. Mertig, R. Zeller, and P. H. Dederichs, Phys. Rev. Lett. **80**, 4309 (1998).

[180] J. Kübler, *Theory of Itinerant Electron Magnetism* (Clarendon Press, Oxford, 2000), pp. 280–287.

[181] S. N. Okuno and K. Inomata, Phys. Rev. Lett. **72**, 1553 (1994).

[182] P. Bruno, J. Magn. Magn. Mater. **121**, 248 (1993).

[183] P. Zahn, I. Mertig, M. Richter, and H. Eschrig, Phys. Rev. Lett. **75**, 2996 (1995).

[184] J. Velev and Y.-C. Chang, Phys. Rev. B **63**, 184411 (2001).

[185] A. Urbaniak, Phys. Stat. Sol. (b) **188**, 795 (1995).

[186] J. E. Ortega, F. Himpsel, G. Mankey, and R. Willis, Phys. Rev. B **47**, 1540 (1993).

[187] S. V. Man'kovsky, D. Baldomir, and M. Pereiro, Int. J. Quantum Chem. **91**, 234 (2003).

[188] R. Q. Hood and L. M. Falicov, Phys. Rev. B **46**, 8287 (1992).

[189] K. Warda, L. Wojtczak, G. Wiatrowski, D. Baldomir, M. Pereiro, and J. E. Arias, Czech. J. Phys. **52**, A157 (2002).

[190] M. Pereiro, D. Baldomir, S. Mankovsky, and J. Arias, Int. J. Quantum Chem. **91**, 245 (2003).

[191] D. M. Edwards, J. Mathon, R. B. Muniz, and M. S. Phan, Phys. Rev. Lett. **67**, 493 (1991).

[192] P. Bruno and C. Chappert, Phys. Rev. Lett. **67**, 1602 (1991).

[193] G. Wiatrowski, D. Baldomir, K. Warda, M. Pereiro, L. Wojtczak, and J. E. Arias, J. Magn. Magn. Mater. **277**, 285 (2004).

[194] R. Q. Hood, L. M. Falicov, and D. R. Penn, Phys. Rev. B **49**, 368 (1994).

[195] P. Zahn, N. Papanikolaou, F. Erler, and I. Mertig, Phys. Rev. B **65**, 134432 (2002).

[196] H. C. Herper, L. Szunyogh, P. Entel, and P. Weinberger, Phys. Rev. B **68**, 134421 (2003).

[197] X. Qian and W. Hubner, Phys. Rev. B **67**, 184414 (2003).

[198] S. Mirbt, B. Johansson, and H. Skriver, Phys. Rev. B **53**, R13310 (1996).

[199] J. L. Pérez-Díaz and M. C. Muñoz, Phys. Rev. B **53**, 13583 (1996).

[200] P. B. Visscher and H. Zhang, Phys. Rev. B **48**, 6672 (1993).

[201] P. D. Johnson, K. Garrison, Q. Dong, N. V. Smith, D. Li, J. Mattson, J. Pearson, and S. D. Bader, Phys. Rev. B **50**, R8954 (1994).

[202] R. E. Camley and J. Barnas, Phys. Rev. Lett. **63**, 664 (1989).

[203] K. Warda, L. Wojtczak, D. Baldomir, and M. Pereiro, Surf. Rev. Lett. **8**, 271 (2001).

[204] M. Ziese and M. J. Thornton, *Spin Electronics* (Springer-Verlag, Berlin, 2001).

[205] K. Fuchs, Proc. Cambridge Philos. Soc. **34**, 100 (1938).

[206] E. H. Sondheimer, Adv. Phys. **1**, 1 (1952).

[207] M. A. M. Gijs, S. K. J. Lenczowski, and J. B. Giesbers, Phys. Rev. Lett. **70**, 3343 (1993).

[208] K. M. Schep, P. J. Kelly, and G. E. W. Bauer, Phys. Rev. B **57**, 8907 (1998).

[209] E. E. Fullerton, D. M. Kelly, J. Guimpel, and I. K. Schuller, J. Magn. Magn. Mater. **184**, 275 (1998).

[210] J. M. Colino, I. K. Schuller, V. Korenivski, and K. V. Rao, Phys. Rev. B **54**, 13030 (1996).

[211] M. Velez and I. K. Schuller, J. Magn. Magn. Mater. **184**, 275 (1998).

[212] J. E. Mattson, M. E. Brubaker, C. H. Sowers, M. Conover, Z. Qiu, and S. D. Bader, Phys. Rev. B **44**, 9378 (1991).

[213] Z. Q. Qiu, J. E. Mattson, C. H. Sowers, U. Welp, and S. D. Bader, Phys. Rev. B **45**, 2252 (1992).

[214] S. S. P. Parkin, Phys. Rev. Lett. **71**, 1641 (1993).

[215] J. Santamaria, M.-E. Gomez, M.-C. Cyrille, C. Leighton, K. M. Krishnan, and I. K. Schuller, Phys. Rev. B **65**, 012412 (2001).

[216] D. R. Yarkony, ed., *Modern Electronic Structure Theory* (World Scientific, Singapore, 1995), vol. II, p. 1191.